

This electronic thesis or dissertation has been downloaded from the King's Research Portal at <https://kclpure.kcl.ac.uk/portal/>



## Development of a peripheral nerve repair device

Bath, Aran

*Awarding institution:*  
King's College London

The copyright of this thesis rests with the author and no quotation from it or information derived from it may be published without proper acknowledgement.

### END USER LICENCE AGREEMENT



Unless another licence is stated on the immediately following page this work is licensed

under a Creative Commons Attribution-NonCommercial-NoDerivatives 4.0 International

licence. <https://creativecommons.org/licenses/by-nc-nd/4.0/>

You are free to copy, distribute and transmit the work

Under the following conditions:

- Attribution: You must attribute the work in the manner specified by the author (but not in any way that suggests that they endorse you or your use of the work).
- Non Commercial: You may not use this work for commercial purposes.
- No Derivative Works - You may not alter, transform, or build upon this work.

Any of these conditions can be waived if you receive permission from the author. Your fair dealings and other rights are in no way affected by the above.

### Take down policy

If you believe that this document breaches copyright please contact [librarypure@kcl.ac.uk](mailto:librarypure@kcl.ac.uk) providing details, and we will remove access to the work immediately and investigate your claim.

# Development of a Peripheral Nerve Repair Device

Aran Singh Batth

Thesis submitted in partial fulfilment of the degree of Doctor of  
Philosophy, King's College London

MMXIX

King's College London  
Faculty of Dentistry, Oral and Craniofacial  
Sciences  
Centre for Oral, Clinical and Translational  
Sciences



ਇਹ ਕਿਤਾਬ ਬੀਜੀ ਨੂੰ ਸਮਰਪਿਤ ਹੈ ।

**Aut viam inveniam aut faciam**

## I: Abstract

This thesis focuses on engineering a repair strategy for use in peripheral nerve tissue after transection injuries. With an estimated 300,000 new cases of peripheral nerve injury reported in Europe each year, the socioeconomic cost of these injuries is multifactorial (Chiardelli and Chiono, 2006). Loss of nerve function often leads to long-term disability and chronic neuropathic pain, which dramatically reduces the number of quality adjusted life years (QALYs) post-injury (Siemionow and Brzezicki., 2009; Ciaramitaro et al., 2010). Some research suggests that nerve repair surgery results in a cost effective increase in number of QALYs and suggests that this field warrants further research (Wali et al., 2017). Further, nerve injury has been shown to correlate with post-traumatic stress disorder, especially when loss of function persists longer than 12 months (Miller et al., 2017). 360,000 people in the US suffer paralysis resulting from upper limb trauma alone, which suggests that the total number of patients with peripheral nerve injury (PNI) is much larger and means a large proportion of the population suffer with a nerve defects and their complications. Often, PNI is concomitant with multiple other acute traumas resulting from incidents such as motor vehicle accidents. Therefore peripheral nerve repair (PNR) is withheld as repair of other traumas is prioritised (Gin-Shaw and Jorden, 2002). Evidence suggests withholding PNR reduces the efficacy of regeneration and if sub-functional repair occurs this has a long-term negative effect on patient well-being and ability to self-care (Faroni et al., 2015). Nerve tissue injury leads to degeneration of functional neural cells and the loss of effective communication between the peripheral nerve and nervous system at large, meaning many vital neurological reflexes are lost. Effective nerve repair strategies that expedite recovery are vital to preventing long term disability and improving patient quality of life.

The current gold-standard of PNR involves use of autologous nerve tissue, which results in comorbidities, and lack of reliable results (autograft repair methods) (di Summa et al., 2014). However, the development of tissue engineering constructs to encourage peripheral nerve regeneration represents an alternative therapy to autograft. Provision of a synthetic implant, a Nerve Guidance Conduit (NGC), is designed to mimic nerve tissue and encourage infiltration by endogenous glial cells (Schwann cells) and neural cell processes (axons) across the graft (Barton et al., 2017).

In contrast to studies that solely focus on the biological events that take part following peripheral nerve injury, this thesis presents an engineering approach to create a more functional design for a synthetic NGC. There is a lack of information related to how regenerating nerve tissue extends through synthetic graft environments and the long-term effect on the regenerated tissue function. This thesis provides a physical solution to the problems encountered in guiding axonal regeneration to establish re-connection with its effector organ. The proposed implant provides a platform for healthy nerve growth within the critical time and length requirements for the animal model studied (the rat Sciatic nerve repair model). If the injury is greater than a critical length (which varies between the specific nerve and specific species), the probability of complete regeneration is low (Petcu et al., 2018). For example, in the rat model the critical length has been evaluated as 1.0 cm and often repaired within 3 months in the rat Sciatic nerve (Mokarizadeh et al., 2016; Tsujimoto et al., 2017).

A novel NGC was designed, featuring properties of flexibility, inertness, biocompatibility and capability of fast implantation with a surgery time of 15 minutes. These design criteria were the focus for the material selection process of poly(amide-6,6) (PA6,6), collagen Type 1 and chitosan, which was validated for in vivo use by in vitro assays, and designed to assess factors including cell adhesion, cytotoxicity, cell differentiation and cell migration.

The NG108-15 neuroblastoma/glioma cell line was used in conjunction with primary Schwann cells to assess the biological response. It was demonstrated that PA6,6 can be used as a substrate for neural tissue engineering applications, showing that neurons remain excitable when cultured on these substrates. Further, PA6,6 supported significant levels of cell proliferation and neurite extension. A bovine collagen Type 1/ chitosan hydrogel was also investigated, demonstrating a supportive substrate for neuroglial interaction and growth, which was validated using Dorsal Root Ganglia explant cultures. These data were used to translate these materials into the novel NGC, which was further examined in vivo with functional assessment (algesimetry, mechanical sensation, paw spreading and histology).

## I: Contents

I Abstract	2
II List of Figures	11
III List of Tables	17
IV List of Abbreviations	18
<u>Chapter 1: Literature Review</u>	20
1.1 Basic Neuroscience	20
1.1.1 Historical Reference to the Nervous System	20
1.1.2 Peripheral Nerve Anatomy	21
1.1.3 Neuron Structure	23
1.1.4 Neuron Function and Electrophysiology	27
1.1.5 Myelination of Peripheral Neurons	28
1.2 Peripheral Nerve Repair	32
1.2.1 Current 'Gold Standard' of Nerve Repair	33
1.2.2 Prevalence of Nerve Injuries	34
1.2.3 Nerve Injury Classification	38
1.2.4 Evaluation of the need for Improved Repair of Peripheral Nerve	42
1.2.5 Surgical Decisions in Peripheral Nerve Repair	42
1.3 Nerve Conduits	44
1.3.1 Rationale for Nerve Conduits	44
1.4 Materials for Peripheral Nerve Regeneration	45
1.4.1 Biopolymers	46
1.4.2 Collagen	52
1.4.3 Chitosan	53
1.4.4 Gelatin	54
1.4.5 Laminin	54
1.4.6 Agarose	55
1.4.7 Alginate	56
1.4.8 Hyaluronic Acid	56
1.4.9 Silk Fibroin	57

1.4.10 Biogenic Conduits	58
1.4.11 Acellular Conduits	58
1.4.12 Synthetic Materials	58
1.4.13 Synthetic NGCs	60
1.5 Fabrication of NGCs	62
1.5.1 Design Specifications	68
1.5.2 Adjunctive Healing Techniques to Nerve Conduits	70
1.5.2.1 Electrical Stimulation	70
1.5.2.2 Molecule-mediated therapy	71
1.5.2.3 Cellular Therapies	71
1.5.2.4 Schwann Cell Therapies	72
1.6 Clinical Trials and Data on Nerve Guides	73
1.7 Summary	75
1.8 Aims	75
1.9 Objectives	76
<u>Chapter 2: Design of a Nerve Conduit Medical Device</u>	77
2.1 Design Inputs	77
2.1.1 Intended Application	77
2.1.2 User Requirements (for the Surgeon)	78
2.1.2.1 Length	78
2.1.2.2 Diameter	81
2.1.2.3 Flexibility	81
2.1.2.4 Sterilisability	82
2.1.2.5 Handling Characteristics	82
2.1.2.6 Supporting Axonal Growth within the Luminal Compartment	82
2.1.3 Recipient Requirements (Patient)	82
2.1.4 Material Chemical and Physical Requirements	83
2.1.5 Design Inputs Acknowledged for Medical Device Manufacture	86
2.2 Design Outputs	87
2.3 Outcomes and Proposed Design	89

2.4 Conclusion on Design and Fabrication Methods	90
<u>Chapter 3: Model of Peripheral Nerve Regeneration In Vitro</u>	92
3.1 Introduction	92
3.2 Materials and Methods	95
3.2.1 Cell Culture of NG108-15 Cells	95
3.2.2 Cell Culture of Schwann Cells	95
3.2.3 Cell Counting	96
3.2.4 Quantification of Neurite Length	96
3.2.5 Live/Dead Cell Viability Staining	99
3.2.6 Alamar Blue Assay	99
3.2.7 Determination of Cell Adherence	99
3.2.8 Immunocytochemical Staining of NG108-15 and Schwann Cells	100
3.2.9 Polyamide Classification	101
3.2.10 Cell Culture on Polyamides	102
3.2.11 Attenuated Total Reflection Fourier Transform Infrared Spectroscopy (ATR-FTIR)	102
3.2.12 Dynamic Scanning Calorimetry DSC)	103
3.2.13 Tensile Testing of Polyamide 6,6	103
3.2.14 Electrophysiological Evaluation of NG108-15 cells on PA 6,6	104
3.2.15 Statistics	105
3.3 Results	106
3.3.1 Evaluation of NG108-15 and Cortical Cells as model cells	106
3.3.2 Determination and optimization of screening protocol to assess NG108-15 cell viability on materials	111
3.3.3 NG108-15 Differentiation Analysis	114
3.3.4 Primary Schwann Cell Culture	116
3.3.5 Investigation of NG108-15 adherence to Polyamide 6,6 materials	118
3.3.6 Quantification of NG108-15 and Schwann cell Viability and Adherence on PA6,6 mesh	120



3.3.7 Action Potential Recordings from NG108-15 cells cultured on PA6,6	124
3.3.8 Fourier Transform Infrared Spectroscopy (FTIR) of Polyamides	126
3.3.9 Dynamic Scanning Calorimetry of Polyamides Tested	127
3.3.10 NG108-15 and Schwann Cell Culture on Polyamides	129
3.3.11 Proliferation of Schwann Cells and NG108-15 Cells on Polyamide	130
3.3.12 Schwann Cell Morphology Quantification on Polyamide	131
<b>Substrates</b>	
3.3.13 Quantification of Schwann Cell Area	132
3.3.14 Effect of Polyamide Hot Embossing on Schwann Cell Alignment	136
3.3.15 Tensile Strength Testing of Polyamide 6,6 Samples	138
3.4 Discussion	140
3.4.1 Cell Culture	140
3.4.2 Materials Tested	143
3.4.3 Polyamides	144
3.4.4 Neural Differentiation	145
3.4.5 Material Properties	147
<b><u>Chapter 4: Evaluation of a Neural-Supportive Hydrogel System as a NGC Filler</u></b>	<b>149</b>
<b><u>Material</u></b>	
4.1 Introduction	149
4.2 Methods and Materials	151
4.2.1 Cell Culture	151
4.2.2 Hydrogel Preparation	151
4.2.3 Chitosan-Collagen Blend Preparation	152
4.2.4 Attenuated Total Reflection Fourier-Transform Infrared Spectroscopy (ATR-FTIR)	152
4.2.5 Dynamic Scanning Calorimetry (DSC)	152
4.2.6 Atomic Force Microscopy (AFM)	153
4.2.7 Scanning Electron Microscopy (SEM)	153
4.2.8 MTT Assay	153

4.2.9 Alamar Blue Assay	154
4.2.10 Live Dead Analysis	154
4.2.11 Immunocytochemical Analysis	154
4.2.12 Schwann Cell Conditioned Media Experiment	155
4.2.13 NG108-15/Schwann Cell Co-Culture Experiments	155
4.2.14 DRG Explant Study	155
4.2.15 Cell Migration Study	157
4.2.16 Gliospheroid Culture	157
4.2.17 Image Analysis (Morphological Characterisation)	157
4.2.18 Statistics	157
4.3 Results	159
4.3.1 Evaluating the effect of Increasing Hydrogel Concentration on	159
Cytotoxicity	
4.3.2 Live/ Dead Viability Staining	162
4.3.3 Fourier Transform Infrared Spectroscopy (FTIR)	167
4.3.4 Dynamic Scanning Calorimetry (DSC)	168
4.3.5 Scanning Electron Microscopy (SEM)	170
4.3.6 Atomic Force Microscopy (AFM)	172
4.3.7 Cell Proliferation Assessment with Alamar Blue Assay	175
4.3.8 Cell Mask Staining of NG108-15 Cells	177
4.3.9 Cell Mask Staining and Morphometric Analysis of Schwann Cells	179
4.3.10 Differentiation Analysis of NG108-15 Cells	184
4.3.11 Neurite Quantification of NG108-15 cells Cultured on	188
Hydrogels	
4.3.12 Cell Density Calculations on Hydrogels	191
4.3.13 NG108-15 Differentiation with Schwann Cell Conditioned Media	193
4.3.14 Schwann Cell-Mediated NG108-15 Differentiation Analysis	195
4.3.15 Dorsal Root Ganglia Organotypic Culture	198
4.3.16 Schwann Cell Migration	202
4.3.17 Gliospheroid Encapsulation and Migration Study	204
4.4 Discussion	206

4.4.1 Biocompatibility of Hydrogel materials with NG108-15 cells	206
4.4.2 Selection of Chitosan and Collagen and Mechanical Analysis	207
4.4.3 Cell Proliferation and Adherence	208
4.4.4 Neuroglial-Material Interaction Analysis	209
4.4.5 Cell Migration Analyses	210
<u>Chapter 5: Animal Trial for Nerve Guidance Conduit</u>	212
5.1 Introduction	212
5.2 Methods and Materials	214
5.2.1 NGC Fabrication	214
5.2.2 Animals	214
5.2.3 Surgical Procedures	214
5.2.4 Von Frey Testing	216
5.2.5 Hargreaves Testing	216
5.2.6 Sciatic Functional Index (SFI)	217
5.2.7 Tensile Testing of Conduit Suture Method	218
5.2.8 Histological Analysis	218
5.2.9 Statistics	219
5.3 Results	220
5.3.1 Weight Data from Trial	220
5.3.2 Von Frey Data from Trial	220
5.3.3 Hargreaves Data from Trial	222
5.3.4 Sciatic Functional Index (SFI) Data from Trial	222
5.3.5 Tensile Testing of NGC Adhesion Methods	224
5.3.6 Weight Measurements for Full Experimental Subjects	226
5.3.7 Von Frey Experimental Data	227
5.3.8 Hargreaves Test Analysis	229
5.3.9 Sciatic Functional Index (SFI) Analysis	231
5.3.10 Haematoxylin and Eosin Staining	232
5.3.11 Luxol Fast Blue Staining	238
5.4 Discussion	247

5.4.1 NGC Final Design	247
5.4.2 Behavioural Data	248
5.4.3 Histology	250
5.5 Supplementary Figures	253
<u>Chapter 6: Thesis Discussion</u>	255
6.1 Discussion	255
6.2 Conclusion	259
<u>Chapter 7: Future Work</u>	260
V Acknowledgements	262
VI Publications/ Abstracts	263

## II: List of Figures

Chapter	Figure Number	Figure Title	Page Number
1	1	Margarita Philosophica cum additionibus novis	21
1	2	Spinal cord (monochrome) with spinal nerve roots and spinal nerve from Gray's Anatomy (1918)	22
1	3	Schematic of General Neuron Structure	24
1	4	Schematic of Hippocampal Neuron Polarity	26
1	5	Electron micrograph of myelination of mouse sensory neuron	29
1	6	Intraoperative Images of Sunderland Classification III and V nerve injuries	41
1	7	Flow diagram of surgical outcomes for nerve injuries of differing length in human	43
1	8	Schematic of Nerve Repair using NGCs	49
1	9	PEG Nerve Guide repair of common fibular nerve in Thy-1YFP-H mouse	61
2	1	Schematic to describe NGC design features	78
2	2	Histogram showing lengths of conduits used in rat sciatic nerve transection models from papers published between 2011 and 2018	79
2	3	Bar chart of mean length of nerve gap injuries tested in NGC models for each species from papers published between 2011 and 2018	79
2	4	Bar chart showing frequency of trials conducted for each species from papers published between 2011 and 2018	80
2	5	Williams and Brady Innovation tool used in the workshop for NGC design ideation	84
2	6	NGC design ideas generated from the group workshop	85

2	7	Schematic of final NGC design and prototype examples	91
3	1	Schematic of measurements taken to quantify neurite outgrowth	97
3	2	NG108-15 cell differentiation at days 3 and 7 quantification using Neuron J tracing tool	98
3	3	Images to illustrate electrode production for patch clamping	105
3	4	Quantification of NG108-15 cell number and cumulative length of neurites as observed using brightfield microscopy	108
3	5	Brightfield images of NG108-15 cells differentiated in media containing IBMX/PGE1 (differentiation media) or control (1% FCS)	109
3	6	Quantification of neurite outgrowth of NG108-15 differentiated with IBMX/PGE1 (differentiation media) or 1% FCS only (control)	110
3	7	Calcein AM and Ethidium Homodimer-1 staining of NG108-15 cultured on prospective materials	112
3	8	Quantification of Cell Viability of NG108-15 cells on prospective materials	113
3	9	Widefield epifluorescence and Expression of Neural Differentiation Markers for NG108-15 cells	115
3	10	Schwann cell culture images including S100 labelling with epifluorescence widefield microscopy and quantification of cell proliferation	117
3	11	Epifluorescence widefield microscopy and quantification of NG108-15 cell adherence to PA Mesh, Micromesh and Monofilament	119
3	12	Calcein AM and Ethidium Homodimer-1 staining of NG108-15 and Schwann cells cultured on PA6,6 Mesh	122

3	13	Quantification of cell viability, percentage increase in alamar blue signal and cell density of NG108-15 and Schwann cells cultured on PA6,6 Mesh	123
3	14	Action Potential recording representative traces and box-plots for the peak membrane potential recorded for NG108-15 cells cultured on control and PA6,6 in differentiation media and NG108-15 cells cultured in growth media (control)	125
3	15	FTIR Spectra of PA materials tested (Transmittance)	127
3	16	DSC Thermograms for PA materials investigated	128
3	17	Spinning disc confocal microscopy of NG108-15 and Schwann cells cultured on PA and stained with CellMask stain at 24 and 72 hours	133
3	18	Quantification of neurite outgrowth of NG108-15 cells cultured on PA	134
3	19	Quantification of Schwann cell morphology, cell area and proliferation, cultured on PA	135
3	20	Representative images of aligned Schwann cells following hot embossing of PA6,6 material and quantification of alignment	137
3	21	Quantification of tensile strength of PA6,6 samples	139
4	1	Schematic of DRG dissection protocol	156
4	2	Quantification from MTT assay of NG108-15 cells cultured on prospective hydrogels	161
4	3	Calcein AM and Ethidium Homodimer-1 staining of NG108-15 cells on prospective hydrogels	164
4	4	Cell viability quantification for cells cultured on COL and CS	165
4	5	Cell viability quantification for cells cultured on AGN, MCL and HA	166

4	6	FTIR Spectra of CS, COL and blend materials (CC and CC2) tested (Transmittance)	167
4	7	DSC Thermograms for CS, CC, CC2 and COL	169
4	8	SEM images of CS, CC, CC2 and COL	171
4	9	Heat map of AFM measurements showing Young's modulus of 256 sampling areas and representative force curve from AFM study	173
4	10	Histograms of Young's Modulus distribution measured on Cs, CC, CC2 and COL hydrogels	174
4	11	Change in absorbance during alamar blue assay for NG108-15 and Schwann cells cultured on CS, CC, CC2 and COL	176
4	12	CellMask staining of NG108-15 cells cultured on CS, CC, CC2 and COL at days 3 and 7	178
4	13	3D plots of NG108-15 cells cultured on CS, CC, CC2 and COL	181
4	14	CellMask staining of Schwann cells cultured on CS, CC, CC2 and COL at days 3 and 7	182
4	15	Quantification of Schwann cell morphology at days 3 and 7 on CS, CC, CC2 and COL	183
4	16	Immunocytochemical staining of NG108-15 cells cultured on CS, CC, CC2 and COL for MAP2 expression	185
4	17	Immunocytochemical staining of NG108-15 cells cultured on CS, CC, CC2 and COL for Ki-67 expression	186
4	18	Quantification of MAP2 and Ki-67 expression in NG108-15 cells cultured on CS, CC, CC2 and COL	187
4	19	Immunocytochemical staining of NG108-15 cells cultured on CS, CC, CC2 and COL for BIII Tubulin at days 3 and 7	189
4	20	Quantification of neurite outgrowth of NG108-15 cells cultured on CS, CC, CC2 and COL	190



4	21	Quantification of cell density of both NG108-15 and Schwann cells at days 3 and 7 cultured on CS, CC, CC2 and COL	192
4	22	Brightfield images of NG108-15 cell differentiation assessment with Schwann cell conditioned medium compared to differentiation medium (control)	194
4	23	Immunocytochemical staining of BIII Tubulin expression in NG108-15 cells co-cultured with Schwann cells on CTRL, CS, CC, CC2 and COL	196
4	24	Quantification of neurite length of NG108-15 co-culture with Schwann cells	197
4	25	Immunocytochemical staining of BIII Tubulin expression in DRGs cultured on CTRL, CC, CC2 and COL	199
4	26	Brightfield images of DRGs cultured on CTRL, CC, CC2 and COL	200
4	27	Quantification of neurite outgrowth from DRGs cultured on CTRL, CC, CC2 and COL materials.	201
4	28	Representative traces of the track length of Schwann cells cultured on CS, CC, CC2 and COL over 24 hours	203
4	29	Spinning disc confocal fluorescent micrographs of S100 stained Schwann cells, counterstained with Hoechst 33342, by immunocytochemistry of gliospheroids cultured on CS, CC, CC2 and COL	205
5	1	Representative paw prints of CONTRA and IPSI sides immediately after surgery and 130 DPO	217
5	2	Weights of animals from 30 day NGC trial and Von Frey quantification	221
5	3	Quantification of Hargreaves testing and SFI testing during 30 day NGC trial	223
5	4	Tensile testing of NGC adhesion methods	225

5	5	Raw weight data of each animal used in Sciatic nerve transection and repair model	226
5	6	Quantification of Von Frey measurements for Empty NGC, Filled NGC and Autograft groups	228
5	7	Quantification of Hargreaves testing for Empty NGC, Filled NGC and Autograft groups	230
5	8	Quantification of SFI for Empty NGC, Filled NGC and Autograft groups	231
5	9	Schematic of histology sectioning protocol, example staining of a healthy nerve imaged in transverse and image of micro-grooved NGC PA6,6	233
5	10	H&E staining of control tissue from 30 day NGC trial	234
5	11	H&E staining of tissue from Empty NGC group	236
5	12	H&E staining of tissue from Filled NGC group	237
5	13	H&E staining of tissue from Autograft group	239
5	14	LFB staining of tissue from Autograft group	240
5	15	LFB staining of tissue from Empty NGC group	241
5	16	LFB staining of tissue from Filled NGC group	242
5	17	Quantification of neuron density and myelin thickness from LFB staining	245
5	18	Quantification of G-ratio for myelination analysis	246
5	S1	Images to show the implant NGC and intra-operative images	254

### III: List of Tables

Chapter	Table Number	Title	Page Number
1	1	Comparison of Meta-Analytical data to show prevalence of PNI by cause, year and injury site	35
1	2	Summary Table of Sunderland Classifications for Nerve Injury (1951)	39
1	3	Search Results of Recent Papers by Specific Term	46
1	4	Analysis of all papers related to biopolymers satisfying criteria for table 3	48
1	5	Analysis of conduit fabrication methods	64
1	6	Comparison of design features of nerve guides	69
1	7	Comparative table of Clinical Data on material Use	74
2	1	Additional design inputs acknowledged by this research	87
2	2	Design outputs	88
3	1	FTIR wavelength of transmittance with corresponding functional chemistry from polaymide samples	126
4	1	FTIR wavelength of transmittance with corresponding functional chemistry from CS, CC, CC2 and COL samples	168
5	S1	Table showing patterns of Von Frey stimuli responses and conversion values to calculate 50% PWT	253

#### IV: List of Abbreviations

<b><u>Abbreviation</u></b>	<b><u>Explanation</u></b>
<b>2PD</b>	Two Point Discrimination
<b>AFM</b>	Atomic Force Microscopy
<b>AGN</b>	Sodium Alginate
<b>ATR</b>	Attenuated Total Reflection
<b>BDNF</b>	Brain Derived Neurotrophic Factor
<b>BIII</b>	Beta-III Tubulin
<b>BSA</b>	Bovine Serum Albumin
<b>C4D</b>	Centre for Design, Cranfield University
<b>cAMP</b>	Cyclic Adenosine Monophosphate
<b>CC</b>	Chitosan/ Collagen 1:1 Blend
<b>CC2</b>	Chitosan/ Collagen 1:2 Blend
<b>CNS</b>	Central Nervous System
<b>COL</b>	Bovine Collagen Type 1
<b>CONTRA</b>	Contralateral Side (Non-Operated Side)
<b>CS</b>	Chitosan
<b>DMEM</b>	Dulbecco's Modified Eagle Medium
<b>DPO</b>	Days Post Operation
<b>DSC</b>	Dynamic Scanning Calorimetry
<b>ECM</b>	Extracellular Matrix
<b>EMG</b>	Electromyography
<b>FCS</b>	Fetal Calf Serum
<b>FDA</b>	Food and Drug Administration
<b>FGF</b>	Fibroblast Growth Factor
<b>FTIR</b>	Fourier Transform Infrared Spectroscopy
<b>H&amp;E</b>	Haematoxylin and Eosin Staining
<b>HA</b>	Hyaluronic Acid
<b>IPSI</b>	Ipsilateral Side (Operated Side)
<b>LFB</b>	Luxol Fast Blue Stain
<b>MAP2</b>	Microtubule Associated Protein 2

<b>MCL</b>	Methylcellulose
<b>MTS</b>	MTT Solution
<b>MTT</b>	3-(4,5-dimethylthiazol-2-yl)-2,5-diphenyltetrazolium bromide
<b>NCV</b>	Nerve Conduction Velocity
<b>NG</b>	NG108-15 Cells
<b>NGC</b>	Nerve Guidance Conduit
<b>NGF</b>	Nerve Growth Factor
<b>PA</b>	Polyamide
<b>PBS</b>	Phosphate Buffered Saline
<b>PDMS</b>	Poly(dimethylsiloxane)
<b>PFA</b>	Paraformaldehyde
<b>PNI</b>	Peripheral Nerve Injury
<b>PNR</b>	Peripheral Nerve Regeneration
<b>PNS</b>	Peripheral Nervous System
<b>PWT</b>	Paw Withdrawal Threshold
<b>RGD</b>	Arginylglycylaspartic Acid
<b>S100</b>	S100 Protein, Neural Crest-Derived Cell Marker
<b>SC</b>	Rat Sciatic Nerve Derived Schwann Cells
<b>SD</b>	Standard Deviation
<b>SEM</b>	Standard Error of the Mean
<b>SFI</b>	Sciatic Functional Index

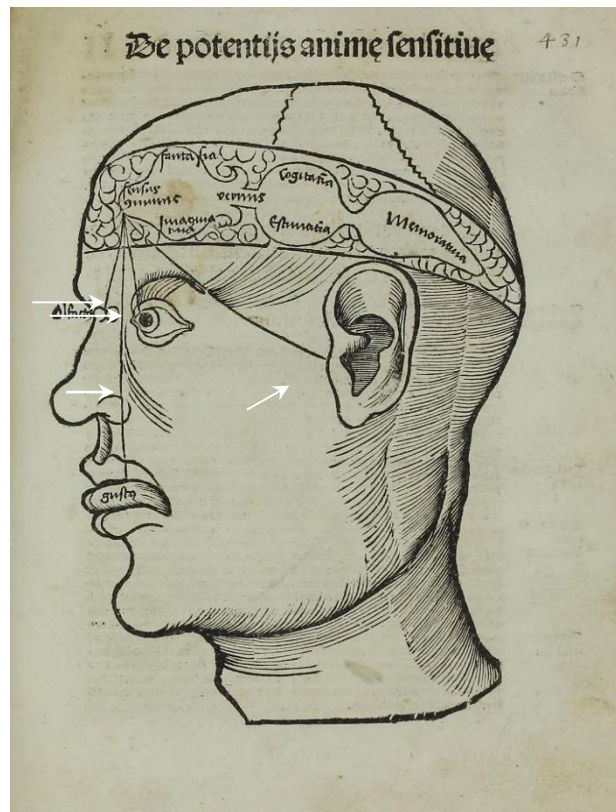
## Chapter 1: Literature Review

Research into peripheral nerve regeneration incorporates the disciplines of neuroscience, materials science and clinical neurology, all of which inform tissue engineering mechanisms to enhance neural regeneration. This literature review focuses on the current state of the art and highlights where technologies could be improved. Additionally previous key results in peripheral nerve repair in animal trials and clinical outcomes are reviewed to provide a foundation to the work undertaken.

### 1.1 Basic Neuroscience

#### 1.1.1 Historical Reference to the Nervous System

Roman physician Galen of Pergamon, active circa 200 AD is argued to have first attributed sensation and movement to the anatomy of nerves (Viale, 2004). By the renaissance, 16<sup>th</sup> century, peripheral nerves were believed to be offshoots of the brain; Reisch draws offshoots from the 'sensus communis', from where the metaphor of common sense is derived, to indicate an area of central instruction within the head (Figure 1.1; Reisch, 1517). Despite medieval theories not being based on dissection, the separation of central and peripheral areas within the nervous system had already been conceived and both domains were speculated to be critical for adequate communication between thoughts and consequential actions. Galen referred to the idea that messages are transported from the head to the body to support human function; the theory stands today.



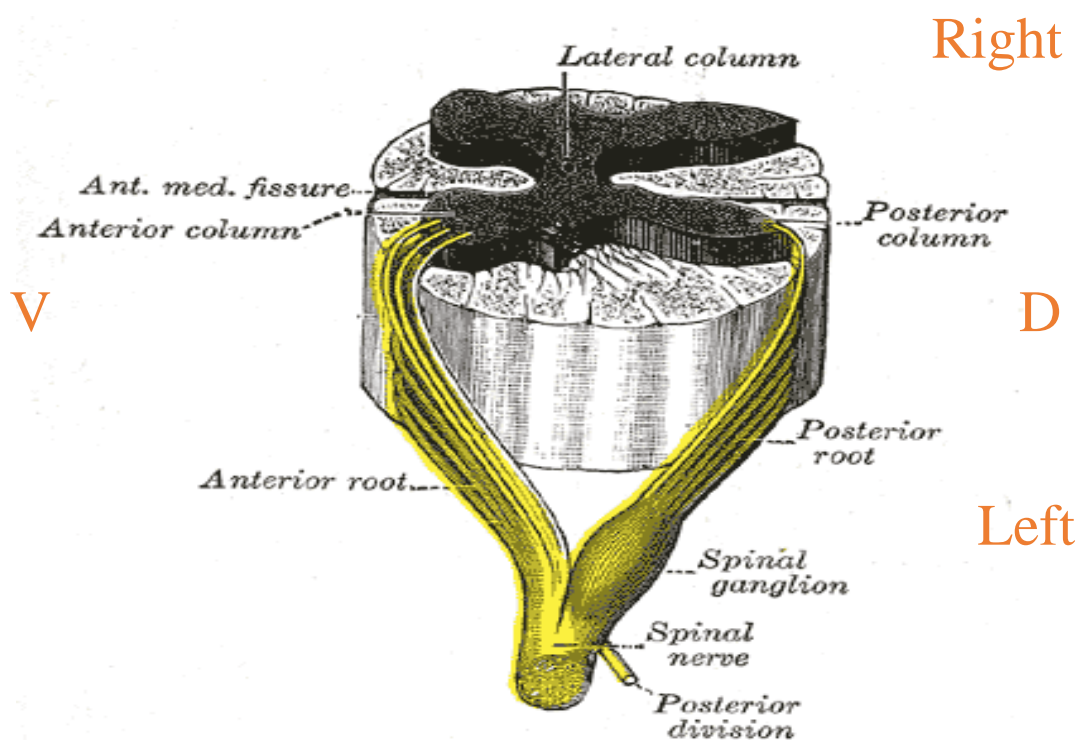
**Figure 1:** *Margarita Philosophica cum additionibus novis*. The nerve fibres described are shown in the image as black lines descending from the *sensus communis* to give perception of senses such as olfaction and gustation as indicated in the image, nerves are shown by white arrows (Reisch, 1517).

Key ideas in Neuroscience have been reviewed to provide context for the experiments reported in this thesis. Neurons are highly specialised cells capable of signal processing and transduction. In nerve regeneration, the neural cells are injured and regenerate as reviewed in section 1.1.8. In this section, the importance of restoring neuron physiology is highlighted, as it allows for nerve to be functional in transducing neural signals.

### 1.1.2 Peripheral Nerve Anatomy

The nervous system is a communication system with a complex structure enabling stimuli to be integrated into actions through a network of neurons. This network aims to maintain the homeostasis a mammal's organ systems and allows for automatic or voluntary actions in response to external and internal stimuli. The nervous system is divided into the Central Nervous System (CNS), comprising the brain and spinal cord, and the Peripheral Nervous System (PNS), comprising nerves and ganglia (collections of neuronal cell bodies).

The PNS communicates information to and from the periphery, allowing communication between the CNS and peripheral tissues including muscles, organs and skin. Inhibitory fibres are also present as they refine the volume of information relayed to the central nervous system. PNS tissue may be itself an important filter of information, as well as a primary source (Melzack, 1996). The PNS comprises both spinal nerves and cranial nerves which convey information for many modalities including sensory, motor, proprioception, and pain perception. The autonomic nervous system coordinates involuntary actions, i.e. subconscious control. The autonomic nervous system includes both parasympathetic and sympathetic nerves, which often work with antagonistic effect. Further, the peripheral nervous system includes reflex arcs, which achieves control of effectors at the same spinal cord level without signalling neurons in the CNS. The premise for restoring neural connectivity by nerve repair is to ensure that peripheral information can be communicated as effectively as pre-injury levels.



**Figure 1.2:** Henry Gray, *Anatomy of the Body*, 1918. Spinal cord (monochrome) with spinal nerve roots and spinal nerve (highlighted in yellow). The dorsal surface is on the right (D) and ventral surface on the left (V). 'Right' and 'Left' refer to the patient's left and right sides if this were a dissection.

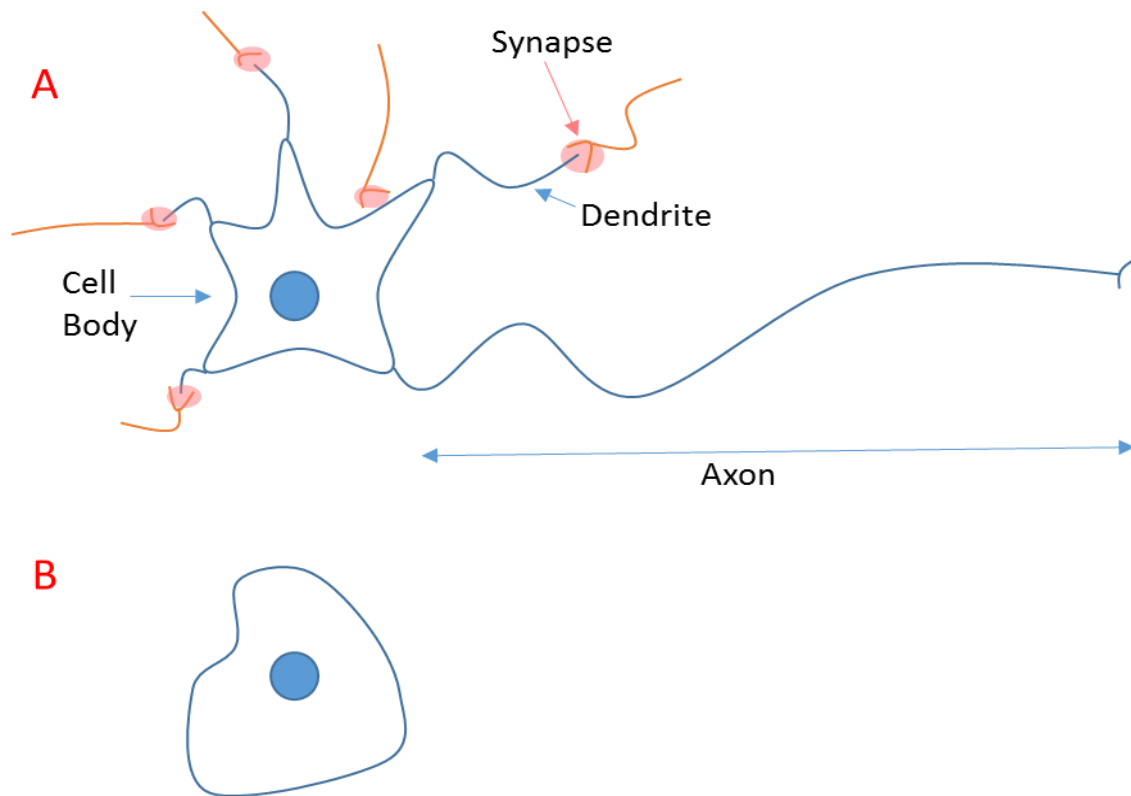


The peripheral nervous system contains the 12 pairs of cranial nerves and the 31 pairs of spinal nerves. The boundary of the peripheral versus central nervous systems is best understood as the point where the nerve roots leave the spinal cord, as the peripheral nervous system comprises all nerves external to the brain and spinal cord and is structurally dispersed throughout the body (Figure 1.2; Gray and Carter, 1918). For the cranial nerves, the distinction is similar as 12 paired nerves are distinguished as peripheral from the location where they sprout from the brainstem.

Cell bodies of the constituent neurons of the spinal nerves are housed within the spinal ganglia (Kozlova et al., 1997; Figure 1.2). In the PNS, neuronal cell bodies remain in ganglia, and their axons travel in 'nerve' bundles (Mazurek et al., 2001). Processes from the dorsal root ganglia carry sensory information into the central nervous system and are termed 'afferents' (Kruse et al., 1995; Gianino et al., 1996). Whereas sprouting from the anterior division of the spinal cord, neuronal processes of motor cells are called 'efferents'. Efferents primarily include motor neurons, which synapse onto skeletal muscle, or autonomic ganglia.

### 1.1.3 Neuron Structure

Neurons are arranged to provide a complex network of cells that make up the nervous system, capable of responding to exogenous and endogenous stimuli and eliciting responses. Neuron structure is conducive to receiving multiple incoming messages in the form of membrane depolarisations, as the neuron is highly branched and thus covers large receptive fields. Neurons generally contain specific domains including an axon, dendrites, synapses and a cell body (Figure 1.3).

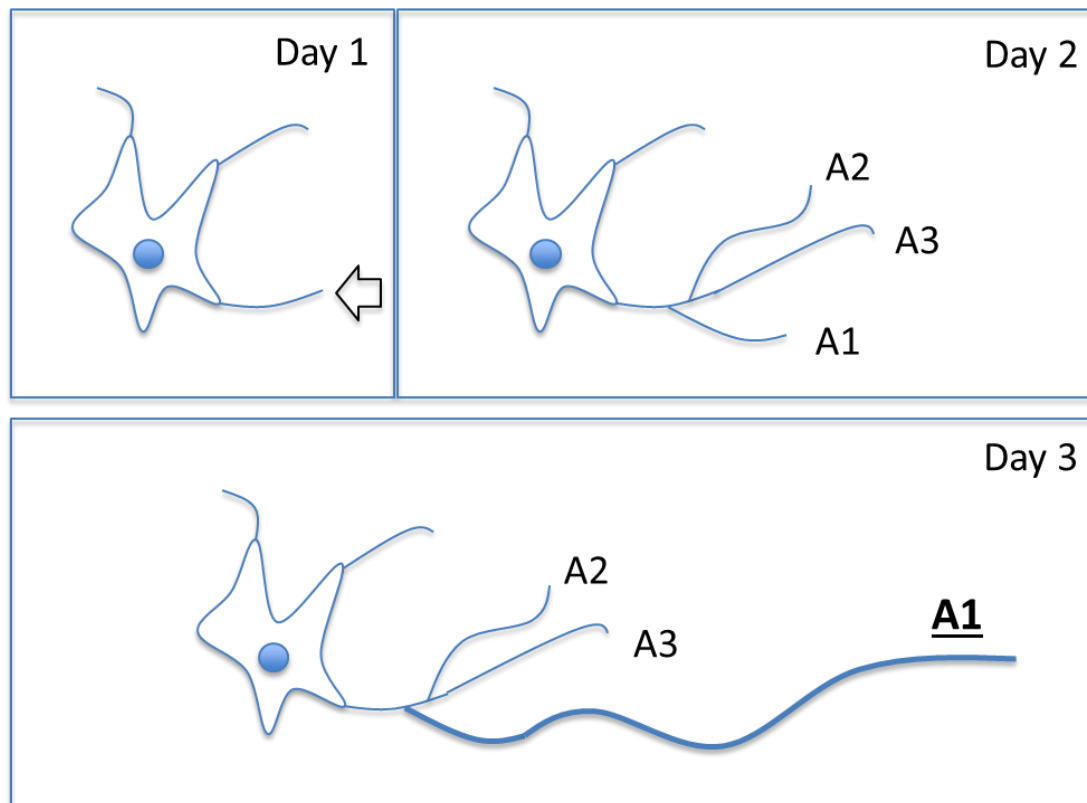


**Figure 1.3:** A schematic to represent general neuron structure (A) and a dissociated neuron (B). In 'A', the cell contains a cell body which houses the nucleus, several short processes which receive electrochemical information (dendrites) via synapses, and a long process to transmit information (the axon). Axons of synapsing cells onto the general neuron are coloured in orange. In 'B', the neuron has been dissociated from its network of dendrites and axons (i.e. these connections have been ruptured) and this cell can be placed in culture to encourage formation of new dendrites and axons.

The dendritic structure of neurons allows communication across remarkable distances at the cellular scale. Santiago Ramon Y Cajal used silver nitrate stain to provide evidence of connectivity of single cells between distinct brain regions within the nervous system (Carlos and Borrel, 2007). Electrophysiology has moved the field further by demonstrating synaptic transmission and providing an electrochemical basis for inter-neuronal communication (Robinson, 2001).

When cultured *in vitro*, neurons will adopt the structure first noted by Cajal *in vivo*; polarizing their morphology. Dissociation of hippocampal neurons has stood as the model of neuron polarisation since the mid-20<sup>th</sup> century; the *in vitro* environment rendering the cell capable of unilateral communication (Fig. 1.4; Dotti et al., 1988). After being plated, the spherical cells spread filopodia and small neurites alternate between retraction and

growth processes. One small neurite subsequently grows rapidly to form the major neurite called the axon. Although not fully understood, this may be related to the setting up of the 'axon initial segment', a dense region of voltage-gated sodium channels which serves to integrate membrane depolarisations, initiate the axon potential and is active during development (Wefelmeyer et al., 2016). These cells establish polarity and constantly refine by laying down permanent microtubules for maintenance of the neurites and temporary actin filaments organise to lead further spreading. Cytokines within the extracellular matrix (ECM) regulate polarisation in vivo including TAG1, brain-derived neurotrophic factor (BDNF), neurotrophin 3 (NT3), Transforming Growth factor  $\beta$  (TGF $\beta$ ), Wnt5a and semaphorin 3A (Funahashi et al., 2014).



**Figure 1.4:** Hippocampal neuronal polarity shown through a cartoon schematic at 1, 2 and 3 days *in vitro*. The axon is already assumed by day 1, as labelled by the black outline arrow. The axon branches (A1, A2 and A3) by day 2. By day 3, minor axonal branches and the major thicker in diameter branch (A1) is set up, creating an elaborate network of axons *in vitro* (adapted from Dotti et al., 1988).

Neural tissue engineering involves study of material-cell interactions to inform design of regeneration promoting environments. As neural circuits develop, the axon participates in path finding, interrogation of the physico-chemical environment by receptors stationed at the axon tip and growth cone (Stoeckli, 2018). The growth cone apparatus contains dynamic F-actin filaments, which allow extension. This results in axon growth, following integration of stimulatory and inhibitory guidance cues (de Ramon Francas et al., 2017).

Axon growth can be manipulated, particularly as axons will selectively grow on stimulatory molecules rather than inhibitory molecules adsorbed onto an isotropic substrate. This sets up a premise for developing *in vitro* models to monitor axon pathfinding. Ephrin A, for instance, repels retinal ganglion cell axons to ensure they synapse at the correct area in the lateral geniculate nucleus (Knöll et al., 2007).

Substrates in nerve tissue engineering must support infiltration of single axons for self-directed assembly of a functional nerve. Capable materials are reviewed in section 1.3. It is clear these data can instruct the subtle interactions between a growth cone, apparatus at the tip of an extending axon rich in receptors that integrate ECM ligands, and its environment (Vensi Basso et al., 2019). This is specifically relevant as during neuritogenesis, the process of extending neurites (precursors to dendrites and axons) by a neuron during differentiation (as in Figure 1.4). Neurites may degrade the Extracellular Matrix (ECM) to generate paths to extend through or bind onto ECM molecules. Materials that are porous and degradable by the neurite membrane may be used as a biomaterial for nerve repair as they must encourage neurite extension.

One mechanism that demonstrates this is the influence of proteolysis on neuritogenesis. Plasmin (active enzyme from plasminogen precursor) is a serine protease which cleaves fibrin and catalyzes laminin degradation, which are common peptides found in ECM (Sumi et al, 1992; Gutierrez-Fernandez et al., 2009). Expression of plasminogen activators u-PA and t-PA have been confirmed to be active in areas of axon growth such as the floor plate of the spinal cord (an early neuroectoderm structure found in the developing embryo whilst axons are directed to their effectors) and associated with differentiating sympathetic neurons including neuroblastoma cells (Krystosek and Seeds, 1981; Dent et al., 1993; Pittman et al., 1989). Engineering an environment conducive to axon growth may involve the combined use of stimulatory molecules and cleavable matrices rather than inert, pre-shaped micro-channels.

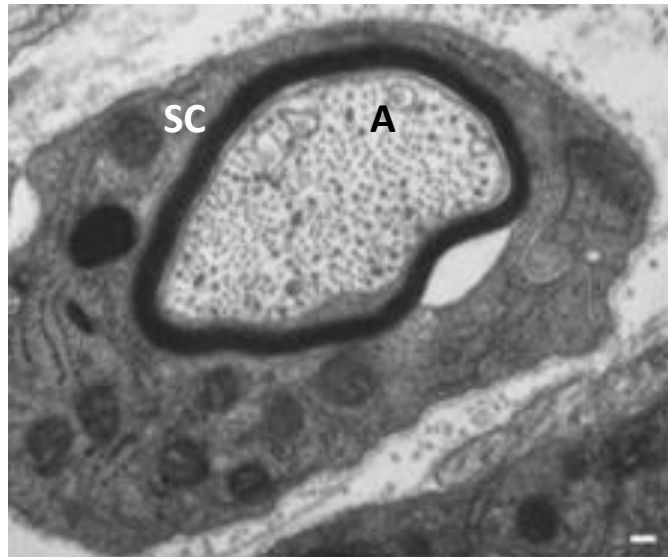
#### 1.1.4 Neuron Function and Electrophysiology

As neurons develop their morphology, the cells express ion channels on the membrane including axon and dendrite regions. Excitable neurons exchange information via electrochemical events by synaptic transmission (Koch, 2004). An unequal distribution of ions sets up an electrochemical gradient of each ion resulting in a potential difference being maintained called resting membrane potential ( $V_m$ ) (Purves et al., 2001).  $Na^+$ ,  $K^+$  and  $Cl^-$  membrane currents are dependent on the potential difference across the membrane, and ions flow down their concentration gradient as the membrane potential ( $V_m$ ) reaches the equilibrium potential for that ion, as demonstrated by Hodgkin and Huxley and expressed in the Nernst equation (Barnes, 1984; Hodgkin and Huxley, 1952).

Thus, a shift in membrane potential opens voltage-gated ion channels specific for that species and an action potential event, a process by which cells transmit electrical signals along their membranes i.e. neurotransmission, can occur. Channelopathies involve dysfunction of the main ion channels regulating excitable cell physiology, and have been shown to influence regeneration by affecting cell differentiation and axon outgrowth (Swayne and Wicki-Stordeur, 2012). Maintaining a hyperpolarised membrane may regulate cell differentiation whereas depolarisation may activate cell de-differentiation although the mechanism is not clear (Simanov et al., 2012). For example,  $K^+$  channels contribute heavily to hyperpolarizing the membrane, or reducing membrane potential under physiological conditions, such as the inward rectifying  $K_{ir}$  isoform which can stimulate proliferation in neural stem cells (Zhou et al., 2011). Therefore it may be helpful to study ion channel expression and activation to demonstrate the benefit or potential toxicity of biomaterials to cultured neurons (Vierbuchan et al., 2010). Reviewing basic neuroscience helps to identify markers of neural regeneration involved in neuritogenesis, excitability and axon pathfinding.

#### 1.1.5 Myelination of Peripheral Neurons

As well as neurons, the other major cell population of the PNS are the glial cells, which support neurons. Glial cells provide structural support to axons, maintain homeostasis, offer immune functions and help signal regenerative events (Milligan and Watkins, 2009; Robel et al., 2011). Within the PNS, the main glial cell is the Schwann cell, which functions to insulate ion currents involved in action potential propagation in axons of neurons and accelerate action potential velocity by salutatory conduction of signals across Nodes of Ranvier (Figure 1.5; Fields and Stevens-Graham, 2002). This is achieved by Schwann cells expressing myelin protein which is rich in lipid moieties that prevent the flow of ion currents. Electrogenic membrane transporters and voltage-gated ion channels expressed in neurons are also found in glia, however unlike in neurons the glial cells do not have excitable membranes (Fields and Stevens-Graham, 2002). This provides evidence that glia help in maintaining excitability of neurons by regulating availability of membrane channels and demonstrates that Schwann cells should also be present in regenerated nerve tissue.



**Figure 1.5:** Electron micrograph of mouse sensory axon (A) being myelinated by a Schwann cell (SC), dark band around the axon is provided by multiple layers of Schwann cell membrane. Scale bar 100nm. (Fields and Stevens-Graham, 2002).

Insulation of currents occurs by the winding of the Schwann cell membrane around the neuronal processes, often in excess of 20 layers, which has been hypothesised to be activity-dependent (Fields, 2009). Schwann cells form a myelin sheath by production of myelin and forming lamellar structures around nerve fibres. This increases nerve conduction by two orders of magnitude compared to non-myelinated fibres of similar diameter due to salutatory conduction (Frankenhaeuser, 1952). Ion channels are expressed at the node of Ranvier, which allows for more efficient action potential propagation along the length of the axon. The main component of the concentric processes from the Schwann cells is myelin, an insulating lipid-rich substance containing cholesterol as well as specific proteins expressed by Schwann cells accounting for 20-30% of dry mass, which can be used as markers such as myelin protein zero (P0), Myelin Basic Protein (MBP) and Proteolipid Protein (PLP) (Morell and Norton, 1980).

The process of myelination is set up through complex signalling between two cell types; Schwann cells and neurons (which provide axons in peripheral nerve that are myelinated). This process has been studied in vitro considering mechanisms underlying the neuroglial signalling that occurs in the development and maintenance of nerve tissue. In a co-culture of Schwann cells and axons from Dorsal Root Ganglia (DRG) explants, Glycoprotein Adhesion Molecule expression was monitored to see if it was affected during myelination to elucidate the role of Schwann cells in axon guidance (Seillheimer et al., 1989).

Immunogold labelling shows L1 and N-CAM expression to be reduced in the co-culture, but not when the supernatant media of the culture was applied to Schwann cells, suggesting cell-to-cell contact is part of the mechanism of myelination. N-CAM expression reduced to a lesser extent than L1, but the evidence suggests both molecules are involved. Electrophysiological activity has also been shown to play a role in maintenance of myelination along the axon. Low frequency firing axons have been demonstrated to downregulate L1-CAM, a cell adhesion molecule, researched for its role in maintenance of myelination (Itoh et al., 1995). A higher frequency of stimulation did not result in upregulated expression of myelination. Neuroimaging studies of white matter changes during learning paradigms suggest that at higher levels of activity, expression of myelin-associated proteins does increase (Zatorre et al., 2012). In a co-culture experiment, when Schwann cells and mouse dorsal root ganglion neurons were stimulated at low frequency via stimulating electrodes, fewer myelinated contacts were observed. This suggests that the mechanism modulating myelination is related to axon pathfinding and may be affected by more variables than neuron excitability alone (Stevens et al., 1998). Studies on Schwann cell physiology allow for the enhancement of tissue engineering approaches to peripheral nerve repair by providing evidence of biochemical pathways that can be modulated for therapeutic effect.

During neuronal recovery from trauma, several genes have been associated with axon growth cones (rich in F-actin containing membrane proteins such as cell adhesion molecules) which aid axon mobility in response to chemical and mechanical cues (Pearse et al., 2004). Activating transcription factor 3 (ATF3) is an effector molecule evaluated for its role in inducing sensory neuron neurite outgrowth following injury: over expression was shown to enhance outgrowth of neurites in a transgenic mouse model (Tanabe et al., 2003). Comparable neurite outgrowth was observed in ATF3 overexpressing DRGs from the transgenic mouse and ATF3 overexpression by use of amplicon vectors. However the neurite outgrowth was not increased in the wild type control neurons. It was hypothesised that ATF3 may contribute to the reduced inhibition of myelin in peripheral nerve and that the factor can form functional heterodimers with c-Jun and CREB, which are both upregulated in DRG neurons following nerve injury (Seijffers et al., 2006). Myelin related signals of cyclic adenosine monophosphate (cAMP) and  $\beta$ -neuregulin-1 (NRG1)



have been used in conjunction to encourage a myelinating phenotype of both mouse and rat Schwann cells in vitro (Arthur-Farraj et al., 2011). The level of cAMP signalling must be sufficient to switch NRG1 expression from a proliferation to myelination signal. This could be important for probing Schwann cell behaviour in nerve graft experiments used to study nerve regeneration because it is often difficult to promote a myelinating phenotype in vitro in a Schwann cell monoculture without axons. Furthermore, SPRR1A mRNA is expressed 60 times more from explanted dorsal root ganglion neurons after 1 week of sciatic nerve transection demonstrating further molecular targets for study in neuron recovery mechanisms (Bonilla et al., 2002). Growth cone associated proteins such as GAP-43 and CAP-23 have been shown to be required for enhancing neurite extension of regenerating spinal neurons, shown when both proteins were co-expressed and are major axon growth cone proteins (Bomze et al., 2001).

Second messenger cAMP cues regeneration genotypes of Schwann cells as they can be induced to become proliferative after injury (Clements et al., 2017). Forskolin mediated increase in neuronal cAMP by activating adenylyl cyclase was shown to sustain a 40% increase in rate of sciatic nerve regeneration, when damaged by freezing (Kilmer and Carlsen, 1984). Although in another study, increase in intracellular cAMP concentration failed to demonstrate an effect on axonal regrowth by addition of dibutyryl cyclic AMP to cultured cells (McQuarrie et al., 1977). A review of the role of cAMP demonstrates evidence for its conditioning role on Schwann cells to give a pro-regenerative effect (Knott et al., 2014). cAMP provides a differentiating signal to Schwann cells to exit the cell cycle and have a phenotype characteristic of pre-myelination (Jessen et al., 1991).

Schwann cell signalling has been demonstrated as important in axon development and guidance through neuregulins (Grinspan et al., 1996). Equally evidence suggests that axon to Schwann cell signalling protects cells from apoptosis. Signalling from the axon plasma membrane can cause Schwann cells to differentiate to a mature state following nerve repair, ultimately causing re-myelination (Fricker and Bennett, 2013). Axo-glial signalling is not well understood, however some receptors and ligands have been identified. Neuregulin-1 Type III is an axonal membrane protein binding Schwann cell erbB2/erbB3 heterodimers, which has a role in nerve regeneration but not in longer term maintenance (Fricker et al., 2013). The juxtacrine neuregulin-1 and erbB signalling between the axon

and Schwann cell drives remyelination and functional recovery of axons, but at later time points function can be restored in the absence of Neuregulin-1. The orphan G-protein coupled receptor gpr126 has been shown to be expressed in Schwann cells and activates transcription factor Oct6 causing induction of myelination (Monk et al., 2009). In developing nerve, the receptor Adam22 is expressed by axons and shown to bind with its ligand Lgi4 expressed by Schwann cells has been demonstrated to have a role in nerve development (Ozkaynak et al., 2010). Ablation of both the receptor and ligand in Schwann cells caused reduction in numbers of myelinated fibres in a mouse model. Another issue with the relying on pathways that encourage nerve repair and myelination by Schwann cells without exogenous stimulation, is the temporal aspect of healing. Chronic denervation leads to reduction in Schwann cell survival and those that are available are less able to support distal axons (Jessen and Mirsky, 2019). This is possibly due to the reduction in the changes that have been mentioned, if there is less erbB receptor signalling occurring distally due to fewer Schwann cells engaging in axon contact, the expression of axo-glial receptors is markedly less. Also a reduction in glial derived neurotrophic factor (GDNF) was correlated with decline in erbB expression in denervated tissue Schwann cells (Monk et al., 2009, Li et al., 1997 and Hoke et al., 2002). Investigating the key modulating molecules involved in regulating Schwann cell phenotype following nerve injury, can help in understanding how to optimise current therapies, as loss of axons is a major contributor to poor functional repair (Boyd and Gordon, 2003).

## 1.2 Peripheral Nerve Repair

In the peripheral nervous system, trauma or damage to a nerve fibre will result in Wallerian Degeneration in which:

1. Transection of nerve tissue results in a gap injury and axons are maintained proximally
2. Axons deteriorate distally due to loss of contact with the cell body.

The gap injury length is defined to be the distance between the remaining nerve stumps (called proximal and distal stumps respectively) (Waller, 1850). As Waller describes, the distal stump will commence total deterioration whilst the proximal portion will only deteriorate to the proximal node of Ranvier where Schwann cells are able to provide trophic support and start to de-differentiate and proliferate. Schwann cells then pay a

role in guiding the axon towards the distal stump which will be predominantly acellular with some conservation of the basement membrane, an ECM structure.

The primary aim for tissue engineering is to increase the rate of axon extension so that extension of Schwann cells and axons from the proximal stump can reconnect with its target of innervation; be it muscle, sensory organs or other neurons, to form a functional circuitry (Heubner and Strittmatter, 2010). Fortunately, the onset of neuronal cell death is slow and provides an opportunity for intervention (Terenghi et al., 2011; Moldovan, 2006). A major method for peripheral nerve repair involves use of Nerve Guidance Conduits (NGCs), which are reviewed in detail in section 1.4.

### 1.2.1 Current 'Gold Standard' of Nerve Repair

Currently, the gold standard for repair of injured peripheral nerve is use of the autograft method (Merolli et al., 2014; Marinescu et al., 2014). This procedure is recognized as a method of repair with low-risk of rejection as endogenous nerve tissue is used. Also the autograft tissue is nerve tissue and as such provides a template on which axons can extend due to affinity with the extracellular matrix. This leads to functional recovery in some cases although there is no data available to suggest a reliable outcome as success is seen in 20-40% of patients with nerve injuries larger than 3cm (Dellon and MacKinnon, 1988; Grinsell et al., 2014).

Nerve tissue is harvested from a subsidiary nerve, commonly the sural nerve which supplies sensory neurons to the posterior surface of the lower leg and heel only, and implanted into the nerve gap injury site. The proximal and distal stumps of the injured nerve are sutured to the autograft tissue. Regenerating axons infiltrate the tissue, which has a conserved basal lamina, and Schwann cells that interact with the axons through neuro-glial signalling. Although the autograft has potential benefit in a wide range of nerve gap injuries (1-90mm), the procedure results in damage to the donation site (comorbidity) without guaranteed benefit of functional recovery (Pfister et al., 2011). Reviewing literature, it seems there has been no improvement or adaptation to the way autografts are implanted since first described in publications as early as 1915 (Law, 1915).

### 1.2.2 Prevalence of Nerve Injuries

To focus the thesis when testing prospective designs and applications of the nerve repair device, prevalence data for nerve injuries was examined to identify common injury sites in human trauma and therefore where most nerve repair applications would be most useful. Peripheral Nerve Injury (PNI) is highly prevalent amongst medical cases globally. Although there are some estimates of the prevalence and socio-economic costs, there is a lack of coherent data to suggest the full scale of peripheral nerve injury incidence. For example, Renton et al. reported prevalence of iatrogenic trigeminal nerve injuries specifically, concluding that 89.5% of patients presenting with neuropathy are due to iatrogenic cause (Carter et al., 2016). However, the high prevalence here arises due to the location of the inferior alveolar nerve which is impacted during wisdom tooth extractions.

Analysis of papers from large-scale trauma centres reveal PNI prevalence stems primarily from trauma and iatrogenic causes. Incidence of PNI from other causes such as stretching and compression injuries may reveal a higher prevalence than calculated however these types of injuries are not focussed on in this thesis as only gap injury models have been researched (Burnett and Zager, 2004). In order to quantify the size of the issue, 21 papers were chosen from searching the Medline database for titles including search terms 'epidemiology' and 'peripheral nerve injury' (listed in Table 1.1). For US comparison, Lundborg reports 20 million US citizens presenting as nerve repair cases, which is a prevalence of 6% in the population (Lundborg, 2003; US Census Bureau, accessed 7/9/19). The prevalence reported was not specified to any cause, site in the body or post-injury time and therefore gives little information on the prognosis following PNI. These variables, which significantly affect functional recovery, can provide information on the range of sizes, severity and prognosis in the population of nerve injuries and can provide foci for models of nerve injury (see Table 1.1). A comparable prevalence for the United Kingdom was not found through literature search, and therefore data from the papers detailed in Table 1.1 has been used to estimate the specific prevalence in the UK from trauma centre studies worldwide.

<b>Table 1.1: Comparison of Meta-Analytical data to show prevalence of PNI by cause, year and injury site</b>						
<b>Legend</b>			Iatrogenic Papers Analysed	Trauma Papers Analysed		
<b>Number of Patients with PNI</b>	<b>Reason</b>	<b>Country</b>	<b>Ref (First Author, Year)</b>	<b>Data Collection (Years)</b>	<b>Injury Site</b>	<b>Prevalence (%)</b>
104	Iatrogenic	Croatia	Rasulic et al., 2015	2000-2010	Ulnar, Median, Radial	-
100	Iatrogenic	US	Joiner et al., 2014	2011-2013	Median, Radial, Ulnar	23%
340	Iatrogenic	Germany	Antoniadis et al., 2014	1990-2012	Median, Accessory, Common Peroneal, Ulnar, Femoral	-
73	Iatrogenic	Turkey	Topuz et al., 2011	1984-2004	Lower Extremity	61%
291	Iatrogenic	UK	Mehta and Birch, 1997	1991-1998	Upper Extremity, Lower Extremity	47.5
14	Iatrogenic	US	Morrison and Dalsing, 2003	1991-2003	Saphenous	17.80%
21	Iatrogenic	US	Mirovsky and Neuwirth, 1999	1993	Femoral Cutaneous Nerve	20%
456	Trauma	Brazil	Kouyoumdjian, 2006	1989-2004	Upper Extremity, Lower Extremity	3.70%
162	Trauma	Canada	Midha et al., 1998	1986-1996	Upper Extremity, Lower Extremity	2.80%
418	Military Trauma	Pakistan	Razaq et al., 2015	2008-2011	Ulnar, Sciatic, Median, Radial, Peroneal	-

66	Trauma	US	Nitz et al., 1985	1983-1984	Peroneal, Posterior Tibial	-
111	Trauma	India	Barman et al., 2012	2009-2011	Brachial Plexus	-
3,151	Trauma	US	Bekelis et al., 2015	2009-2011	-	2.7-4.9%
245,470	Trauma	US	Missios et al., 2014	2009-2011	-	0.33-1%
-	Trauma	Mexico	Castillo-Galvan et al., 2014	2008-2012	Brachial Plexus, Ulnar	1.12%
42	Military Trauma	US	Beltran et al., 2012	2003-2007	Peroneal, Tibial	22%
3,617	Trauma	US	Taylor et al., 2008	1998	Upper Extremity, Lower Extremity	1.64%
158	Trauma	Italy	Ciaramitaro et al., 2010	2007-2008	Brachial Plexus, Radial, Ulnar, Peroneal	-
156	Natural Disaster Trauma	Iran	Ahrari et al., 2006	2003	Sciatic, Radial	31.20%
146	Trauma and Iatrogenic	Puerto Rico	Miranda and Torres, 2016	-	Facial, Brachial Plexus, Ulnar	-
137	Trauma and Iatrogenic	Canada and US	Bogdan et al., 2015	2012-2015	L5, S1, L4, L2-3	-
76	Trauma and Iatrogenic	Germany	Lehmann et al., 2014	2001-2012	Lower Extremity	4%

The papers summarised in Table 1.1 were then analysed to calculate a prevalence of nerve injury from trauma centres. Prevalence of Iatrogenic causes of nerve injury, injuries caused during medical treatment for trauma, range from 20% to 61% amongst the highlighted papers and are markedly high: demonstrating that nerve injury correlates with surgical intervention particularly in acute, life-threatening surgeries rather than planned surgeries where the risk of nerve injury is much lower. Furthermore, looking at nerve injuries occurring from the trauma papers alone (highlighted red in Table 1.1), defined as a physical injury; the values range from 0.33% to 4.9%. This range does not include data from trauma centres reporting on trauma following military events or patient trauma following natural disasters, for which 3 papers indicated a higher prevalence when compared to iatrogenic causes. This demonstrates the need for nerve repair technologies that can be applied quickly and without a large degree of pre-assembly (Miranda and Torres, 2016; Yelena, 2015). A median was calculated for both Iatrogenic and Trauma prevalence of PNI and averaged 33.9% (n=5, SD=19.3%; papers highlighted in blue in Table 1.1) and 2.5% (n=6, SD=1.6%; papers highlighted in red in Table 1.1) respectively. The higher median in iatrogenic causes is specifically for iatrogenic interventions during trauma intervention, not routine surgery. A subset of these cases will be linked, as some papers report both iatrogenic and traumatic nerve injuries. The analysis highlights the importance of providing functional solutions to those encountering nerve injuries clinically, and that nerve repair devices must be readily implantable and easily adaptable, available at the correct size of the injury site and applicable to both cable and plexiform nerves (Stewart, 2003). Prevalence was quoted by review papers to be between 22% from combat related injuries to 31.2% in a report on earthquake derived peripheral nerve injuries (Ahari et al., 2006; Beltran et al., 2012). As these data are based on surgical cases of PNI arising from trauma centre admission, a lower prevalence is more likely in the general population. A subset of routine surgeries however would require peripheral nerve repair, such as nerve guides to direct nerve growth and restore function due nerve tissue transection or loss.

Surgical intervention by use of a peripheral nerve repair device such as a nerve guide or nerve guidance conduit (NGC) is the cornerstone of the tissue engineering approach to PNR. In upper and lower limb PNI cases alone, from US emergency room data, it is estimated

558,862 cases annually have the possibility for surgical repair by nerve guide although the current available technology can be much improved (Brattain, 2014).

As nerve injury often occurs through trauma, most parts of the nervous system are vulnerable to PNI. Examples include nerve damage in the extremities, orthopaedic fractures, Cauda Equina syndrome and stretch Brachial Plexus injuries. From the reviews analysed in Table 1.1, the most common areas of injury include the upper limb (e.g. radial and ulnar nerves) and lower extremity (e.g. common peroneal and sciatic nerves) (Antoniadis et al., 2014; Razaq et al., 2015). Therefore this thesis focuses on specifically upper and lower limb spinal PNR. Work in the area of enhancing surgical outcomes for PNR has the opportunity to be vital in the rehabilitation of patients.

### 1.2.3 Nerve Injury Classification

To better understand the specific nerve injuries suitable for repair by a nerve guide, the current classifications of PNI have been examined. Seddon proposed a classification system in the 1940s, which is simple in nature, using three terms to describe the injury character, which increases in severity, and lists the provision for regeneration accordingly (Panesar, 2012). The terms are:

1. Neuropraxia (temporary loss of conduction, loss of motor or sensory function)
2. Axonotmesis (disruption to the axon but not connective tissue or glial component of nerve)
3. Neurotmesis (Damage of nerve and nerve sheath)

The Sunderland classification system (1951) provides input for understanding the hierarchy of injuries, as detailed in Table 1.2. Sunderland provided more comprehensive sub-categories under Axonotmesis injuries in terms of nerve disruption and capability for regeneration.



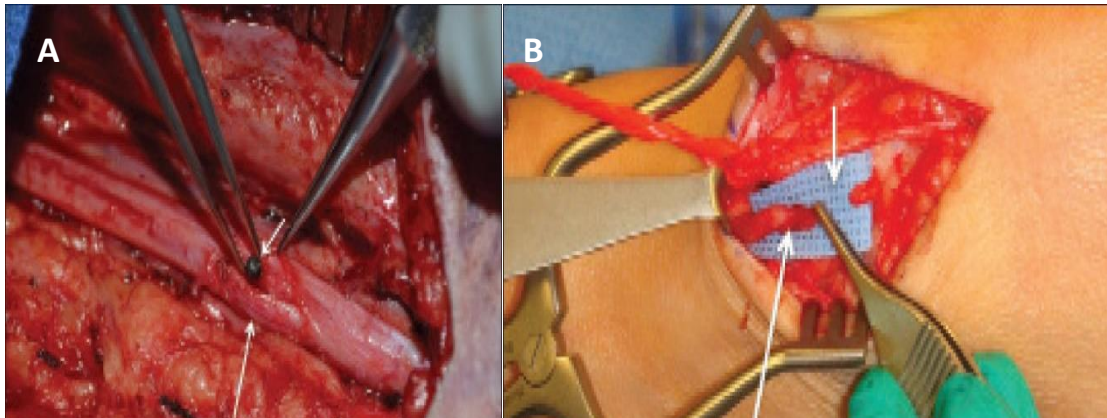
Table 1.2: Summary Table of Sunderland Classifications for Nerve Injury (1951)

Sunderland Class	Wallerian Degeneration	Nerve Conduction	Surgical Intervention
<b>Class I</b>	Absent	Conduction intact, except for injury site	No surgery required
<b>Class II</b>	Present Distally	<ul style="list-style-type: none"> <li>○ No Distal Nerve conduction</li> <li>○ Fibrillation Potentials present</li> </ul>	<ul style="list-style-type: none"> <li>○ Possible without surgery</li> <li>○ If scar forms, surgery may be required</li> </ul>
<b>Class III</b>	Present Distally	No Distal Nerve Conduction	Possible
<b>Class IV</b>	Present Distally	<ul style="list-style-type: none"> <li>○ No Distal Nerve Conduction</li> <li>○ Only Epineurium intact</li> </ul>	Required
<b>Class V</b>	Present Distally	<ul style="list-style-type: none"> <li>○ No Distal Nerve Conduction</li> <li>○ Complete Axotomy</li> </ul>	Imperative

Table 1.2 demonstrates that nerve injuries can be graded according to clinical observation. For example, surgical intervention is considered after a Class II diagnosis, supporting the need for innovative surgical tools. At the cellular level, the degenerative process affecting the particular axons must be studied to allow more specific solutions to be provided, that may translate to more specialised medical devices. Re-functionalisation of the nerve may be inhibited if cellular level responses are not fully researched or understood. In this thesis, an engineering approach was taken to develop an adaptable system that may include active components, researched necessary for axon regeneration. This thematic approach allowed

for hypothesis formation to remain relevant throughout as the peripheral nerve regeneration field continually advances. Hypothetically, this thesis focuses on Sutherland Class IV and V injuries (Figure 1.6), where surgical intervention is appropriate (Campbell, 2008).

MacKinnon and Dellon (1988) did made addition to the classification by adding Class VI, a mixed nerve injury. All classifications, I-VI, have variable surgical and prognostic outcomes. Neither the Seddon nor the Sunderland classification systems are entirely representative of the total spectrum of injuries. Thomas and Holdorff (1984) proposed a simpler classification system with two options, 'degenerative' when axons are disrupted and 'non-degenerative' when axons are not disrupted. However, such a simplistic view may not help a clinician assessing the prospective success of surgery as this depends on more variables than axon structure disruption alone, such as age of patient for example. Classifications could be importantly stratified on age of patient, anatomical location of PNI and size of lesion. Clinical audits have identified that paedriatic and younger adult patient have higher prospects of recovery demonstrating that the research may focus on adult nerve repair as a relatively difficult challenge for new regeneration devices (Glaus et al., 2011).



**Figure 1.6:** Intraoperative images of nerve injuries according to Sunderland classifications. Image A, Sunderland classification III, shows a fragment of a bullet (white arrow) which has caused disruption of distal conduction and swollen median nerve. Image B shows a fully severed neurotmesis of deep peroneal nerve with an obvious gap indicated by the placement of forceps between nerve ends (indicated by arrows, Class V) (Chhabra et al., 2014).

Classification system values are often disputed however, as difficulties in pre-operative and functional assessment of a nerve injury may also contribute to ineffective repair strategies being chosen. Electrophysiological assessment can give information on nerve impulse conduction but lacks clarity on when conduction becomes ineffective as electrical stimuli can be recorded up to a week after injury (Dyck, 1990). Neural tissue should integrate signals from depolarisations with varying conduction velocities that range between 200 m/s and less than 1 m/s (Stanford, 1987). The velocity of signal propagation is a product of effective myelination from Schwann cell and axon communication reviewed in section 1.1.5, and hence this is difficult to engineer and measure (Belkas et al., 2004). Thus, effective models are called for, when designing devices that restore nerve function, by encouraging Schwann cell myelination.

The need for improved functionality of a regenerated nerve is still a driver for innovative research in this field. Although autografts provide restoration of some abilities, up to 80% at best, the deficit calls for approaches that reduce co-morbidity within the donor sites (Schmidt and Leach, 2003). Nerve guide repair has been shown to be comparable to autograft repair when considering small nerve gaps, but less promising over areas further than a few millimetres (Weber et al., 2000; Hood et al., 2009).

#### 1.2.4 Evaluation of the need for Improved Repair of Peripheral Nerve

Tissue engineering may provide the answer to this as an effective device may be manufactured outside the body and implanted into the recipient site. Recently research into peripheral nerve regeneration has provided devices offering comparable functionality to autograft (reviewed in 1.3).

Normal nerve functionality and that of a regenerated nerve differ. So new devices producing better sensory and motor functionality should be researched (Hopper et al., 2016; Kumar and Prasad, 2016). These devices provide a barrier from excess scar tissue and fibrosis developing along the nerve and blocking the outgrowth from the proximal stump, and confine the release of neurotrophic factors and regenerative factors secreted by regenerating neural and connective tissue within the conduit (Isaacs and Browne, 2014).

Several approaches can be taken to address PNI outcomes. Methods include:

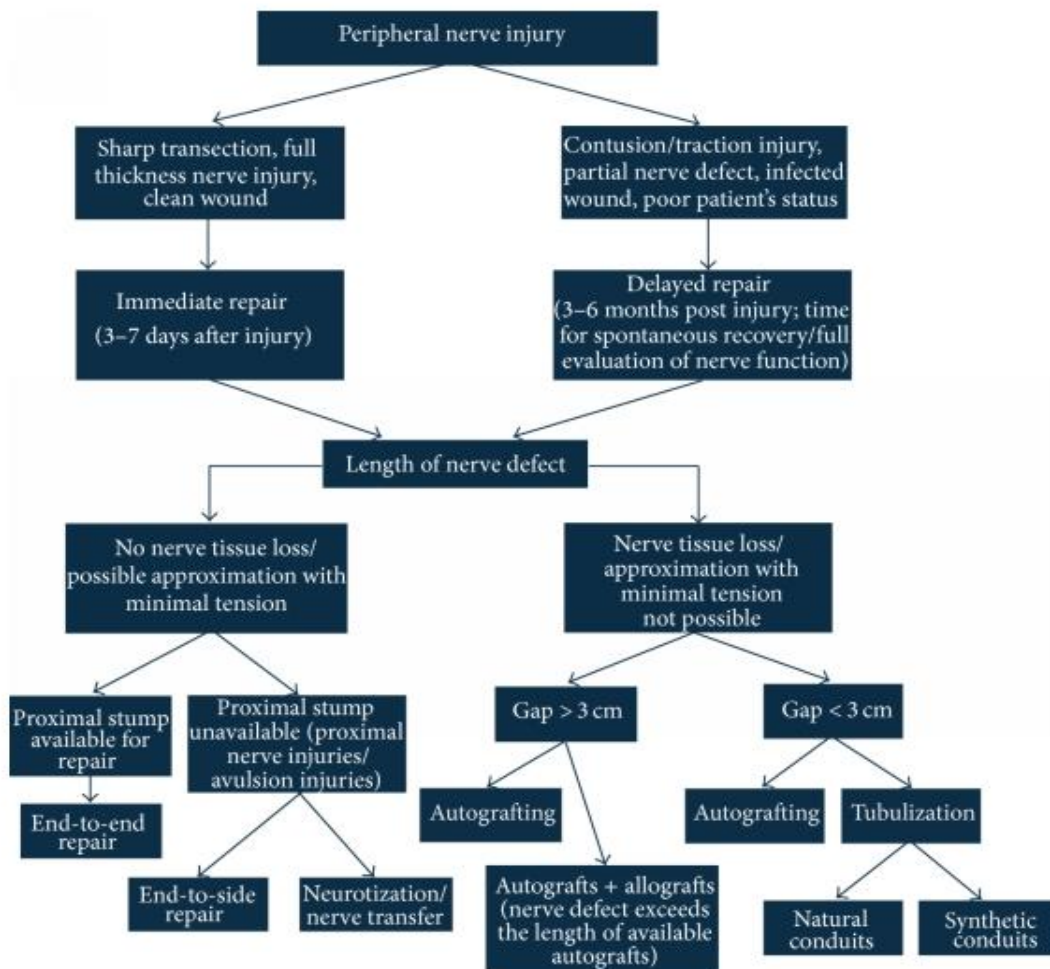
- Nerve conduits (see 1.5)
- Electrical Stimulation (see 1.5.2.1)
- Molecule-mediated therapy (see 1.5.2.2)
- Cell Therapy (see 1.5.2.3)
- Schwann Cell Therapies (see 1.5.2.4)
- Acellular Conduits (see 1.5.2.5)

A key component to any device intended to regenerate an injured nerve gap would be the material's specifications and ability to offer comparable repair outcomes with autografting and with less side effects.

#### 1.2.5 Surgical Decisions regarding peripheral nerve repair

The current decision-making tree to address clinical cases of PNI have been highlighted (Figure 1.7; Siemienov and Brzezicki, 2009). For full nerve transection, contusion (damage to neural blood vessels) and partial defects, the tubulisation technique, which involves use of an NGC, is only applicable to gaps less than 3cm. Larger gaps are repaired with autograft or allograft. A primary aim is to increase the 0-3 cm limit for nerve tubulisation, which is the critical length beyond which nerve tubulisation is currently less effective. This could allow

more patients to receive repairs with less co-morbidity, following an autograft. Hence this is an area of focus for this work. Donor nerves for transfer are usually taken from sacrificial nerves from the upper and lower limb (Grinsell and Keating, 2014).



**Figure 1.7:** Flow diagram to illustrate surgical outcomes of differing peripheral nerve injury classifications (Siemienov and Brzezicki, 2009)

Isaacs discusses the timeframe for effective repair to be within 3-6 months from the primary injury when optimal surgical intervention should best take place (Isaacs, 2010). Nerve guides may be used to implant multiple autograft specimens into the same site to capitalise on the perineurium structure within native nerve and to provide nerve guidance over long distances greater than 3cm (Dahlin, 2008). There are a lack of effective surgical decision trees published, indicating that there is no set standard for when a nerve guide ought to be used and the decision is up to the discretion of the surgeon.

### 1.3 Nerve Conduits

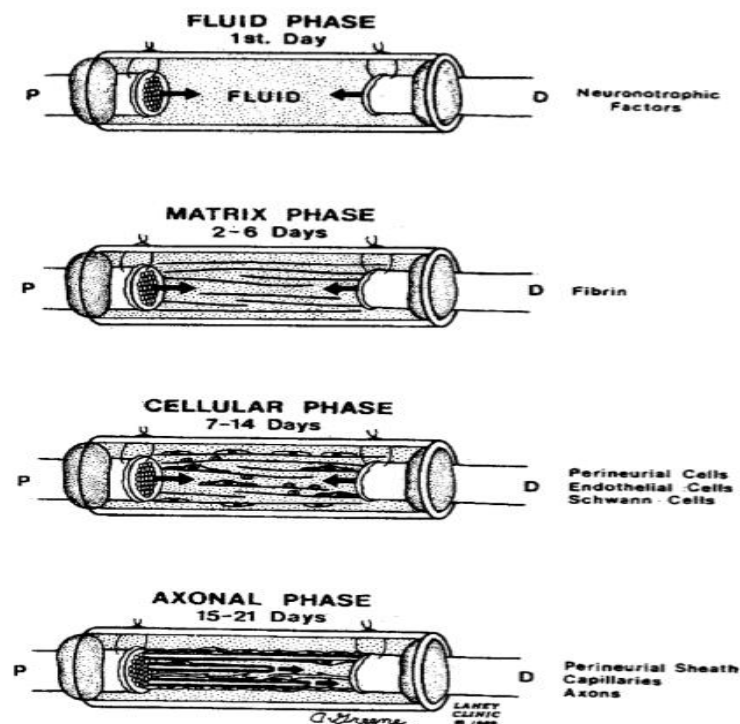
Nerve guides have become the standard as implantation devices, designed to improve peripheral nerve regeneration surgery outcomes. It has been demonstrated that tubular devices with an internal hollow lumen allow for confinement of neurotrophic factors and provides a physical cue for axon outgrowth.

#### 1.3.1 Rationale for Nerve Conduits

Events following injury of a nerve for modelling PNR within a silicone tube (a model NGC) has been divided into stages based on cellular events:

1. Initially ECM is laid down before cells infiltrate the space.
2. Then the NGC is infiltrated by axons which sense the regenerative environment for tracks along which to extend which can be quantified to give measures of axon density (Belkas et al., 2004). Williams et al. (1983) were first to characterise the temporal profile of regenerative events, across a 10mm sciatic rat nerve defect.
3. After 12 hours, the injury site is fluid-filled with a high concentration of neurotrophic factors released into the tissue fluid - peaking after 3-6 hours.
4. After 2 weeks, a fibrin matrix forms providing scaffolding to infiltrating cells such as Schwann cells, endothelial cells and fibroblasts. Schwann cells and fibroblasts advance ahead of axons, and myelination of axons occurs by 4 weeks (Figure 1.9).

Any design features of NGCs that can expedite this process may be beneficial in increasing functional outcomes for PNR.



**Figure 1.8:** Stages of nerve repair within a silicone nerve guide after full transection of the Sciatic nerve. The proximal stump (p) and distal stump (d) are labelled to show that axon fibres cross the injury site from proximal to distal stump, which takes up to 21 days. (Belkas et al., 2004)

#### 1.4 Materials for Peripheral Nerve Regeneration

Current methods of repair for PNI often involve artificial NGCs alone or combined with other therapeutic techniques such as neurotrophic soluble factors. Possible materials for use in NGCs include both natural and synthetic polymers (Wang and Cai, 2010); including silicone, collagen, laminin, hyaluronic acid, gelatin, silk fibroin and fibronectin based systems, which are all first generation biomaterials used in studies on PNR (Ciardelli and Chiono, 2005). These materials mainly comprise extracellular matrix (ECM) and promote neurite extension, offering excellent biocompatibility as well as biodegradability. A valuable property of a good NGC will be to limit over-infiltration of macrophages, and to be of a diameter large enough to limit nerve swelling in the process of regeneration. Schwann cells express specific integrin, e.g.  $\beta 1$  that couple to laminin, that bind to the ECM during myelination and therefore biopolymers emulating ECM proteins can be useful to stimulate nerve repair (Chernousov and Carey, 2000).

A common in vivo model for conduit based nerve repair is the Rat Sciatic nerve transection and repair model (Palsson et al., 2003). The sciatic nerve, which innervates the plantar muscle group, is transected to leave a gap with defined length over which a NGC is implanted. The size of the gap must be large enough to monitor the mechanism of repair and be a relevant size to compare to gap lengths that are encountered clinically in humans (3 cm), therefore 10-15 mm gaps have been used. However this critical gap size varies between in vivo models (Georgiou et al., 2013; Isaacs and Browne, 2014). The Lundborg research group has used the Rat animal model of nerve transection to reliably model the course of PNR (Lundborg et al., 1981; Lundborg et al., 1994). Nylon 8-0 suture material was used to join the perineurium of each nerve stump and the wall of the guide together, in a peroneal nerve dissection and regeneration study of adult Wistar rats.

#### 1.4.1 Biopolymers

Major biomaterials used in PNR are listed in Table 1.3.

Table 1.3: Search Results of Recent Papers by Specific Term

<b>Search Terms (Title/Abstract)</b>	<b>Specific (Title)</b>	<b>Number of Search Results</b>
Peripheral + Nerve	Collagen	221
Peripheral + Nerve	Chitosan	99
Peripheral + Nerve	Gelatin	25
Peripheral + Nerve	Laminin	120
Peripheral + Nerve	Agarose	6
Peripheral + Nerve	Alginate	18
Peripheral + Nerve	Hyaluronic	21
Peripheral + Nerve	Silk	40

The number of papers from a PubMed database search of each materials and its use in PNR was listed. It is clear that some biopolymers are more studied than others, i.e. collagen, chitosan, gelatin, laminin and silk, due to material properties that support neural and glial cell attachment. The inclusion and exclusion criteria for Table 1.3 were as follows.

Inclusion criteria for Table 1.3:



- search terms 'peripheral' AND 'nerve', in title or abstract
- AND specific material, e.g. 'collagen', in title
- Context of nerve repair or nerve regeneration, in title or abstract

Exclusion criteria for Table 1.3:

- Mention of specific material search term in abstract but not title

A meaningful analysis from the 550 papers that were identified from Table 1.3 would be difficult to obtain as the objective for this section is to highlight novel research ideas currently in development. Therefore, a stricter set of inclusion and exclusion criteria were applied to create Table 1.4 as follows.

Inclusion criteria for Table 1.4:

- In vivo experiment or clinical trial
- Conducted between 2011-2016
- Search terms 'peripheral' AND 'nerve' (in title/ abstract) AND specific (in title) from Table 1.4
- Peer-reviewed journal
- Gap Injury Model

Exclusion criteria for Table 1.4:

- Materials laboratory testing, in vitro testing
- Published before 2010, to ensure that current technologies were reviewed
- Blends of two biopolymers from Table 1.3
- Review articles
- Trials for research on pain
- In vitro testing or mechanical testing papers
- Use in Spinal Cord Injury/ Repair
- Nerve crush injury model

**Table 1.4: Analysis of all papers related to biopolymers satisfying criteria for Table 1.3**

<b>Material</b>	<b>First Author</b>	<b>Year</b>	<b>Length (mm)</b>	<b>Model, Nerve</b>	<b>Functional Test</b>
<b>Collagen</b>	Saeki	2018	12.6	Human, Sensory (Hand)	2PD, Sensory Qualitative Assessment
<b>Collagen</b>	Mohamedi	2018	10	Rat, Sciatic	EMG, Toe Spread, Hot Plate, Histology
<b>Collagen</b>	Cui	2018	40	Canine, Sciatic	EMG, Histology
<b>Collagen</b>	Ma	2018	9	Rat, Facial	Whisker Movement, EMG, Histology
<b>Collagen</b>	Bozkurt	2017	20	Human, Sural	Qualitative Sensory and Pain Assessment, Hoffman-Tinel's Sign
<b>Collagen</b>	Tsujimoto	2017	10	Canine, Facial	NCV, EMG and Histology
<b>Collagen</b>	Fujimaki	2016	15	Rat, Sciatic	Gait analysis, Histology
<b>Collagen</b>	Bozkurt	2016	20	Rat, Sciatic	Toe Spread, Histology
<b>Collagen</b>	Marinescu	2014	10	Rat, Sciatic	SFI, 2PD and Gastrocnemius Weight
<b>Collagen</b>	Ma	2014	15	Rat, Sciatic	Walking Track Analysis, NCV, Histology
<b>Collagen</b>	Cui	2014	35	Minipig, Facial	EMG, Histology
<b>Collagen</b>	di Summa	2014	10	Rat, Sciatic	Histology
<b>Collagen</b>	Maturana	2013	10	Rat, Sciatic	Histology
<b>Collagen</b>	Berrocal	2013	15	Rat, Sciatic	Footprint Analysis, Histology
<b>Collagen</b>	Lee	2012	10	Rat, Sciatic	EMG
<b>Collagen</b>	Lee	2012	10	Rat, Common Peroneal	EMG, Gait Analysis, Histology
<b>Collagen</b>	Masand	2012	5	Mouse, femoral nerve	Gait Analysis, Limb Extensometry, Histology
<b>Collagen</b>	Bozkurt	2012	20	Rat, Sciatic	Histology
<b>Collagen</b>	Dornseifer	2011	14	Rat, Sciatic	Gait Analysis, EMG, Histology
<b>Chitosan</b>	Yin	2018	12	Rat, Sciatic	Histology
<b>Chitosan</b>	Stoßel	2018	12	Rat, Sciatic	EMG, NCV, Histology
<b>Chitosan</b>	Peng	2018	30	Canine, Sciatic	Gait Analysis, EMG, Gastrocnemius Weight, Histology
<b>Chitosan</b>	Li	2018	10	Rat, Sciatic	EMG, NCV Gastrocnemius Weight, Histology
<b>Chitosan</b>	Stoßel	2018	15	Rat, Sciatic	EMG, Gastrocnemius weight, Histology
<b>Chitosan</b>	Zhang	2018	10	Rat, Sciatic	EMG, NCV, Histology
<b>Chitosan</b>	Guo	2018	10	Rat, Sciatic	SFI, EMG, NCV, Gastrocnemius Innervation
<b>Chitosan</b>	Turner	2017	6	Rat, Sciatic	Histology
<b>Chitosan</b>	Stenberg	2017	15	Rat, Sciatic	Histology
<b>Chitosan</b>	Iman	2017	14	Rat, Sciatic	SFI, Gastrocnemius Weight, Histology

<b>Chitosan</b>	Gonzalez-Perez	2017	15	Rat, Sciatic	EMG, Algesimetry, Histology
<b>Chitosan</b>	Muheremu	2017	30	Goat, Peroneal	Gait Analysis, MRI, EMG, Histology
<b>Chitosan</b>	Fregnan	2016	10	Rat, Sciatic	Grasp test, Histology
<b>Chitosan</b>	Mehrshad	2016	10	Rat, Sciatic	BBB, Gait Analysis, Histology
<b>Chitosan</b>	Kusaba	2016	15	Rat, Sciatic	EMG, Histology
<b>Chitosan</b>	Mokarizadeh	2016	10	Rat, Sciatic	BBB, Gait Analysis, Histology
<b>Chitosan</b>	Meyer	2016	15	Rat, Sciatic	EMG, Algesimetry, Histology
<b>Chitosan</b>	Meyer	2016	15	Rat, Sciatic	NCV, Algesimetry, Histology
<b>Chitosan</b>	Azizi	2015	10	Rat, Sciatic	NCV, Histology
<b>Chitosan</b>	Gonsalez-Perez	2015	15	Rat, Sciatic	EMG, Algesimetry, Histology
<b>Chitosan</b>	Sarabia-Estrada	2015	5	Rat, Sciatic	Gait Analysis, EMG, Histology
<b>Chitosan</b>	Zhao	2014	10	Rat, Sciatic	Algesimetry, SFI, Histology
<b>Chitosan</b>	Zhao	2014	-	Rat, Sciatic	EMG, Histology
<b>Chitosan</b>	Hsueh	2014	10	Rat, Sciatic	EMG, Histology
<b>Chitosan</b>	Mohammed	2014	10	Rat, Sciatic	BBB, Gait Analysis, Histology
<b>Chitosan</b>	Liu	2013	10	Rabbit, Facial	EMG, Histology
<b>Chitosan</b>	Hu	2013	50	Macaque, Median	EMG, Histology
<b>Chitosan</b>	Gu	2013	30	Human, Median	2PD, EMG
<b>Chitosan</b>	Wang	2012	10	Rat, Sciatic	EMG, Gait Analysis, Histology
<b>Chitosan</b>	Liu	2011	20	Macaque, Radial	EMG, NCV, Histology
<b>Gelatin</b>	Salehi	2018	14	Rat, Sciatic	SFI, Hot Plate, EMG, Gastrocnemius Weight, Histology
<b>Gelatin</b>	Ko	2017	15	Rat, Sciatic	EMG, Histology
<b>Gelatin</b>	Salehi	2017	14	Rat, Sciatic	SFI, Hot Plate, EMG, Gastrocnemius Weight, Histology
<b>Gelatin</b>	Matsumine	2014	10	Rat, Facial	Histology
<b>Gelatin</b>	Beigi	2014	10	Rat, Sciatic	Gait Analysis, EMG, Histology
<b>Gelatin</b>	Koudehi	2014	10	Rat, Sciatic	EMG, Histology
<b>Laminin</b>	Gonsalez-Perez	2018	15	Rat, Sciatic	EMG, Algesimetry, Histology
<b>Laminin</b>	Zhang	2018	10	Rat, Sciatic	Gait Analysis, Histology
<b>Laminin</b>	Roam	2015	7	Rat Sciatic	Histology
<b>Laminin</b>	Kakinoki	2014	20	Rabbit, Tibial	EMG
<b>Laminin</b>	Seo	2013	10	Rat, Sciatic	Histology
<b>Laminin</b>	Neal	2012	10	Rat, Tibial	Algesimetry, Gait Analysis, EMG, Histology
<b>Agarose</b>	Gao	2016	15	Rat, Sciatic	Histology
<b>Agarose</b>	Carriel	2013	10	Rat, Sciatic	2PD, SFI, EMG, Histology

<b>Agarose</b>	Suzuki	2013	7	Human, Digital	2PD, Tinel's Sign
<b>Agarose</b>	Szarek	2013	10	Rat, Sciatic	Histology
<b>Hyaluronic</b>	N/A				
<b>Silk</b>	Ebrahimi	2018	10	Rat, Sciatic	Histology
<b>Silk</b>	Wang	2018	10	Rat, Sciatic	Histology
<b>Silk</b>	Rao	2017	10	Rat, Sciatic	NCV, EMG, Histology
<b>Silk</b>	Das	2017	10	Rat, Sciatic	NCV, EMG, Histology
<b>Silk</b>	Xie	2015	5	Rat, Sciatic	SFI, NCV, Histology
<b>Silk</b>	Zhang	2015	20	Rat, Sciatic	EMG, Histology
<b>Silk</b>	Das	2015	10	Rat, Sciatic	NCV, EMG, Histology
<b>Silk</b>	Teuschl	2015	10	Rat, Sciatic	Gait analysis, NCV
<b>Silk</b>	Sivak	2014	17	Rat, Sciatic	Histology
<b>Silk</b>	Mottaghtalab	2013	10	Rat, Sciatic	NCV, Histology
<b>Silk</b>	Hu	2013	10	Rat, Facial	EMG, Histology
<b>Silk</b>	Li	2012	10	Rat, Sciatic	Histology
<b>Silk</b>	Huang	2012	10	Rat, Sciatic	EMG, Histology
<b>Silk</b>	Lin	2011	15	Rat, Sciatic	Gastrocnemius Weight, Histology
<b>Silk</b>	Yang	2011	10	Rat, Sciatic	Histology

The results from the refined literature search (displayed in Table 1.4) show information on popularity of prospective materials used for clinical trials of peripheral nerve repair, biomaterials produced from collagen, chitosan and silk matrices are most studied (64 papers between 2010 and 2018). This has been mostly reported due to the cell adhesive qualities of collagen, and the control on hydrogel properties such as stiffness, porosity and is commonly modelled for use as a material for peripheral nerve grafting by cell biocompatibility assays. In contrast, gelatin, laminin, agarose, alginate and hyaluronic acid have been studied to a lesser extent in their pure state without modification with other biopolymers (16 papers between 2010 and 2018). This may indicate that these systems are less studied due to their negative effect on neuronal populations or difficulty in matching the physical characteristics of nerve. A comprehensive screen of all these systems with the same cellular model can be useful to determine the most suitable systems for supporting nerve growth. Which can then be translated for validation in an animal model. The most common animal model is the rat sciatic nerve model, which has been studied since Lundborg's description of the model (Lundborg et al., 1981). A key differentiator on the relative use of papers published with Human subjects in contrast to animals is the relevance of behavioural assessment paradigms. For Humans, common tests include nerve conduction (NCV), qualitative assessment by questionnaires on pain, Tinel's sign (a sensation of tingling derived from nerve irritation), two-point discrimination (2PD, the resolution, in length, of somatosensory feedback) and electromyography (EMG) (Saeki et al., 2018; Bozkurt et al., 2017; Gu et al, 2014). Some of these measures can be recorded from animals, such as EMG, EMG and 2PD (Das et al., 2015; Marinescu et al., 2014). However, measures of nerve health during regeneration must be interpreted from animal behaviour – hence some strategies have evolved to be common in vivo experiments investigating NGCs. Particularly behavioural tests focussed on gait analysis, motor function of the nerve being repaired, algesimetry are common to studies due to being indirect measures of nerve function (Lee et al., 2012; Meyer et al., 2016). This data is then compared to histology of the regenerated nerve fibres to confirm the structures responsible for observations made during behavioural tests. The most common style of medical device for use in peripheral nerve repair was the NGC to ensure that the nerve stumps connect unidirectionally (thus providing coaptation of the nerve stumps) and to maintain a localised gradient of growth factors and cytokine signalling between the proximal and distal stumps (discussed further in section 2.4). The papers listed in Table 1.4 were evaluated in further detail according to the biomaterial as follows (sections 2.3.2 to 2.3.9).

### 1.4.2 Collagen

Collagen is a naturally occurring ECM protein with 30 types identified and a helical structure, the protein motifs present recognizable to cell integrin receptors and supports cell adhesion. Naturally sourced from rat tail, porcine skin or bovine tendon for example. Collagen provides the base material for numerous FDA-approved NGCs including Neuragen<sup>®</sup>, Neuroflex<sup>®</sup>, NeuroMatrix<sup>®</sup> and Axogen<sup>®</sup> (Kehoe et al., 2012). Collagen offers excellent biocompatibility and adequate elasticity hence providing structural support following implantation. Collagen has been used extensively for luminal and outer surface construction of nerve guides due to its low antigenicity, which may decrease further by enzymatic removal of telopeptide regions or cross-linking of amine groups on glycine residues (Hardin-Young et al., 1996). Cross-linking agents include glutaraldehyde and formaldehyde. The benefit of cross-linking is that the process can affect the physical characteristic of the neural scaffold, for example by increasing the viscoelastic stiffness of a hydrogel material and providing solid phase properties as opposed to gel-phase properties. Neuragen was the first NGC to gain approval from the FDA and is available in 2 or 3 cm length sections meaning that Collagen can easily be moulded into a conduit shape using casting and gelation methods. The fibrillary structure of Collagen hydrogel allows for controlled resorption (< 4 years) and good permeability, also achieved through a microporous network of collagen fibrils. In vitro, targeted orientation of collagen fibrils by high power electromagnets has been used to enhance neurite extension (Dubey et al., 2001). Despite popularity with the FDA and promising results in vivo, collagen-based systems demonstrate failure to provide increased regeneration when compared to the autograft method of repair as results are as good as the control (Lee et al., 2012; Berrocal et al., 2013; di Summa et al., 2014). This has led to more recent trials of conduits with oriented channels or fibrils, in which the research argues to encourage directed growth of axons and expedite recovery (Bozkurt et al., 2016; Fujimaki et al., 2016). Ma et al. have shown more favourable electrophysiological outcomes during gait analysis (post-surgery walking assessment) by increasing action potential conduction velocity when ordered collagen fibrils were used to refine the outgrowth of axons from the proximal stump following nerve injury. In addition to mimicking the aligned structure of intact nerve, endothelial growth factor was introduced into the conduit lumen to simulate the effect of cells releasing cytokines from the autograft method. Interestingly, authors have concluded that use of mesenchymal stem cells does not provide better results than use of collagen conduits without mesenchymal stem

cells. This finding is challenged by Berrocal's study which included autologous Schwann cells, not stem cells. They reported a statistically significant increase in gap length recovery time with such materials (Berrocal et al., 2013; Marinescu et al., 2014). Biodegradability and excellent biocompatibility has secured collagen's place in much research however. This warrants its use in further studies as the cell adhesive property and mimicry of the ECM can help direct migratory cells and instruct proliferative cells.

#### 1.4.3 Chitosan

Chitosan ([1-4)-2-amino-deoxy- $\beta$ -d-glucan] is a deacetylated derivative of chitin; used in PNR because of its due to high proportions of polysaccharides mimicking tissue found in the nervous system (Xie et al., 2008). Chitosan is depolymerized to form units of glucosamine which is non-toxic and permits a biodegradable mechanism when used as a neural scaffold material. Chitosan can be blended to improve material properties to enhance nerve growth, where use of the natural biopolymer offers biocompatibility and can be combined with a synthetic polymer to give more elastic properties and porosity to the final material. Use of chitosan-only NGCs presents difficulties to surgeons, due to its stiffness risking rupture and splitting during suturing. However, when implanted carefully under controlled conditions in an animal trial, functional recovery was demonstrated by video gait analysis (Patel et al., 2006). This highlights an important aspect in designing NGCs; the technology must be readily available and easy to implant by a clinician; hence NGCs often comprise more than one polymer system as compromises are sought. Chitosan NGCs can host bone marrow derived stem cells, which are thought to increase axon outgrowth from the proximal stump; one study showing an increase in new axon fibre density after 6 weeks of healing (Zheng and Cui, 2012). Some studies argue that chitosan is an optimal biopolymer for use in NGCs due to its porous interconnected structure following gelation, which allows for nutrient exchange, thus acting as a biocompatible stem cell delivery scaffold (Hsueh et al., 2014; Meyer et al., 2016). Chitosan also effectively acts as a drug delivery system, demonstrating slow and steady release of FGF, NGF, Alpha-lipoic acid and BDNF in animal model experiments which all report axon outgrowth across the nerve injury (Lui et al., 2013; Zhao et al., 2014; Azizi et al., 2016; Meyer et al., 2016). Some researchers argue that chitosan can be better employed when blended with a synthetic polymer, to increase mechanical stiffness. This can have the advantageous effect of delivering more robust material during implantation surgery and encouraging cell alignment across the injury gap: e.g. use of poly(lactic-co-glycolic acid) (PLGA)

and poly(ethylene glycol) (PEG) in conjunction with chitosan to raise tensile strength from 3.10MPa (chitosan) to 4.32MPa (chitosan with PLGA and PEG) which provided a stiffer material to ensure encapsulated cells remain in the pro-regenerative environment for longer (Zhao et al., 2014; Mekarizadeh et al., 2016).

#### 1.4.4 Gelatin

Gelatin is formed from chemical (hydrolysis) or physical (thermal) denaturation of collagen and therefore has similar cell adhesion properties to collagen due to the presence of integrin binding sites (Bigi et al., 2001). Gelatin is highly water-soluble which is advantageous due to its high diffusion coefficient but has low elastic and stiffness properties (Davidenko et al., 2016). This means that as a scaffold, gelatin is resorbed too quickly in vivo therefore gelatin blends are common (Wang and Cai, 2010). Poor stiffness and high solubility would suggest that gelatin is not suitable for use in fabrication of NGCs alone hence the lack of papers reporting this between 2011 and 2018 (Table 1.4). Gelatin has been blended with electrospun poly( $\epsilon$ -caprolactone) fibres to enhance the stability of the conduit in vivo and to enhance alignment of axon fibres, in addition gelatin has also been used as a carrier for Schwann cells (Beigi et al., 2014; Koudehi et al., 2014; Matsumine et al., 2014). Use of a novel sol-gel technique to include 25-50nm bioglass nanoparticles within a gelatin NGC to repair 10mm rat sciatic nerve gap demonstrated increased mechanical performance, leading to no significant difference between the bioglass/ gelatin NGC and autograft controls (Rezwan et al., 2006; Koudehi et al., 2014). More recently, gelatin has been formulated into nanofibrils for use within the lumen of NGCs to enhance guidance of axons whilst providing a cell-adhesive matrix in poly(urethane) NGCs (Salehi et al., 2018). Following evaluation by algometry (measurement of pain sensation to indicate pain perception recovery), electromyography (EMG) and myelin staining, it was confirmed that these conduits were able to deliver faster regeneration only when filled with platelet rich plasma and melatonin; hence reconfirming that gelatin alone may not be suitable as a cell adhesive filler for NGCs.

#### 1.4.5 Laminin

Laminin comprise a family of glycoproteins, the peptide contains three heterotrimeric chains. Laminin- $\gamma$ 1 has been reported to play an important role in Schwann cell instruction for enhancing myelination of both peripheral nerve and spinal cord tissue. The mouse gene coding for laminin- $\gamma$ 1 was disrupted by mutagenesis (using the lox-cre system) resulting in mice with hind leg



paralysis, tremor and motor axons deficient in laminin-  $\gamma$ 1 binding. This demonstrates the importance of laminin within the ECM of nerve tissue (Chen and Strickland, 2003). The same group investigated peripheral nerve lesion in the mutant mice. 28 days after lesion surgery the regeneration was significantly disrupted in mutant mice compared to control wild type mice providing further evidence of the role of laminin-  $\gamma$ 1 in nerve regeneration.

In a NGC study, the rat sciatic nerve was regenerated using a collagen nerve guide, which was either coated with laminin or recombinant acidic Fibroblast Growth Factor (aFGF). Results demonstrated that laminin specifically supports increased axon density within the gap injury area (Trigg et al., 1998). Additionally, laminin coated collagen fibrils were used to bridge a 80mm gap in a canine nerve injury model and evoked action potentials were recorded, although this was 1 year post surgery (Matsumoto et al., 2000). Use of Laminin has been reported in conjunction with growth factors including genetically engineered GDNF adsorbed onto microfibrillar conduits and as a peptide coat for NGCs (Roam et al., 2015; Kakinoki et al., 2015; Seo et al., 2013). The use of laminin may be an important aspect of NGC design however it must be used in conjunction with biopolymers as the peptide cannot be polymerised.

#### 1.4.6 Agarose

Agarose has been reported to provide a polymer system suitable for cell entrapment and delivery rather than cell adhesion as some cells do not adhere well to agarose when produced in gel phase. Agarose has been valuable in delivering cytokines to macrophages in vivo to control macrophage differentiation and enhance the number of cells guiding axons in PNR (Mokarram et al., 2012). Interleukin-4 was delivered via agarose gel to modulate M2 macrophages into an anti-inflammatory role, causing matrix remodelling and mediating angiogenesis - which was demonstrated to promote regeneration significantly. Viscoelastic stiffness of the agarose hydrogel (defined as the force exerted by the hydrogel on an advancing growth cone of an axon) has been demonstrated to be inversely proportional to length of neurite extension, indicating that mechanical properties such as stiffness are important factors to control when designing NGCs (Balgude et al., 2001). From Table 1.4, between 2011-2018, only four papers report the use of agarose in nerve regeneration demonstrating that there are stronger candidate natural systems due to its cell-repulsive surface property although agarose was combined with adhesive fibrin molecules in the collagen FDA-approved conduit Neuragen<sup>®</sup> to enhance directional guidance of axons (Carriel et al., 2013).

#### 1.4.7 Alginate

Alginate is an anionic polysaccharide derived from brown seaweed, offering cross linkage between 'M' ((1,4)-linked  $\beta$ -D-mannuronate) and 'G' ( $\alpha$ -L-guluronate) residues (Lee and Mooney, 2012). Consecutive G residues constitute a G block, which take part in cross-linking by interaction with  $\text{Ca}^{2+}$  cations. The immunogenic properties of high M residue containing alginate has been reported although not fully understood and counter evidence suggests that this response has been due to impurity rather than any biogenic cause (Lee and Mooney, 2012). Alginate has been used in rat and cat models of PNR, demonstrating that alginate is capable of early outgrowth of axons within 2 weeks and encourages Schwann cell infiltration by 8-14 days (Hashimoto et al., 2001). Axons later increased in diameter and produced normal nerve fibre distribution following analysis at 21 months after surgery. The same group investigated shape of NGCs, concluding that a tubular structure is not mandatory in a 50mm cat sciatic nerve model, paving the way for amorphous systems that adhere the proximal and distal stump together (Hashimoto et al., 2005). Alginate has been researched when blended with synthetic polymers poly(urethane) and poly(dl-lactide) to provide increased stiffness and increase resorption delay which may encourage a greater axon density (Szarek et al., 2013). Although Alginate can be blended to enhance properties of composite NGCs, the lack of literature may suggest that this biopolymer system leads to poorer results (in the same post-surgery follow up period) when compared to more prolific biopolymers in the literature such as chitosan, collagen and silk, alginate may be combined with cytokines such as FGFs to mitigate the lack of bioactive effect (Suzuki et al., 2016).

#### 1.4.8 Hyaluronic Acid

Hyaluronic acid (HA) is commonly found in human ECM and is considered a high molecular weight glycosaminoglycan. Endogenous breakdown of hyaluronic acid has been studied and shown to encourage activation of astrocytes to form an astrocytic scar within the CNS, when introduced in vivo at high concentration (Struve et al., 2005). At lower concentrations, hyaluronic acid can inhibit astrocyte proliferation demonstrated in vitro. HA may be modified in preparation for crosslinking by cinnamic acid, which can encourage a higher viscosity and ensure that the material remains in situ for longer which can result in increased cellular infiltration. In turn this offers excellent biocompatibility but still suffers from a relatively fast degradation rate due to the presence of hyaluronidases in nerve tissue (Sherman et al., 2015). There may be increased fibrosis rather than axonal growth when used for PNR. HA produces soft hydrogel matrices which

makes it difficult to use in the production of NGC outer layers. HA does however offer suitable viscoelastic properties to match that of the ECM owing to it being a native ECM molecule and can be used as a NGC luminal filler (Ryan et al., 2017). Use of hyaluronic acid is more prevalent when used as an anti-scar formation agent within the epineuria when compared to its use in PNR (Agenor et al., 2015). HA can be produced as a nerve wrapping film and was investigated in conjunction with carboxymethylcellulose as a thickening agent and anti-axonal barrier to direct axons towards the distal stump whilst reducing the extent of fibrosis (Mekaj et al., 2016).

#### 1.4.9 Silk Fibroin

The Oliviera group produced patented silk fibroin scaffolds for use in many tissue engineering areas such as peripheral nerve regeneration (Ribeiro et al., 2017). Silk fibroin consists of mechanically strong natural fibres capable of cross-linkage to form a viscoelastic hydrogel. Silk fibroin has a high solubility in water providing the ability to incorporate soluble growth factors within the scaffold capable of influencing nerve regeneration and guidance. Silk worm fibroin was used in a study to encapsulate nerve growth factor (NGF), an attractant molecule for extending neurites (Uebersax, 2007). This resulted in 50% adsorption to the matrices as demonstrated by enzyme linked immunosorbent assay (ELISA), however the follow up trial in vivo was not found.

Interestingly, reconstituted silk fibroin was coated with hyaluronic acid to make a neural scaffold whilst the NGC wall was made from bombyx mori fibroin, rendered porous by freezing (Huang et al., 2012). The two distinct fibroins were selected for their variance in mechanical properties and used for long term stability and elasticity for supporting cell expansion respectively. As well as fibroin chains, additives have been used to increase axon density including growth factors, vitamins or nanoparticles (Sivak et al., 2014; Xie et al., 2015, Bhutto et al., 2016). Some authors argue that the use of stem cells are key to providing comparable regeneration to autograft repair of PNI (Yang et al., 2011). However others report the same level of repair with empty electrospun silk fibroin conduits (Hu et al., 2013). This highlights the current debate concerning whether the benefits of addition of luminal fillers and active substances to scaffolds (molecular or cellular) and whether they truly result in comparable or improved repair compared to autograft. A promising feature of silk fibroin scaffolds is the ability to create aligned microfibrils through electrospinning which serve to direct axonal growth and increase functional recovery time, however controlling the consistent alignment of fibres parallel to conduit from electrospinning is

difficult to achieve and fibres are often aligned within 10° of each other (Fan et al., 2013; Bhutto et al., 2016). Correct alignment of axons is vital for guiding towards the correct effectors, as outlined by Sperry's classic experiment where retinal ganglion axons synapsed to laterally opposite regions of the lateral geniculate nucleus due to rotating the optic nerve by 180° after full transection of the nerve (Grafstein, 2006).

#### 1.4.10 Biogenic Conduits

Biogenic materials suggest that the graft material has been derived from living cells which have been cultured in bulk for use as an NGC. Polyvinyl chloride (PVC) tubes have been used as a template to produce biogenic scaffolds – fibroblasts and endothelial cells that infiltrate the PVC tube and proliferate into a tissue scaffold for nerve growth of the correct size for the nerve (Penna et al., 2011). Implanted into the sciatic nerve repair model, the effect of time for generation of the 'in vivo engineered' biogenic conduit was evaluated for nerve repair outcomes. The conduits demonstrated regeneration within the conduit by providing a biological scaffold that is alternative to the autograft with optimum results in scaffold prepared for 4 weeks however axon count and nerve area were reduced in the test group compared to autograft.

#### 1.4.11 Acellular Conduits

Decellularisation techniques offer the advantage of preserving the extracellular matrix, offering guidance cues and architecture, to regenerating axons. Porcine nerve decellularisation offers a compromise between xenotransplantation and allografting. In a study, porcine sciatic nerve branches were decellularised using sodium dodecyl sulphate in a hypotonic solution (Zilic et al., 2016). The nerves were shown to maintain collagen and laminin content following the protocol.

#### 1.4.12 Synthetic Materials

Synthetic polymer systems provide improved control of biodegradability, biocompatibility and structural formulae, as conditions can be controlled during manufacturing. Although FDA approved NGCs offer satisfactory biocompatibility as they all are biopolymer based, their degradation rates cannot be easily altered or controlled to only degrade after full recovery, hence synthetic systems may offer better outcomes (Nectow et al., 2012).

Poly(dl-lactide-ε-caprolactone) (PDLLA-ε-CL) was used to bridge a 10mm sciatic nerve defect (Den Dunnen et al., 1996). The polymer composition is 50% lactide (non-degradable) and 50% ε-

caprolactone (biodegradable) providing biodegradability. It was also shown qualitatively that use of the DLLA- $\epsilon$ -CL system (filled with denatured muscle tissue providing a natural luminal filler scaffold) provides a faster reconstruction than autograft (Meek and Coert, 1996). In 2006, the same group published quantitative electromyography (EMG) results and gait analysis to confirm this, focussing on re-innervated gastrocnemius or tibialis anterior muscles via repaired sciatic nerves. Although EMG traces were abnormal compared to control (non-operated contralateral side muscles), traces were available and gait analysis showed improved function in animals with the NGC compared to autograft. Poly(L-lactic acid) (PLA) is also commonly used as an NGC material. In a study in which a porous PLA scaffold was generated and used in a 10mm Sciatic nerve defect, axon density similar to controls indicated no adverse effect of using the degradable system in nerve repair (Evans et al., 1999). Furthermore, microfilament bundles and PLA and poly(L-lactide-co-DL-lactide) in a 75:25 weight % blend were produced as NGCs with the PLA microfilaments aligned inside the lumen. Evaluation for repair of 18mm sciatic nerve lesions showed that the filament scaffold demonstrably enhanced tissue cable formation and Schwann cell migration, compared to controls, providing significant healing improvement (Cai et al., 2005). Poly( $\epsilon$ -caprolactone) however has received more attention due to its FDA approval as a biocompatible material for use in medical devices and viscoelasticity when compared to PLA.

Poly( $\epsilon$ -caprolactone) and PLA have subsequently been used in conjunction, to create micro-patterned grooves on the internal luminal surface of NGCs, showcasing how synthetic systems can be easily combined to enhance regeneration outcomes (Mobasseri et al., 2015). The blended system was investigated for supporting photolithographic motifs to enhance neurite extension creating sloped, square and v- shaped grooves (Mobasseri et al., 2014). Again, the grooves are important to encouraging nerve guidance towards the distal stump and can be achieved by various methods including photolithography or electrospinning to create anisotropic NGCs. Further, the study investigated use of sloped walls of varying wall thicknesses and used 70 $\mu$ m wall thickness in a Sciatic nerve repair model evaluated after 16 weeks, to enhance axon density and compound muscle action potential recovery.

Polyglycolic acid (PGA) is another FDA-approved material for use as a NGC (Neurotube) which provides a longer time for degradation of 3 months which was demonstrated to provide improved repair outcomes when compared to other biopolymer based systems (Meek and Coert 2008).

Important findings suggest that a blend between natural and synthetic polymers aids biocompatibility. NGCs with highest regenerative ability include collagen used in conjunction with synthetic biodegradable polymers PLA and blends such as the PLA- $\epsilon$ -CL system, as well as synthesized poly(ester-urethane) as an alternative (Ciardelli and Chiono, 2006). The specific blend of PLA- $\epsilon$ -CL is also FDA approved called Neurolac (Polyganics<sup>®</sup>, Groningen, The Netherlands). However the NGC is double layered and therefore presents a lower porosity than biopolymer based NGCs, which could hinder regeneration. Permeability is important for exchange of factors and encouraging micro-circulation by angiogenesis mechanisms, and a higher degree of crystallinity of synthetic systems is inversely proportional to repair.

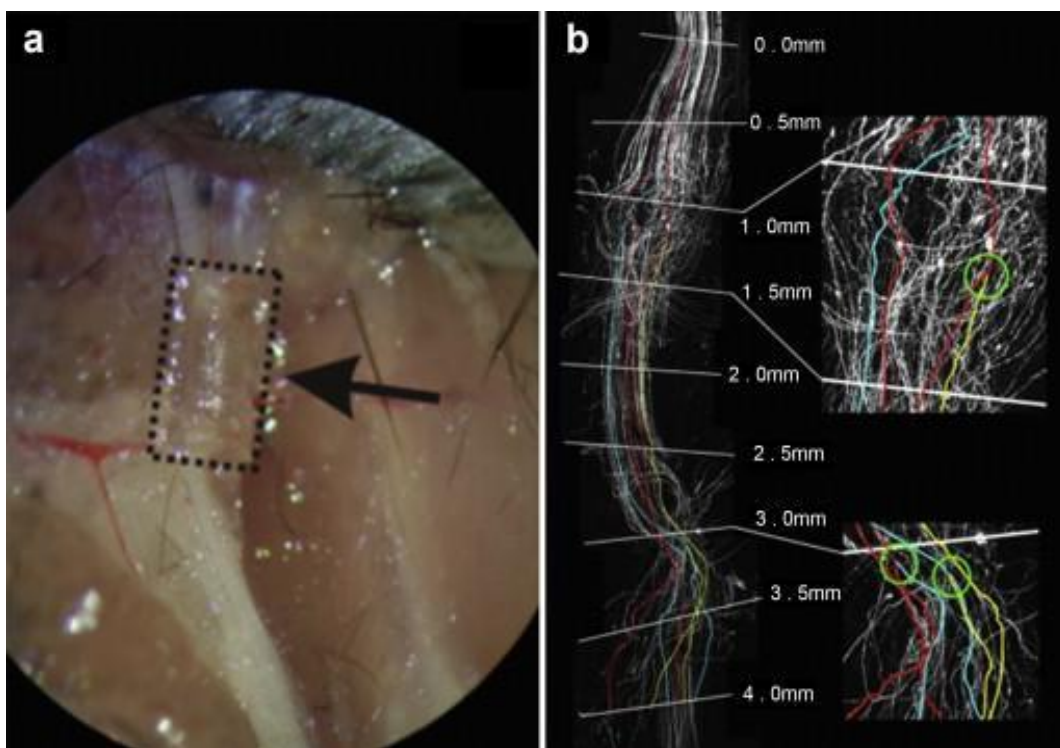
A non-degradable nature results in inflammatory response and possible nerve compression by fibrosis, which must be overcome to guarantee the necessary level of biocompatibility (Merle et al., 1989). However, careful design of the synthetic component of NGCs can reduce nerve compression.

Using degradable polymers provides time-dependent control over degradation and also can ensure low immune-reactivity should the right degradation products be released to encourage neural cell attachment. Common polymer systems used are Poly(L-Lactic) acid, Poly(glycolic) acid, Poly(caprolactone) and Poly(1,3-trimethylenecarbonate- $\epsilon$ -caprolactone). Other materials of interest include Diamond-Like Carbon (DLC), which due to its covalent structure should provide enhanced stability and has been shown to be biocompatible in vivo (Hopper et al., 2016). DLC was functionalised with amine or aldehyde groups at the surface promoting cell adhesion (due to reduction of DLC surface hydrophobia) and neurite growth, as well as maintaining Schwann cells phenotype. Outgrowth matched that of conventional PLL, both amine- and aldehyde-functionalised surfaces performed comparably.

#### 1.4.13 Synthetic NGCs

Transgenic models can provide improved quantification of outcomes of PNR. An emergent model is the Thy-1-YFP-H fluorescent axon mouse peripheral common fibular nerve injury model (Pateman et al., 2015). Disruption of nerve re-organization was reported when a PEG conduit was used in this murine model, but was comparable to a control nerve graft using a littermate's nerve, at the proximal stump. There is concern that using a littermate's nerve could lead to a mismatch of tissue type which could reduce results if an immunogenic response is caused. However,

towards the distal stump, axons returned to a more organized state (Figure 1.8). Axon density in the distal portion of the regenerated nerve in the guide and control groups were similar. Average Young's modulus of the PEG was 470 MPa, which is comparable to silicone conduits (the standard in the first generation of synthetic NGCs) often used as control synthetic NGC in these studies. The elastic modulus of nerve tissue is seen to vary according to thickness of nerve trunk, species and whether it is stretched or not although testing methods and assumptions vary resulting in a large range of values reported for both nerve and NGC materials. However, it is worth noting, nerve tissue elastic modulus is observed to vary between  $1.0 \times 10^2$  to  $1.0 \times 10^5$  Pa (Topp and Boyd, 2006).



**Figure 1.9:** (a) Implantation of 5mm x 1.5mm x 250  $\mu$ m PEG guide into a THY-1YFP-H common fibular mouse small gap 3mm injury model. (b) Image of Thy-1-YFP-H repair showing axon tracing from 0.0mm to 4.0 mm. Axons counted and compared to -0.05mm interval to produce sprouting index value. (Pateman et al., 2015)

In an evaluation of discrete diameters of PCL microfibers, effects were examined on neuronal and primary rat Schwann cells as single cultures and as a co-culture derived directly from dorsal root ganglion explants (Daud et al., 2012). PCL fibre alignment is well exhibited, with 85% of fibres being within  $4^\circ$  variation from the axis of alignment. Fibre density was largest amongst the

smallest diameter fibres (1 $\mu$ m), being 80% higher than on 5  $\mu$ m fibres and 117% higher than on 8 $\mu$ m fibres. Maximum neurite length was significantly improved when cultured on smaller (<5 $\mu$ m) fibres compared to 8 $\mu$ m fibres – this was supported by the result that maximal primary Schwann cell length was achieved in the 1 $\mu$ m group. In the neuronal-glial co-cultures, 1 $\mu$ m fibres supported better neurite outgrowth, Schwann cell migration and elongation compared to larger diameters.

However, when modelled in the animal model, a high density of the fibres has been reported to inhibit axon extension within the NGC meaning packing density is an important parameter to control (Fields et al., 2018). Furthermore, poly(hydroxyalkanoate) blends were analysed for neuronal cell biocompatibility involving ratios of poly(3-hydroxybutyrate), P(3HB), and poly(3-hydroxyoctanoate), P(3HO) (Lizarraga-Valderrama et al., 2015). The 25:75 P(3HO)/P(3HB) blend showed greater biocompatibility attributed to an appropriate tensile strength (Young's modulus was 143.3  $\pm$  2.2 MPa) which additionally supported neurite extension, growth and differentiation of NG108-15 neuronal cells.

### 1.5 Fabrication of NGCs

Classic techniques for fabricating nerve guide from polymers include injection moulding, or precipitation/dip coating on rotating mandrels (Li et al., 1992; den Dunnen et al., 1996). These techniques often rely on cross-linking agents to alter the system from liquid phase to solid phase, increasing viscoelastic stiffness, as is the case for collagen for example. Another technique more relevant to synthetic fibrous materials is rolling of the polymer sheet to the desired size (Dellon and Mackinnon, 1988). Collagen may be extruded into water containing cross-linking agents to produce coagulating fibres which are drawn out, dried and moulded to form an NGC. Often, collagen and other charged polymer solutions can be electrospun to create aligned fibres without forming any inconsistency within the final product (Ouyang et al., 2013). This method creates porous three-dimensional structures rather than planar two-dimensional polymer films which must be sutured together across joints when shaping the NGC.

Natural polymers must often be extracted from the native tissue e.g. extraction of fibroin from silk fibres is achieved by an aqueous boiling process, to remove sericin which is the sticky protein that adheres fibroin fibres together (Ki et al., 2007). The aqueous solution can either be



lyophilized to reveal a spongy, porous interconnected network or electrospun to form aligned fibres (Uebersax et al., 2007; Chew et al., 2008).

For acellular grafts, the ECM structure is conserved through decellularisation. Cell lysis is achieved through freezing of explanted tissue or mechanical agitation to preserve the basal laminae and other protein matrices matching the viscoelastic stiffness of native tissue, which are further lysed by using hyperosmotic pressure (Arslantunali et al., 2014). Axogen is a US-based company specialising in providing decellularised nerve tissue from cadavers as NGCs providing a native tissue scaffold with specificity for either motor or sensory nerves (Moore et al., 2011).

Photolithography methods have been extensively researched to give complex three-dimensional structures, where solid structural motifs at a micrometre scale are stamped or engineered into surfaces and are often functionalised with substrates to influence cell attachment and growth patterning. In a study by Ni et al. (2013), fibroblast growth factor-1 was adsorbed onto PLA NGCs by photolithography. PLA solution was poured into a poly(dimethylsiloxane) (PDMS) mould which contains microgrooves fashioned from a silicon wafer itself cast from a mould using photolithography (Hsu and Ni, 2009). The width and spaces between microgrooves were both 20 $\mu$ m and depth was 3 $\mu$ m to provide a similar orientation to growing axons through this highly reliable technique.

X-ray diffraction (XrD) and Fourier Transform Infrared Spectroscopy (FTIR) are commonly employed to assess changes in surface chemistry of synthetic materials (Nazarov et al., 2004). Providing information on functional group chemistry to confirm success of modifications and blending processes in polymer systems.

Novel printing techniques allow for specific features to be created on NGCs. Lee et al. (2010) have demonstrated the use of bio-printing to produce collagen/ fibrin hydrogel system containing Vascular Endothelial growth factor (VEGF) and printed with live cells. A rapid technique was developed by Mills et al. (2013), where complex structural patterning on NGCs, using a digital multi-mirror device (DMD) through laser sintering technique was used to fuse polymer particles. Using photocurable resins, this technique has been assayed and evaluated for neural cell adhesion demonstrating neurite outgrowth but was not evaluated further in vivo (Pateman et al., 2015).

3D structured light scanning of sciatic nerve branches with sensory and motor paths has been modelled and used to design a silicone NGC with specific regions of flexural strength to match the nerve tissue, the design data being based on torsional loading in vivo (Johnson et al., 2015). Various neuro-compatible materials were assessed and validated for use in printing including poly(caprolactone), alginate, poly-(lactic-co-glycolic) acid but silicone was chosen, due to use in previous studies (Williams et al., 1983; Labrador et al., 1998). As silicone can be produced as a soft material, complex compression loading tests are less important for nerve tissue matching although mechanical stress from surgical manipulation of the NGC during implantation should be taken into account to ensure no breakage occurs (Sundback et al., 2005).

A range of fabrication techniques have been listed in Table 1.5 to summarise the various methods available. The papers analysed and listed in Table 1.4 were used to produce Table 1.5. The fabrication techniques listed in the table provide a summary of the most common NGC fabrication techniques that are used to produce predominately tubular devices. These ensure that both proximal and distal stumps can be inserted into the lumen of the device and axons can be guided in theory. The difficulty in producing nerve guides fit for the sciatic nerve model comes in producing reliably very small diameter NGCs with a small thickness to ensure that diffusion of waste materials can occur (discussed further in section 2.1.2.2). The ease of producing the correct dimensions that match the model nerve is dependent on the fabrication method.

Table 1.5: Analysis of conduit fabrication methods

Reference	Year	Format	Fabrication Method
Radtko	2010	Acellular vein graft	Decellularisation
Dornseifer	2011	Conduit	Denatured muscle filling
Liu	2011	Conduit	Injection moulding
Li	2011	Conduit	Dip moulding
Yang	2011	TENG	Electrospinning
Ghaznavi	2011	Conduit	Dip moulding
Lee	2012	Conduit	Neuragen, commercial source
Lee	2012	Conduit	Electrospinning
Masand	2012	Hydrogel	-

Bozkurt	2012	Hydrogel, microchannels	with	Uni-directional freezing
Wang	2012	Conduit		Injection moulding
Gu	2012	Conduit		-
Neal	2012	Conduit		Electrospinning
Huang	2012	Conduit		Spidrex, commercial biomaterial
di Summa	2013	Conduit		Neuragen, commercial source
Maturana	2013	Conduit		Membrane from solvent technique
Berrocal	2013	Conduit		Neuragen, commercial source
Hu	2013	Conduit		Injection moulding
Seo	2013	Conduit		Injection moulding
Carriel	2013	Conduit		Neuragen, commercial source
Mottaghtalab	2013	Conduit		Freeze-drying, electrospinning
Hu	2013	Conduit		Dissolve and air dry, electrospinning
Li	2013	Conduit		Electrospinning
Marinescu	2014	Elastic membrane, fixed with PVA		Solvent and drying
Ma	2014	Ordered Collagen Fibres		Rolling
Cui	2014	linear ordered collagen		Aponeurosis sheet
Zhao	2014	Nanofibrous Scaffold		Electrospinning
Zhao	2014	Conduit		Cast moulding
Hsueh	2014	Conduit		Silicone tube fill
Matsumine	2014	Conduit		Gelatin microspheres
Beigi	2014	Conduit		Electrospinning
Koudehi	2014	Conduit		Sol-gel technique
Sivak	2014	Conduit		Degumming
Azizi	2015	Conduit		Injection moulding
Sarabia-Estrada	2015	Conduit		Dip moulding
Gonzalez-Perez	2015	Conduit		Washing and hydrolysis process

Roam	2015	Conduit	Microspheres with GDNF
Kakinoki	2015	Conduit	Electrospinning
Xie	2015	Conduit	Injection moulding
Zhang	2015	Conduit	Electrospinning
Das	2015	Conduit	Electrospinning
Teuschl	2015	Conduit	Degumming
Gao	2016	Conduit	Poly(styrene) fibres cast in Agarose gel
Fujimaki	2016	Oriented strings	Extrusion
Bozkurt	2016	Oriented microchannels	Freeze-drying
Fregnan	2016	Flat membrane	Solvent casting
Mehrshad	2016	Conduit	Injection moulding
Kusaba	2016	Mesh tube	Injection moulding
Mokarizadeh		Conduit	Injection moulding
Meyer	2016	Conduit	Film manufacture
Meyer	2016	Conduit	Washing and hydrolysis
Suzuki	2016	Non-tubular Gel	Solvent based technique
Szarek	2016	Conduit	Immersion
Das	2017	Conduit	Electrospinning
Rao	2017	Conduit	Degumming and Unidirectional freeze-drying
Ebrahimi	2017	Conduit	Degumming and Electrospinning
Ko	2017	Conduit	Mandrel coating
Muheremu	2017	Conduit	Freeze-drying
Gonsalez-Perez	2017	Conduit	Solvent casting and rolling
Guo	2017	Conduit	Mandrel coating
Stenberg	2017	Conduit	Solvent casting and rolling
Turner	2017	Conduit	Solvent casting and rolling
Iman	2017	Conduit	Injection moulding
Tsujimoto	2017	Conduit	Knitting of PGA fibres and backfilling

Bozkurt	2017	Conduit	Freeze-drying
Yin	2018	Conduit	Injection moulding/ Freeze-drying
Wang	2018	Conduit	Degumming and Electrospinning
Zhang	2018	Conduit	Electrospinning
Gonsalez-Perez	2018	Conduit	Solvent casting
Salehi	2018	Conduit	Electrospinning
Zhang	2018	Conduit	Injection moulding
Stößel	2018	Conduit	Injection moulding
Ma	2018	Conduit	Freeze-drying
Cui	2018	Conduit	Solvent casting and rolling
Mohamadi	2018	Conduit	Electrospinning
Saeki	2018	Conduit	Freeze-drying

The most common methodology for NGC fabrication involves the use of solvents to dissolve biopolymer into a fluid phase which can be stiffened by gelation or crosslinking (Mehrshad et al., 2016; Azizi et al., 2015). The material can be moulded to a predefined shape which is ideal for ensuring that the NGC can fit easily onto nerve stumps, however it is difficult to ensure the wall thickness is controlled when using a double layer mould due to fracture when removing the device after crosslinking. Another method to produce porous conduits stiff enough to be implanted with sutures is by use of freeze-drying (Mottaghitlab et al., 2013). Freeze drying has the advantage of physically crosslinking the biopolymer chains and avoids chemical crosslinking which can involve the use of harmful chemical species. Freeze-drying can also be controlled to encourage alignment of polymer fibrils, for instance for collagen the fibrils have been demonstrated to align along a controlled temperature gradient during freeze-drying (Bozkurt et al., 2016). Both injection moulding, freeze-drying and electrospinning techniques provide easy ways to produce hollow tubular NGC structures. Electrospinning is favoured as a method for producing both nano-fibrous meshes and aligned microfibres as it can be carefully controlled by adjusting either the distance for collection or the voltage applied. Electrospinning is therefore more reliable and provides some control over pore density thus controlling diffusion of enzymes which degrade the NGC over time within the material, which can then be rolled into the shape of

an NGC. Some papers discussed the use of ordered fibrils which can be used as a method to direct axon alignment (Ma et al., 2014; Cu et al., 2014; Fujimaki et al., 2016). These fabrication techniques have been investigated further (sections 4.3.10 and 6.2) and have been considered as design specifications for a novel NGC design (section 2.1.4).

#### 1.5.1 Design Specifications

Nerve conduits are designed to give adequate space to regenerating tissue by matching the cross sectional area of the nerve, without causing extra pressure on regenerating fibres which can lead to scarring (Hasirci et al., 2014). Most designs follow the same template - a hollow conduit with internal lumen. An external diameter of 2mm is often used for Sciatic nerve models. The internal diameter is often 1.8mm and length varies according to injury size and implant nerve. For animal models, typical length is usually between 5-15mm for the rat Sciatic nerve repair model (Hansen et al., 2016; Gonzalez-Perez et al., 2018).

Conduit design has been compared in Table 1.6. Information was sourced from papers that involved an animal or human trial, and reported behavioural or electrophysiological testing. The design of NGCs does not vary much between trials and is commonly carried out on the rat sciatic nerve model.

Table 1.6: Comparison of design features of nerve guides

Internal Diameter (mm)	External Diameter (mm)	Length (mm)	Wall Thickness (mm)	Reference
1.8	2	10	0.2	Mehrshad et al., 2016
1.8	2.1	10	0.3	Mokarizadeh et al., 2016
2.1	-	19	-	Meyer et al., 2016
2	-	12	-	Azizi et al., 2015
1.5	2.1	10	0.6	Sarabia-Estrada et al., 2015
1.2	1.6	15	0.4	Zhoa et al., 2014
1.8	2	-	0.2	Lui et al., 2013
-	-	-	0.5	Kakinoki et al., 2015
1.6	-	15	-	Neal et al., 2012
2	2.07	-	0.07	Szarek et al., 2016
1.5	2.25	7	0.75	Xie et al., 2015
-	-	-	0.045-0.075	Teuschl et al., 2015
1.5	-	-	-	Lie et al., 2013
1.5	2.2	-	0.7	Lie et al., 2011
-	-	-	0.6	Ghaznavi et al., 2011
Mean = 1.69	Mean = 2.06	Mean = 12.25	Mean = 0.1	

The papers used to compile Table 1.4 were used to produce Table 1.6. Although, not all measurements were available for outer diameter, inner diameter, total length and wall thickness. Overall, the specification data that was available confirms that there is agreement amongst papers that the diameter for sciatic nerve repair must be between 1.7mm and 2.0mm, and that very thin walls of 40µm are often fabricated however this depends on the fabrication technique used. Again, the mean length was calculated close to 10mm (10.5mm), the length of the conduit

is usually slightly longer than the size of the gap injury to allow space for attaching the nerve stumps to the NGC (Wolford and Stevao, 2003).

### 1.5.2 Adjunctive Healing Techniques to Nerve Conduits

Nerve guides alone have been shown to experimentally provide support to regenerating neural tissue. Amongst studies on peripheral nerve repair however, complementary technologies are used to attempt to increase the speed of recovery, length of axon outgrowth and final functionality. Some techniques are described in sections 1.5.2.1 to 1.5.2.5.

#### 1.5.2.1 Electrical Stimulation

Weak electrical DC currents have been shown to direct and enhance regenerating neurons in vitro (Hinkle et al., 1981). Electrical stimulation increases concentration of neuroprotective factors such as NGF and BDNF, cAMP for secondary messaging and switching on of growth-associated genes in vivo (Gordon, 2016). In vitro, pulsed 50mV/mm DC electric fields provide optimal alignment and less variation in orientation of cultured Schwann cells (Koppes et al., 2014). Pulsed electromagnetic fields (PEMFs) allow for non-invasive control of speed of regenerating axons, without altering functionality (Rusovan et al., 1992). Brief electrical stimulation following ligation of the rat sciatic nerve was shown to promote motor neuron innervation without increasing recovery speed and myelination thickness demonstrating that could be developed for use on patients prior to NGC implant closure (Brushart et al., 2002; Pei et al., 2015). In vitro characterisation of the conductive polymer oxidised polypyrrole (PP) was evaluated and was shown to give improved neurite outgrowth of PC12 cell line cells, compared to conventional materials such as PLA and PLGA when subjected to electrical stimulation through the films (Schmidt et al., 1997).

Advances in optogenetics proposes that electrical stimulation of neurons can be controlled through viral vectors of DNA, encoding optically controlled voltage-gated ion channels. This technology offers the ability to excite specific targeted neurons via coalescence of Channelrhodopsin-2, an important biochemical photon transducer in the sensory light adaptation mechanisms of retinal cone cells, on neuronal cell membranes. These can be opened with LED light and coupled to voltage-gated Na channels to selectively excite neurons (Grubb and Burrone, 2010). The tool was used to excite murine embryonic stem cell-derived motor neurons implanted into a partially denervated sciatic nerve model. This technology has been



demonstrated to restore function to the nerve in hind limb muscles, measured by EMG analysis although excess stimulation can be toxic to neurons and the technology needs further research (Bryson et al., 2014).

#### 1.5.2.2 Molecule-mediated Therapies

Chemical stimulants have also been used to encourage effective nerve guidance such as NGF, laminin, or cellular cues by Schwann cells and astrocytes (Wang-Bennett and Coker, 1990). Particularly when compared to controls such as NGCs filled with saline, empty silicone NGCs or autografts (Chen et al., 2000; Faroni et al., 2015). Various conduits have been designed to encourage neurotrophic cytokine signalling between nerve stumps, as cytokine to cellular to ECM messaging in a spatiotemporal manner is required for optimal regeneration (Pearson et al., 2003). The most common factors include Nerve Growth Factor (NGF), Brain Derived Neurotrophic Factor (BDNF), Glial Derived Neurotrophic Factor (GDNF), Neuregulin-1 (NRG1) and Fibroblast Growth Factor (FGF). However for clinical efficacy, the administration of growth factors must occur at the correct dosage and release must occur over a relevant time period. For example, overdose of BDNF can actually lead to neuronal cell death (Boyd and Gordon, 2002).

Commercial poly( $\epsilon$ -caprolactone), 20-500 $\mu$ m, and poly(ester-urethane), 300-500 $\mu$ m, have been compared for wall thickness. The increased wall thickness may be responsible for a slower rate of diffusion of fluids across the NGC wall and the wall rigid enough to reduce nerve compression (Chiardelli and Chiono, 2006). Pearson et al. (2003) concluded that neurite extension is independent of conduit diameter (which varied from 200 to 635  $\mu$ m), however this may be the case when biopolymer rather than synthetic NGC luminal fillers are used as a collagen type 1 hydrogel-filled NGC made of non-porous glass was used.

#### 1.5.2.3 Cellular Therapies

Another family of support cells being researched for use in conjunction with NGCs are stem cells, specifically adipose-derived neural stem cells (NSCs) derived from subcutaneous or perinephric fat most effective for promoting increased BDNF and NGF levels (Kaewkhaw et al., 2011). Adipose-derived stem cells offer an advantage over harvesting Schwann cells, as there is less risk of donor site damage and Schwann cells often enter quiescence during expansion (di Summa et al., 2011).

However cell-free devices are more clinically attractive due to a reduction in the complexity of the implant system and possible immunogenic risks from the implanted cells (Bell and Haycock, 2012). However, cellular-inclusive therapies are argued to produce better results in vitro. Another issue with preparing Schwann cell cultures for loading NGCs is the presence of a mix population of cells when derived from explants particularly fibroblasts (Kaewkhaw et al., 2012). A protocol involving rapid selection of Schwann cells has been developed by the Haycock research group using inhibitory factor to fibroblasts, D-valine, and Schwann cell mitogenic factors, forskolin and N2 supplement plus bovine pituitary extract within DMEM media to achieve a purity rate of 97%.

#### 1.5.2.4 Schwann Cell Therapies

Inclusion of Schwann cells in NGCs, to increase myelin production, has proven to improve axon regrowth (Kalbermatten et al., 2008; Borlongan, 2010). Schwann cells provide tracks along which peripheral nerve axons extend as they are activated into a pro-regenerative phenotype, during repair processes following injury (Geuna et al., 2009). The basal lamina of Schwann cells can provide some support for regenerating axons, as they have also been shown to give direction and a substrate for regrowth after Schwann cell degradation, by freeze-thaw cycling (Ide et al., 1983). Furthermore, Schwann cells were shown to be vital for directing axonal growth of regenerating motor neurons onto the Soleus muscle, evaluated using anti-neurofilament labelling to trace axons (Son and Thompson, 1995). Stem cells producing Schwann cell-like cells may also allow for a more complete cocktail of the necessary growth factors for PNR. The Phillips group have produced engineered neural tissue, using a collagen hydrogel and aligned Schwann cell cells to produce a three-dimensional mimic of nerve (Schuh et al., 2018). Experiments have shown that Schwann stem cells are supportive to regenerating axons, providing significantly more axons when compared to control (autograft) and nerve guides without cells.

Schwann cells have also been derived from bone marrow stem cells and adipose derived stem cells, for use in NGCs, with comparable success of regeneration to controls (Kingham et al., 2007; Xu et al., 2008, Borlongan, 2010). Schwann cells have been modified to over-express neurotrophic factors such as BDNF and FGF-2 within a hyaluronic acid and laminin hydrogel filled chitosan NGC resulting in decreased regeneration when compared to control due to leakage of the filler from NGC which must be controlled to ensure delivery of the cytokines (Meyer et al., 2016).

## 1.6 Clinical Trials and Data on Nerve Guides

Four commercially available NGCs are listed (with the manufacturer) as follows:

- Neurotube® (Synovis)
- Neurolac® (Ascension)
- Salubridge® (SaluMedica)
- Neura-Gen® (Integra).

Currently all NGCs have given results comparable to that of autograft but comparing these devices is difficult due to differential analysis criteria amongst animal model studies (de Ruyter et al., 2009). There is a large level of variability amongst the human clinical data available, primarily due to the variation in age of patient, latency of surgical intervention and site of nerve injury (Gerth et al., 2015). At present, there are few meta-analyses of the clinical data. Clinical data on the success of nerve regeneration using conduits in long gap injuries are presented in Table 1.7. A meta-analytical approach has been conducted to provide a range of time and both positive (functional regeneration) and negative (lack of regeneration) outcomes of surgery. The prospects of positive outcomes of surgery correlate negatively with length of the nerve defect. The shorter the distance axons must travel to regenerate the nerve defect, the more likely surgical success. Therefore, when developing a model to monitor nerve repair strategies, a critical nerve gap length must be determined to avoid spontaneous regeneration from being considered as a positive outcome.

**Table 1.7: Comparative Table of Clinical Data on Material Use**

<b>Nerve Guide Material</b>	<b>Number of Patients</b>	<b>First Author</b>	<b>Year</b>	<b>Overall Outcome</b>	<b>Percentage of Cases (%)</b>
Silicone	2	Lundborg	1994	Positive	100
	26	Braga-Silva	1999	Positive	-
Poly(tetrafluoroethylene)	43	Stanec	1998	Positive	74.6
	7	Pogrel	1998	Negative	71.4
	1	Wrede	1909	Positive	100
Vein	1	Platt	1919	Negative	100
	22	Walton	1989	Positive	50
	3	Tang	1993	Positive	100
	15	Pogrel	2001	Negative	60
Collagen	3	Ashley	2006	Positive	67
	3	Lohmeyer	2007	Positive	67
	12	Brushnell	2008	Positive	92
	9	Dienstknecht	2013	Positive	89
	50	Merolli	2015	Positive	100
	96	Wangensteen	2010	Negative	57.3
Decellularised NerveAllograft	7	Mackinnon	2001	Positive	86
	7	Karabekmez	2009	Positive	100
	123	Brooks	2012	Positive	84
	5	Guo	2013	Positive	100
	14	Taras	2013	Positive	86
Poly(Glycolic Acid)	15	Mackinnon	1990	Positive	87
	98	Weber	2000	Positive	24
	1	Kim	2001	Positive	100
	7	Navissano	2005	Positive	71
	17	Battiston	2005	Positive	76
	6	Rosson	2009	Positive	100
Poly(Glycolic Acid) and Collagen	2	Nakamura	2004	Positive	100
Poly (DL-Lactide-ε-caprolactone)	54	Bertleff	2005	Positive	100

Most guides offer promising therapies at the lower end of nerve gap length investigated (<4mm). Also, the time delay associated with regeneration of a nerve differs greatly on account of the guide used and the location of the implant. The range in follow up time, which varied from 3 months to 2 years, are expected to be at least as long as the relevant time for functional recovery. Clinical assessment may occur very late compared to functional recovery. Furthermore, it should be considered that negative results amongst clinical data are not published as often as positive

results, hence the success rate of current NGCs evaluated in clinical trials may be lower than the estimated 74.4% calculated from patients included in Table 1.7. This calculation means that clinical devices do not provide optimal repair of injured nerves. Overall, the smaller the injury, the higher the probability of functional repair as was evaluated by Stanec et al. (1998) where injuries smaller than 4cm had a 74.6% probability of regeneration. The most popular materials included collagen, reflecting the substantial publication on the material's properties as a neural scaffold in vitro. Interestingly, the use of decellularised nerve shows the benefit of preserving the ECM or mimicking it (the premise for using collagen). Vein grafts have also been used clinically, although have decreased in popularity, which suggests that use natural materials is generally accepted clinically. The rise of use of poly(glycolic acid) may be attributed to its relative inert properties. Hence further study of peripheral nerve devices is needed to produce more carefully designed NGCs, capable of better biomimicry and scaffolds that are capable of meeting all the requirements discussed in this literature review including biocompatibility, porosity, cell adhesive/ ECM mimicking features, the optimal dimensions, biodegradability and strong mechanical properties for handling purposes.

### 1.7 Summary

The field of peripheral nerve injury and repair has seen much growth and interest due to its highly prevalent nature within communities around the world. In the UK, the estimated prevalence indicates the need for suitable medical devices that are easily handled and readily available as off the shelf cell-supportive, active scaffolds for implantation in surgery and trauma cases. This may minimise operating time and encourage single time repair of injured nerve which has been demonstrated to be a vital indicator of successful repair. A strong NGC product is also available in variable sizes to match the site dimensions of the nerve damage. It is clear from promising research analysed, that nerve guides of novel materials are at the forefront of this research. Currently, there is a need for increased clinical research to supplement innovatory design with novel data.

### 1.8 Aim

The aim of this thesis is to innovate, evaluate and manufacture a peripheral nerve conduit device. Through a design process, the design will be used for peripheral nerve repair of a rat sciatic nerve

model and intended for use as clinical nerve repair device. The resultant design will be evaluated using cell and animal testing.

### 1.9 Objectives

The objectives of the thesis are:

1. To generate design criteria to identify critical parameters of a peripheral nerve repair medical device, that must be satisfied for the system to encourage nerve regeneration between two transected ends of a critical length peripheral nerve and result in recovery.
2. To evaluate an in vitro culture method (using both neural and glial cells) to reliably screen potential materials intended as structural materials for the NGC wall for their efficacy in encouraging cell adhesion, cell biocompatibility, cell proliferation, neuritogenesis, neural differentiation, glial cell extension and to characterise the material for its physical and chemical properties.
3. To use the optimised in vitro model (both neural and glial cells) to evaluate the effect of using a hydrogel system as an intraluminal aspect of the NGC by examining its effect on cell adhesion, cell biocompatibility, cell proliferation, neuritogenesis, neural differentiation, glial cell extension and migration, cell encapsulation and organotypic cultures and characterise its physical and chemical properties.
4. To evaluate the methodology to produce the NGC allowing a simple 'in theatre' production of the medical device to ensure that the device would be suitable for quick implantation.
5. To evaluate the final design of the NGC for proof of concept by repairing the transected sciatic nerve rat model and measuring both functional and structural outcomes using behavioural tests in vivo and histology respectively.

## Chapter 2: Design of a Nerve Conduit Medical Device

### 2.1 Design Inputs

The research and development, plus the final production methodology should follow a structured pathway to ensure accountability in the design process and clear parameters that can be optimised in future iterations of the device. Following such standards allows the technology to be readily translatable into a medical device company or allows the further clinical research via a human trial.

For standardisation purposes, ISO 13485 will be used for the generation of design inputs and outputs criteria.

These inputs have been generated by: A Batth

The inputs were reviewed by: I Thompson and a cohort of the Masters of Design Class (2018), Centre for Design (C4D) at Cranfield University. The Masters students were selected for their expertise in concept design and valued for their non-biased creativity as they were given minimal information about the scientific nature of the research area of PNR.

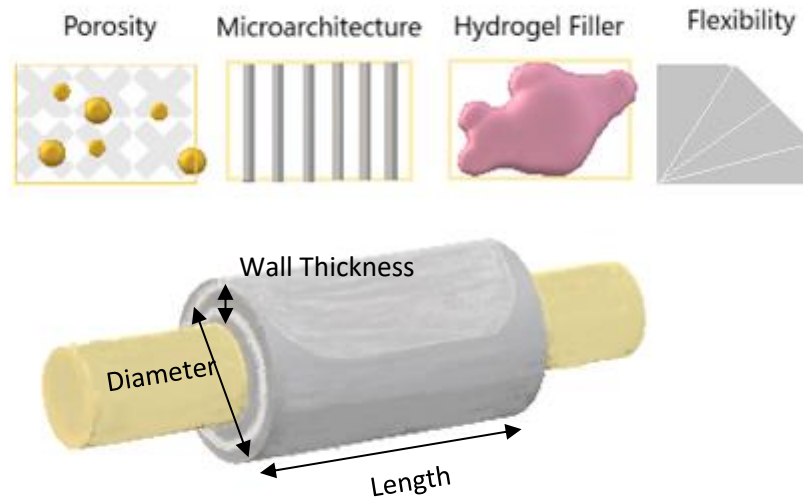
#### 2.1.1 Intended Application

The design specification for this thesis is:

A tubular nerve grafting device for repair of peripheral nerve injuries ranging from 0-15mm in length in a nerve transection and repair model (Dun and Parkinson, 2018). Figure 2.1 illustrates the design features of a nerve guidance conduit (NGC) to provide clarity.

Most NGCs encapsulate damaged nerve stumps and thus physical and chemical cues are presented internally within the NGC, such as microarchitecture and filler materials. Aspects of the external NGC wall that can be designed include porosity, to allow for exchange of gases and metabolites, and flexibility which can improve handling characteristics.

# Nerve Conduit Designs



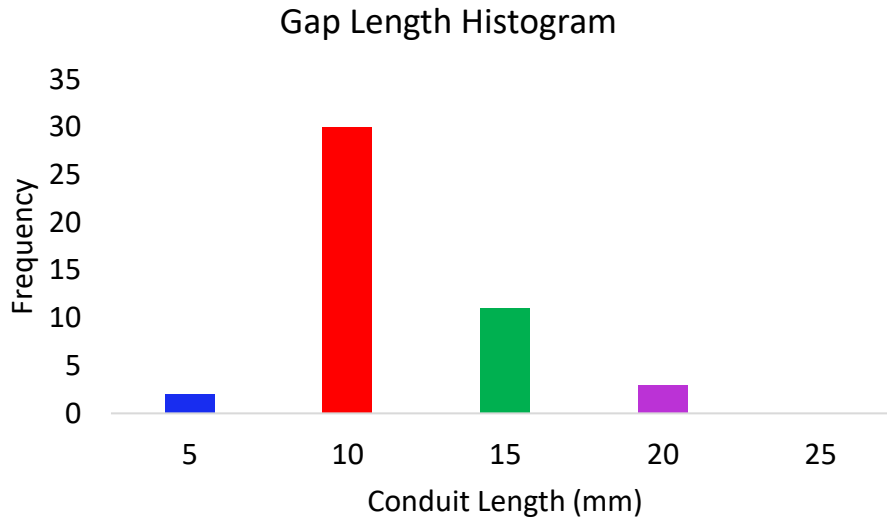
**Figure 2.1:** A schematic to describe design features of nerve conduits. Features discussed include dimensions (length, diameter and wall thickness) and design features of the conduit material which can be altered (including porosity, microarchitecture, hydrogel fillers and flexibility).

## 2.1.2 User Requirements (for the Surgeon)

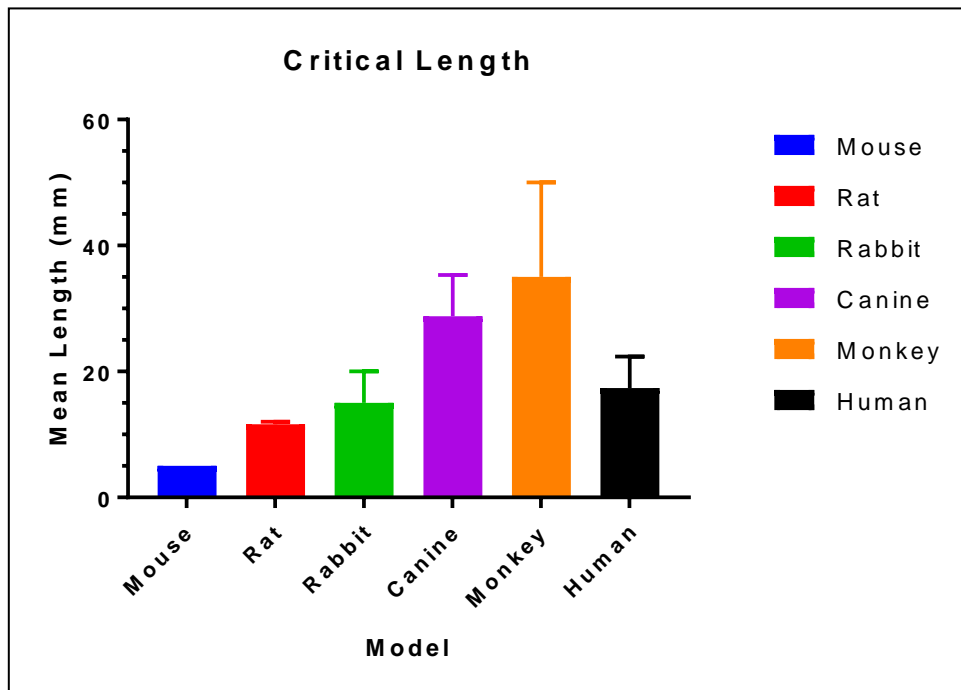
### 2.1.2.1 Length

To evaluate the use of a nerve conduit design, the length of the conduit must be both comparable to other studies in the literature and of a critical length to ensure that nerve regeneration would not be possible via spontaneous recovery (Moore et al., 2015). The ideal length to be tested has been determined to be 10mm for the Rat Sciatic Nerve Model reflecting the modal length of conduits used in animal studies (Table 1.5 and Figure 2.2). This is because there is a wide range of studies that measure the effectiveness of nerve conduit by transecting the nerve to a critical size of 5-15mm. The 46 papers published between 2011 and 2018 (presented in section 1.3.1 (Table 5)) have been examined for design features of natural biopolymer conduits. The studies that used the Rat as an animal model for nerve gap injury and repair have been plotted in a frequency distribution and 10mm is the modal average for conduit length (Figure 2.2).



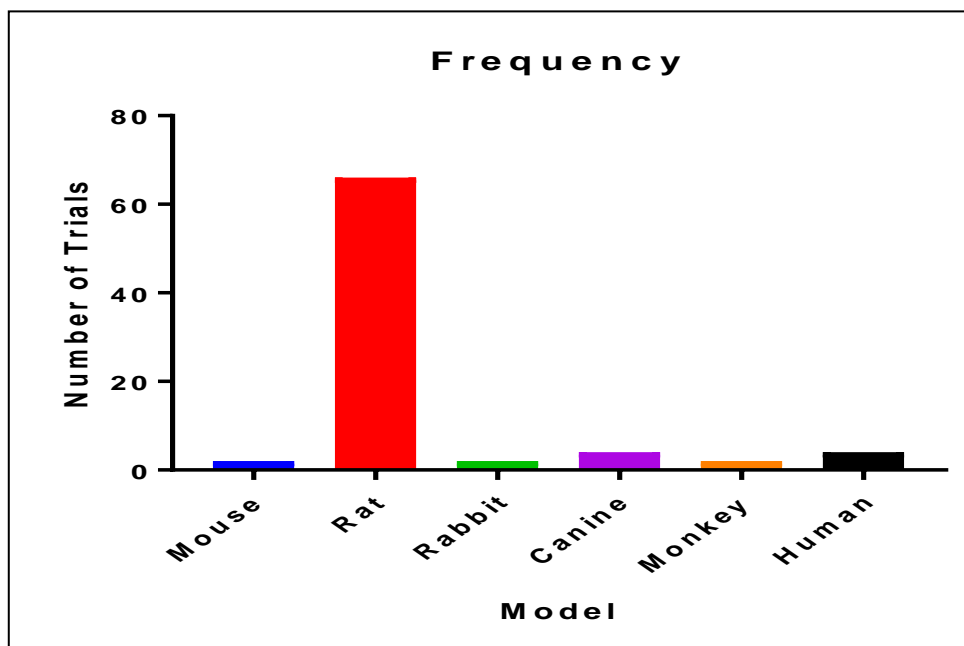


**Figure 2.2:** Histogram showing lengths of conduits used in Rat Sciatic nerve transection models between 2011 and 2018.



**Figure 2.3:** A bar chart to show the mean length of nerve gaps produced in the animal models of peripheral nerve transection and repair with conduit detected from the papers analysed between 2011 and 2018.

The Rat model is an appropriate selection as there are 66 directly comparable studies which can be used as a reference to ensure optimisation of the methodology as well as reliability of the results as regeneration of the nerve can be measured within a comparable time frame. The median average for data collected from papers researching the rat model was calculated at 10mm and the mean length was calculated at 11.2mm, which fits the critical gap length size identified in many PNR papers (Figures 2.2 and 2.3) (Mokarram et al., 2017). In addition, the frequency of papers publishing data derived from the Rat nerve gap injury and repair model was much higher than other animal models, with 66 papers using the model from the selected papers (Figure 2.4). The second most common animal model was the canine which included 4 studies. We have proposed the use of 10mm as the conduit length as it is critical size and comparable to the mode gap length within the studies cited which provides measurable comparisons provided that similar quantification techniques are used when assessing recovery.



**Figure 2.4:** Bar chart to show the frequency of trials conducted in the common animal models of peripheral nerve transection and repair with conduits. The Rat model is the most popular animal model.

### 2.1.2.2 Diameter

The diameter of the nerve conduit must be of adequate fit so that the device does not compress the remaining healthy nerve tissue in the conduit at the proximal nerve stump. Hence, biodegradable materials were selected by preference as they were hypothesised to reduce compression as they degrade from the literature (de Ruiters et al., 2009). The diameter of the NGC should not exceed the diameter of the model nerve either as this can affect the formation of the fibrin matrix which is the first stage of nerve repair, as reviewed in section 1.4 (Zhao et al., 1993). Further, there is evidence to suggest that size matching is a critical design factor, as a study using a collagen conduit larger than the test Rat Sciatic nerve diameter, resulted in significantly less recovery. Both Tibialis Anterior muscle force at 12 weeks and evidence of tissue regeneration (assessed by histomorphometry using toluidine blue staining to show myelinated nerve fibres) showed poorer results compared to autograft control (Giusti et al., 2014).

According to the papers analysed in section 1.3.1 the mean diameter of nerve conduits used for transection and repair of a Rat Sciatic nerve gap model was  $2.22 \pm 0.180$  mm (SEM). Therefore, a maximum diameter of 2.2 mm was chosen to accommodate the nerve stumps. However an additional design feature would include the capability to produce nerve conduits that can accommodate a range of 0.5mm to 15mm for other models nerves.

### 2.1.2.3 Flexibility

Anatomically there is a requirement for nerve tissue to pass across joints and supply muscles surrounding mobile tissues; nerve tissue itself is flexible. Following transection, the nerve stumps may not be in the same tissue plane and the nerve may need repairing across a joint (de Ruiters et al., 2009). Demonstration of flexibility of the NGC must be carried out to show that the conduit is capable of movement above and below a plane, across a range of obtuse angles and to some extent elastic to resist plastic change. Over-extension of brittle nerve guides could lead to fracture, and tearing could occur from pulling on adhesive seals to healthy nerve tissue post-implantation. These risk factors to the design may be mitigated by flexibility, this importantly affects design parameters including conduit porosity and luminal microarchitecture which can increase or decrease conduit flexibility (Figure 2.1). Also dimensions of the conduit (such as wall thickness, conduit length and material) can all affect flexibility, therefore flexibility must be validated for each intended animal model.

#### 2.1.2.4 Sterilisability

All components of the nerve conduit must be sterilisable and readily accessible when using aseptic techniques to prevent infection. This means the NGC must not be closed to the size of the diameter of the nerve to ensure the luminal surface can be adequately washed and sterilised. Following production, the treatment must be aseptic up to the point of implantation and device can be easily rolled in surgery to the nerve diameter size.

#### 2.1.2.5 Handling characteristics

Following discussions with a veterinary surgeon and animal technician, it was concluded that flexible designs allow for better control when handling the conduit. As the length is short, it must be easily picked up with forceps without crushing the walls. Also, an elastic aspect to the design is ideal, as the conduit can withstand being deformed during implantation and recover its shape to cuff the transected stumps. In addition, the wall thickness and resilience must be suitable to allow it to adhere to the surrounding tissue, using a tissue sealant or sutures. On average, conduits have a wall thickness of 0.2mm when used for repair of the rat Sciatic nerve (Li et al., 2018; Turner et al., 2017). The handling characteristics can directly affect the flexibility of the conduit and so ideal parameters for both design inputs must be realised (de Ruiter et al., 2009).

#### 2.1.2.6 Supporting Axonal Growth within the Luminal Compartment

Within nerve conduits, the lumen may be filled with a matrix that can be supportive of Schwann cell infiltration, which can increase axon growth into the conduit (Chen et al., 2006). Therefore, the use of collagen filler has been assessed in non-porous and porous conduits. Inclusion of a matrix can encourage both neuronal and non-neuronal cells to infiltrate and proliferate. In addition, collagen allows the inclusion of other regenerative factors, e.g. human natural killer cell protein (HNK), which has shown reduced fibroblast infiltration and increased axon counts in grafting studies over 15 weeks (Ezra et al., 2016).

#### 2.1.3 Recipient Requirements (Patient)

After analysing clinical data available on nerve repair in human patients, section 1.6 (Table 1.7), it was concluded that patients require a technology that is capable of reliably repairing nerve and bringing functional recovery at least as well as an autograft and any similar products available on the market. For repair procedure using collagen nerve conduits, sensory recovery was evident

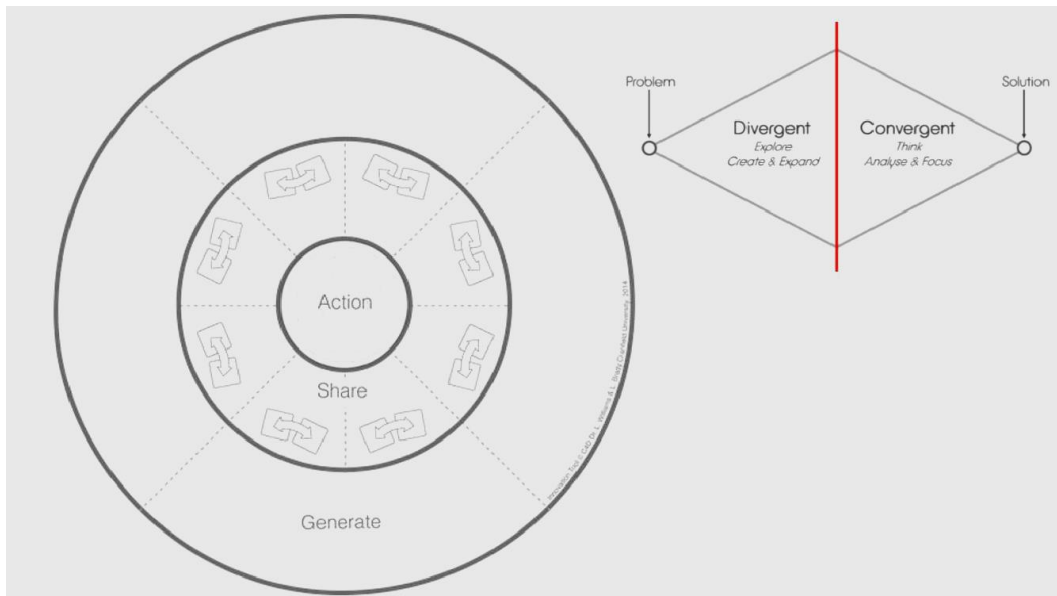
when nerve regeneration was seen in the nerve guide, indicating that these fibres are first to recover (Merolli et al., 2014). Motor recovery however is less uniform and is often not complete in injuries longer than 10mm; this is an area of focus for new designs.

#### 2.1.4 Material Chemical and Physical Requirements

In collaboration with the Centre for Competitive Design (C4D), Cranfield University, an innovation process called an idea generation workshop used a specific tool created by Williams and Brady from C4D (proprietary tool belonging to the Directors of C4D, created 2014) to generate design ideas for a novel method of nerve repair (Figure 2.5). A group of seven Masters of Design researchers were recruited, with two academic principal investigators. Participants had no prior medical knowledge but were presented with a short presentation on the mechanisms of nerve repair and the size of the product by Aran Batth. Participants were split into two teams to enable two designs for a prototype nerve conduit to be submitted.

The principle of the idea generation workshop relies on the use of the design tool (Figure 2.5) to guide the teams to a final prototype design which can be produced and tested for its application, in this case the use of the nerve guide in an animal trial.

1. Ideas are first generated by individuals within the group with no consultation amongst peers permitted. This ensures the number of ideas generated within the 15 minute time period is not disturbed by communication with others.
2. Following this, the next stage involves sharing ideas with peers within teams and ideas can be collaborated on and criticised through communication.
3. Finally, the idea is submitted by an action taken collectively amongst the group to pursue one of the designs by prototyping.



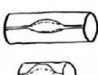
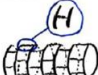








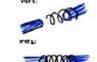




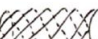






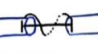
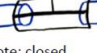













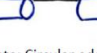











**Figure 2.5:** Innovation tool created by Williams and Brady, 2014. The tool is used to guide group discussions and encourage a single solution to be produced from one group. The first stage is 'Generate' for creating prototype designs. The second stage is 'Share' which encourages group communication and critical appraisal of generated ideas. The final stage, 'Action', involves

The groups were initially given scientific insights from the literature review (evaluated in sections 1.2 and 1.3) of this thesis. Specifically, the nerve conduit must have:

1. A solid phase wall to support and hold the nerve stumps in place that remain in the transection and repair animal model
2. The NGC must be 10mm in length
3. The NGC must be 2mm in diameter
4. The teams were also informed that a cell-supportive hydrogel would be included as this was evaluated in Chapter 4 in vitro and Chapter 5 in vivo.

The designs generated by the two groups are shown in Figures 2.6A and 2.6B.

<b>A</b>	 Note: open Challenge: B	 Note: spiral spring Challenge: A, B	 Challenge: E	 Challenge: E	 Note: EM force to keep channels in position Challenge: B	 Note: squared mesh closed Challenge: B	 Note: Screw on Challenge: B
	 Challenge: D	 Challenge: B	 Challenge: B	 Challenge: C	 Note: Break down Challenge: D	 Challenge: B, C	 Challenge: A
	 Challenge: A	 Note: Tubular 'puzzle' pieces Challenge: E	 Note: Tubular 'puzzle' pieces Challenge: E	 Challenge: E	 Note: EM signal Challenge: B	 Note: Tubular 'puzzle' pieces Challenge: E	 Challenge: D
	 Challenge: B, E	 Note: Break apart Challenge: D	 Challenge: D	 Note: open Challenge: B	 Note: closed Challenge: B	 Challenge: E	 Challenge: E
<b>B</b>	 Note: Spring & prif on inner surface Challenge: D	 Note: Telescopic configuration Challenge: B, E	 Note: Suspension bridge type Challenge: B	 Note: Multilayer, orthotropic material Challenge: B	 Challenge: B	 Challenge: A	 Note: Tape printed Challenge: C, D
	 Challenge: A, B	 Challenge: A	 Challenge: B	 Note: Circular edge Challenge: A, B	 Note: Circular edge, edge tapering Challenge: A, B	 Note: Wire Challenge: B, E	 Note: Sticker patch Challenge: C, D
	 Note: Imbedded wireframe Challenge: B	 Note: Pneumatic jacket Challenge: A, B	 Challenge: C, D	 Note: Fill with gel Challenge: A, B	 Note: Wax welding Challenge: C, D	 Note: Groove channels Challenge: B	 Challenge: B

**Figure 2.6:** Ideas from the 'Generate' portion of the idea generation workshop. (A) Group A designs, (B) Group B designs. As part of the initial briefing stage, challenges presented from current available technologies in nerve guidance were listed and ideas were generated to address these challenges.

The designs produced were intended to address challenges that were discussed during the initial brief prior to the idea generation workshop. Specifically, current technologies must address development of path-finding of axons to their targets and provision of a microenvironment close to nerve tissue (Gu et al., 2014). The challenges were as follows:

- A. Adequate adhesion to the nerve stumps
- B. Guidance of regenerating axons, to ensure each axon reaches the distal end
- C. Tissue damage and nerve stretching must be minimised during application of the device in vivo
- D. Provision of microgrooves which can be rolled into a conduit shape
- E. Adjustability in the size of the device for use in other nerves and animal models

In Figure 2.6, the challenges addressed have been noted beside the design sketch. The workshop concluded practical considerations that include:

1. The device has a capability for closing on its own, which can be supplemented using glue to adhere panels together to affirm closure.
2. The device provides a physical environment which can be used for axon guidance, it was proposed that the device consists of multilayers with grooves presented on the internal surface.
3. The walls of the device are flexible to ensure that the device can be handled and secured into place.
4. A biphasic device was submitted, in which the NGC includes a flexible wall material and a soft hydrogel, which was developed to encourage cellular growth.
5. As the device is intended for soft tissue repair, the materials used for the wall structure should be biologically inert and non-bonded to surrounding tissues.
6. Furthermore, NGC may be porous for nutrient exchange (Ezra et al., 2016).
7. The device may be degradable or non-degradable, however it must support nerve regeneration for the entire duration of the animal trial which is 12 weeks in the animal model as comparable to literature (Liu et al., 2018; Yurie et al., 2017).

#### 2.1.5 Design Inputs Acknowledged for Medical Device Manufacture

For the NGC to be translatable into a medical device, following successful results obtained from the animal trial, the other design inputs that would require validation have been summarised in Table 2.1. Although these additional inputs are outside the scope of the work in this thesis, they are required for future work in creating a commercial device.



Table 2.1: Additional Design Inputs acknowledged by this research

Design Input	Requirement	Information
Packaging	Double-packed sterile pouch	Ensure that the device is non-infectious and can be handled aseptically during surgical implantation
Sterilisation Materials	ISO11737 Standard	Any materials used for sterilisation should not interfere with the intended use of the device
Sterilisation Method	ISO11737	Ensure the sterilisation method is compliant with the ISO standard. This includes gamma irradiation or Ethylene Oxide treatment
Shelf-Life	3 Years	The device and packaging must not perish under storage conditions over an adequate time so that it is accessible when required
Product Safety	ISO10993	The product should not cause any damage to the user, recipient or the environment
Product Biocompatibility	As per ISO10993 Class III Device	According to Category C, the device materials should be tested for Cytotoxicity, Sensitisation, Irritation, Systemic Toxicity (acute), sub-acute and sub-chronic toxicity, genotoxicity, implantation, haemocompatibility
Environmental Requirements	Device not affected by environmental conditions during transport and storage	Must validate that materials can be shipped with temperature, humidity and special conditions
Interface Requirements	No adverse reaction between individual materials used	Gel material and internal architecture must not react with outer shell material nor must there be any interaction or accelerated degradation with adhesive materials which may be used to secure the device

## 2.2 Design Outputs

With reference to ISO 13485:2016, design outputs offer a test to validate the conformation of the prototype to the design inputs discussed in section 2.1 (International Organization for Standardization, 2016). It is the responsibility of the manufacturer to establish procedures to document the design outputs and procedures should refer to acceptance criteria or the final design. For each of the design inputs discussed, a design output has been listed to explain how the design will be evaluated and then discussed in the following chapters (Table 2.2).

Table 2.2: Design Outputs Criteria

Input		Acceptance Criteria
Intended Application		After initially testing potential acute toxicity, the NGC will be implanted and monitored in a long-term model of peripheral nerve repair (up to 3 months in vivo).
User Requirements (Surgeon)	Length	Conduit prototypes will be measured and cut to the standard length of 10mm.
	Diameter	Conduit prototypes will be heated and rolled over a controlled 2mm diameter rod until the inner diameter measures the standard 2mm diameter.
	Flexibility	Conduits materials that withstand tensile mechanical tests will be measured for their flexibility or stiffness.
	Sterilisability	Methods of sterilisation will be evaluated, and in vitro cytotoxicity analysis carried out to ensure the materials are non-toxic in cell culture.
User Requirements (Patient)		Behavioural tests and histological evaluation will be carried out during the trial to characterise sensorimotor outputs and evaluate the efficacy of the device in supporting peripheral nerve regeneration.
Material Chemical and Physical Requirements		Neural cell line (NG108-15), Rat Sciatic nerve-derived Schwann cells and Dorsal Root Ganglion explants will be used to evaluate the effectiveness of candidate materials for use in the NGC as previously used to model nerve-material interactions before testing in vivo (Pateman et al., 2015).

### 2.3 Outcomes and Proposed Design

Following the discussions from the collaboration with C4D and reviewing the literature in this field, it was decided that the device have three key features which provide a novel combination to be evaluated in the sciatic nerve model. These outcomes are:

1. Flexible wall material that can wrap around the stumps and hold securely to remove the need for suturing
2. Microgroove presentation on the internal luminal surface to provide guidance to axons and prevent misdirection
3. Hydrogel filler component to increase the availability of ECM-like substrates on which Schwann cells can adhere and proliferate to guide axons

It has been reported that for nerve guides to be more effective, they must provide a combination of design features to encourage alignment and minimal damage that is tension-free (Daly et al., 2011). Many aspects discussed in this chapter, including microarchitecture and hydrogels can be evaluated in vitro and show positive results, however often they do not provide comparable repair to autograft in vivo. Specifically, microsurgical techniques such as suturing nerve stumps to the ends of a conduit can present a limiting factor to effective repair as nerve tissue damage can be caused and alignment may still not be optimal (Turner et al., 2017). Nerve anastomosis is technically challenging, can increase fibrosis and can elicit a local inflammatory response, and therefore we will avoid this in the final design. Cyanoacrylate and fibrin based glues have been used as alternatives to suturing. There is supporting evidence to suggest that adhesives make the surgical technique easier and compression on the nerve can be limited, by applying small amounts of glue to the edge of the NGC (Barton et al., 2014). Choi et al. concluded that cyanoacrylate repair gave better histological and functional outcomes albeit there was some evidence of local tissue adhesion of the NGC to the surrounding muscles, indicating that the surgeon must take care (Choi et al., 2004). Therefore, we will use glue as an alternative to suture.

Flexibility is encouraged, to enhance the ease of implantation and to connect stumps that are not aligned well in vivo (de Ruyter et al., 2009). However, excess flexibility can lead to conduit collapse as demonstrated by Belkas et al. (2005), where a minority of poly(2-hydroxyethyl methacrylate-co-methylmethacrylate) NGCs collapsed possibly due to inflammation or calcification encouraging brittleness and concluded that long term-stability is an important factor for flexible designs.

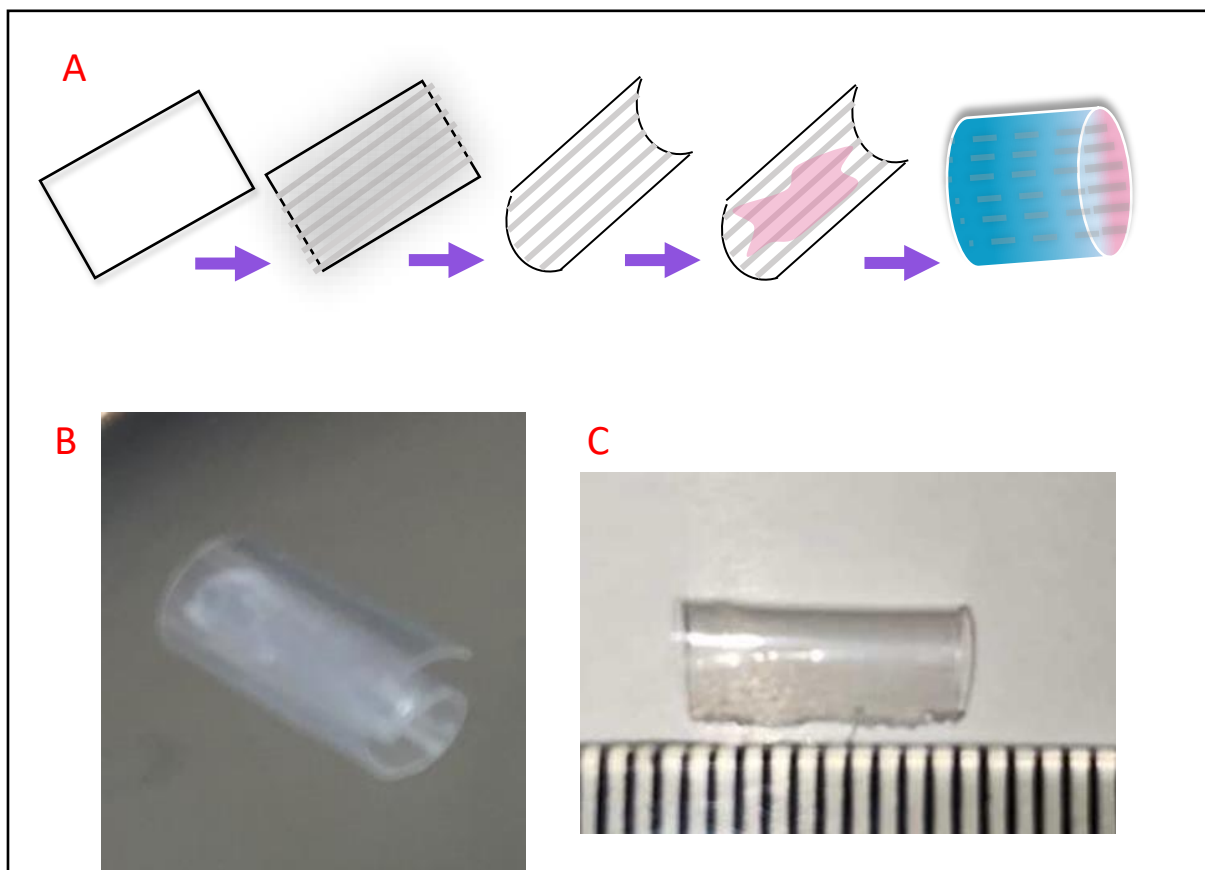
Inclusion of microgrooves has been evaluated to be beneficial for directing axonal sprouting (Yamada et al., 2016). Interestingly, groove dimensions can be precisely controlled and features such as sloped, straight or v-shaped walls have been studied in the rat sciatic transection model (Mobasseri et al., 2015). Microgroove structure was shown to significantly affect adipose derived stem cell adhesion and sloped grooves significantly increased nerve fibre density at the mid-point of the conduit. In vitro, microgrooves within the range of 8-10 $\mu$ m width spacing were shown to reliably promote neural cell and Schwann cell alignment (Sun et al., 2010). Mechanical signal transduction occurring from the interaction of neural cells and micro-grooved substrates has been shown to affect gene expression, differentiation and migration, which could enhance NGC efficacy (Chen et al., 2004). Directional control of axonal outgrowth is a requirement as it provides guidance and encourages the correct phenotype of elongated cells (Sun et al., 2010). The design of grooves must be carefully managed as microgrooves are imprinted on flat surfaces and the geometry of the grooves changes when the surface is rolled into an NGC. The change in size is dependent on the aspect ratio of the cross-sectional area of the groove.

Hydrogel fillers have been shown to increase Schwann cell infiltration into the conduit, as cells interact with the ECM-like matrix and start to colonise the injury site (Chen et al., 2004). A cell supportive hydrogel encourages Schwann cells to lay down their own extracellular matrix and interact with one another to form bands of Büngner which is a critical stage in forming a supportive cable on which axons extend and form synapses with targets, this was shown in collagen and laminin interpenetrating network hydrogels, introduction of laminin for instance increased production of neurotrophic factors NGF and GDNF from Schwann cells (Suri and Schmidt, 2010). This can be highly advantageous in nerve repair as a limiting factor to functional repair is hypothesised to be speed of initial nerve cable formation as this provides repair cells to the distal stump.

#### 2.4 Conclusion on Design and Fabrication Methods

The schematic (Figure 2.7A) provides an insight to the final conduit design and fabrication method. A PDMS stamp was used in a process called 'hot embossing' to imprint the microgrooves into the base material. This was then rolled to the desired diameter (2mm) with heat to encourage memory of the cylindrical shape. The whole conduit can be cut to the desired length (10mm). During implantation, the conduit is wrapped around the nerve stumps and sealed using histoacryl glue (cyanoacrylate), which is also used to secure it to the stumps. If the hydrogel filler

is included in the study group, the filler is applied prior to sealing by injection into the nerve gap. Example prototypes have been included to provide an indication of the final design (Figures 2.7B and 2.7C). This fabrication technique was devised following selection of the key design features (shown in section 2.1.4). The final NGC design was chosen for its simplicity, availability of the solid phase wall and gel phase filling, ability to achieve sutureless repair and the ease for altering the size to match the diameter of the nerve being repaired.



**Figure 2.7:** Schematic showing the manufacturing process for producing NGCs, the flat sheet is embossed, rolled and filled for the final design (A). Photographs of prototype NGCs, (B) shows a rolled version which can cuff the nerve and be sealed and (C) shows a closed version which was cut to the desired length of 10mm.

## Chapter 3: Two-Dimensional Model of Peripheral Nerve In Vitro

### 3.1 Introduction

Two-dimensional (2D) cell culture studies can be used to assess the suitability of materials intended for nerve grafting by measuring key parameters such as cell proliferation and neural cell differentiation (Tse et al., 2016). A critical step to determine the success of a NGC includes confirmation that an appropriate scaffold material supports the spreading of target cells, i.e. Schwann cells and neural axons. This can be achieved by quantifying the number of neurites that sprout from neural cells or extension of Schwann cells (Tse et al., 2016). They showed that objective measures such as neurite length can vary according to the culture method as this is directly related to the immediate environment that cells interact with and as a result can affect how the cell behaves.

These measures were used to assess the ability of neural cells (NG108-15 cells commonly used as a neural model cell in relevant studies) to integrate with a variety of 2D materials and hypothesise the relative cytotoxicity of these materials. Flanagan et al. showed that varying shear moduli of polyacrylamide gels ranging 50-500Pa resulted in increased frequency of neuritogenesis, but glial cells did not survive on the soft gels and showed a preference for the hard glass control substrate (Flanagan et al., 2002).

Micron level features, commonly grooves, steps, fibres and pores, provide biomimetic environments of ECM proteins, neuronal cell bodies and axons/dendrites of neighbouring cells (Wrobel and Sundararaghavan, 2014; Morelli et al., 2010). The Terenghi group were able to demonstrate that the shape of microgrooves on a conduit surface can have significant effects of the extent of neural axon infiltration when implanted in vivo (Mobasseri et al. 2015). The observation that Schwann cells respond to surface topography has been reported elsewhere and can be an important step in increasing the effectiveness of NGCs and measures such as cell adhesion, proliferation and morphology have been validated as relevant indicators of efficacy so these methodologies were adapted in this study (Mitchel and Hoffman-Kim, 2011; Zhou et al., 2009).

Assays can be optimised to demonstrate the proliferation and differentiation abilities of cells presented on a given surface, which has been shown to inform material development and surface properties of biomaterials (Derda et al., 2010). An important factor in these studies is

biocompatibility, as it ensures proper functions of cells on the surface of the material such as cell adherence and cell migration on a scaffold of interest (Bernard et al., 2018). Surface modification allows for bioactive molecules to be adsorbed onto the surface to modulate cell responses. Hydrophilicity for example, can dictate how well cells will adhere to the material surface which in turn affects the numbers of cells available for introduction to the grafting site (Subramanian et al., 2009). Synthetic, biocompatible polymers show potential as NGC materials, as their physical properties can be tuned according to the application, for example co-polymer systems can be designed to degrade quickly or be mechanically stiffer, using multiblock poly(caprolactone) and poly(lactic acid) systems (Cohn and Salomon, 2005). Material microstructure can be further enhanced by altering the physical features presented to cells and providing a three-dimensional (3D) surface scaffold – the materials used must still provide the stiffness required for stimulating cell adhesion, as well as providing features that are optimised to support specific cell types. This was shown using direct laser sintering techniques to make 3D ultrastructures on poly(caprolactone) scaffolds where cell morphology of NG108-15 cells were assessed qualitatively (Melissinaki et al., 2011). Therefore, as materials were studied further, the cell morphology of cells relevant to peripheral nerve repair (NG108-15 and Schwann cells) was investigated. NG108-15 cells were chosen for their reliability in producing neurites, which can be measured with a variety of neural markers, and using a neural cell line allowed differentiation to be studied which helped assess the biocompatibility of the materials tested (Tojima et al., 2000). Primary Schwann cells were chosen to model the materials because they are the native cell in nerve tissue and have shown to be vital in coordinating nerve regeneration (Jessen et al., 2016). Rat Schwann cells were chosen to translate findings from in vitro experiments presented in this chapter to the in vivo experiments (Chapter 5), provided that the graft can support Schwann cell proliferation and maturation.

The naturally occurring scaffold for cells, the extracellular matrix (ECM), provides an instructive role in controlling cell behaviour and ensures cell viability by providing diffused nutrients (Barker, 2011). The mimicry of the ECM by materials in supporting cell growth and proliferation was therefore measured to confirm suitable culture substrates in vitro. There are a number of cellular-material interactions that lead to generation of biomaterials, as they are based on observing the influence of the ECM (or ECM mimicking surface) on cell behaviour and matching these results to the biomaterial therefore specific morphological measures such as Schwann cell

area and neurite length were measured. Biomaterials must provide physicochemical support to both cell types, as failure to match the viscoelasticity of ECM results in poor differentiation of target cells. However, anisotropy of physical features is common in natural tissue where parallel arrangement of fibres supports tissue functions. Instructions to cells can be beneficial in contributing to the function of the tissue and can be controlled in 2D cultures with porosity and adhesive motifs. The ability of a range of 2D surfaces was first investigated for cell adherence and cytotoxicity, after which the most effective material was further examined for its physical properties and resultant effect on neural cell differentiation and Schwann cell polarisation.



## 3.2 Materials and Methods

### 3.2.1 Cell Culture of NG108-15 Cells

The culture method for NG108-15 cells was optimised from previous work by Robbins and Sim (1990). NG108-15 cells (AATC. Trading as LGC Standards, UK) were cultured in low glucose Dulbecco's Modified Eagle Medium (Sigma-Aldrich, UK) containing 10% (v/v) FCS, 1% (v/v) L-glutamine (Gibco, UK), 1% (v/v) Penicillin/ Streptomycin (Thermo-Fisher Scientific), 100µM Hypoxanthine, 0.4 µM Aminopterin and 16µM Thymidine (HAT Supplement, Sigma-Aldrich, UK).

Cells were cultured in aseptic conditions, in a humidified incubator with a 37°C, 5% CO<sub>2</sub>/ 95% Air (v/v) environment for up to 7 days. To induce neural cell differentiation, cell media was totally replaced with low glucose DMEM containing 1% (v/v) FCS, 1% (v/v) L-glutamine, 1% (v/v) Penicillin/ Streptomycin. In some cultures 0.25mM 3-Isobutyl-1-methylxanthine (Sigma-Aldrich) and 3µM Prostaglandin E1 (Sigma-Aldrich) was also added to the media. These two media compositions were evaluated for differentiation efficiency (section 3.3.1). Cells were incubated for 24 hours in this medium and 50% of the media replaced every 1-2 days with low glucose DMEM containing 1% (v/v) FCS, 1% (v/v) L-glutamine, 1% (v/v) Penicillin/ Streptomycin until the experimental endpoint.

To plate out, the confluent, adherent NG108-15 cells were mechanically detached from the flask surface without using trypsin and were counted using a haemocytometer (Neubauer cell counting chamber). Cells from passages 6-18 were used in experiments. Working with cells from passage 6 onwards ensured that cells were robust and acclimatised to the culture method (specifically the media exchange schedule) and cells were not used after passage 18 to limit genetic drift amongst cultures compared.

### 3.2.2 Cell Culture of Schwann Cells

Rat derived primary Schwann cells (Sigma-Aldrich, UK) were cultured in a defined, proprietary Schwann Cell media (ScienCell Research Laboratories, UK) containing 10% FCS (ScienCell Research Laboratories, UK), Schwann cell growth supplement containing (SCGS) (ScienCell Research Laboratories, UK) and Penicillin/Streptomycin. For plating, cells were grown to confluence and detached with 0.05% (w/v) trypsin/EDTA (Gibco, Germany). The culture method was taken from the manufacturer's protocol. A haemocytometer was used to count cells and

passages 3-9 were used. Passage 3 was the earliest passage available as these were commercial cells and passage 9 was used as a limit to ensure that cells with a similar cell cycle time were used and could be compared in proliferation experiments.

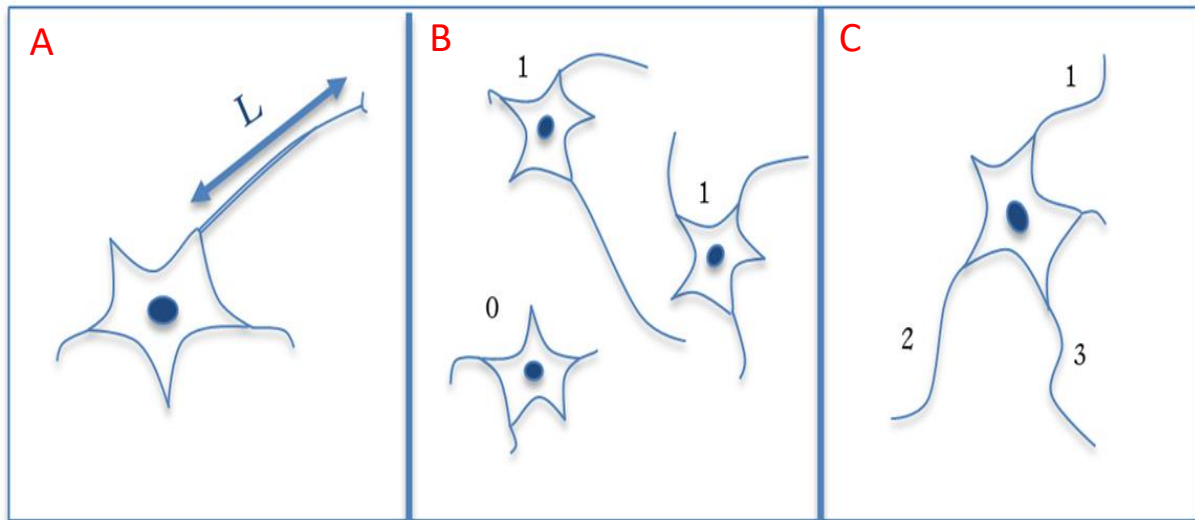
### 3.2.3 Cell Counting

To assess numbers over time, cells were cultured in 6-well plates and initially seeded at a density of 25,000 cells per well. Each day cells were detached from the wells as described in 3.2.1 and 3.2.2 and a 20 $\mu$ l aliquot of cell suspension was mixed with Trypan Blue in a 1:1 ratio. Trypan Blue staining was used to label dead cells indicating reduced membrane integrity, which were excluded in calculating cell number (Cadena-Herrera et al., 2015). Cells were counted using a haemocytometer by pipetting 10 $\mu$ l of the cell/ Trypan blue suspension into each side of the chamber. The average number of non-labelled cells present in the large grid was counted and multiplied by 20,000 to give an estimate of cell number per ml of suspension. Cell number was counted up to 7 days in vitro for both Schwann cells and NG108-15 cells. 3 wells were used as technical repeats and 3 separately plated populations of cells from separate cell passage sources were used for biological repeats, at each time point.

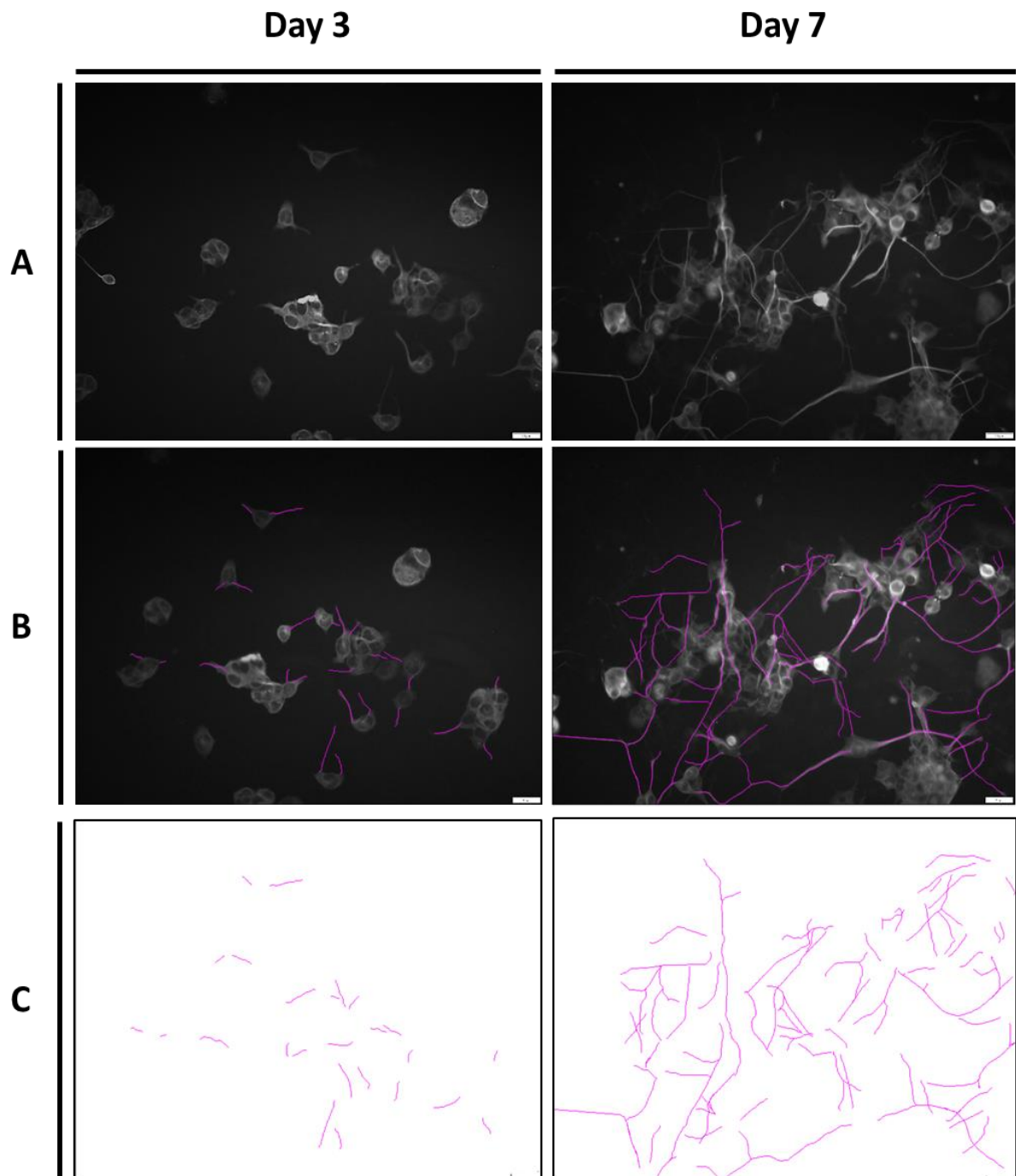
### 3.2.4 Quantification of Neurite Length

Neurite length was quantified using Fiji (Image J) and a plugin called Neuron J from the Image Science open source software (copyright Erik Meijering). Images were opened and converted to an 8-bit format, and then skeletonized to reliably display the neurites. The neurites could then be digitally traced over and length measured according to the scale tool. Total length of neurites was measured in the field of view of 8 images at 24 hour intervals for 7 days. Average total neurite length was calculated for each time point to plot the cumulative increase over the 7 day period, to demonstrate the total length of the neurite network and compare methods of differentiation. Only neurites that were longer than the cell body were counted. In addition, the number of neurons bearing neurites longer than the soma and the number of neurite outgrowths per cell were also calculated. The three measurements are summarized by the schematic (Figure 3.1). Traces of neurite length measurements using the software are also provided (Figure 3.2). As the same process of staining and then measuring neurites digitally was used and measured by the same person, reliability could be prioritised however precision may have been reduced if the

image resolution was not high. Where possible, a confocal microscope was used to increase image resolution.



**Figure 3.1:** Schematic to show three methods to measure neuron differentiation. Neurite length ( $L$ ) is the length of the longest neurite within a given cell, provided the neurite is longer than the diameter of the soma (A). For number of neurite bearing cells, if cells have neurites that are longer than the soma then they are counted ('1') and cells without neurites long enough are discounted ('0') (B). Number of neurites per neuron was counted for each cell, including only neurites that were longer than the soma i.e. 1, 2 and 3 (C).



**Figure 3.2:** Representative images of NG108-15 cells cultured on tissue culture plastic at day 3 and day 7 (A). Neuron J neurite tracing tool was used to manually trace over visible neurites (B). The tracings were then converted into a binary image before automated measurements were taken (C).

### 3.2.5 Live/Dead Cell Viability Staining

In 24-well plates,  $10 \times 10^3$  cells were plated into each well containing the sample analysed. Live/Dead cell viability assay (Sigma-Aldrich, UK) was performed with reference to the manufacturer's protocol, using a labelling solution containing fluorescence markers - Calcein AM (4 $\mu$ l) and Ethidium Homodimer-1 (10 $\mu$ l) diluted into 10ml of PBS (Sigma-Aldrich, UK). 24-well plates containing cultures were aspirated to remove the media and a minimal volume of 200 $\mu$ l of the live/dead imaging solution containing Calcein AM and Ethidium Homodimer-1 was applied per well and incubated for 40 minutes at 37°C, 5% CO<sub>2</sub>/ 95% Air (v/v). Images were obtained by epifluorescence widefield microscopy. 3 wells per plate were imaged for technical repeats, and 3 separate cultures were analysed for biological repeats. 30 representative fields of view were selected per experimental condition.

### 3.2.6 Alamar Blue Assay

To assess cell proliferation, Alamar blue assay was used as it measures mitochondrial activity as they reduce resazurin dye to resorufin, which is fluorescent. The protocol was adapted from White et al. (1996). Alamar Blue solution was prepared by dissolving resazurin (Sigma-Aldrich, UK) in PBS at a 1% (w/v) concentration. This was dissolved into warmed PBS (1:10 v/v) to make the incubation medium. In 24-well culture plates,  $10 \times 10^3$  cells were cultured on 1cm<sup>2</sup> 0.5mm PA 6,6 samples per well for 24 hours, 72 hours, 3 days and 7 days. After the incubation time, media was fully removed from the wells and 0.5ml solution applied and allowed to incubate at 37°C, 5% CO<sub>2</sub> for 4 hours. Following incubation a colour change was observed in the solution from blue to pink, 100 $\mu$ l aliquots from the wells were removed and loaded into a 96-well plate. At least 12 wells were filled to provide technical repeats. Using a microplate reader, absorbance was measured at 570nm and referenced at 600nm. The percentage change in absorbance at 570nm between 24 and 72 hours was measured which correlates the live population of cells in the culture and provides a measure of the relative number of cells when comparing conditions. The experiment was performed in triplicate, to give biological repeats with 12 readings per experimental condition.

### 3.2.7 Determination of Cell Adherence

Materials were sterilised by washing with 70% ethanol twice, for 5 minutes each, air-dried and then UV-irradiated for 10 minutes (Chitnis et al., 2008). Cells were cultured on static, uncoated,

non-treated materials placed in polystyrene 12-well culture plates. Cells were suspended and plated onto the materials and allowed to attach for 24 hours in growth medium (10% FCS content), the culture was maintained as described in 4.2.1 and 4.2.2 according to the cell type until the time point of 72 hours or 7 days. After 24 hours, the samples were removed and placed into a new well plate allowing initial attachment of cells to the material but ensuring that metabolic activity recordings were solely from cells adherent to the materials being tested. Fibres selected for screening were Linen, Cotton, Silicon, Silk fibres, Polyester, Vicryl Rapide suture and PA 6,6 mesh. Fibres were used due to their availability and ease to cut for cell culture, this ensured the relative adherence properties in static cultures could be measured in a simple set up. Although the final material must be available as a flat sheet, use of fibres for a range of materials were readily available and once the material was selected, the fabrication process for the NGC could be determined. As fibres were easily sourced, they were used to optimise the cell adherence assay because a range of materials were used with varying cell adherence properties due to differences in surface chemistry.

### 3.2.8 Immunocytochemical Staining of NG108-15 and Schwann cells

To verify that the neurite outgrowth observed in experiments in Figure 3.9 was a result of neuronal differentiation, neural marker expression was monitored throughout the 7 day time period. Class III  $\beta$ -tubulin (or  $\beta$ III Tubulin as annotated in Figure 3.9) is a microtubule protein specific to neuronal cells, and is a pan-neuron marker. Microtubule-associated protein 2 (MAP2) is a specific marker of neuronal differentiation, expressed during neuritogenesis and hypothesized to be involved in microtubule assembly. Ki-67 is a proliferation marker used to indicate nuclei of cells undergoing mitosis and the expression was monitored to provide evidence that NG108-15 cells exit the cell cycle during differentiation.

Immunolabelling with a Microtubule Associated Protein 2 antibody (MAP2; Sigma-Aldrich, UK; MAB3418X) and  $\beta$ III Tubulin (Merck Millipore, UK; AB15708A4) protein were used as neural markers to determine presence of neurites. Immunolabelling with an antibody specific to the S100 protein (Abcam, UK; ab868) was used as a Schwann cell marker. Cells were labelled at days 1, 3, 5 and 7. At each time point, the medium was aspirated and the sample with adherent cells was washed 3 times with PBS (5 minutes per wash). 500 $\mu$ l of 4% Paraformaldehyde solution in PBS was applied for 10 minutes at room temperature to fix the cells. The samples were then washed 3 times (for 5 minutes per wash). Cells were then permeabilised with 500 $\mu$ l 0.2% (v/v)

Triton-X100 diluted in PBS for 20 minutes. The samples were then washed 3 times (for 5 minutes per wash). Cells were incubated with 1% Bovine Serum Albumin (BSA) solution for 30 minutes to block non-specific binding sites of the antibodies. The solution was aspirated off and the cells were incubated in primary antibody diluted in 1% BSA overnight (>12 hours) at 4°C. Concentrations of antibody dilutions were 1:100 for  $\beta$ III Tubulin, 1:400 for MAP2 and 1:250 for S100. The  $\beta$ III Tubulin and MAP2 antibodies were both conjugated with Alexa Fluor® 488 fluorophore. The samples were washed three times (for 5 minutes per wash).

The samples stained for presence of S100 protein were then further incubated with a secondary antibody (donkey anti-rabbit IgG H&L Alexa Fluor® 647 conjugated; Abcam, UK; ab150075) diluted into 1% BSA solution at a concentration of 1:1000 (v/v). The solution was aspirated and the cells washed three times in PBS (5 minutes per wash). Cells were counterstained by incubating with 0.1 $\mu$ g/ml Hoescht 33342 (2'-[4-ethoxyphenyl]-5-[4-methyl-1-piperazinyl]-2,5'-bi-1H-benzimidazoletrihydrochloridetrihydrate; ThermoFisher Scientific, UK) for 5 minutes at room temperature. Well plates containing samples were then imaged using a Nikon Eclipse Ti inverted spinning disk confocal microscope (Nikon Instruments, UK) connected to a Yokogawa CSU-1 disk head and Andor Neo sCMOS camera (Nikon Instruments, UK) imaging system. 10x and 20x air objectives were used for image acquisition. At least random 3 images were taken per well, and 3 wells were imaged for technical repeats. The experiment was performed in triplicate for biological repeats using cells from separate passage populations.

### 3.2.9 Polyamide Classification

Primarily, Polyamide 6,6 mesh was tested for cell viability experiments with 27 $\mu$ m diameter polyamide fibres with an aperture of 80 $\mu$ m, which is the distance between two parallel fibres in the mesh. This size was selected to match parameters of a mesh previously researched (Yoo et al., 2011).

Results from the initial material screen (method presented in 3.2.7) demonstrated that poly(amide) (PA) materials could be suitable for culture of neural cells. Additional culture of NG108-15 cells on PA6,6, to match the mesh, was carried out to validate that PA6,6 is cell adhesive in section 3.3.5. Materials were labelled as 'Mesh' (the control substrate used in Figure 3.7), 'Micromesh' and 'Monofilament'. The Micromesh has a fibre diameter of 20 $\mu$ m and an aperture width (open space between two parallel fibres) of 2 $\mu$ m. The Mesh consisted of larger

27 $\mu$ m fibres with an aperture width of 80 $\mu$ m. Finally, the Monofilament was also investigated which had a large fibre diameter of 60 $\mu$ m. Therefore flat sheets of various PA samples were purchased from Goodfellow as they could then be further modified for use in the NGC if results showed that these materials should be investigated in the in vivo model (Goodfellow Cambridge Ltd, Huntingdon, UK). It was important to examine the in vitro results first. PA samples studied include Polyamide 6, Polyamide 6,6, Polyamide 12 and Polyamide 4,6. 0.5mm thick sheets were purchased for use in cell culture, FTIR and DSC.

#### 3.2.10 Cell Culture on Polyamides

Four polyamides were examined in cell culture. For these experiments, NG108-15 and Schwann cells were cultured in growth medium for up to 72 hours. The polyamide samples tested included polyamide 6 (PA6), polyamide 6,6 (PA6,6), polyamide 4,6 (PA4,6) and polyamide 12 (PA12). Polyamide samples were cut to 0.5cm<sup>2</sup> pieces with 100 $\mu$ m thickness and washed in 100% ethanol before being sterilised by UV irradiation for 10 minutes per side. Cultures were on non-treated, uncoated, static and sterile polyamide samples. The samples were then placed into 24-well plates and 10,000 cells were pipetted onto the surface and allowed to settle for 30 minutes in a 37°C, 5% CO<sub>2</sub> sterile incubator. Following this incubation, 0.5ml per well of media was applied and exchanged every 1-2 days.

#### 3.2.11 Attenuated Total Reflection Fourier Transform Infrared Spectroscopy (ATR-FTIR)

PA samples were cleaned using 70% ethanol and air-dried. ATR-FTIR was performed using a Spectrum One FTIR Spectrometer (Perkin Elmer, Massachusetts, US) equipped with an ATR germanium crystal accessory. Dried samples were pressed tightly against the crystal, which sampled a 2mm diameter circular region of interest of the sample. A baseline substrate scan was taken away from the sample spectra. Three replicate ATR-FTIR spectra were obtained per scan of sample. The spectra were averaged from 8 scans collected from a 650 to 4000cm<sup>-1</sup> scanning range in transmission mode. The spectra were corrected for the wavelength-dependent penetration depth, baseline and background corrected through the Spectra™ 10 software (Perkin Elmer, Massachusetts, US).



### 3.2.12 Dynamic Scanning Calorimetry (DSC)

DSC was used to investigate the thermal stability of the polyamides using Jade DSC instrument (Perkin Elmer, Massachusetts, US). Samples were washed in 70% ethanol and dried in an incubator at 50°C. 20mg were weighed of the material and placed into a sample pan, with a sample pan containing air only used as the reference. PA was heated from 0°C to 300°C at a rate of 10°C/min with a nitrogen flow rate of 20ml/min. The curves were analysed using Pyris™ software (Perkin Elmer, Massachusetts, US).

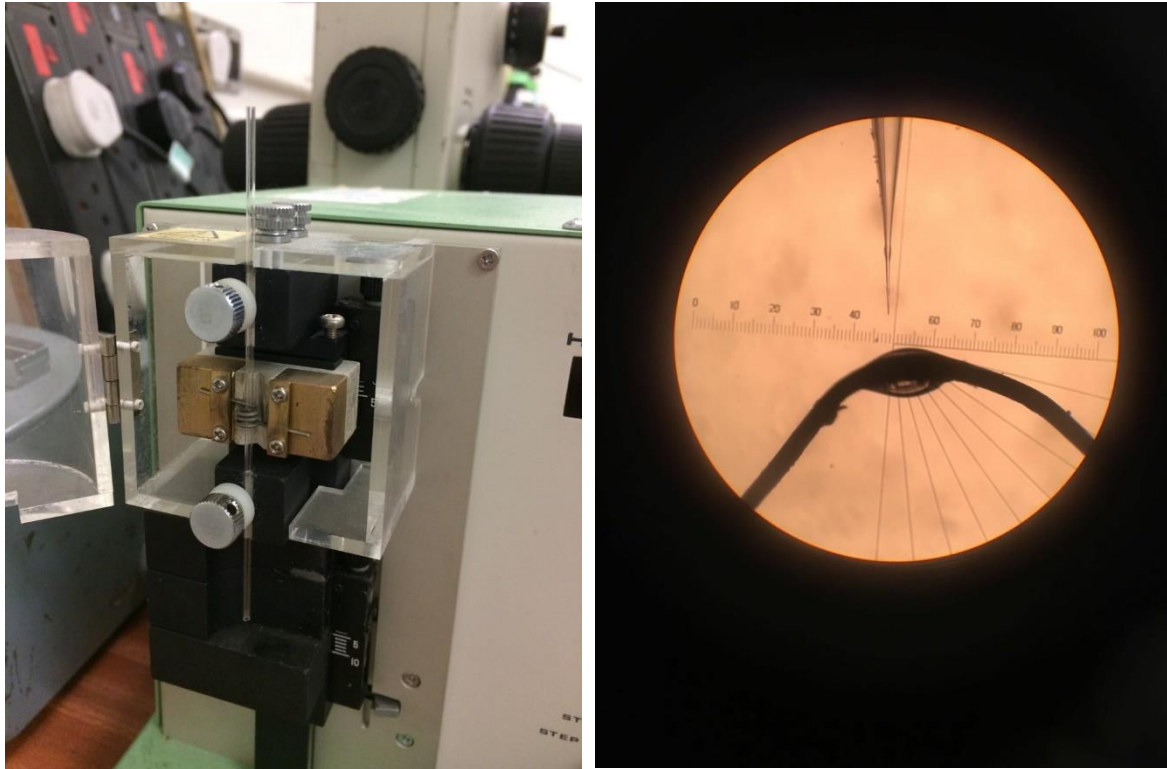
### 3.2.13 Tensile Testing of Polyamide 6,6

Polyamide 6,6 samples were cut into 40mm x 10mm dumbbell shapes uniformly, with a thickness of 0.35mm. Dry samples were prepared by heating at 60°C for 4 hours and placing in an airtight container. Wet samples were prepared by soaking in media at 37°C overnight to simulate physiological conditions. Using a Universal Testing Machine (Instron 5569A, Norwood, Massachusetts), the dumbbell samples were loaded between two grips (image in Figure 4.21) which were coupled to a 10 KN load cell. Samples were pulled by two grips at a rate of 1mm/s until the samples reached a plateau of linear extension as polyamide 6,6 is a highly ductile material which can extend to 140% of the original size, according to the manufacturer (Goodfellow, UK). Stress ( $\sigma$ ) and Strain ( $\epsilon$ ) values were calculated to calculate the Young's Modulus. The load vs extension were also plotted to characterise ductility. Stress ( $\sigma$ ) was calculated by dividing the force (F) applied by the cross-sectional area of the specimen (A), as in Equation 1. Strain ( $\epsilon$ ) was calculated by the change in length ( $\Delta L$ ) divided by the initial length ( $L_0$ ), as in equation 2. Young's Modulus (E) was calculated by dividing  $\sigma$  by  $\epsilon$ , as in equation 3.

$$\begin{array}{ccc} \text{Equation 1} & \text{Equation 2} & \text{Equation 3} \\ \sigma = \frac{F}{A} & \epsilon = \frac{\Delta L - L_0}{L_0} & E = \frac{F \times L_0}{A \times \Delta L} \end{array}$$

### 3.2.14 Electrophysiological Evaluation of NG108-15 cells on PA 6,6

Electrophysiology was carried out to verify that NG108-15 cells were excitable, using pulled borosilicate electrodes (Figure 4.3) (Robbins and Sim, 1990). Cells were cultured in 35-mm petri dishes Nunclon® (Sigma-Aldrich, UK) either on the surface (positive control) or on Polyamide 6 mesh. Cells were differentiated and used at day 4-7 for recording. Non-differentiated cells were recorded before differentiation medium was applied, between day 1 and day 2, used as a negative control. For recording, the medium was aspirated and replaced with a superfusate solution comparable to extracellular fluid osmolality containing 120mM NaCl, 3mM KCl, 1.2mM MgCl<sub>2</sub>, 22.6mM NaHCO<sub>3</sub>, 11.1mM glucose, 5mM HEPES (N-2-hydroxyethyl piperazine N'-2-ethane sulfonic acid), 2.5mM CaCl<sub>2</sub> adjusted to pH 7.36 with 1M KOH. Cells were patch clamped in the whole-cell mode, using a discontinuous current-clamp. Electrodes (3-5MΩ) were filled with 90mM C<sub>2</sub>H<sub>3</sub>KO<sub>2</sub>, 20mM KCl, 40mM HEPES, 3mM EGTA ([ethyleneglycol-bis-(β-aminoethylether)-N,N,N',N'-tetraacetic acid), 3mM MgCl<sub>2</sub>, 1mM CaCl<sub>2</sub> adjusted to pH 7.4 with 1M KOH. Action potentials were evoked by current jumps, ranging from 1-5.5 nA, generated by PC-based software pCLAMP (Axon Instruments, California, US) via a current clamp amplifier (Axoclamp2, Axon Instruments). Voltage was digitally recorded on computer. The membrane potential was held at -50mV and intermittently the current was clamped to a series of test currents in 0.5nA intervals over a range of 1-5.5nA, for 1 second every 15 seconds. For the Maximal Voltage (V<sub>max</sub>) of action potentials elicited were recorded.



**Figure 3.3:** Images to illustrate the patch clamp methodology. Borosilicate glass capillaries were pulled to provide electrodes with a very narrow lumen of approximately  $0.06\mu\text{m}$  (left hand image). The electrodes were then coated with sylgard to increase resistance of the seal and polished to avoid plasma membrane rupture using a heated glass bead (right hand image).

### 3.2.15 Statistics

All data is reported as mean  $\pm$  SEM in this chapter to show precision of the means calculated. Statistical analyses were performed using GraphPad Prism (GraphPad, US) to compare for significant differences. One-way or Two-way Analysis of Variance (ANOVA) with multiple comparisons (Tukey-Kramer's) post hoc tests were carried out to analyse significant differences amongst mean data because the data was normally distributed after assessing by 3 sigma test. For comparison of tensile testing data, a parametric, non-paired, one-tailed student's T-test was used because the data was assessed as normally distributed using the 3 sigma test. The confidence interval for all statistical analysis was 95%. Asterisks have been used on graphs to demonstrate statistically significant differences, \* $p < 0.05$ , \*\* $p < 0.01$ , \*\*\* $p < 0.001$ , \*\*\*\* $p < 0.0001$ .

### 3.3 Results

#### 3.3.1 Evaluation of NG108-15 and Cortical Cells as Model Cells

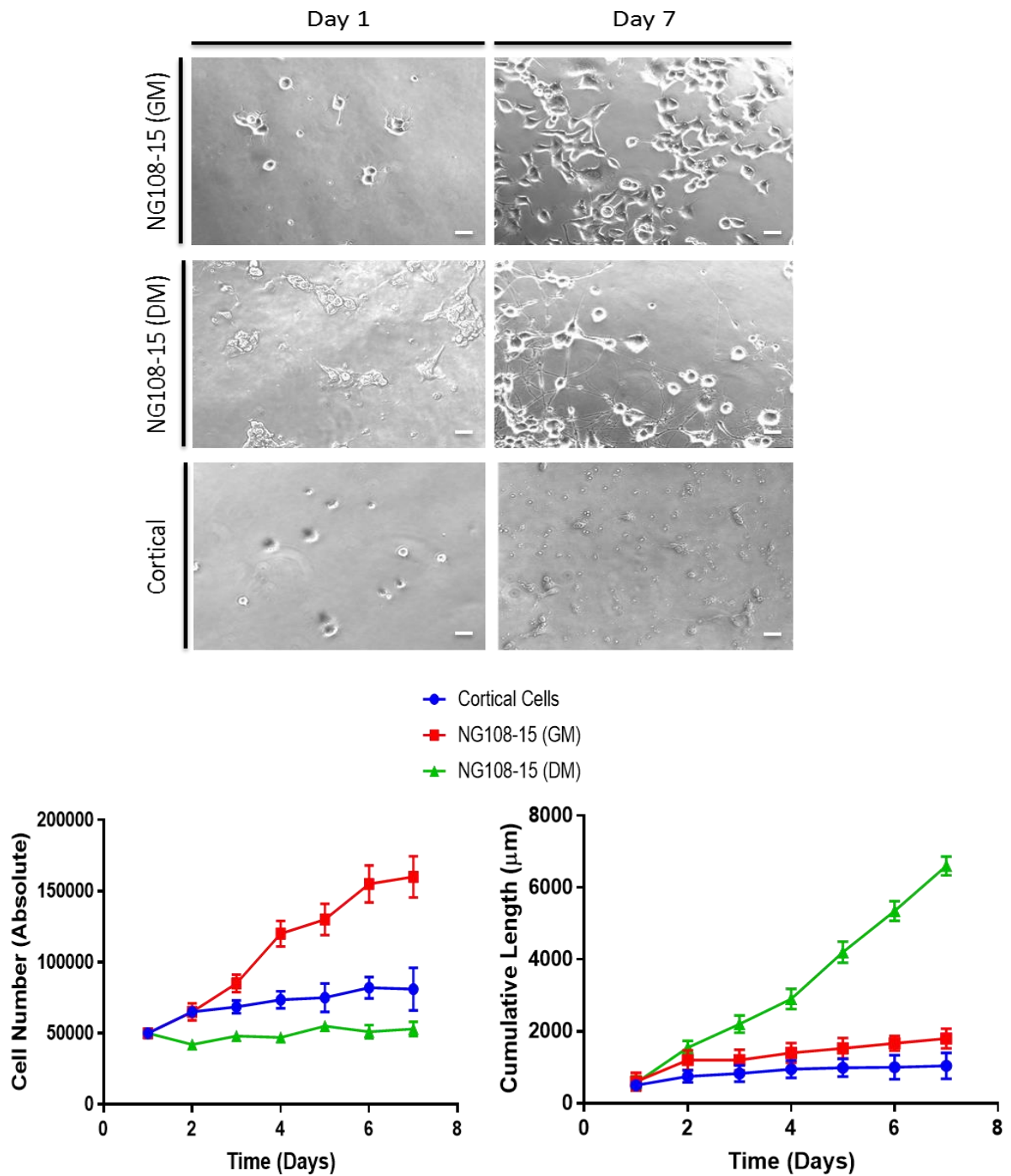
NG108-15 cells and cortical cells were evaluated for culture as potential model cells. Figure 3.4 shows representative brightfield photomicrographs of the culture conditions at day 1 and day 7. From qualitative observations, it is clear that NG108-15 cultured in growth media (GM) proliferated over the time period, whereas NG108-15 cells cultured in differentiation media (DM) did not proliferate as much and the cells show a differentiated phenotype with longer neurites. In the cortical culture, the cells did not proliferate but showed some neuronal differentiation indicated by neurite outgrowth. Also, cell debris built up to a higher degree than in the NG108-15 cultures, despite exchanging 50% of the media every 1-2 days.

Quantification revealed that high serum content in the NG108-15 GM culture increased the cell number measured at 24 hour intervals for 7 days by haemocytometer, increasing from  $50,000 \pm 500$  cells at day 1 to  $160,000 \pm 14,500$  cells at day 7. In contrast, cell proliferation for the NG108-15 DM culture was slower, increasing from  $50,000 \pm 1,000$  cells at day 1 to  $67,500 \pm 5,000$  cells at day 7. For the cortical cell culture, the increase was also lower than the NG108-15 GM culture, increasing from  $50,000 \pm 500$  cells at day 1 to  $81,000 \pm 15,000$  cells at day 7. The rate of neuronal proliferation was calculated in NG108-15 GM, NG108-15 DM and Cortical cultures at 15,714 cells per day, 428 cells per day, and 10,857 cells per day respectively.

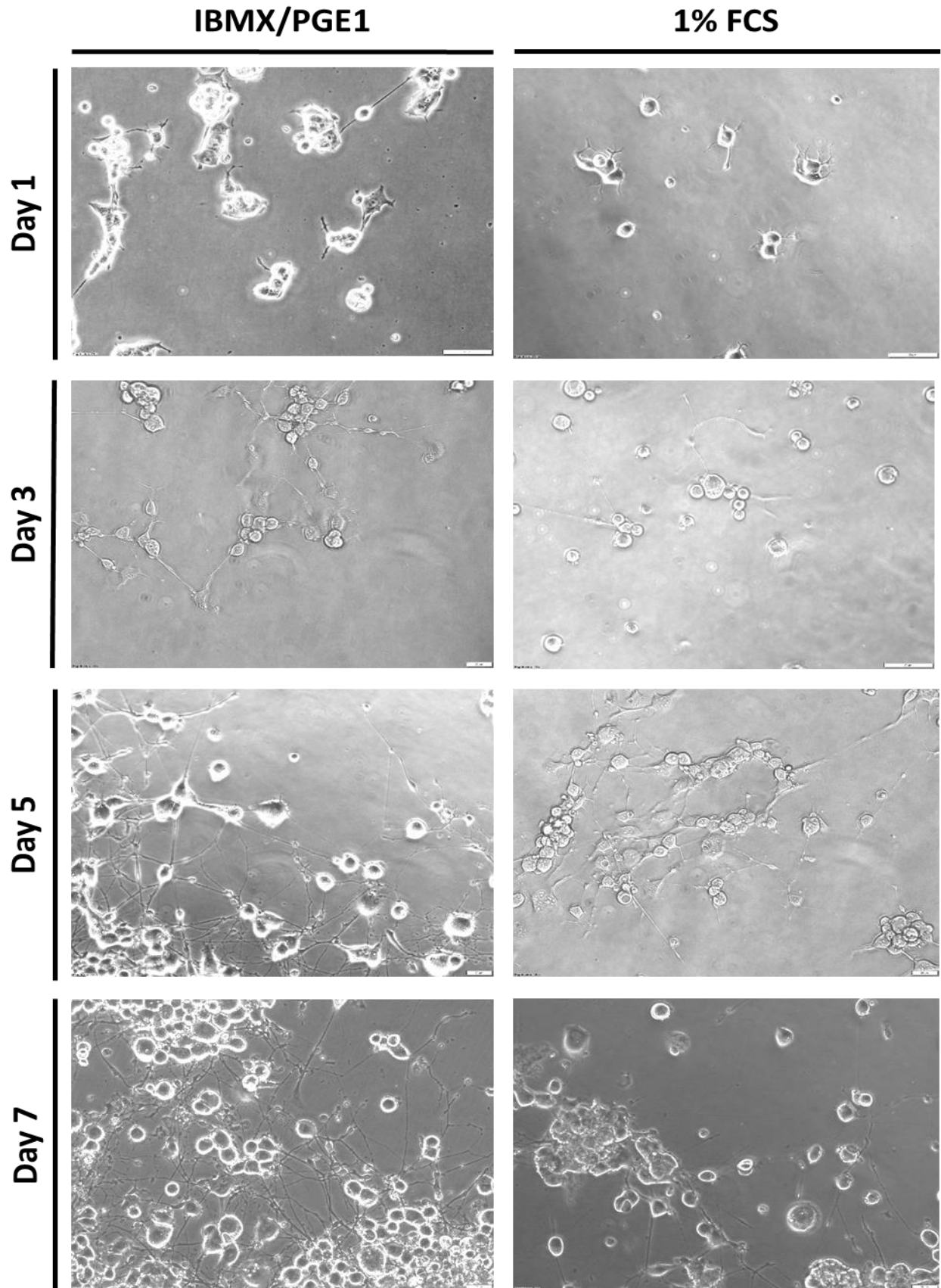
Neurite length was also measured as a product of neuronal differentiation. In differentiation medium, DM, NG108-15 cells showed the largest increase in neurite outgrowth from  $570 \pm 180\mu\text{m}$  at day 1 to  $6,600 \pm 265\mu\text{m}$  at day 7. Fewer neurites were detected in the growth medium condition, NG108-15 GM, increasing from  $600 \pm 250\mu\text{m}$  at day 1 to  $1,800 \pm 275\mu\text{m}$  at day 7. The neurite length from cortical cells was much less, increasing from  $500 \pm 135\mu\text{m}$  at day 1 to  $1,040 \pm 367\mu\text{m}$  at day 7. NG108-15 DM condition revealed significant increases in cumulative neurite length between days 3 and 7. Overall rate of neurite outgrowth in NG108-15 DM cells was  $861.4\mu\text{m}$  per day, which was 80.1% higher than the rate in the NG108-15 GM condition ( $171.4\mu\text{m}$  per day).

NG108-15 cell differentiation was then assessed using two differentiation media methods which consisted of the same media conditions as the growth media with 1% FCS content rather than 10% FCS in the growth media, and inclusion of IBMX/ PGE1. This differentiation media was

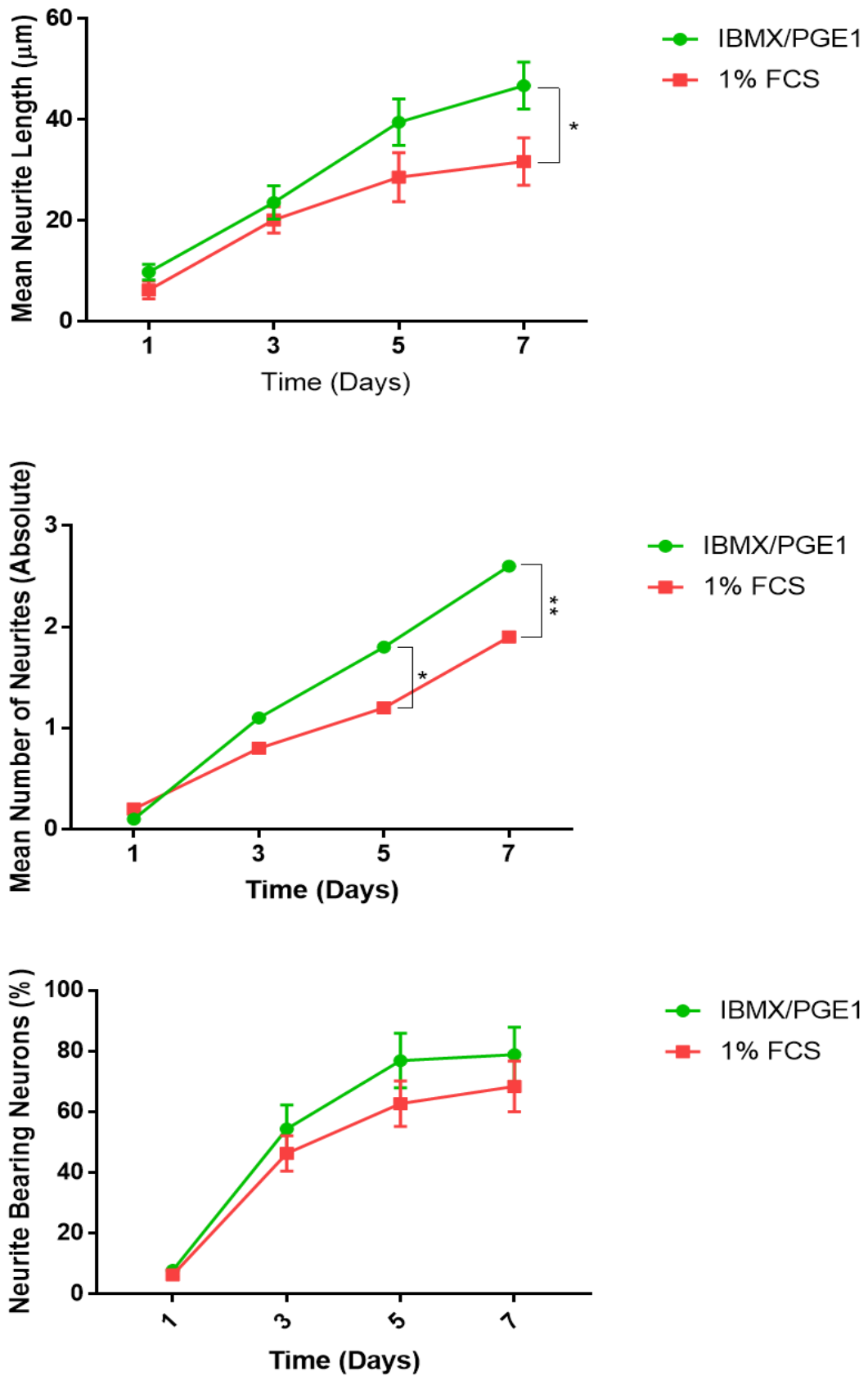
compared to differentiation media without IBMX/ PGE1 (control) to compare the differentiation of NG108-15 cells. Cells were cultured in the differentiation media from day 1 and analysed at days 3, 5 and 7. Although neurites were observed on NG108-15 cells differentiated in both IBMX/PGE1 and control differentiation media, there were considerably more neurites, when IBMX/PGE1 were present in the media (Figure 3.5 and Figure 3.6). When comparing mean neurite length (day 7) with IBMX/PGE1 media ( $46.8 \pm 4.73 \mu\text{m}$ ) were 47.6% longer than control ( $31.7 \pm 4.97 \mu\text{m}$ ). Similarly, the number of neurites was also higher at both days 5 and 7. For IBMX/PGE1 differentiated NG108-15 cells, there were  $1.82 \pm 0.24$  neurites at day 5 and  $2.6 \pm 0.019$  neurites at day 7 compared to  $1.2 \pm 0.092$  neurites and  $1.9 \pm 0.28$  neurites on control on days 5 and 7 respectively. There was a trend that percentage of neurons bearing neurite was higher for IBMX/PGE1 cells compared to control ( $78.9 \pm 9.23 \%$  and  $68.4 \pm 8.31 \%$  at day 7 respectively).



**Figure 3.4:** Panel (top) shows brightfield photomicrographs of NG108-15 cells cultured in growth media (GM), NG108-15 cells cultured in differentiation media (DM) and primary cortical cells harvested from E14 CD1 mice at 1 and 7 days in vitro. Significant neurite outgrowth was measured from the NG108-15 (DM) condition compared to NG108-15 (GM) and Cortical conditions (right graph). In contrast, cell number increased at a faster rate in the NG108-15 (GM) condition compared to the other two (left graph). Data points represent mean values calculated from triplicate experiments. Scale bar 20μm.



**Figure 3.5:** Representative images of NG108-15 cells differentiated in differentiation media (containing IBMX/ PGE1) and control differentiation media (1% FCS). Images were taken at 1, 3, 5 and 7 days in differentiation media. Scale bar - 20 $\mu$ m.



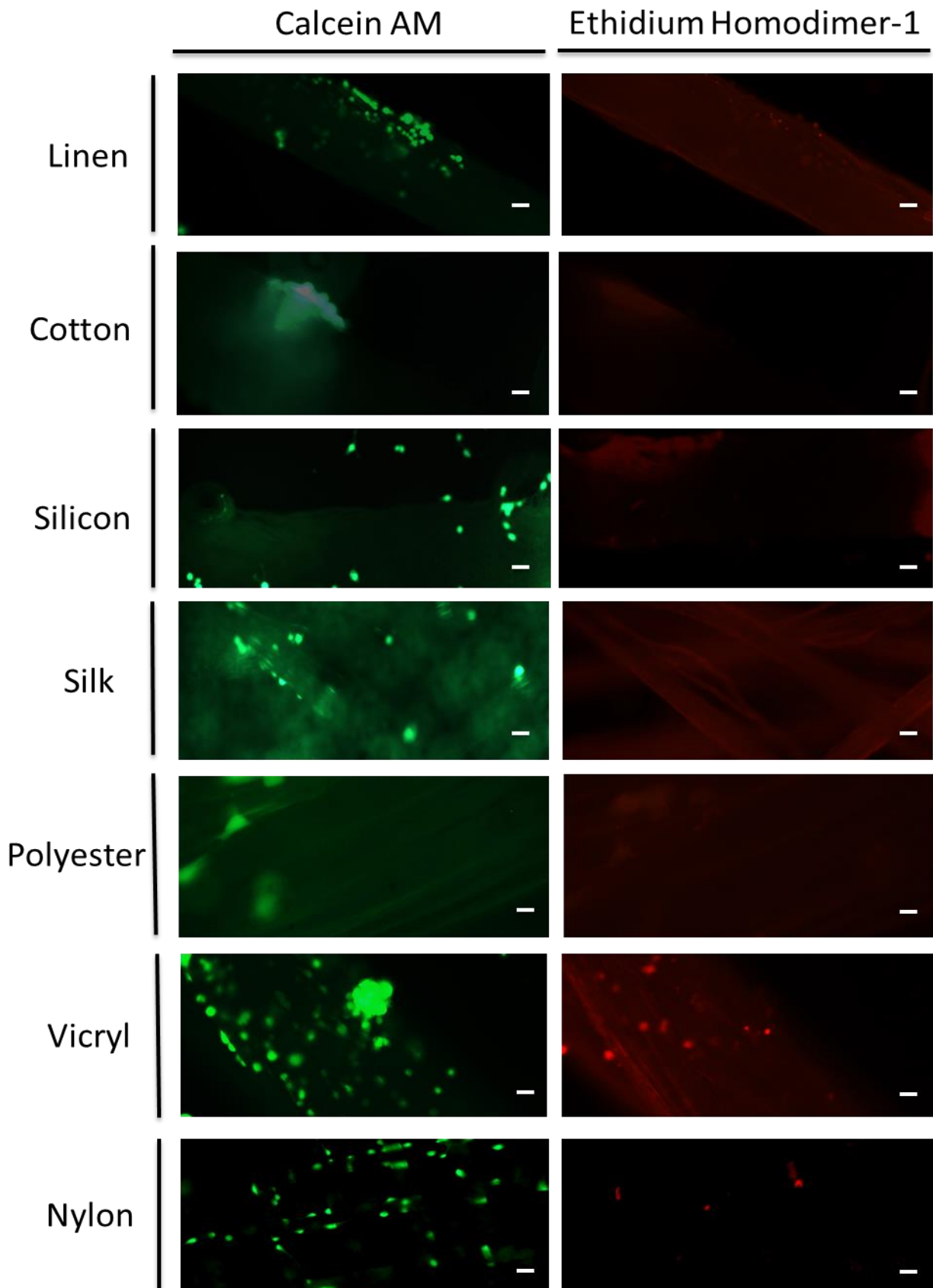
**Figure 3.6:** Quantification of mean neurite length, mean number of neurites per neuron and the mean percentage of neurons bearing neurites for NG108-15 cells cultured in differentiation media containing IBMX/PGE1 or control (1% FCS) at 1, 3, 5 and 7 days.



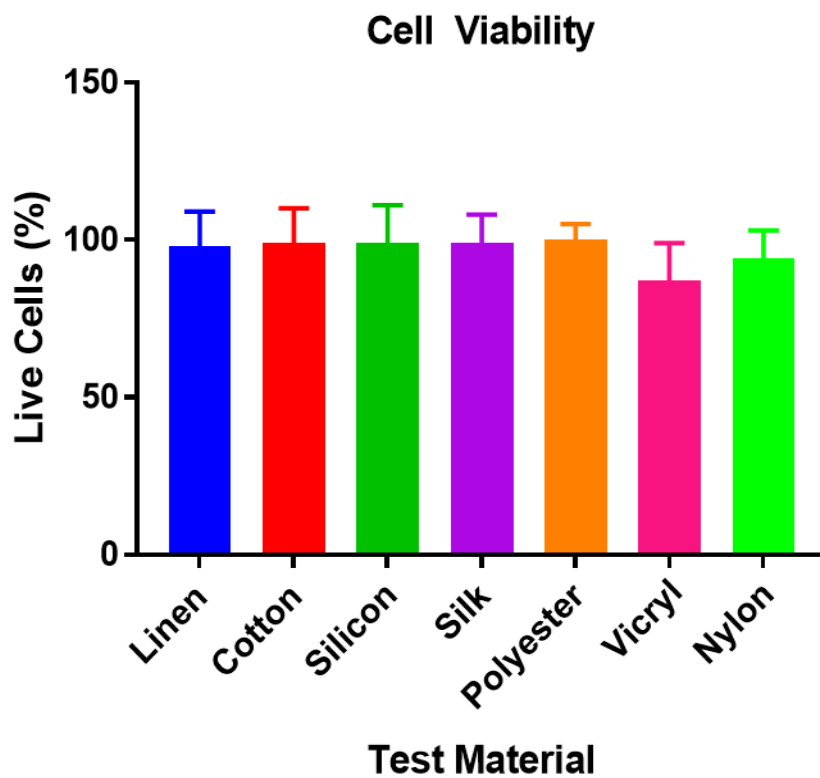
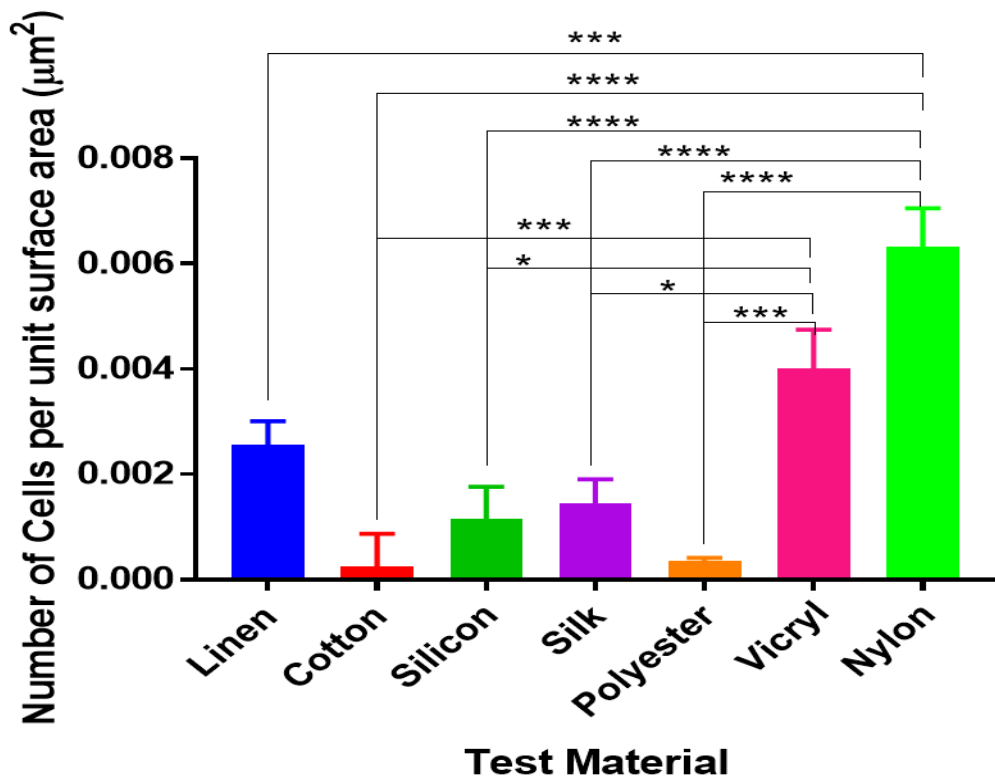
### 3.3.2 Determination and optimization of screening protocol to assess NG108-15 cell viability on materials

Calcein AM staining revealed healthy cells through epifluorescence imaging, and cell density was quantified. As can be observed in Figure 3.7 and 3.8, cells were more highly adherent on Nylon, Vicryl and Linen materials, compared to cotton, silicone, silk and polyester. 1-way ANOVA calculations confirmed that cell density on the nylon material was significantly higher than cotton, silicon, silk and polyester ( $p < 0.0001$ ). There were also significantly more cells on nylon compared to linen ( $p = 0.0004$ ) but not on vicryl ( $p = 0.0756$ ). Vicryl also showed modest levels of cell adherence, with a significantly higher cell density when compared to polyester ( $p = 0.0006$ ), silk ( $p = 0.0378$ ), silicon ( $p = 0.0135$ ), and cotton ( $p = 0.0004$ ). Cell density on nylon, referred to as PA hereon, ( $0.0063 \pm 0.000723$ ) was 33.3% higher than the second highest density of cells on vicryl ( $0.0042 \pm 0.000752$ ).

As well as staining healthy cells, ethidium homodimer-1 was used to label nucleic acid of cells that have undergone apoptosis as the cell membranes become porous. The dual staining was used to calculate the percentage of healthy cells. Irrespective of cell density, the majority of cells that were adherent were healthy with percentage of live cells being lowest on vicryl ( $87 \pm 12\%$ ) and highest on silk ( $99 \pm 9\%$ ).



**Figure 3.7:** Calcein AM staining of healthy NG108-15 cells, and Ethidium Homodimer-1 staining of dead cell nucleic acids, cultured for 3 days *in vitro*. Scale bar – 20 $\mu$ m.

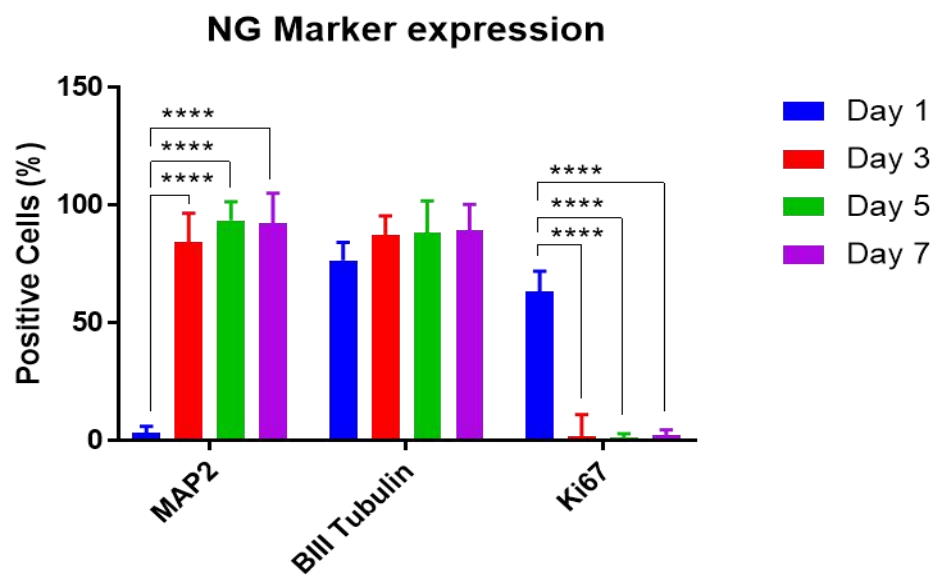
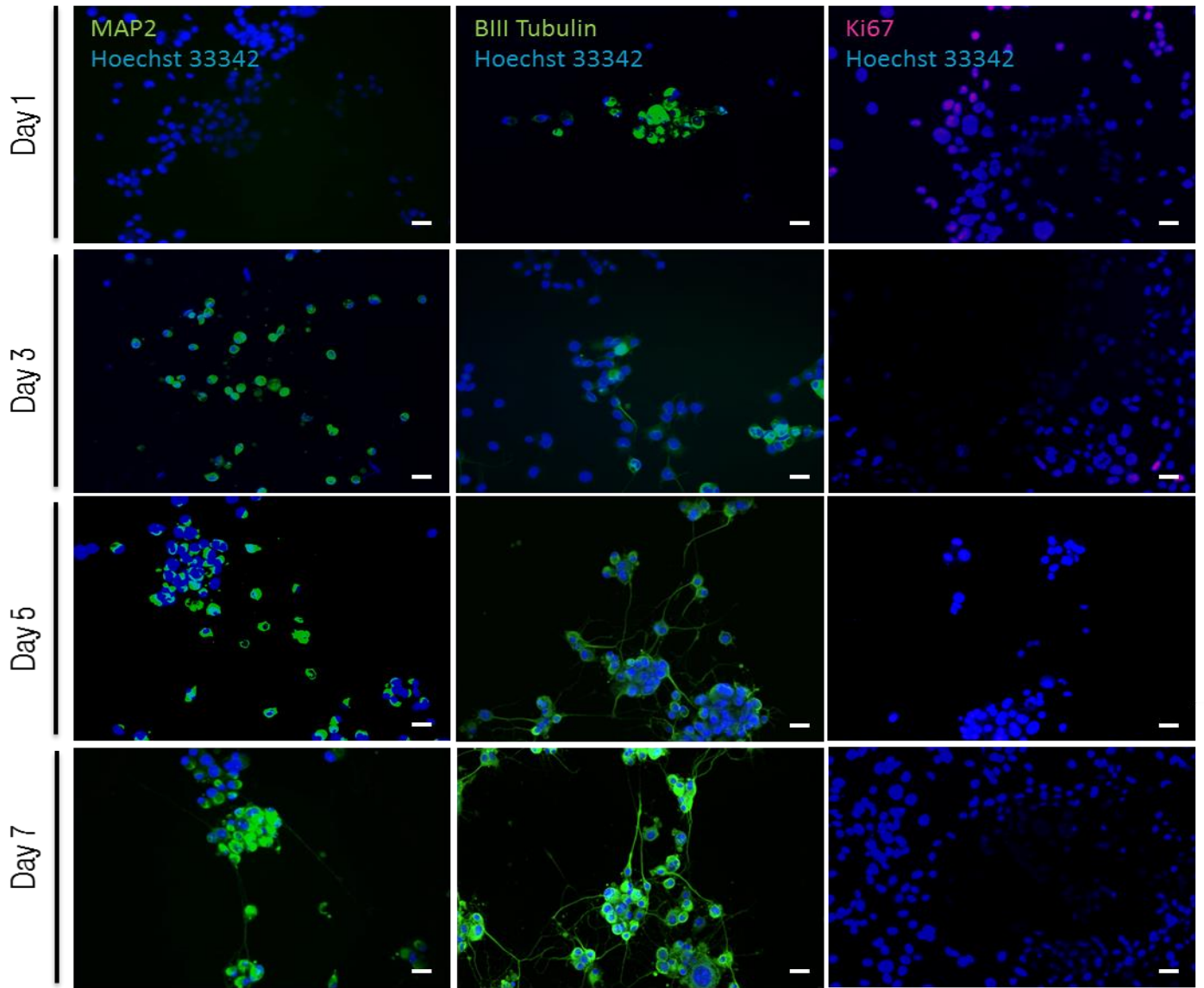


**Figure 3.8:** Quantification of cell viability. Cell density of adherent Calcein AM positive cells was plotted (top) and cell viability calculated as percentage of live cells in the field of view was also plotted (bottom).

### 3.3.3 NG108-15 Differentiation Analysis

Qualitative assessment confirms that MAP2 expression was very low at day 1, with only  $3.4 \pm 2.70\%$  of cell positively stained, however this increased to  $84.3 \pm 12.4\%$  at day 3,  $93.7 \pm 7.8\%$  at day 5 and was maintained within a high percentage of cells ( $92.6 \pm 12.6\%$ ) at day 7 (Figure 4.9). The expression on days 3, 5 and 7 was significantly higher than at day 1 ( $p < 0.0001$ ) when calculated using a 2-way ANOVA with post-hoc analysis. The other neural marker,  $\beta$ -Tubulin, was highly expressed at all time points ranging from  $76.7 \pm 7.62\%$  at day 1 to  $89.5 \pm 10.93\%$  at day 7. No significant difference was calculated between the time points ( $p > 0.74$  for all comparisons amongst time points).

Conversely, Ki-67 expression was highest at day 1, in  $63.5 \pm 8.52\%$  indicating the proliferative ability of cells when cultured in the growth medium (Figure 4.9). However, at subsequent time points, Ki-67 expression was much lower coinciding with the change in culture medium (differentiation medium). The percentage of positively stained Ki-67 cells was  $2.1 \pm 0.34\%$  at day 3,  $1.6 \pm 0.21\%$  at day 5, and  $2.4 \pm 0.15\%$  at day 7. 2-way ANOVA revealed highly significant differences between days 1 and 3, 5 and 7 ( $p < 0.0001$ ).

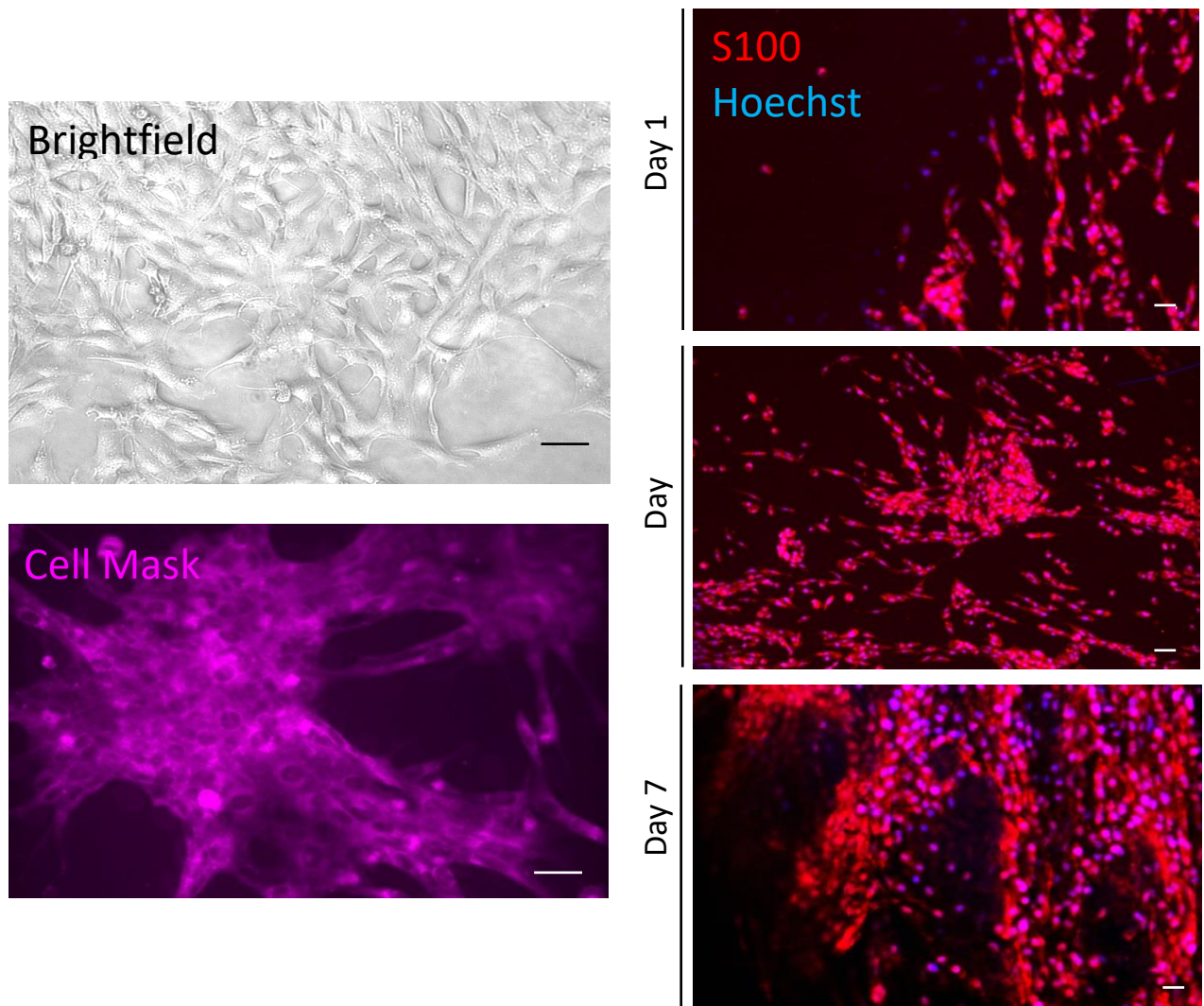


**Figure 3.9:** Protein marker expression within NG108-15 cells indicating neural differentiation (MAP2), neural microtubules (BIII Tubulin) and proliferation (Ki-67) at day 1, 3, 5 and 7 (Top panel), Percentage of NG108-15 cells positively stained with markers was measured and plotted (bar chart).

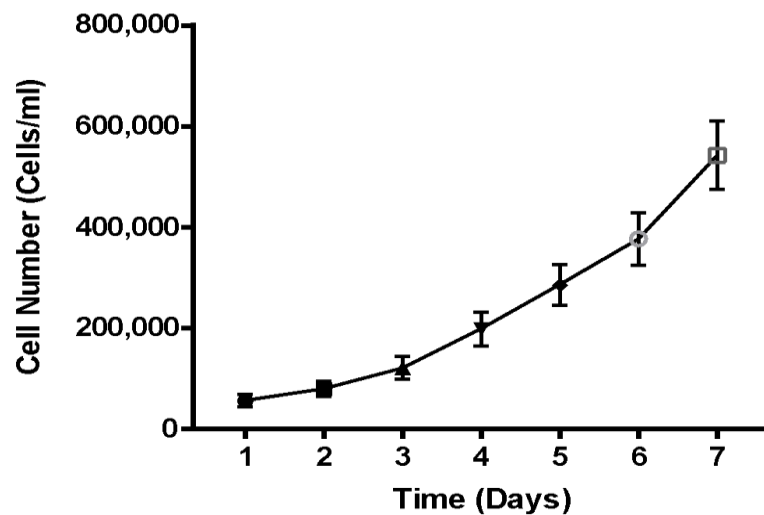
#### 3.3.4 Primary Schwann Cell Culture

To further develop the in vitro model of peripheral nerve outgrowth on 3D substrates, primary Schwann cells that were derived from Rat Sciatic Nerve were cultured in growth medium, and cell proliferation and morphology were assessed (see section Literature Review Section 1.2). To effectively culture Schwann cells and provide a comparison for future experiments measuring cell adherence, Schwann cells were cultured for 7 days and characterized.

Schwann cells clearly increased in cell number from day 1 to day 7, and have a spindle-shaped phenotype (Figure 3.10). The majority of the cells had a bipolar or multipolar morphology and proliferated in clusters at higher cell density. Schwann cell number was quantified every 24 hours for 7 days. The cell number increased from 50,000 cells plated at day 1 to  $564,300 \pm 43,500$  cells, representing a 91.1% increase in cell number.



### Schwann Cell Count

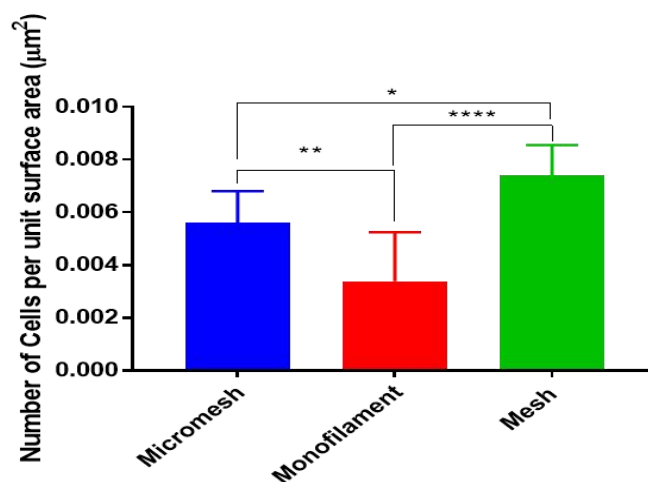
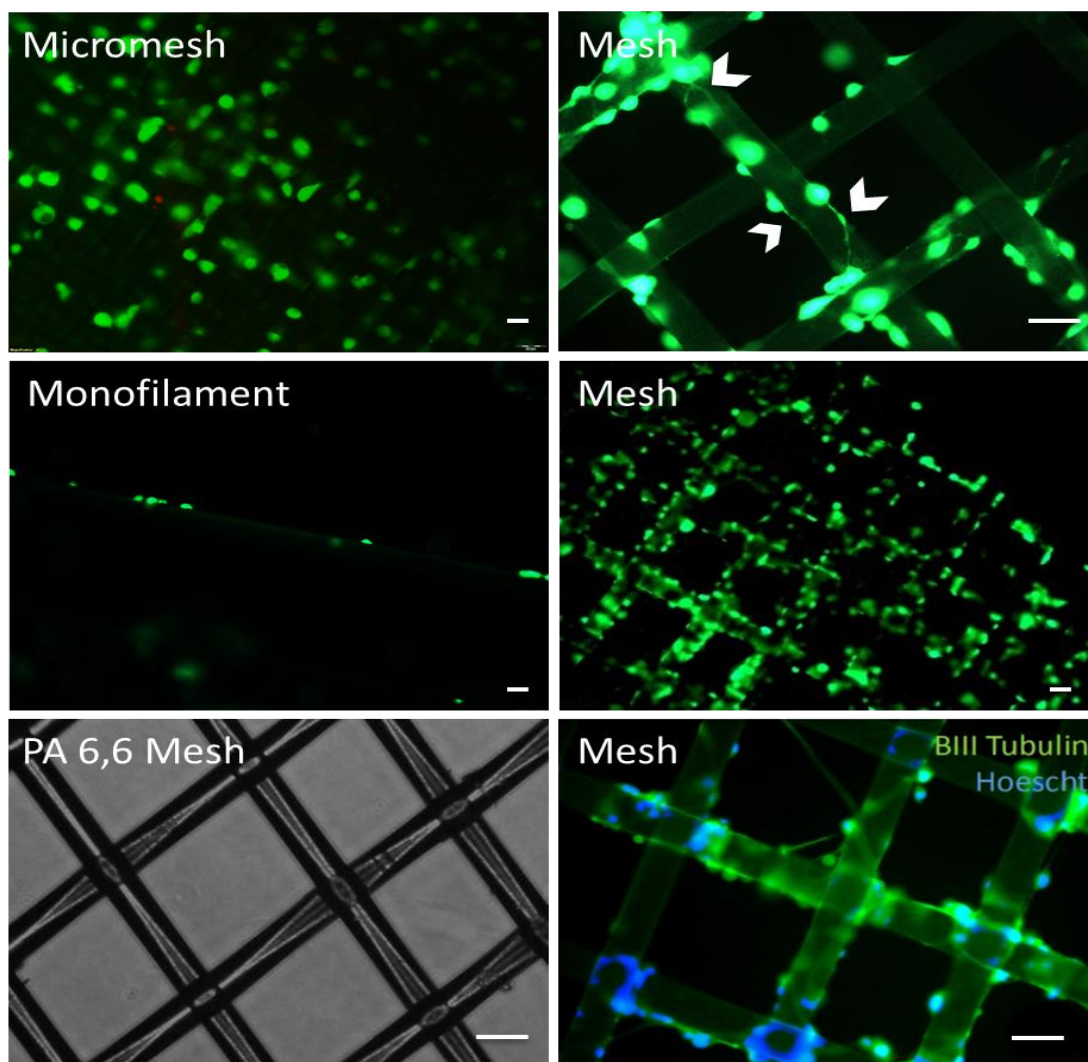


**Figure 3.10:** Brightfield photomicrograph, CellMask plasma membrane stain and S100 (day 1, 3 and 7) immunolabelling of Schwann cells with nuclei counterstained with Hoechst nuclear label (scale bar 20 $\mu$ m). Spinning disc confocal microscope was used to obtain the images displayed. The line graph shows Schwann cell proliferation with cell number quantified at time points every 24 hours for 7 days.

### 3.3.5 Investigation of NG108-15 adherence to Polyamide 6,6 materials

Adherence of NG108-15 cells to polyamide 6,6 (PA 6,6) materials was then studied to investigate the effect of fibre diameter on cell adherence following the increased cell density when NG108-15 cells were culture on the PA mesh (Figure 3.7) on three formats of PA 6,6 at 7 days (Figure 3.10). Quantification of cell density on the polyamide 6,6 materials revealed that the 3D format of the culture surface affected the number of adherent cells that were able to attach to the fibres, which also resulted in reduced visible neurite extension. Cell density measured on the Mesh was highest ( $0.0074 \pm 0.0003$  cells per  $\mu\text{m}$ ) which was a 24.3% increase when compared to the Micromesh ( $0.0056 \pm 0.0003$  cells per  $\mu\text{m}$ ) and a 54.1% increase when compared to Monofilament ( $0.0034 \pm 0.0005$  cells per  $\mu\text{m}$ ). 1-way ANOVA confirmed significant differences between Mesh and Micromesh ( $p=0.0115$ ), and Mesh and Monofilament ( $p<0.0001$ ). Cells on the Mesh could extend neurites along the longitudinal axis of the fibres (white arrowheads, Figure 3.10). Whereas cells were more spherical, by qualitative assessment, when cultured on the Micromesh, albeit a fairly high cell density could be achieved. Cells also stained positively for the neural marker on the Mesh, including neurites, demonstrating the capability to track neurites with the BIII Tubulin antibody staining in future experiments.





**Figure 3.11:** Widefield Epifluorescence microscopy of PA 6,6 (Nylon) Micromesh, Monofilament and Mesh showing NG108-15 cells stained with Calcein AM (top two rows of panel). Brightfield photomicrograph showing the PA6,6 Mesh format and immunostaining of adherent NG108-15 cells with BIII Tubulin and counterstained with Hoechst (lowest row of panel). Bar chart to show quantification of adherent cell density on the three formats of PA6,6 tested. Scale bar - 20 $\mu\text{m}$ .

### 3.3.6 Quantification of NG108-15 and Schwann cell Viability and Adherence on PA6,6 mesh

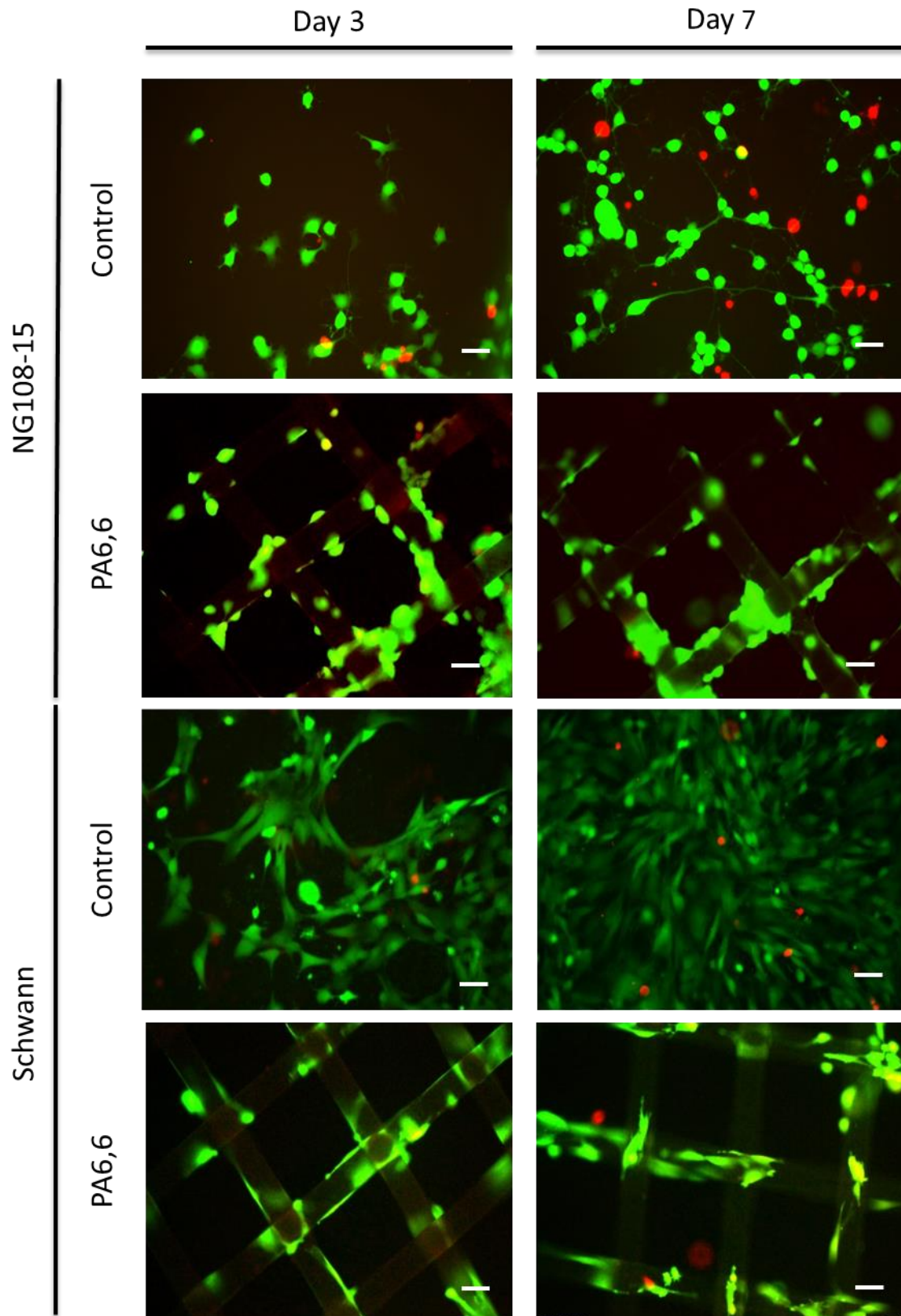
Cell adherence to the Mesh format of PA6,6 ('Nylon' in Figure 3.7) was then further quantified with both NG108-15 and Schwann cells to determine the suitability for the material to be used in longer term in vivo experiments. The model cells were cultured for up to 7 days and also cultured on tissue culture plastic (control) and stained with Calcein AM/ Ethidium Homodimer-1 as before (Figure 3.12).

Both cultures of NG108-15 cells and Schwann cells remained viable, with over 94.2% live cells achieved in cultures on the control and PA6,6 Mesh (Figure 3.13). When grown on the Mesh, Schwann cells showed the highest cell viability at  $98.6 \pm 4.2\%$  live cells on day 7. This was similar to NG108-15 levels ( $95.6 \pm 3.4\%$  live cells) at the same time point. No significant difference in mean live cell percentage was calculated between the Mesh and control at neither 3 nor 7 days. Qualitative assessment demonstrates that Schwann cells were instructed by the physical arrangement of the fibres and spread along the longitudinal axis, affecting the cluster arrangement of cells seen on the control surface (Figure 3.13).

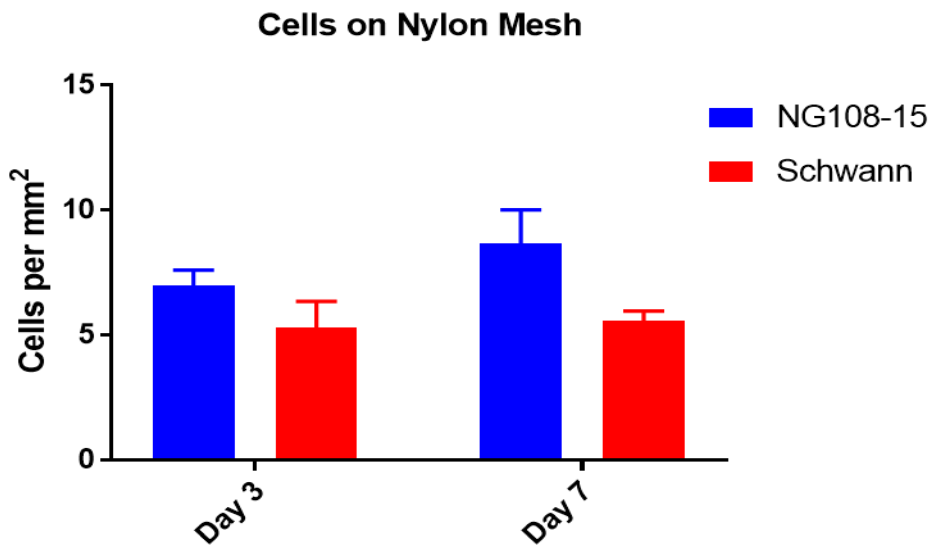
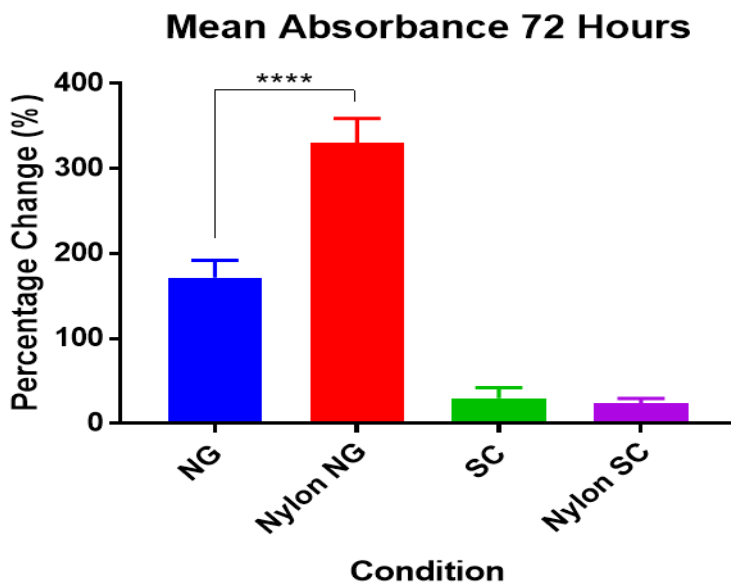
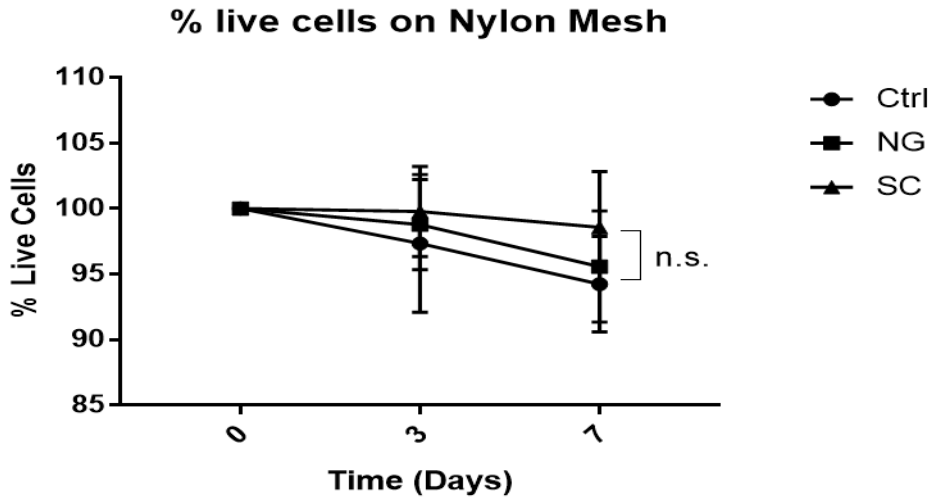
Cell density on the Mesh was further quantified at both day 3 and 7, demonstrating strong cell adherence. NG108-15 cells increased from  $6.98 \pm 0.62$  cells per  $\text{mm}^2$  at day 3 to  $8.67 \pm 1.34$  cells per  $\text{mm}^2$  at day 7; cell density was maintained. Schwann cell density was maintained on Mesh fibres, calculated at  $5.29 \pm 1.05$  cells per  $\text{mm}^2$  at day 3 and increasing slightly to  $5.56 \pm 0.39$  cells per  $\text{mm}^2$  at day 7. This slight increase was not statistically significant either.

Using the Alamar Blue assay, cell proliferation was assessed in both cell types following a 72 hour time period on the control and Mesh. Mean percentage change in absorbance between 24 hours and 72 hours was calculated for cells grown in growth media (NG108-15 and Schwann cells). NG108-15 cells proliferated on both control (increasing  $16.7 \pm 4.3\%$ ) and Mesh (increasing  $33.8 \pm 5.8\%$ ), showing that cell proliferation was not hindered by the difference in culture surface (Figure 3.13). In contrast, Schwann cell proliferation did not increase at an equal rate but remained stable on both surfaces, confirmed by the microscopy which shows strong Schwann cell adherence to the fibres at the earlier time point. Schwann cell signal from the assay increased by  $3.2 \pm 1.8\%$  on the control surface and  $2.7 \pm 0.9\%$  on the Mesh. When calculated by 2-way ANOVA, the larger increase in cell proliferation of NG10815- cells on the mesh compared to the control surface was highly significant ( $p < 0.0001$ ). However, no statistical difference in cell

proliferation was observed between changes in absorbance values from Schwann cells on the two surfaces.



**Figure 3.12:** Live/ Dead cell viability staining and widefield epifluorescence microscopy of Calcein AM and Ethidium Homodimer-1 stained cells. Cells were cultured on tissue culture plastic (control) and PA6,6 Mesh for 3 and 7 days. Scale bar - 20 $\mu$ m.

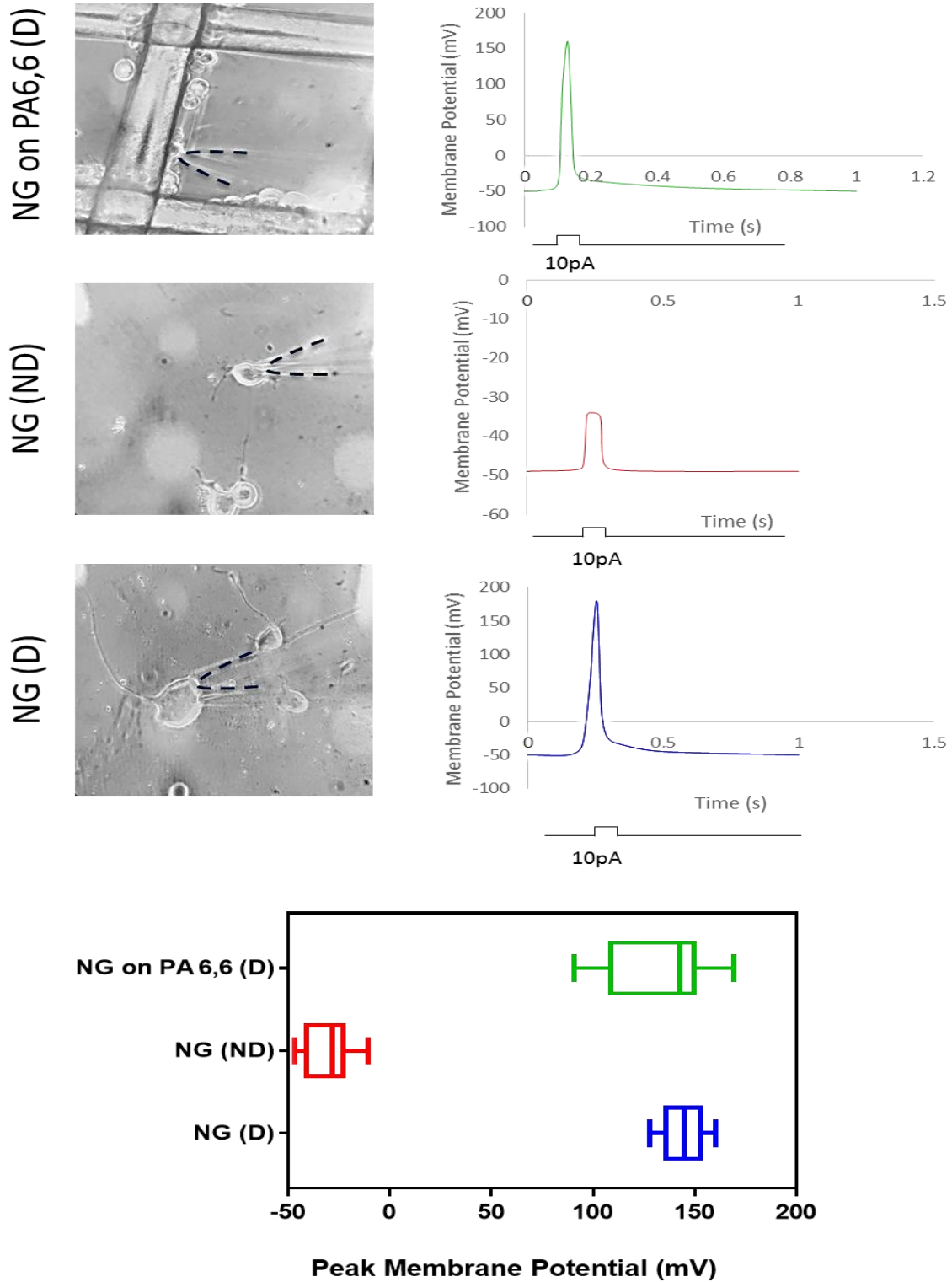


**Figure 3.13:** Quantification of cell viability (% live cells) was calculated at both time points (line graph). Adherent cells on the Mesh and mean percentage change in absorbance from Alamar blue assay was plotted (middle and bottom bar charts respectively).

### 3.3.7 Action Potential Recordings from NG108-15 cells cultured on PA6,6

To confirm functional activity of the NG018-15 cell model, and compare activity on the control culture surface to the mesh material, electrophysiological recordings were taken from the neural cells using a patch clamp technique. Cells were cultured on control surface (tissue culture plastic) and were either kept in growth medium (ND) or differentiation medium (DM) or recordings were taken from adherent cells on the mesh (NG on PA6,6) as in Figure 3.14. Specifically, microelectrodes were produced and patched onto the NG108-15 plasma membrane as highlighted (dotted lines, Figure 3.14). Membrane potential was held (clamped) at -50mV and the maximal membrane voltage at the peak of the action potential (peak membrane potential) was plotted in the box plot (Figure 3.14). Example recordings show that action potentials were recorded from cells that were cultured in the differentiation medium.

No spontaneous action potentials were recorded throughout the experiment but action potentials were elicited on current injections (10pA for 0.1s). Action potential configuration from cells cultured on both surfaces was highly similar for action potential width. However, the distribution of peak membrane potential (mV) had a larger range from cells cultured on the PA6,6 (90.6 to 169.3 mV) compared to differentiated cells cultured on the control surface (127.8 to 160.3mV). No action potentials were elicited in non-differentiated cells cultured on control surface, only artefacts from the current injection were recorded (peaking at a median of -28.1 mV). The median voltages were very similar for cells cultured on PA6,6 (144.75 mV) and those cells cultured on control (142.9 mV) suggesting very similar function regardless of culture surface.



**Figure 3.14:** Brightfield microscopy images showing example cells and microelectrode patching, with corresponding representative action potential traces for NG108-15 cells differentiated on PA6,6 mesh (NG on PA6,6 (D)), non-differentiated NG108-15 cells cultured on tissue culture plastic (NG (ND)) and NG108-15 cells differentiated on tissue culture plastic (NG (D)). The box plots show the maximal membrane voltage recorded from the action potentials for each culture condition.

### 3.3.8 Fourier Transform Infrared Spectroscopy (FTIR) of Polyamides

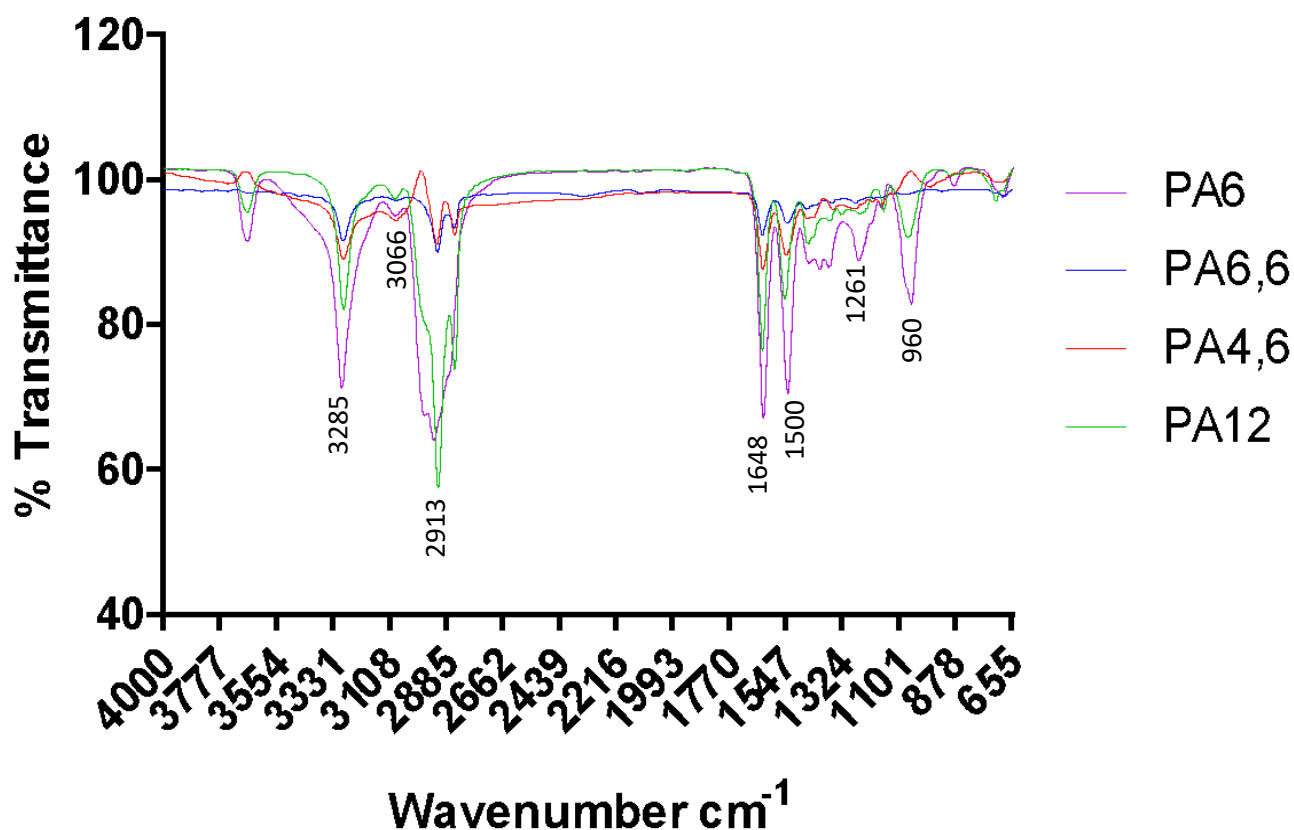
FTIR analysis was used to characterise and confirm purity of the surface chemistry of polyamide samples intended for cell culture by attenuated total reflectance method to retrieve the spectra. Four polyamides were selected to be used in further cell adherence studies which were polyamide 6 (PA6), polyamide 6,6 (PA6,6), polyamide 4,6 (PA4,6) and polyamide 12 (PA12). The FTIR spectra for the polyamides are displayed in Figure 4.15, and formulae in Figure 4.16.

Data from table 1 was derived from the FTIR spectra and confirm the presence of key functional groups expected to be presented from the polyamides (Figure 3.15). The spectra for all materials shared important peaks at  $3285\text{cm}^{-1}$  which confirmed the amine functional group (N-H). Amide I and Amide II peaks at  $1648\text{cm}^{-1}$  and  $1500\text{cm}^{-1}$  respectively confirmed typical peaks in polyamide chemistry that correspond to the amine functional group.

Table 3.1: FTIR wavenumbers of Transmittance from Polyamide Samples

<b>Wavenumber (<math>\text{cm}^{-1}</math>)</b>	<b>Functional Group</b>
<b>3285</b>	N-H stretching
<b>3066</b>	$\text{CH}_2$ stretching
<b>2913</b>	$\text{CH}_2$ stretching
<b>1648</b>	Amide I (C=O and C-N stretching)
<b>1500</b>	Amide II (N-H bending and C-N stretching)
<b>1261</b>	$\text{CH}_2\text{-CH}_2$ stretching



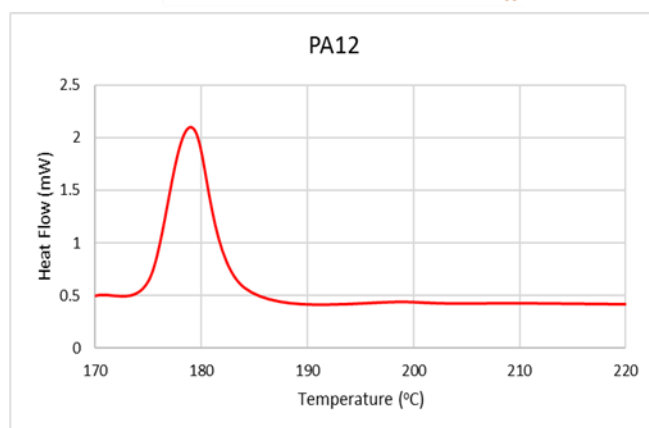
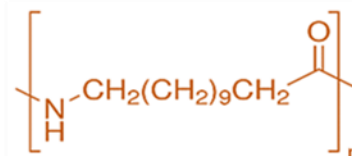
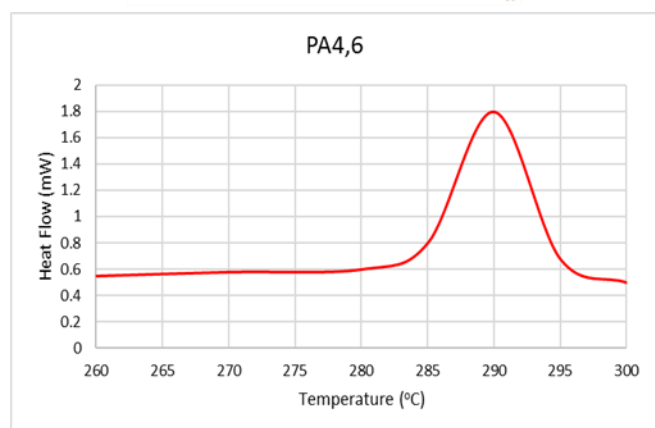
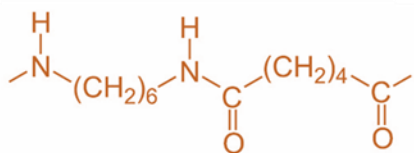
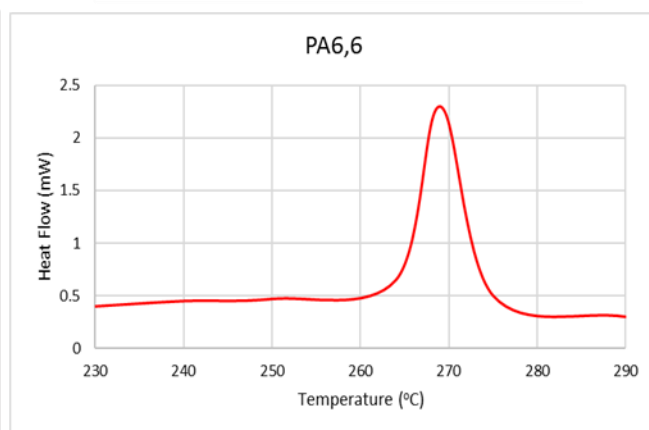
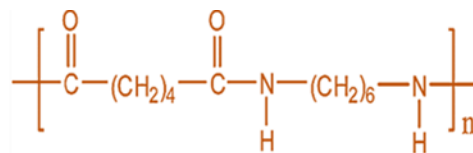
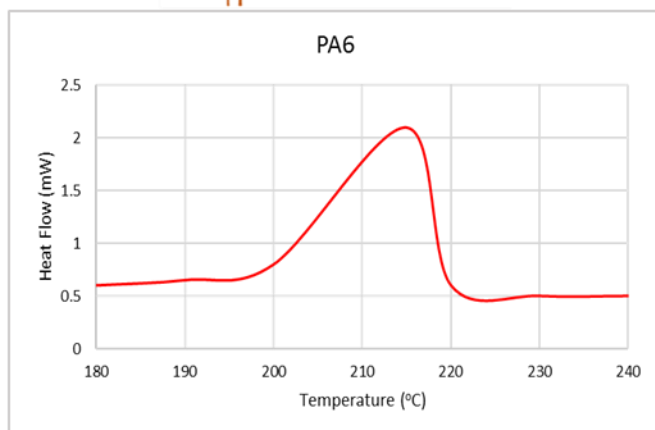
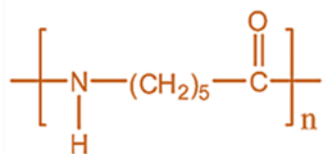


**Figure 3.15:** FTIR Spectra of polyamide 6, polyamide 6,6, polyamide 4,6 and polyamide 12 with numbers quoting common transmittance peak wavelenghts.

### 3.3.9 Dynamic Scanning Calorimetry of Polyamides Tested

Dynamic Scanning Calorimetry (DSC) was carried out to determine the thermosoftening properties of the polyamides tested as this could be used to develop engineering strategies to make nerve guidance conduits. The melting temperature was determined after drying the samples as PA is sensitive to moisture at a heating rate of 10°C per minute. Over the broad temperature range 80-190°C glass transition ( $T_g$ ) is very difficult to determine as a number of simultaneous thermal transitions occur. The relevant exothermic peaks showing melting temperature ( $T_m$ ) are provided (Figure 3.16). Melting temperatures were determined at 215.4°C, 268.2°C, 292.6°C and 189.6°C for PA6, PA6,6, PA4,6 and PA12 respectively. All samples showed strong hydrogen bonding which results in the high melting temperatures recorded.

↑  
Endothermic Up



**Figure 3.16:** DSC melt curves revealing melting temperatures for polyamides tested: PA6, PA6,6, PA4,6 and PA12. Structural formulae have also been provided.

### 3.3.10 NG108-15 and Schwann Cell Culture on Polyamides

Following quantification of cell proliferation and viability of cells cultured on PA6,6 fibres in a mesh format (Figure 3.12), the same cells were cultured on the four polyamide samples investigated by FTIR and DSC for 24 and 72 hours (Figures 3.15 and 3.16). Qualitative analysis revealed that cells showed their typical phenotype when cultured on PA6, PA6,6 and PA4,6 as demonstrated by the plasma membrane staining with CellMask™. A higher density of both NG108-15 and Schwann cells were observed to adhere to the PA6,6 material compared to PA6 and PA4,6 samples, at both time points (Figure 3.18). However, length of neurites, an indicator of neural cell differentiation, was longer on PA6 and PA4,6. Schwann cells showed clear polarity when cultured on the PA6, PA6,6 and PA12 materials with cell spreading pronounced at 72 hours on PA6 and PA6,6.

Neuronal differentiation measurements were analysed from fluorescent microscopy images taken of NG108-15 cells cultured on all four polyamide samples (Figure 3.17). A slight increase in mean neurite length was observed on the PA6, neurite length increased by 52.5% from  $6.4 \pm 0.8\mu\text{m}$  on day 3 to  $13.6 \pm 2.4\mu\text{m}$  on day 7 (Figure 3.18). Neurite length was further pronounced on PA6,6 compared to PA6. Neurites increased by 88.5% from  $23.7 \pm 3.3\mu\text{m}$  on day 3 to  $44.2 \pm 6.5\mu\text{m}$  on day 7 on the PA6,6 material. This increase was statistically significant when compared using a 1-way ANOVA, with  $p < 0.0001$ . Similarly, an increase in neurite length was calculated on PA4,6 which increased by 44.9% from  $14.5 \pm 0.7\mu\text{m}$  on day 3 to  $26.3 \pm 2.3\mu\text{m}$  on day 7. This difference was also calculated to be statistically significant by 1-way ANOVA,  $p = 0.0145$ . When NG108-15 cells were cultured on the PA12 material however, a similar trend in increase of mean neurite length was not observed. Mean neurite length remained very low ( $0.6 \pm 0.1\mu\text{m}$  on day 3 and  $0.4 \pm 0.0\mu\text{m}$  on day 7) and indicated that neurites were inhibited by the surface properties.

The percentage of neurite bearing neurons was also calculated to compare the efficacy of the materials as substrates in promoting differentiation of NG108-15 cells. It was observed that NG108-15 cells bear more neurites as the culture time in differentiation media increases. A larger proportion of cells differentiated on PA6 substrate were bearing neurites ( $64.8 \pm 18.5\%$  on day 3 and  $76.2 \pm 22.6\%$  on day 7) compared to PA6,6 ( $34.6 \pm 5.6\%$  on day 3 and  $42.5 \pm 6.4\%$  on day 7) (Figure 3.18). Although the percentage of cells initially at day 3 bearing neurites was lower ( $56.7 \pm 8.6\%$  of cells), there was a similar percentage of cells bearing neurites on PA4,6 as PA6 by day 7 ( $72.4 \pm 4.6\%$  of cells). NG108-15 cells cultured on PA12 material did not bear neurites,

corresponding with the lack of neurite outgrowth previously observed. The percentage of neurite bearing neurites was  $1.4 \pm 0.2\%$  on day 3 and  $1.1 \pm 0.5\%$  on day 7. Comparison of mean percentage of neurite bearing neurons by 1-way ANOVA with post-hoc analysis confirmed a statistically significant difference between neurons cultured on PA6 and PA12 at 7 days ( $p=0.0473$ ) but no other significant differences were calculated. This revealed that neurite outgrowth may be highly dependent on the surface material and cannot be overridden by time of culture.

The mean number of neurites per neuron was then calculated and revealed differences in this variable amongst NG108-15 cells cultured on the polyamides. Particularly, neural cells cultured on PA12 predominately did not have neurite outgrowths ( $0.2 \pm 0.02$  neurites per cell at day 3 and  $0.4 \pm 0.06$  neurites per cell at day 7), whereas on the other materials there were more neurites quantified. Mean number of cells with neurites was highest on PA6,6 ( $1.8 \pm 0.2$  neurites/cell at day 3 and  $2.3 \pm 0.3$  neurites per cell at day 7). Surprisingly the number of neurites could not be maintained on PA6 and PA4,6 as the mean number decreased from  $2.1 \pm 0.2$  neurites/cell at day 3 to  $1.7 \pm 0.3$  neurites/cell at day 7 on PA6 and  $1.5 \pm 0.03$  neurites/cell at day 3 to  $1.2 \pm 0.2$  neurites/cell at day 7 on PA4,6. When means were compared in a 1-way ANOVA, the number of neurites per cell on PA12 was significantly lower than PA6, PA6,6 and PA4,6 on day 3 ( $p<0.0001$ ). Similarly, PA12 mean number of neurites on NG108-15 cells was significantly lower than PA6 and PA6,6 ( $p<0.0001$ ), and PA4,6 ( $p=0.0239$ ) at day 7. Also there was a significant difference between the number of neurites per cell cultured on PA4,6 and PA6,6 at day 7 ( $p=0.006$ ).

#### 3.3.11 Proliferation of Schwann Cells and NG108-15 Cells on Polyamide

The Alamar Blue assay was used to quantify the increase in cell number when NG108-15 or Schwann cells were cultured on the four polyamide materials (PA6, PA6,6, PA4,6 and PA12). NG108-15 cell signal increased on all materials, especially PA6 ( $13.5 \pm 2.42\%$ ), PA6,6 ( $35.6 \pm 4.53\%$ ) and PA4,6 ( $23.2 \pm 4.67\%$ ) (Figure 3.19). The percentage increase on PA12 ( $3.4 \pm 2.62\%$ ) was minimal and 90.44% less than the largest increase in signal on PA6,6. The mean increase in absorbance (%) was compared by 1-way ANOVA, significant differences were calculated between NG108-15 cells cultured on PA6,6 and PA6 ( $p=0.0069$ ), PA6,6 and PA12 ( $p<0.0001$ ) and PA4,6 and PA12 ( $p=0.0191$ ). These increases in cell number correlated with the qualitative analysis previously assessed (Figure 3.17).

Similarly, Schwann cells were calculated to proliferate well on PA6, PA6,6 and PA4,6 materials, although absorbance did not increase as much on PA12 ( $4.1 \pm 3.52\%$ ) (Figure 3.19). The largest increase was observed on PA6 ( $36.2 \pm 9.34\%$ ) in contrast to the NG108-15 cells which produced a larger increase in absorbance on the PA6,6. Schwann cell proliferation was also observed on PA6,6 ( $23.0 \pm 3.44\%$ ) and PA4,6 ( $18.3 \pm 3.57\%$ ) materials however the lower rate of proliferation suggested that fewer cells initially adhered onto these materials in comparison to the higher absorbance values measured on PA6 for Schwann cells. 1-way ANOVA confirmed significant differences between mean absorbance values for Schwann cells cultured on PA6 and PA4,6 ( $p=0.0412$ ), PA6 and PA12 ( $p<0.0001$ ) and PA6,6 and PA12 ( $p=0.1448$ ).

### 3.3.12 Schwann Cell Morphology Quantification on Polyamide Substrates

Schwann cell morphology was then quantified to determine how the culture condition affected the spreading and interaction of cells and material surfaces. Schwann cells that were not in contact with neighbouring cells were traced and the number of filopodia protruding from the cell were counted. Cells with no filopodia were identified as non-polar cells, whereas cells with two filopodia were identified as bipolar cells and cells with more than 3 filopodia were identified as multipolar cells. At 24 hours, Schwann cells had already polarised and were predominately bipolar which matched the phenotype observed on tissue culture plastic previously (Figure 3.10). Specifically more bipolar cells were measured on PA6 (73.6%), PA6,6 (47.4%) and PA12 (53.7%) (Figure 3.19). However, fewer bipolar cells were identified on PA12 (22.9%) and the majority of cells were non-polarised on this material (74.4%). At this time point, the vast majority of cells were polarised on PA6 with 22.5% of cells being multipolar. However, on both PA6,6 and PA4,6 at 24 hours, cells sub-populations that were non-polar (28.5% and 23.9% respectively) and multipolar (24.1% and 22.4% respectively) were similar in percentage of the total population of cells.

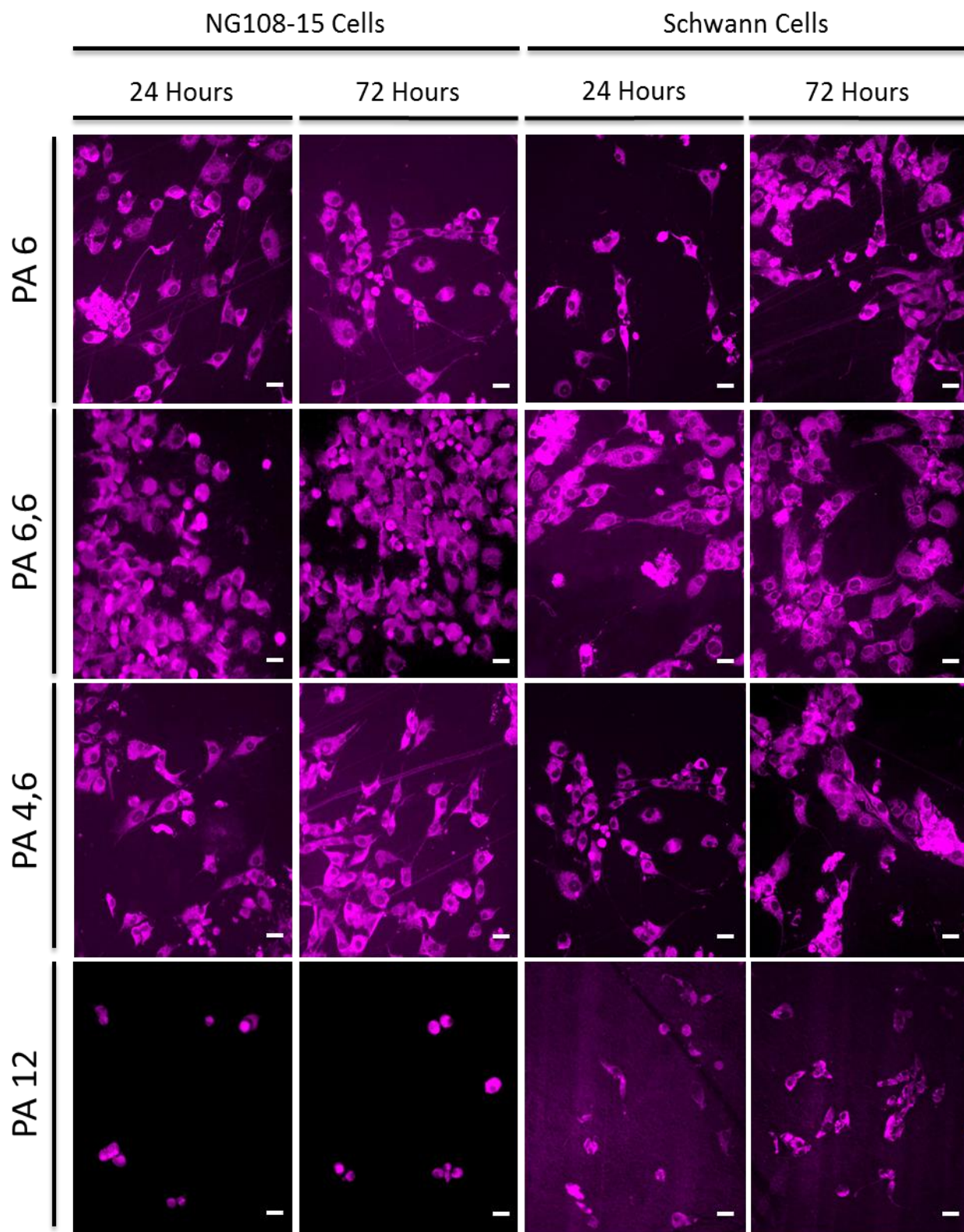
Schwann cell morphology was then assessed on the materials at 72 hours to confirm whether the morphologies assessed at 24 hours remained constant or were dynamic. Schwann cells on PA6 were mainly bipolar as before (57.3%) although to a lesser extent as the percentage of non-polar cells had increased (32.4%) and few cells were multipolar (10.3%). The cell morphology on PA6,6 remained fairly constant over 48 hours as there were similar percentages of non-polar (17.9%) and multipolar cells (23.6%) as at 24 hours and mainly bipolar cells (58.5%). The majority of cells present on PA12 at 72 hours also remained constant for cell morphology as most were

non-polarised (87.8%). However, Schwann cells cultured on PA4,6 showed that they were able to polarise further over the 48 hours as there were more multipolar cells (37.8%) and a majority of cells were bipolar (47.9%). Schwann morphology was more constant on PA6 and PA6,6. However there was a tendency for cells to become multipolar on PA4,6. Cells cultured on PA12 remained predominately non-polar demonstrating that the cells were less able to interact with the surface chemistry.

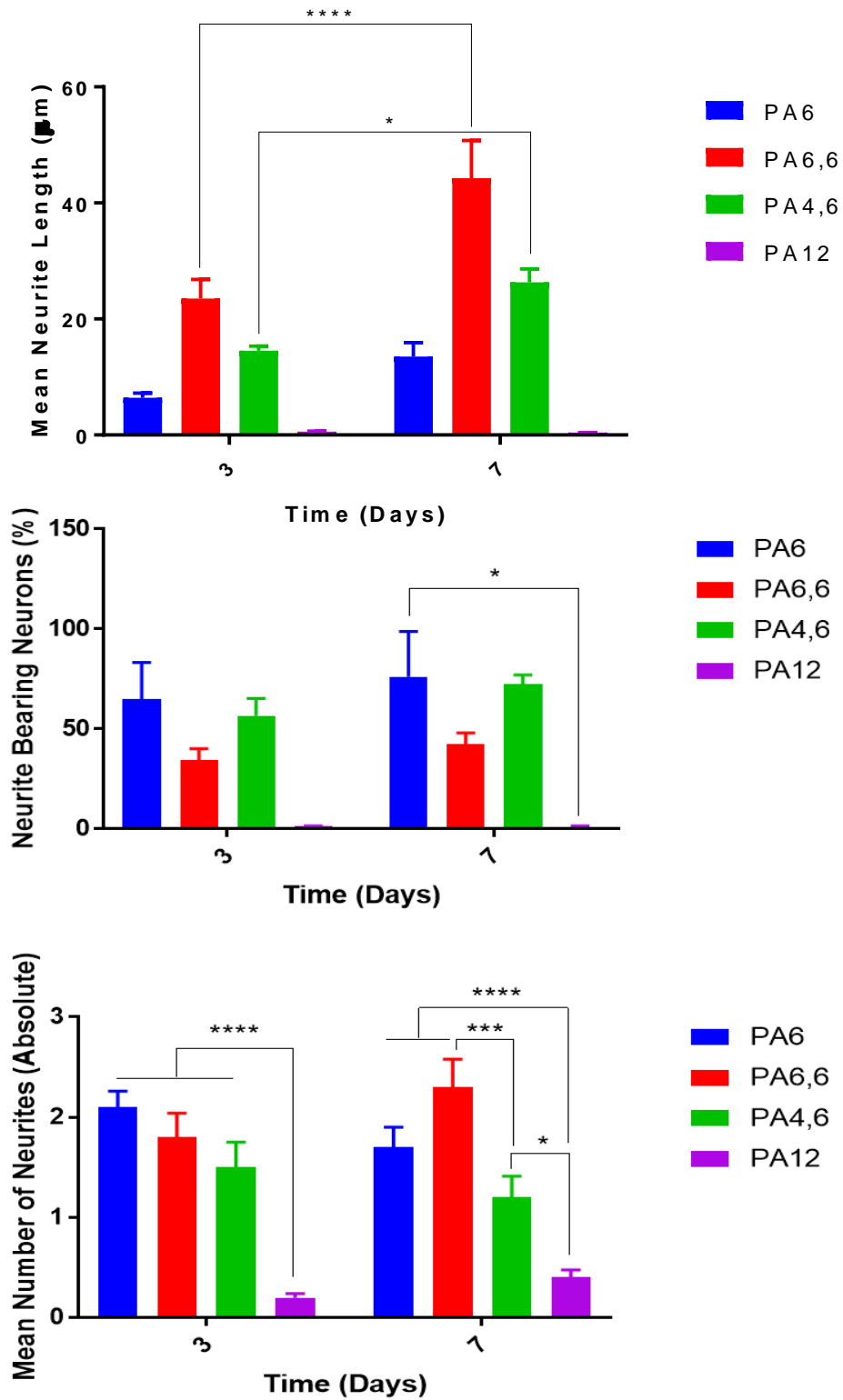
### 3.3.13 Quantification of Schwann Cell Area

Schwann cell area was then quantified on the same polyamide surfaces to investigate whether the cells were capable of increasing surface area and spread on the material. At 24 hours, Schwann cells demonstrated that they were able to spread along the polyamide material regardless of surface chemistry. On PA6, the cell area was  $48.5 \pm 8.62 \mu\text{m}^2$  which was the greatest mean cell area in comparison to PA6,6 ( $42.4 \pm 7.46 \mu\text{m}^2$ ), PA4,6 ( $43.3 \pm 10.9 \mu\text{m}^2$ ) and PA12 ( $31.9 \pm 13.7 \mu\text{m}^2$ ). The means were compared using a 1-way ANOVA however no significant differences between the cell area measurements on the polyamide surfaces were calculated ( $0.6839 \leq p < 0.9999$ ) in all comparisons).

Mean cell area was then calculated at 72 hours to assess how cell morphology properties may have changed over the 48 hour period. Cells remained the same size at 72 hours on PA6 ( $44.1 \pm 11.5 \mu\text{m}^2$ ), PA4,6 ( $49.3 \pm 7.89 \mu\text{m}^2$ ) and PA12 ( $33.5 \pm 9.25 \mu\text{m}^2$ ). However for the Schwann cells cultured on the PA6,6 surface, cells were observed to increase in surface area by 53.6% to  $65.3 \pm 12.5 \mu\text{m}^2$ . The increased cell area on the PA6,6 material was calculated to be significantly different to cell area on PA12 between 24 and 72 hours by 1-way ANOVA ( $p=0.0003$ ). However, no other significant differences were calculated between the materials at either time point suggesting that PA6,6 enables increase in cell surface area over time.

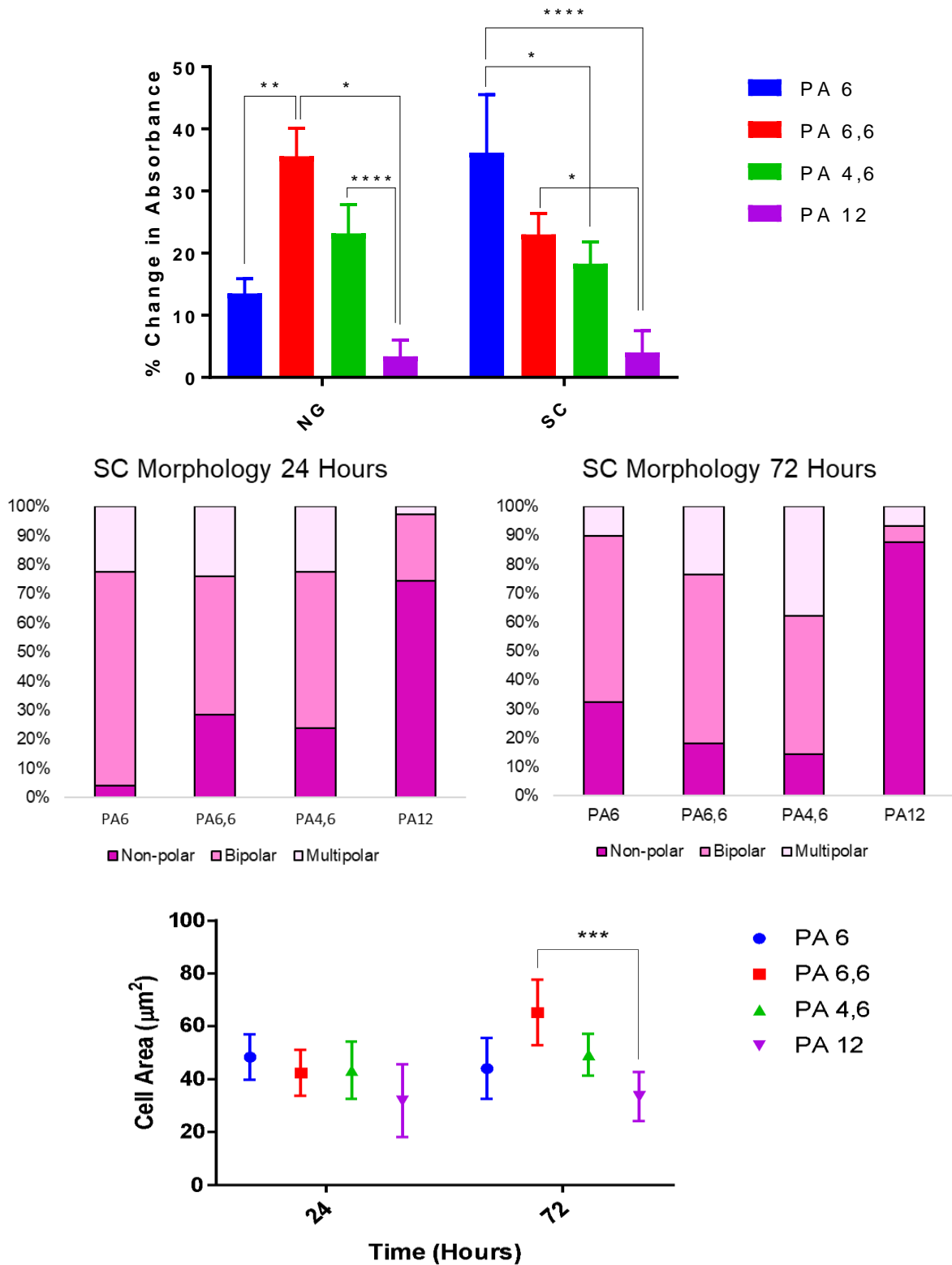


**Figure 3.17:** Fluorescent spinning disc confocal microscopy images showing culture of NG10815 neural cells and Schwann cells cultured on polyamides (PA6, PA6,6, PA4,6 and PA12 at both 24 hours and 72 hours. Scale bar - 20 $\mu$ m.



**Figure 3.18:** Bar charts showing quantification results of neural differentiation markers including mean longest neurite (upper graph), mean percentage of neurite bearing neurons in the culture (middle graph) and mean number of neurites counted per neuron (lower graph).





**Figure 3.19:** Bar chart showing mean change in absorbance from Alamar Blue assay between 24 and 72 hours of NG108-15 and Schwann cells cultured on PA6, PA6,6, PA4,6 and PA12 respectively (upper graph). Stacked bar charts to show sub-populations of Schwann cells that had a non-polar, bipolar or multipolar phenotype at 24 and 72 hours on PA6, PA6,6, PA4,6 and PA12 respectively (middle graphs). Mean Schwann cell area plotted at 24 and 72 hours on PA6, PA6,6, PA4,6 and PA12 respectively.

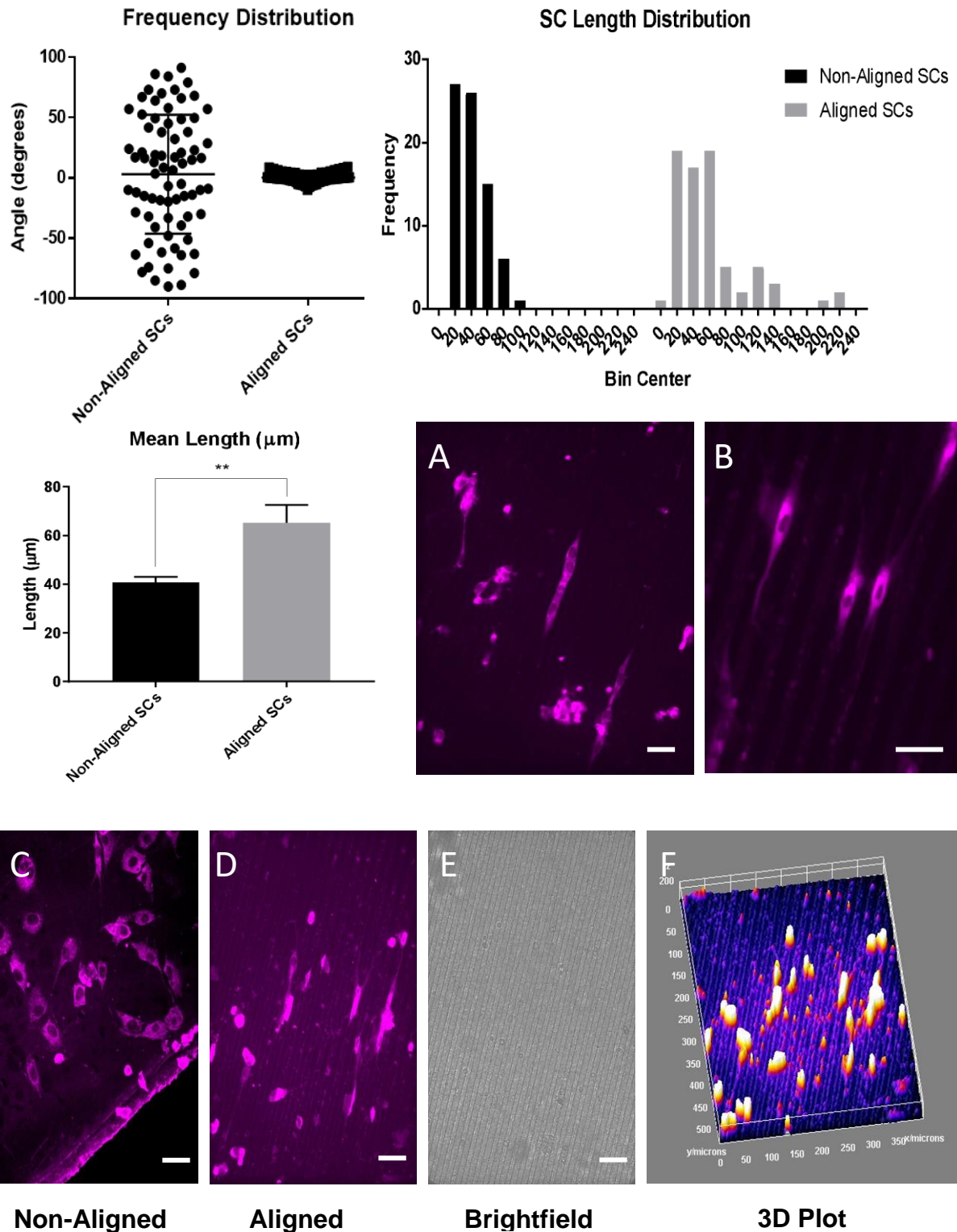
### 3.3.14 Effect of Polyamide Hot Embossing on Schwann Cell Alignment

Following assessment of the four polyamides (PA6, PA6,6, PA4,6 and PA12) in cell adhesion, biocompatibility, cell spreading and neural differentiation, polyamide 6,6 (PA6,6) was examined further for use its cell adherence properties following hot embossing. Hot embossing is a technique that was developed to provide a physical stimulus to cells cultured on the PA6,6 surfaces as previously examined (Figure 3.20). Schwann cells were cultured on the same PA6,6 surfaces as before as a control (labelled as non-aligned) as well as surfaces with 10 $\mu$ m x 10 $\mu$ m grooves that had been prepared prior to cell culture for 3 days.

The distribution of the angle of the longest axis of the cell with respect to a defined plane (the y-axis of the image was set to 0°) along the y-axis of the image was plotted after measuring. It was clear that the physical differences between the non-aligned and aligned surfaces had a significant effect on Schwann cell phenotype. Schwann cells on non-aligned surfaces ranged between angles of -90° and 90° with a mean angle of  $4.6 \pm 52.7^\circ$  (Figure 3.20). The large SEM indicated that a large spread of values for the angle of alignment, demonstrating that Schwann cell alignment did not occur. However, in contrast, when Schwann cells were cultured on the aligned PA6,6 surface, Schwann cells were clearly aligned. Measurement of mean angle of alignment from the y-axis was  $80 \pm 8.3^\circ$ . This demonstrated that Schwann cell alignment could be controlled on this surface.

The mean length of Schwann cells cultured on both non-aligned and aligned surfaces was then measured as the physical cue of grooves could be beneficial to encouraging longer Schwann cells and specifying the direction of growth. Length was defined as the longest measurable axis of the cell. Distribution of Schwann cell lengths was plotted to demonstrate the higher frequency of shorter cells on the non-aligned surface compared to the aligned surface. For example the first 50 cells measured has lengths  $20\mu\text{m} < x \leq 40\mu\text{m}$  on the non-aligned surface. However, the first 50 cells on the aligned surface had a longer range of lengths,  $0\mu\text{m} < x \leq 60\mu\text{m}$ . Mean length was 35.01% longer for aligned cells ( $63.7 \pm 12.84 \mu\text{m}$ ) than non-aligned cells ( $41.4 \pm 3.62 \mu\text{m}$ ).

Fluorescence imaging shown in Figure 3.20 demonstrates the alignment of Schwann cells labelled with plasma membrane stain CellMask™. Most cells showed a bipolar phenotype with typically a longer longest axis. A low density of cells was cultured (10,000 cells per ml) to ensure measurement from individual, non-clustered cells, and the cells had very fine filopodia which could only be resolved using spinning disc confocal microscopy.



**Figure 3.20:** Quantification of Schwann cells cultured on non-aligned and aligned (grooved surface) for 72 hours. The scatter plot shows mean angle of orientation of cultured cells. Schwann cell length frequency distribution shows the lengths of all cells measured. Bar chart shows mean length of cells cultured on both aligned and non-aligned surfaces. Spinning disc confocal microscopy (SDCM) of aligned and non-aligned Schwann cells cultured on PA6,6 with a 20X and 40X objective (A+B). Maximum intensity SDCM images of cells with 20X objective (C+D), brightfield photomicrograph of the aligned sample shown (E) and a 3D render of a 120 $\mu\text{m}$  z-stack of the same aligned image (F) to show cell depth on the surface. Scale bar - 20 $\mu\text{m}$ .

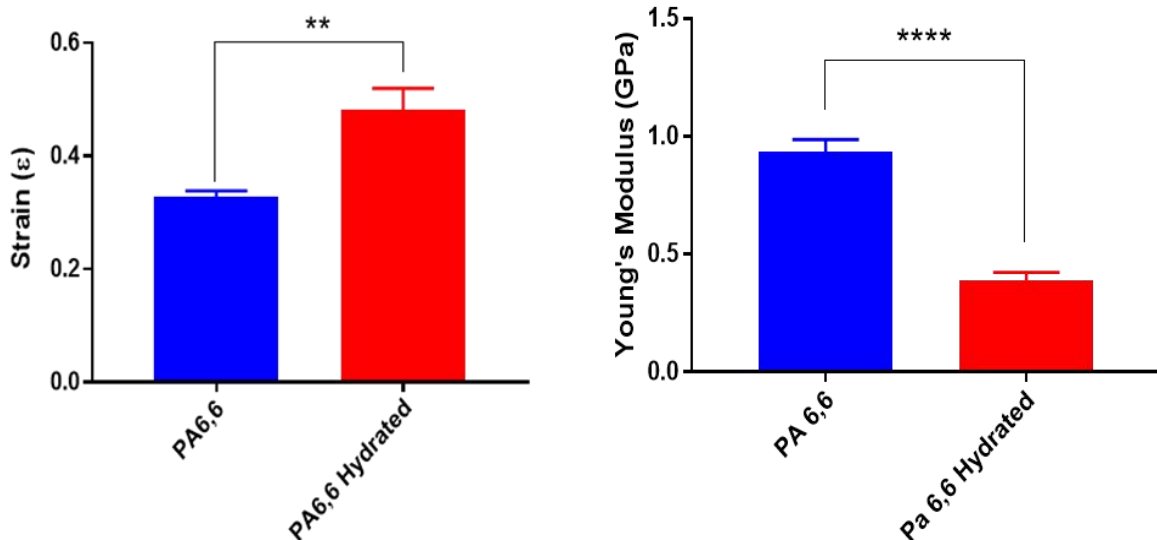
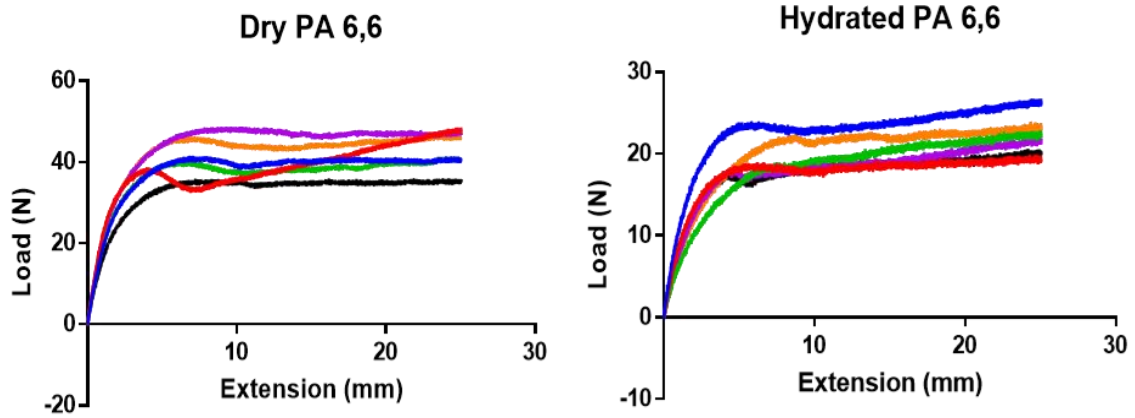
### 3.3.15 Tensile Strength Testing of Polyamide 6,6 Samples

Following the confirmation that the PA6,6 supported cell attachment and Schwann cell alignment, the PA6,6 material was investigated by tensile strength testing to characterise the physical characteristics of the material. Specifically, the elastic behaviour of the material was examined by calculating the Young's modulus and the effect of force on material strain.

Tensile testing revealed that the PA6,6 materials had a high tensile strength in both the dry and hydrated state (Load/Extension graphs, Figure 3.21). Dry PA6,6 could withstand  $33.3 \pm 6.8$  N of load before yielding to stress and extending. The hydrated PA6,6 however was less elastic and markedly less able to withstand the load and yielded at  $18.4 \pm 8.6$  N, however the ductile characteristic was conserved.

Strain,  $\epsilon$ , was calculated from the change in specimen length from the initial specimen length (Figure 3.21). Strain was significantly higher on the PA6,6 hydrated specimens following extension compared to the dry PA6,6 specimens. Strain was 31.74% lower when calculated from dry PA6,6 specimens ( $0.329 \pm 0.010$ ) compared to hydrated specimens ( $0.482 \pm 0.038$ ). This difference between mean  $\epsilon$  was calculated to be statistically significant when compared using an unpaired t-test ( $p=0.0031$ ).

Young's modulus was then calculated from the stress ( $\sigma$ ) and strain ( $\epsilon$ ) values calculated from the extension data. Young's modulus was higher on dry PA6,6 ( $0.936 \pm 0.051$  GPa) compared to the hydrated PA6,6 specimens ( $0.039 \pm 0.003$  GPa). The difference between modulus values was highly significant when calculated using an unpaired t-test ( $p<0.0001$ ).



**Figure 3.21:** Load (N) vs Extension (mm) graphs for both dry state and hydrated state PA6,6 specimens illustrated the ductile properties of the polymer. The extension and load were used to calculate strain (bottom left graph) and then Young's modulus (bottom right graph). The tensile strength testing was performed by stretching PA6,6 samples using grip hooks (central image).

## 3.4 Discussion

### 3.4.1 Cell Culture

In this chapter, the aim of the investigation was to prove a reliable method for culturing cells that can be used to model sprouting axons, developing from the injured nerve's proximal stump (MacKinnon et al., 1991). Multiple methods were used to quantify aspects of cell-material interactions, developing an array of assays able to predict the efficacy of candidate implant materials for use in NGC design.

The results from section 3.3.1 confirmed that inclusion of a high serum content in NG108-15 cell culture promoted cell proliferation significantly, but inhibited neurite outgrowth. In contrast, lowering the serum content in NG108-15 cell culture and including 3-isobutyl-1-methylxanthine promotes neurite outgrowth significantly. Cortical cells were also capable of neurite outgrowth, but to a lesser extent than NG10815 cells. The experiments summarized in Figure 3.5 were used to provide information on cell differentiation and culture protocols, informing later experiments (Chapters 4 and 6). Neural cells were disassociated from their axonal/dendritic networks by trituration (both cortical and NG108-15 cells were trialled) and then the cells were re-plated and neuritogenesis observed and quantified (Figure 3.6; Banker and Cowan, 1977). Cortical cells were not efficiently plated after trituration, shown by the increase in debris seen during brightfield microscopy. Also the large number of ethidium homodimer-1 stained nucleic acid fragments outnumbered the number of live cells, leading to large variation by day 7 and meaning the dead cell number may have been an overestimate (Figure 3.4). Excess cell debris was observed to transfer from the embryonic cortices following tissue trypsinisation and made quantification of cell viability very difficult, using the Live/Dead assay. Cortical cell survival has been correlated with the presence of neurotrophic factors which could not be added to the culture medium, as they may affect neurite outgrowth measurements; as calculated in section 3.3.6 (Facci and Skaper, 2018). Furthermore, the survival of dissociated neurons and limiting glial overgrowth was encouraged by lowering the FCS content to 1% after 24 hours incubation in neurobasal medium with 10% FCS. This has been previously shown to limit neural cell differentiation, axon growth and detection of neuron morphology (Yiu and He, 2006; Piret et al., 2015). However, this treatment did not remove astrocytes completely and astrocytes would have been included in the cell counting and live dead analysis, therefore cortical cultures were not suitable for quantifying

number of neural cells or neural differentiation when comparing substrates (Georges et al, 2006; Hilgenberg and Smith, 2007).

NG108-15 cells, however, clearly showed the advantage that they could be reliably cultured and expanded whilst in 10% FCS media whereas the cortical cell number increased at a far lower rate. This demonstrated the reliability of culturing NG108-15 cells compared to cortical cells. Experiments evaluating the culture method and differentiation protocol (section 3.3.1 and 3.3.3) confirmed that NG108-15 cells were a robust model for use on various culture surfaces and the conditions used to stimulate neurite sprouting coincided with electrophysiological activity, which was recorded (section 3.3.14).

Another advantage for using the NG108-15 cell line was that neuritogenesis could be reliably induced by inclusion of cAMP promoting signalling molecule (IBMX and PGE1). Neurons in this medium demonstrated differentiation by positive MAP2 expression, coinciding with extension of neurites measured up to 7 days in vitro and shown by comparing the use of IBMX and PGE1 in conjunction with lowering the FCS content to low FCS media as evaluated in section 3.3.1 (Tojima et al., 2000). Neuritogenesis could be reliably imaged for quantification using the microtubule, neural specific BIII Tubulin which enabled measurement of neurite length to confirm the differentiation efficiency of the culture at distinct time points (1, 3, 5 and 7 days) shown in section 3.3.3. Importantly, this work correlated with other published work validating the use of BIII tubulin for labelling neurites (Geisert and Franfurter, 1989; Ramli et al., 2018). According to the analysis, the differentiation protocol resulted in more than 80% of cells in the population being differentiated by day 3. As expected, Ki67 expression decreased markedly following application of the differentiation medium as cells exit the cell cycle and Ki67 binds chromosome surface during active phases of the cell cycle (G1, S, G2 and mitosis) (Scholzen and Gerdes, 2000).

Following determination of a reliable method for neural cell quantification, Schwann cell culture and methods for quantification were evaluated in section 3.3.4 and section 3.3.10 as these cells have been proven to be a key modulator of axon outgrowth (Jessen and Mirsky, 2016). Injury to nerve causes the conversion of both myelinating and non-myelinating Schwann cells to de-differentiate and activation of myelin autophagy as Schwann cells form tracks for regenerating axons. Further observation from tracking myelinating Schwann cells in vivo after nerve injury has confirmed that the cells adopt a new phenotype that is up to 7-fold elongated and thus materials that support this phenotype could be interpreted to be conducive in encouraging repair-cell

activity (Gomez-Sanchez et al., 2017). Interestingly an increased Schwann cell length was measured when physical guidance cues were embossed onto PA6,6 (section 3.3.14).

Intracellularly, repair Schwann cells have increased levels of c-Jun, a transcription factor highly expressed in cells that have converted from a myelinating to repair cell phenotype. When c-Jun messaging was inhibited, the result was inhibition of nerve regeneration, as shown by a transgenic mouse model where the gene encoding c-Jun expression was knocked out and resulted in Schwann cells being unable to form regeneration tracks in injured nerve (Arthur-Farraj et al., 2012). Mean Schwann cell area during culture was used to compare the extensions of filopodia and spreading of cell membrane on selected polyamide materials. Cell area could be reliably measured using the Cell Mask plasma membrane stain and confocal microscopy. Alignment of Schwann cells on electrospun substrates has demonstrated that expression of myelin protein zero (P0) was significant in cells cultured on a 3D surface compared to cells cultured on flat tissue culture surface (Chew et al., 2007). This confirms that Schwann cells respond differently, depending on the 3D structure of the culture surface. This can ultimately lead to Schwann cells with a repair phenotype and provide a template to regenerating axons thus morphology of the cells was an important variable to measure (Miller et al., 2001). Other investigations have also confirmed that Schwann cells are capable of aligning along micro-patterned grooves dependent on groove width between 10-20 $\mu\text{m}$  independent of groove depth (Schmalenburg and Urich, 2004; Hsu et al., 2005). This was further proven on filaments when both neurite outgrowth and Schwann cell migration was significantly decreased on larger fibres of 200 $\mu\text{m}$  compared to 5 $\mu\text{m}$ , suggesting that the lower order of dimension provides beneficial effects. This was confirmed in this study when 10 $\mu\text{m}$  grooves were embossed onto the PA6,6 sheet and Schwann cell alignment was measured within the interquartile range of 22.6° meaning that the majority of cells aligned within this range (Figure 3.20). This is highly relevant as the effect of microgrooves has been studied extensively in vitro but studying the effect in vivo has not confirmed whether microgroove presence provides a significant spatial cue to Schwann cells to self-organise into bands of Büngner faster and thus leading to faster functional recovery. 3D scaffold structures may enhance Schwann cell maturation and lead to a quantifiable increase in nerve regeneration (Chew et al, 2007).



### 3.4.2 Materials Tested

Initially, an array of materials was selected to validate the static culture technique used to evaluate adhesive cells on 3D culture topography (section 3.3.5). Linen, Cotton, Silk, Polyester, Silicon, Vicryl and Nylon have all been used as biocompatible materials in medical applications (often as suture materials for instance) and were available as 3D culture surfaces for optimising a micro-seeding technique adapted for this study (Tajirian and Goldberg, 2010).

Cells were cultured for 72 hours on each material (section 3.3.3). To ensure that only adherent cells were analysed, the material was removed from the growth medium and suspended into a new well containing differentiation media, leaving non-adherent cells behind. As the materials varied in fibre diameter, cell density was identified as a fair comparison of cell adherence to the materials, so data was normalised for image area analysed. This was achieved by measuring the surface area of the fibres present in the field of view per image and dividing by the number of cells counted on the fibres.

Polymeric materials were more biocompatible compared to natural material sutures (e.g. nylon and vicryl rather than silk), confirmed by Live/Dead data. The materials were selected because they are pliable, easy to handle and generally accepted for implant uses by clinicians but would be used in a different format when constructing the final NGC (Pillai and Sharma 2010). Further, the use of highly biocompatible material fibres with narrow diameters (30-40  $\mu\text{m}$  as confirmed by brightfield microscopy) can be woven into a NGC as shown with poly-d-lactide conduits. They were implanted into injured digital nerves of patients ranging 4 to 25mm in gap length achieving regeneration in some patients (Rinker and Liao, 2011; Yang et al., 2015). Calculating cell density (number of cells per  $\mu\text{m}^2$ ) allowed adequate comparison amongst material groups. However, measuring the total surface area available and using confocal microscopy to capture a z-stack of images covering the full diameter of the fibre and dividing this surface area by the number of cells counted could have provided a more precise comparison of cell density.

Therefore, when evaluating adherent cells on the polyamide samples, confocal microscopy was used to produce z-stacks and capture all adherent cells on the surface of the sample. Nevertheless, significant differences in the cell density were calculated. Both Nylon and Vicryl Rapide demonstrated cell-adhesive properties. Although there were adherent cells on Vicryl, the cells were spherical and less closely associated to the fibres when compared to the tapered cell

bodies observed on Nylon. Also, a lower cell viability was calculated on Vicryl compared to the other materials tests (statistically insignificant). This experiment confirmed that the cell adhesive property of the nylon material (PA6,6) warranted further investigation. It has been shown to provide an anisotropic cue to extending neurites in vitro in previous studies (Bellamkona, 2006; Yoo et al., 2011).

### 3.4.3 Polyamides

Additional formats of PA6,6 were investigated to confirm that the material supports cell adhesion, regardless of the 3D topography. PA6,6 was then evaluated, compared to other polyamides, with the same cells to objectively confirm this effect. Polyamide is an interesting material to propose for use in peripheral nerve regeneration and has been cited in the literature as being used for orbital floor reconstruction, sutures in nerve ligation, implantation of endometrial mesenchymal stem cells and indicated for use in neural tissue engineering (Ulrich et al., 2013; Timoney et al., 2014; Grob et al., 2019; Terashima et al., 2019). The advantages of polyamide include that it can be thermoset, showing biocompatibility, it isn't cytotoxic and is available in many formats including flat sheets (from 0.025mm), rods, nanofibres, meshes and nanoparticles (Canal et al., 2004; Gruber et al., 2009; Ulrich et al., 2013).

The aim addressed by these experiments was to identify a suitable material to be used as an outer layer material for the proposed nerve guidance conduit device. As such, the material must be flexible, easily handled, non-toxic and biocompatible as a minimum standard with emphasis placed on the luminal environment being in direct contact with regenerating stumps as seen in histological samples of nerve repair using silicon conduits (Frost et al., 2018).

The same Live/Dead protocol evaluated on the suture materials was used to further evaluate the biocompatibility of the PA6,6 mesh for both NG108-15 and Schwann cells. This confirmed that there was no significant difference in the biocompatibility of the mesh compared to tissue culture plastic (control). Further, NG10815 cells were able to proliferate on the mesh and Schwann cell number stayed constant between 3 and 7 days in culture suggesting that confluence had been reached by the 3 day time point which was comparable to Schwann cells on the control material. PA6,6 was confirmed to not be cytotoxic by Alamar Blue assay, as cell proliferation was not inhibited (not the case for either cell type).

Schwann cell morphology was also an important variable to measure as it was hypothesised that strong material interactions correlated with the proliferation data determined by Alamar Blue assay. Protrusions of the cell membrane can also indicate that the surfaces encourage cell motility and the material could be translated into the NGC because cells are able to spread on the surface which is necessary for proliferation (Chen et al., 2013).

Additionally, electrophysiology was used as a tool to determine that neural excitability had not been significantly altered when cultured on PA6,6. Cell excitability correlated with cell differentiation, measured by calculating the total number of neurites. By 4-7 days in differentiation medium, cells reliably demonstrated transmission of action potentials in response to the 10pA stimulus. This result was also confirmed in cells that were cultured on PA6,6 at the same time point. However, non-differentiated cells did not exhibit action potentials, which compares well to previously published work where NG108-15 cells that were differentiated up to 21 days could produce bursts of action potentials when stimulated for 1s at 100pA (Liu et al., 2012). This demonstrates that protein level expression of voltage gated sodium channels had occurred and it can therefore be inferred that they had already been inserted into the cell membrane by 4 days. These proteins are primarily responsible for membrane excitability (Grubb and Burrone, 2010).

Electrophysiology signatures have been compared amongst neural cells cultured on biomaterials. Further investigation was outside the scope of the project. We conclude that further experiments can reliably use the NG108-15 cell line as single action potentials can be evoked and compared for their maximal voltage (as plotted in this study). Variations in the action potential widths provides more detailed information about spontaneous or elicited activity of neuron populations (George et al., 2019). This may be regulated by plasticity mechanisms and could play a role in the organisation of neural circuit regeneration and excitability, following tissue regeneration (Wislet-Gendebien et al., 2005; Cellot et al., 2008; Zhang et al., 2018). However, the latter is the focus of this research.

#### 3.4.4 Neural Differentiation

After confirming that cells could produce ionic currents that were coordinated into an action potential by 4-7 days of differentiation, the time points for evaluating neural differentiation morphometrically was confirmed.

The 3 and 7 day time points were chosen as an early and late differentiation time point respectively based on observations during optimisation of immunocytochemistry for neural cell differentiation markers (Figure 3.9). Neurites were measured up to 7 days in differentiation medium but did not significantly increase in length 3 and 7 days in vitro. Mapping of neurites using the neurite tracer tool provided a consistent, reliable and objective measure of neurites due to using the semi-automated program Neuron J and was comparable to other studies (Longair et al., 2011; Figure 3.2). Neurites were identified as an important measure when comparing materials for applications in nerve regeneration as it serves as a comparable quantifiable variable to other in vitro studies and in vivo studies (Thompson and Buettner, 2006; Daud et al., 2012; Frost et al., 2019). The NG108-15 cell line was an objective model for assessing the interaction between materials and neurite outgrowth, although other models are available. The PC12 cell line models sensory neurons and has been shown to increase neurite outgrowth on stimulation with pharmacological cues (Terada et al., 2018; Zhao et al., 2019). However, NG108-15 cells have been shown to be cholinergic and synapse with myocytes in vitro and could be compared to future in vivo results assessing behaviour where muscle re-innervation is vital to functional recovery (Higashida and Ogura, 1990; Whitmarsh et al., 2012). The percentage of neurite bearing cells gives an overview of differentiation within the population of cells and could be compared between polyamide culture substrates (Figure 3.18).

Quantifying the percentage of cells bearing neurites revealed that although the percentage of cells remains fairly constant between 3 and 7 days at a population level, single cells can lose their average number of neurites, according to the culture surface. Thus, surface properties have been shown to exert a significant effect on phenotype. PA substrates can permit both the adherence of neuron cells and neurite growth although PA6, PA6,6 and PA4,6 enhanced neural differentiation to differing degrees. PA12 did not support neural differentiation as evidenced by a lack of neurites (Figure 3.18). Additionally, axon outgrowth rather than neurite outgrowth could have provided a clearer measurement of how well axons would extend and path-find when cultured on polyamide. This may provide a better model as these materials were assessed for translation to in vivo models of nerve repair (Isaacman-Beck, 2015; Dun et al., 2019).

These results confirmed quantitatively that the choice of polyamide material can affect the number of adherent cells following implantation and that both NG108-15 and Schwann cells were able to proliferate to an extent on all materials (section 3.3.12). As PA was found to be a suitable

material for the outer layer of the proposed NGC, the cell line provided adequate data for assessing the material as an implant in vivo however dorsal root ganglion organotypic cultures have been used to assess axon extension and was later used for finding a suitable 3D culture environment within the lumen of the NGC (Dubovy et al., 2019; Roselló-Busquets et al., 2019; section 4.3.15).

### 3.4.5 Material Properties

Polyamides were assessed to confirm the chemical properties of the materials and evaluate how surface chemistry (assessed by FTIR in section 4.3.8), thermal processing (assessed by DSC in section 3.3.9) and elastic properties (assessed by tensile testing in section 3.3.15) could be beneficial for the application in a NGC.

FTIR confirmed the presence of functional groups common to polyamides including alkyl chains and amide linkage. Although PA6,6 was not expected to mimic the ECM, some functional groups available include the amine group capable of hydrogen bonding to polar moieties present in the hydrophilic cell membrane. Although the interaction between cells and biomaterials is not fully understood, the surface chemistry (and intermolecular forces present) of the PA6,6 was conducive to cell membrane adherence (Deopura et al., 2008; Shrestha et al., 2016). The material could be further functionalised to enhance the cell adherence properties with peptides such as RGD or Laminin, however the polyamide and polycaprolactone are both related materials and the latter has already shown to be conducive to NG108-15 and Schwann cell culture (Santiago et al., 2006; Kijeńska et al., 2014; Qian et al., 2018). The advantage of polyamide being non-resorbable however, is that it continuously provides a surface on which cells can continue to form a tissue bridge between the proximal and distal stumps. Silicone NGCs, which are non-resorbable, were the first generation of synthetic NGCs and were compared to autografts but discounted due to possible constrictive pressure on the regenerating nerve tissue. However, this effect could be overcome if the wall is flexible and does not warrant decreased research on non-resorbable NGC options (Deal et al., 2012; Gerth et al., 2015; Xie et al., 2015; Ezra et al., 2016).

PA6,6 was shown to be highly ductile when pulled in tensile mode using the Instron testing apparatus, extending at a linear rate under a minimum tensile stress of  $18.4 \pm 8.6$  N when hydrated (shown in section 3.3.15). The yielding and extension at this magnitude of force would not be expected to occur within the Rat Sciatic nerve in vivo model as Young's modulus of

acellular Rat sciatic nerve was previously measured at approximately 550 kPa, where the polyamide NGC was intended for further testing (Borschel et al., 2003). However, the ductile property of the material is important, as it ensures that fracture of the device during prototyping would not occur even when hydrated, given the withstanding of tensile tests. Additionally, the melting temperature was determined by DSC to optimise the embossing technique to produce microgrooves. This data helped to devise a strategy to develop features on the luminal surface of the NGC, employing temperatures just below the  $T_m$  to cast the conduit shape as PA is thermoplastic, the mould being based on lithography techniques using a poly(dimethylsiloxane) material (section 3.3.14).

Given all the data presented in this chapter, PA6,6 material was selected as a suitable material for use in prototyping a NGC for use in vivo, when repairing a nerve gap injury in the Rat Sciatic nerve repair model. The advantages of this material discussed allowed a novel design for sutureless NGCs to be investigated as outlined in Chapter 1 and evaluated in vivo in Chapter 5.

## Chapter 4: Evaluation of a Neural-Supportive Hydrogel System as a NGC Filler Material

### 4.1 Introduction

Following the tissue loss in a peripheral nerve injury, it is vital that axons can extend across the injury site, to restore function (reviewed in Chapter 1, Section 1.2). If there is sustained Wallerian degeneration, the probability that function of the injured nerve will be restored decreases as post-injury time increases (Gerth, 2015). Therefore, providing an optimised 3D microenvironment for axon extension is a key aim in regenerative therapies that intend to treat peripheral nerve damage in a timely fashion (Aurand et al., 2012).

Strategies to enhance functional repair include use of hydrogels as they can be selected for their cell-supportive structure and function to direct cell extension or proliferation leading to migration across the fibrin tissue bridged formed during Wallerian degeneration (Valentini, 1999; Jiang et al., 2010). Additionally, hydrogel materials can be designed to degrade after regeneration is complete or can be modified to include cell-adhesive protein domains to aid regeneration (Farrukh et al., 2017; Chen and Zou, 2019). Natural hydrogels are non-toxic and have been shown to be supportive to neural cell expansion (Aurand et al., 2012). Hydrogels can serve as either a Schwann cell delivery device into a defined region (including growth factors or vectors) or used as scaffolds for cell infiltration once implanted in vivo (Wells et al., 1997; Valderrama-Treviño et al., 2019).

Biopolymers are versatile materials in both composition and method of formation, making them suitable for optimising as neural tissue implants and their viscoelastic properties are amenable to host cells (Zhang et al., 2016). The variety of literature published arguing for the use of various systems in this application makes it difficult to compare polymer systems to find the most suitable for modelling neural cell growth in vitro (Gil et al., 2012). Therefore, candidate natural hydrogels were compared during selection for use in an NGC. Crucially, the selected hydrogel for use in the NGC had to support expansion and self-organisation of Schwann cells into mock Bands of Büngner given their pro-regenerative phenotype (as discussed in Chapter 3).

Further, natural hydrogels were chosen, rather than synthetic, because they have been shown to closely mimic the ECM, whilst maintaining control of the stiffness and degradation of the scaffold (Leipzig and Shoichet, 2009). Of note fibrin produced as an exogenous material was not investigated, due to the fast resorption when implanted as a NGC filler in long gap injuries

(Malafaya et al., 2007). To increase the speed of neural regeneration whilst mimicking the fibrin tissue bridge, peripheral nerve regeneration experiments using NGCs filled with hydrogel have been studied with matrices made from collagen, chitosan, and alginate for example (Hashimoto et al., 2002; Lin et al., 2008; Zhu et al., 2010; Kehoe et al., 2012; Gerth et al., 2015).

Commonly discussed in these studies is the ineffective level of sensory or motor feedback in the rat sciatic nerve transection and repair model when compared to the autograft. New material composites could offer improved or possibly optimal repair results (reviewed in Chapter 1, Section 1.5). Hydrogels can be blended to provide interpenetrating networks which may offer advantages over the constituent systems and could expedite recovery (Mosahebi et al., 2001; Mosahebi et al., 2003). The same in vitro model of nerve repair used to confirm the suitability of polyamide for the NGC application was used to compare hydrogels, as baseline data on biocompatibility, proliferation and extension of NG108-15 and Schwann cells was useful in identifying the hydrogel environments that were objectively more supportive of the model cells (see Chapter 3, Section 3.3.5 and Figure 3.12).

The use of hydrogels as opposed to other luminal fillers such as oriented fibres is debated within the literature (Daud et al., 2012; Ezra et al., 2016). Hydrogels were investigated in this study as they have been rarely compared, to prove the benefit of one natural polymer over another when used as materials for NGCs (Wells et al., 1997). The aim of the work in this chapter was to investigate whether a specific hydrogel could be used to formulate a filled NGC. We further tested the hypothesis that inclusion of hydrogels in NGCs provides both stability and improved results attracting infiltrating cells when implanted. Both NG108-15 and Schwann cell viability, phenotype and extension were quantified, as well as the mechanical properties of the materials, which was characterised in anticipation of use in the in vivo rat sciatic nerve transection and repair model (Chapter 5).



## 4.2 Materials and Methods

### 4.2.1 Cell Culture

NG108-15 and Schwann cells were cultured using the same protocol as described in Chapter 3 (see sections 3.2.1 and 3.2.2 respectively). Cells were cultured for up to 14 days in vitro depending on the experimental endpoint and all experiments were performed using 24-well culture plates made of culture grade polystyrene under aseptic conditions. For monoculture,  $2.5 \times 10^4$  cells per ml were cultured. For co-cultures,  $1.25 \times 10^4$  cells per ml of each cell type were cultured unless stated otherwise.

### 4.2.2 Hydrogel Preparation

Bovine Collagen Type 1 solution (2mg/ml in 2% First Link Ltd., UK) was diluted with growth media in a 1:1 v/v solution, and then 8% w/v 1M NaOH was added to neutralise the solution (indicated by the colour change from yellow to pink) to cause gelation by self-assembly of collagen fibrils on ice. The solution was pipetted into wells and incubated for 24 hours to form the collagen gels (Burkel et al., 2016).

For chitosan hydrogels, chitosan ( $M_w$  60,000-120,000; Sigma-Aldrich, UK) was dissolved in 2% acetic acid (pH = 4) on a rotating shaker over 24 hours on ice. The chitosan was diluted into growth media in a 1:1 v/v solution and then 8% (w/v) 1M NaOH was added for gelation, which occurred over 24 hours in a 37°C incubator.

Methylcellulose ( $M_w$  40,000; Sigma-Aldrich, UK) was dissolved in sterile deionised water on a rotating shaker for 24 hours, and gelation occurred when sterile 10% (w/v) 10x Phosphate Buffered Saline (PBS) was added, which stiffened to form a semi-gelatinous viscous material when incubated at 37°C.

Sodium Alginate (Sigma-Aldrich, UK) was dissolved in sterile deionised water. Then the solution was cross-linked by adding 8% of 1M calcium chloride solution.

Hyaluronic Acid (laboratory grade hyaluronic acid sodium salt from *Streptococcus zooepidemicus*, Sigma-Aldrich, UK) was dissolved in 2% acetic acid (pH = 4) at a 1mg/ml concentration for 24 hours on a rotating shaker.

All hydrogels were then incubated for 24 hours with excess growth media before cell culture.

Abbreviations used are as follows:

- COL – Collagen Type 1
- CS – Chitosan
- AGN – Sodium Alginate
- MCL – Methylcellulose

Where percentages are given, e.g. COL 1% indicates the w/v % weight fraction of solute used.

#### 4.2.3 Chitosan-Collagen Blend Preparation

Chitosan and Collagen (CS-COL) blends were produced after validation of biocompatibility. The blends were produced, on ice, by mixing 1% chitosan and 1% collagen, both dissolved in 2% acetic acid in a 1:1 or 1:2 v/v ratio, after which 12.5% (v/v) Schwann Cell media containing 10% (v/v) 1M NaOH was added and the mixture vortexed. Then, 8% 1M NaOH was added which was enough to neutralise the acid shown by a colour change from yellow to pink and self-assembly gelation was allowed to occur over 24 hours at 37°C. Abbreviations for the CS-COL blends were CC (1:1) and CC2 (1:2) respectively (Kaczmarek and Sionkowska, 2017).

#### 4.2.4 Attenuated Total Reflection Fourier-Transform Infrared Spectroscopy (ATR-FTIR)

Dehydrating 1ml of hydrogel by air-drying at 60°C in an incubator for 48 hours produced anhydrous samples. The anhydrous material was collected and 50mg was measured. The sample was placed over the germanium crystal on the FTIR spectrometer (Perkin Elmer, Massachusetts, US) and transmission spectra measured between wavelengths of 600 and 4000  $\text{cm}^{-1}$ . The spectra were collected as described in Chapter 4 (section 4.2.11).

#### 4.2.5 Dynamic Scanning Calorimetry (DSC)

As described in Chapter 4 (section 4.2.12), the Jade DSC machine (Perkin Elmer, US) equipped with Pyris™ software (Perkin Elmer, US) was used to investigate the thermograms. 20mg of air-dried hydrogel samples (dried at 60°C for 48 hours) was collected and placed in the sample pan and compared against a reference pan containing air only. The temperature was held at -10°C for 5 minutes, increased to 100°C, decreased to -10°C and then increased to 260°C at a rate of 10°C per minute to ensure that all the water had been evaporated before analysing the heat flow of the anhydrous polymers.

#### 4.2.6 Atomic Force Microscopy

The Asylum MFP-3D AFM instrument was used for nano-indentation tests to confirm the elastic modulus of hydrogels sampled from force curve measurements. All force curve measurements were performed on an Asylum Research MFP-3d AFM (Oxford Instruments, UK). Probes used had a 3.6  $\mu\text{m}$  Polystyrene colloidal sphere mounted on one end, with a force constant of 0.01 N/m. Before each experiment the inverse optical lever sensitivity (Invols) were calibrated by collecting a force curve on a hard surface, and the spring constant was determined using the built-in function on the AFM software, GetReal (Oxford Instruments, UK). This software uses the thermal noise spectrum and the Sader method to calibrate the spring constant of the cantilever.

Once the probe was approached on the surface force maps consisting of 8 x 8 (n=64) data points were collected over a 90  $\mu\text{m}$  square. The resulting force curves were fitted using the hertz model, with the modulus of the probe of 3 GPa.

#### 4.2.7 Scanning Electron Microscopy (SEM)

Samples of hydrogel were lyophilised using a VirTis 4KBTZL Benchtop Freeze Drier for 24 hours. SEM was performed on lyophilised hydrogel samples were placed on aluminium stubs using conductive blue tape before being sputter-coated with a thin layer of gold and being placed in a vacuum within a Quanta field emission scanning electron microscope (FEI Quanta 200F) using 10-20kV at 10,000X magnification.

#### 4.2.8 MTT Assay

MTT Assay was conducted using 5mg/ml tetrazolium MTT (3-(4,5-dimethylthiazolyl-2)-2,5-diphenyltetrazolium bromide) solubilized in PBS, and then further diluted in ascorbic acid free growth media to a final concentration of 0.167mg/ml to make MTT Solution (MTS) (van Tonder et al., 2015). MTT assay was carried out in a 96-well plate containing 100 $\mu\text{l}$  of hydrogel sample. Cells were cultured on the test hydrogel at a concentration of  $4.0 \times 10^3$  cells per well and allowed to attach and proliferate for an incubation period of 3 or 7 days. The media was aspirated and 100 $\mu\text{l}$  of MTS was applied to each sample and incubated for 4 hours. The plate included a negative control, where no hydrogel was present. A positive control where the hydrogel and cells were incubated in 20% (v/v) ethanol in the media resulting in cell death was also included.

After the incubation time, the MTS had crystalized to precipitate Formazide crystals. The excess MTS was aspirated and 100µl of dimethylsulfoxide (DMSO) was applied to dissolve the crystals by disrupting the plasma membrane. The crystals were solubilised by shaking on an orbital shaker and the well plate inserted into a Dynex Opsys MR microplate reader (Aspect Scientific, Cheshire, UK). 15 replicate wells were used for each group tested and the experiment repeated in triplicate. Absorbance was measured by the plate reader and calculated automatically using the excitation wavelength of 570nm against a reference of 620 nm.

#### 4.2.9 Alamar Blue Assay

Alamar Blue assay was used as a colorimetric assay to monitor cell concentration as a function of time as previously used in Chapter 3 (section 3.2.6).

#### 4.2.10 Live/ Dead Analysis

The Live/Dead staining was used in the same way as in Chapter 3 (section 3.2.5) to assess cell viability. The hydrogels were produced in 24 well plates and cells were cultured on the gels for up to 7 days. Calcein AM and Ethidium Homodimer-1 were used as before to label live and dead cells respectively, and viability was calculated as the percentage of live cells in the population. Images were obtained by epifluorescence widefield microscopy. Excitation/ Emission wavelengths for Calcein AM and Ethidium Homodimer-1 were 494/417 nm and 528/617 nm respectively.

#### 4.2.11 Immunocytochemical Analysis

Samples were fixed in 4% paraformaldehyde solution for 5 minutes at 4°C. Samples were then permeabilised in ice-cold 95% methanol in phosphate buffered saline (PBS, pH 7.4) for 10 minutes on-ice. Samples were then incubated with the primary antibody ( $\beta$ -III tubulin Alexa Fluor 488, S100 or MAP2) as detailed in Chapter 3 (section 3.2.8). After washing with PBS, cells were counterstained with nuclear Hoechst 33342 at a concentration of 1:100,000 in PBS for 5 minutes and rinsed with PBS. Samples were imaged immediately using the spinning disc confocal microscope (Nikon Instruments, UK).

#### 4.2.12 Schwann Cell Conditioned Media Experiment

Schwann cells were cultured for 3 days in growth media and passaged, splitting in a 1:5 ratio, into 5ml of media per 75cm<sup>3</sup> flask. The media was then collected and used neat (100% conditioned media) or diluted into 1% FCS NG108-15 Differentiation Media (50% conditioned media) and cultured in 1% FCS NG108-15 Differentiation Media as a control (as in section). The media was sterile filtered using a 0.22µm filter (Invitrogen, UK) before use in culture. Cells were cultured for up to 7 days and imaged at 1, 3 and 7 days.

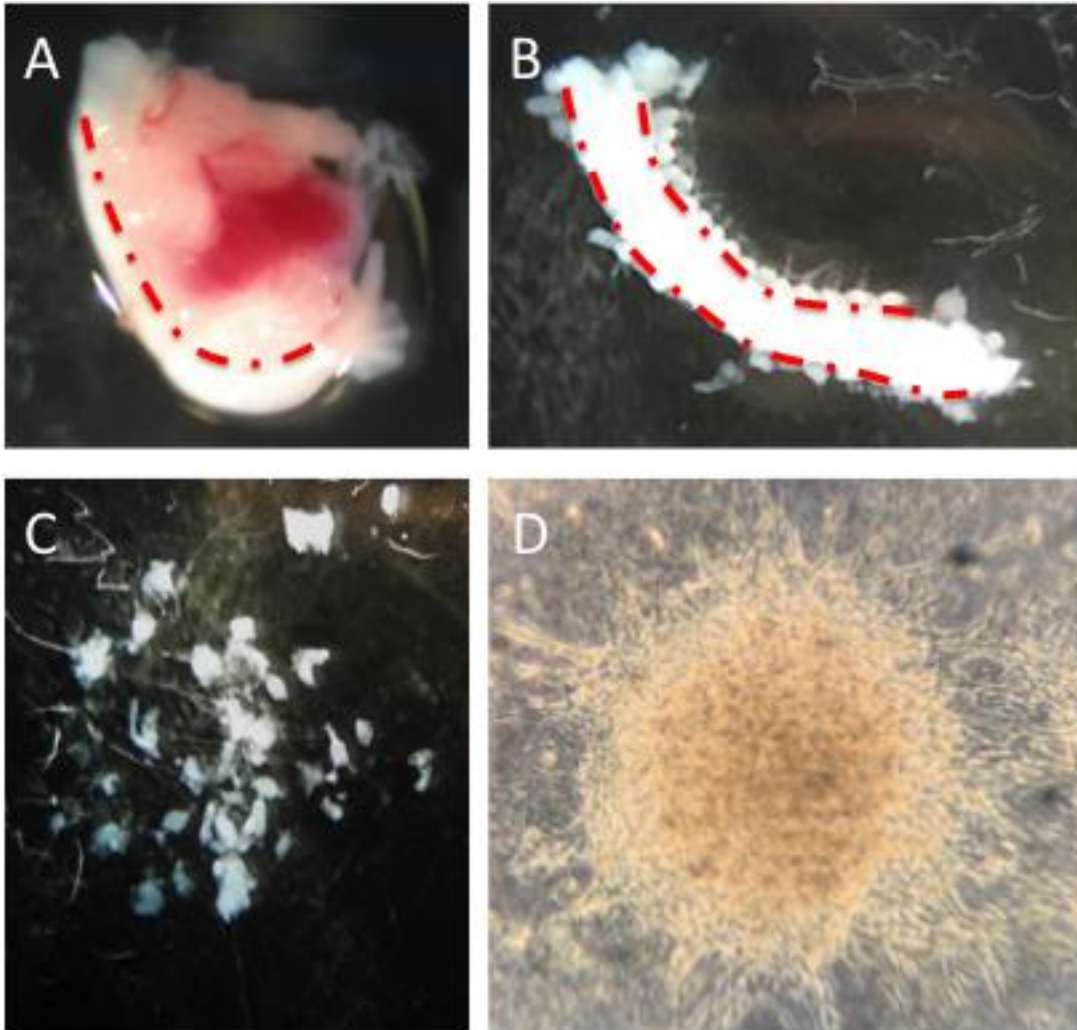
#### 4.2.13 NG108-15/Schwann Cell Co-Culture Experiments

NG108-15 and Schwann cells were co-cultured on CTRL (tissue culture plastic), CS, CC, CC2 and COL in either equal numbers (1:1) or the Schwann cell population was doubled in comparison to the number of NG108-15 cells (1:2). This was carried out to assess the ability for materials to support neuroglial interactions. As a control, to ensure that Schwann cells were not altering the surface properties of the hydrogel to expedite neurite outgrowth, Schwann cells were also removed prior to plating NG108-15 cells. Growing Schwann cells on the surfaces for 3 days prior to the co-culture seeding allowed controlling for loss of direct contact between Schwann cells and NG108-15 cells.

Schwann cells were removed by applying surfactant (1% Triton X-100, Sigma Aldrich, UK) for 5 minutes and then washing three times in PBS. The cultures were then grown for 3 days in Schwann cell media (not NG108-15 differentiation media) with a low FCS content (1%) (Jonsson et al., 2013). The growth media was not expected to cause NG108-15 cell differentiation ensuring that only the effect of the co-culture within that material environment affects neurite outgrowth.

#### 4.2.14 DRG Explant Study

The vertebral columns from embryonic day E15.5 CD1 mouse pups were dissected to isolate and retrieve Dorsal Root Ganglia (DRGs) (see Figure 4.1). These were plated on hydrogels and cultured for 10 day in vitro in Neurobasal medium (Sigma-Aldrich, UK) containing 20µl/ml B27 supplement (Thermo Fisher Scientific, UK), 2mM Glutamax (Thermo Fisher Scientific, UK), 10,000 units/ml penicillin, 10 mg/ml streptomycin (Sigma-Aldrich, UK) and 10% FCS. Media was half-exchanged every 2 days and then explants were fixed with 4% paraformaldehyde for immunocytochemistry (section 4.2.11).



**Figure 4.1:** Images to illustrate DRG dissection. The vertebrae were exposed from the corpus (A). Then the spinal cord was exposed with DRGs attached (B). Single DRGs were dissected from the spinal cord using forceps and collected (C). DRGs were cultured for 10 days and neurite outgrowth (black arrow heads) quantified (D).

#### 4.2.15 Cell Migration Study

Schwann cells were cultured on hydrogels that had been set in 24-well plates. The cells were then imaged using a widefield Eclipse Ti-2 inverted microscope (Nikon Instruments, UK) with DS-Qi2 sCMOS camera attached in brightfield mode with a 20X objective. Regions of Interest (ROIs) were selected using the automatic stage, and these ROIs were imaged every 30 minutes for 24 hours. The environment during imaging was maintained at 37°C with 5.0% CO<sub>2</sub> using an Oko-Lab chamber. Using the Perfect Focus System equipped on the Ti2 microscope, focal drift compensation was provided to ensure the maintenance of the focal plane between time points.

#### 4.2.16 Gliospheroid Culture

Schwann cells were cultured into a spheroid by plating 100µl of 1% agarose gel in 94-well plates.  $4.0 \times 10^3$  Schwann cells were cultured on the agarose gel for 24 hours, in growth media. The resultant sphere of cells was termed a 'gliospheroid' and could be reliably collected from the gel using a modified P-1000 Gilson pipette tip, with a diameter approximately 50% of the well. The gliospheroids were then cultured within hydrogels by initiating gelation of the hydrogel solution (by neutralisation with NaOH) 2 hours prior to placement of the gliospheroid. Once plated, the gliospheroids were incubated for 1 hour and then the culture medium was added. Only gliospheroids suspended in the gel were quantified for outgrowth.

#### 4.2.17 Image Analysis (Morphological Characterisation)

Well plates were imaged using inverted epifluorescence microscopy and images were taken using CellSens software (Olympus Scientific Solutions, US). The objective used was 20X and three images were taken randomly with at least 4 wells prepared of each material per experiment, this was repeated in triplicate experiments. Fluorescence images were analysed using Fiji software, and Image Science plugin used for analysis.

#### 4.2.18 Statistics

Measurements taken from image analysis were tabulated and means were compared by ANOVA with bonferroni correction post-hoc tests, which were performed using GraphPad Prism (GraphPad Inc.) software. This test was chosen after establishing the data was normally distributed by the three sigma test and the correction applied as a more stringent test for

significance due to multiple comparisons being carried out. For statistical significance an alpha value of 0.95 was used. For all graphs, the error bars indicate standard error of the mean (SEM). Experiments were performed in triplicate with at least three technical repeats per experiment. Significance between values is indicated on graphs in figures as follows: \* $p < 0.05$ , \*\* $p < 0.01$ , \*\*\* $p < 0.001$ , \*\*\*\* $p < 0.0001$ .



## 4.3 Results

### 4.3.1 Evaluating the effect of Increasing Hydrogel Concentration on Cytotoxicity

MTT assay was used to assess the cytotoxicity of the biocompatible gels at increasing concentrations. These results were compared with a negative control surface (tissue culture plastic) and a positive control (tissue culture plastic with ethanol included in the media) to quantify the upper and lower limits of absorbance levels (at 570/620nm). Higher absorbance levels indicated higher levels of metabolic activity indirectly, and therefore increased numbers of healthy cells.

For COL (Bovine Collagen Type 1), the highest absorbance levels were recorded on the higher concentration (COL 1.0%) at both 3 and 7 days in culture (Figure 4.2). At day 7, COL 1.0% absorbance ( $0.291 \pm 0.004$ ) was 37.1% higher than COL 0.5% ( $0.183 \pm 0.007$ ) which was calculated to be significant when compared by two way ANOVA ( $p < 0.0001$ ).

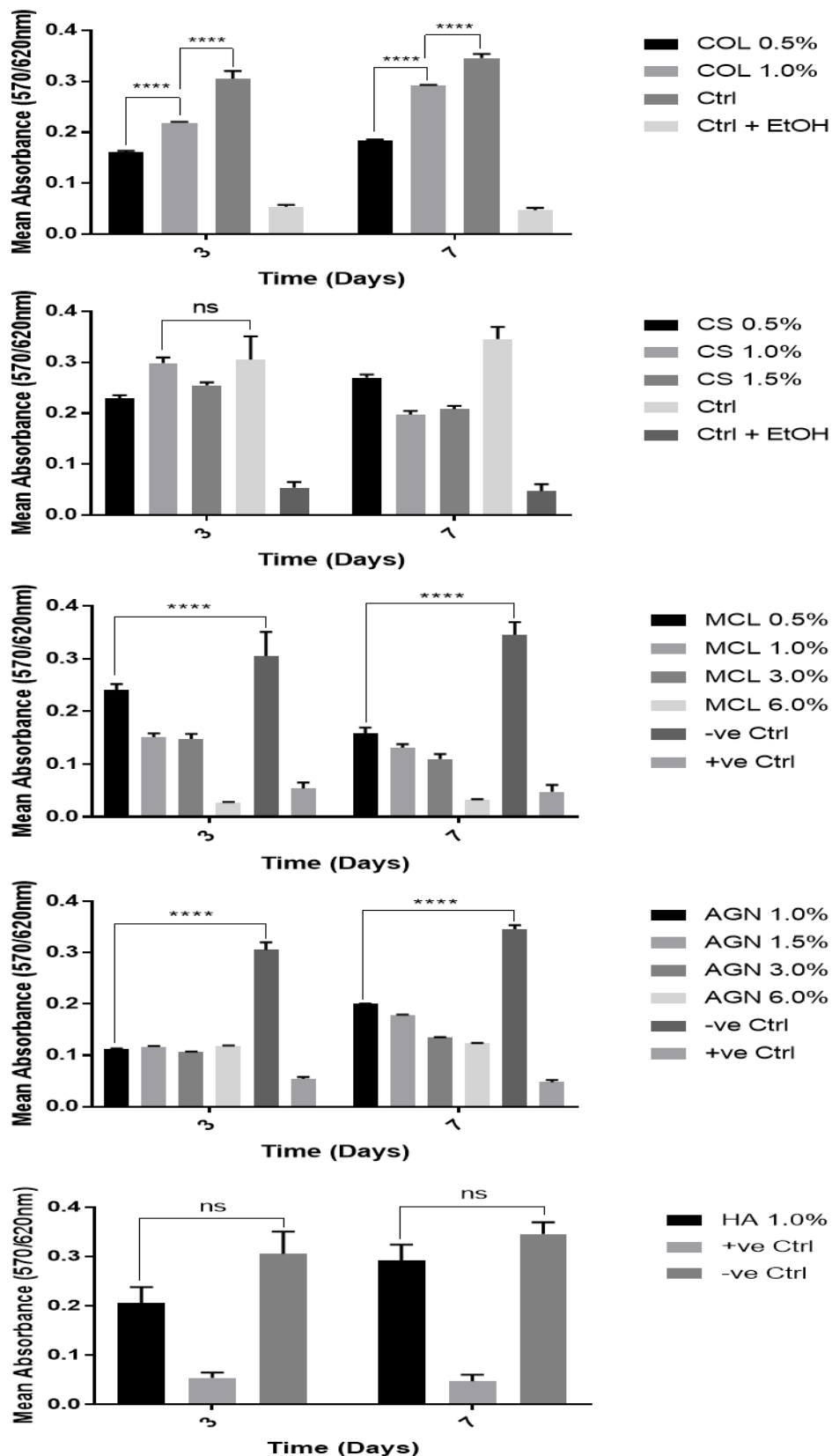
For Chitosan, the lowest concentration CS 0.5% resulted in high absorbance levels at day 3, comparable to the control condition. For the range of concentrations tested, all hydrogels maintained a high level of cell activity with CS 0.5% increasing to  $0.270 \pm 0.016$ , but the higher concentrations of CS 1.0% and CS 1.5% decreased to  $0.198 \pm 0.017$  and  $0.209 \pm 0.014$  respectively.

Testing NG108-15 cell metabolic activity on the Methylcellulose hydrogel confirmed that although cells were present at day 3 on MCL 0.5% ( $0.242 \pm 0.026$ ), MCL 1.0% ( $0.152 \pm 0.016$ ) and MCL 3.0% ( $0.028 \pm 0.002$ ), the absorbance decreased by 7 days in culture to  $0.159 \pm 0.026$ ,  $0.132 \pm 0.016$  and  $0.033 \pm 0.002$  respectively. These decreases were statistically significant for the change in absorbance for MCL 0.5% ( $p < 0.0001$ ) and MCL 3.0% ( $p = 0.0349$ ). The values for MCL 0.5%, which demonstrated the highest metabolic activity amongst MCL samples, was significantly lower than the CTRL values at both days 3 ( $0.305 \pm 0.045$ ) and day 7 ( $0.346 \pm 0.023$ ) – which was also significantly different ( $p < 0.0001$ ). Finally, for the 6% concentration gel, the mean absorbance remained low throughout the incubation period culminating at an absorbance of  $0.0328 \pm 0.002$  at day 7.

Sodium Alginate hydrogels clearly did not support cell metabolic functions as well as the control at both time points. At day 3, the control ( $0.305 \pm 0.043$ ) was 62.9% higher than AGN 1.0% ( $0.113 \pm 0.002$ ). At day 7, the control ( $0.346 \pm 0.024$ ) was 41.3% higher than AGN1.0% ( $0.203 \pm 0.003$ ),

which was the sample demonstrating the highest levels of cell metabolic activity. Both of these differences between CTRL and AGN 1.0% were highly statistically significant at day 3 and 7 ( $p < 0.0001$ ).

Hyaluronic Acid was also evaluated, although at one concentration due to availability. The HA 1.0% sample demonstrated a strong ability to support cell metabolic activity resulting in a 41.7% increase in absorbance between day 3 ( $0.206 \pm 0.032$ ) and day 7 ( $0.292 \pm 0.029$ ).



**Figure 4.2:** MTT Absorbance values plotted onto bar charts to compare absorbance levels of NG108-15 cells cultured on the test hydrogels (collagen – COL, chitosan – CS, methylcellulose – MCL, sodium alginate – AGN and hyaluronic acid – HA) at concentrations (w/v) ranging from 0.5% to 6.0% at both day 3 and 7 of culture.

### 5.3.2 Live/ Dead Viability Staining

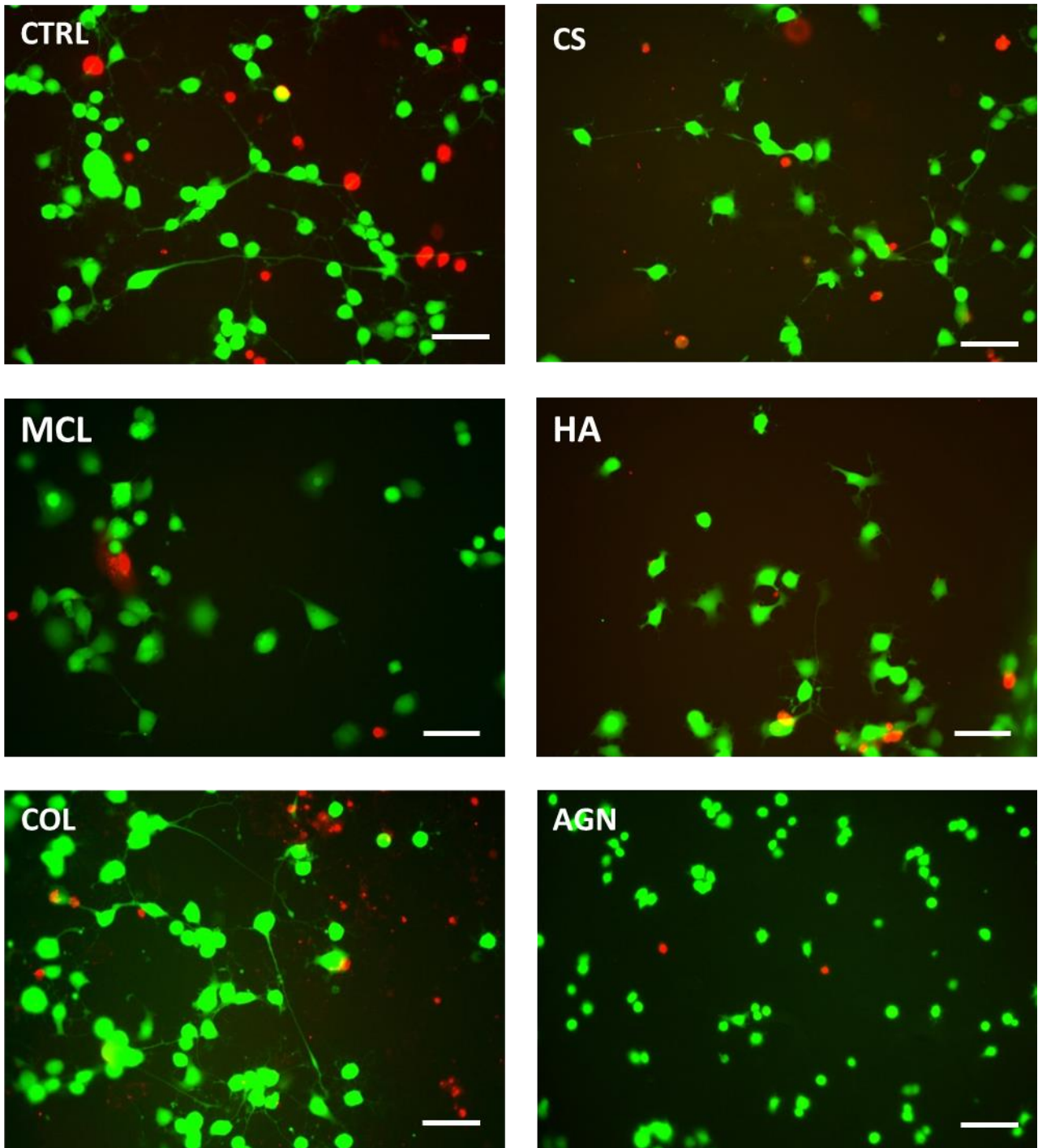
The Live/ Dead cell viability Assay was performed to validate the observations viewed from the MTT assay when examining cell cytotoxicity and biocompatibility of the concentrations used. The percentage of live cells viewed using the Calcein AM and Ethidium Homodimer-1 stain (similar to previous observations on PA6,6 in section 3.3.6). Calcein AM staining provides fluorescent labelling of cell morphology in addition demonstrating that neurite extension was clearly possible on the CTRL and COL at 7 days (Figure 4.3).

On COL hydrogels, the percentage of live cells was maintained above 96.1% at day 3 for all conditions (Figure 4.4). By day 7, differences were measured between COL 1.0% hydrogels ( $88.2 \pm 12.46\%$ ) and the COL 0.5% ( $92.4 \pm 7.33\%$ ) when compared to control, which was significant for COL 1.0% ( $p < 0.0001$ ). However, COL 0.5% was not significantly different to control ( $95.3 \pm 7.35\%$ ). The CS 0.5% and CS 1.0% hydrogels maintained a high cell viability ranging from  $79.6 \pm 11.2\%$  to  $87.7 \pm 8.5\%$  at day 7 respectively (Figure 4.4). Whereas, cell viability on CS 1.5% ( $28.8 \pm 12.92$ ) was significantly lower at day 7 when compared to CTRL, CS 0.5% and CS 1.0% ( $p < 0.0001$  for all comparisons).

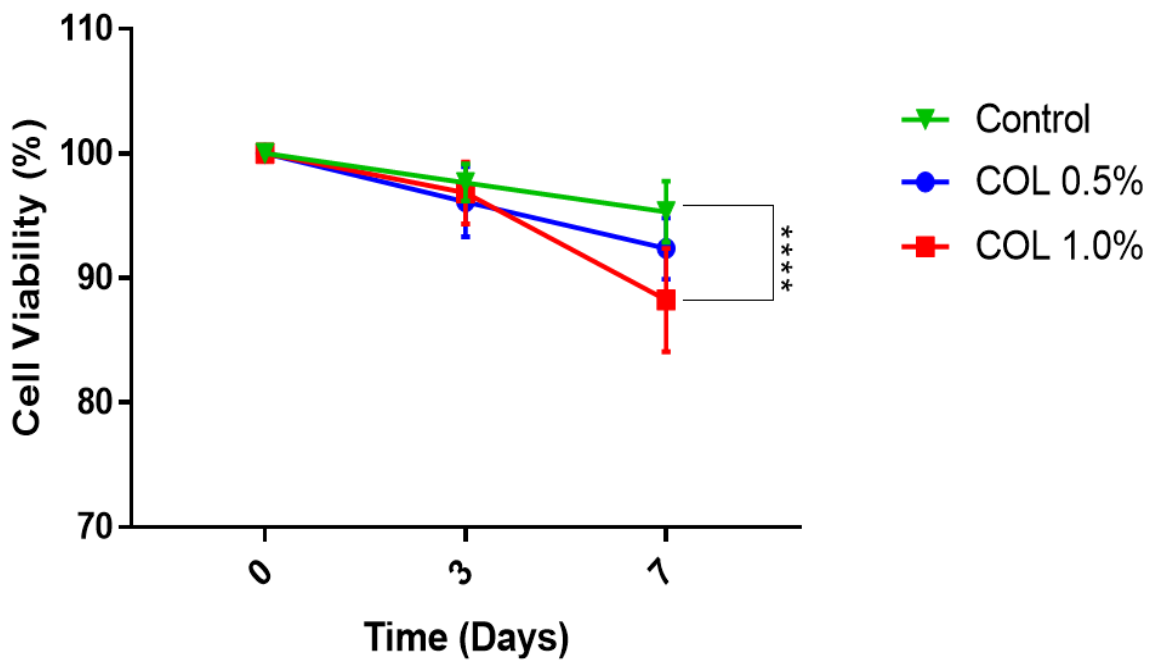
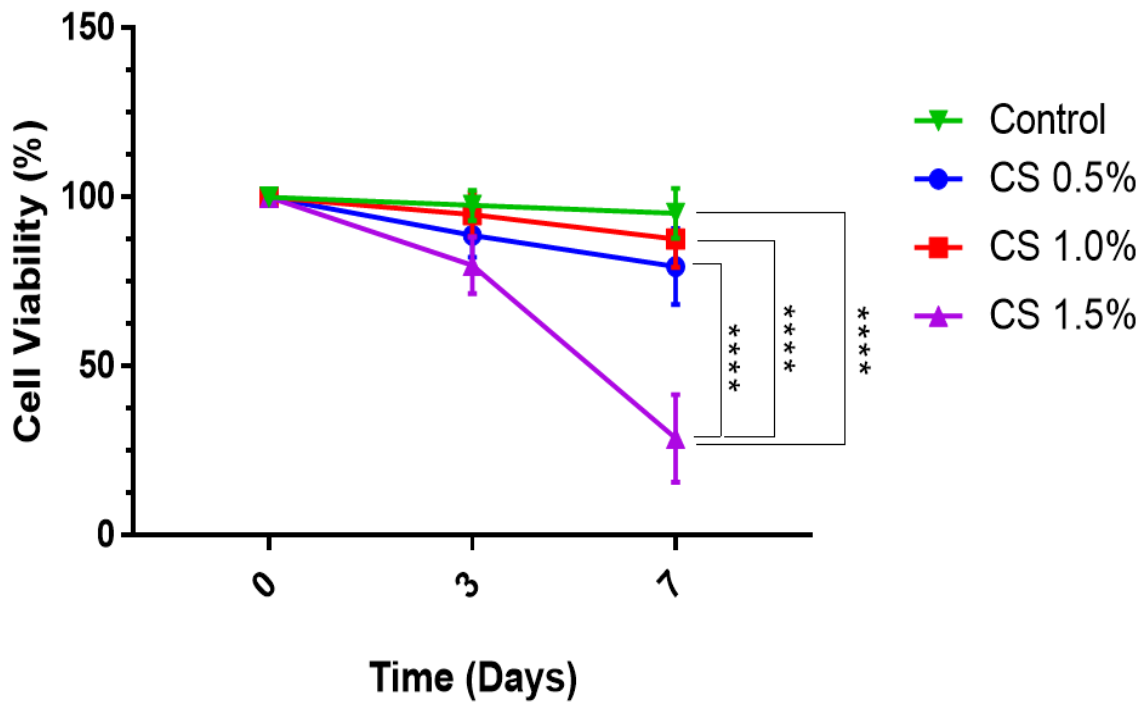
Percentage live cells ranged from  $22.1 \pm 14.6\%$  to  $67.5 \pm 12.4\%$  on day 3 for alginate-based hydrogels (Figure 4.5). Significant differences were calculated between the CTRL ( $95.3 \pm 7.4\%$ ) and AGN 1.0 %, AGN 1.5%, AGN 3.0%, AGN 6.0%. The lowest concentration of AGN was 29.2% lower than the CTRL. MCL hydrogels did not support cell viability as well as CTRL at both day 3 and day 7 (Figure 4.8). This difference was statistically significant at 7 days, where the CTRL ( $95.3 \pm 7.4$ ) was 25.6% higher than MCL 0.5% ( $70.9 \pm 12.6$ ) and 35.9% higher than MCL 1.0% ( $61.1 \pm 13.6$ ). The difference between the percentage of live cells calculated on MCL 1.0% and CTRL was statistically significant ( $p = 0.0114$ ). On HA 1.0% hydrogels, high cell viability was maintained by day 7 ( $80.7 \pm 8.4\%$ ), which was similar to CTRL ( $95.3 \pm 7.4\%$ ) (Figure 4.5).

Cell number increased between day 3 and day 7 by 79.8% on the CTRL surface which was used to compare proliferation on the hydrogels between the same time points. Comparable increases in cell number were only observed on COL 1.0% (130.9%), CS 1.5% (98.6%) and AGN 3% (80.0%). However, on AGN 3% the mean cell number was very low at day 7 (11.25 cells). Comparing against COL 1.0% ( $46.5 \pm 4.8$  cells) hydrogel and the hydrogels tested, the number of cells was

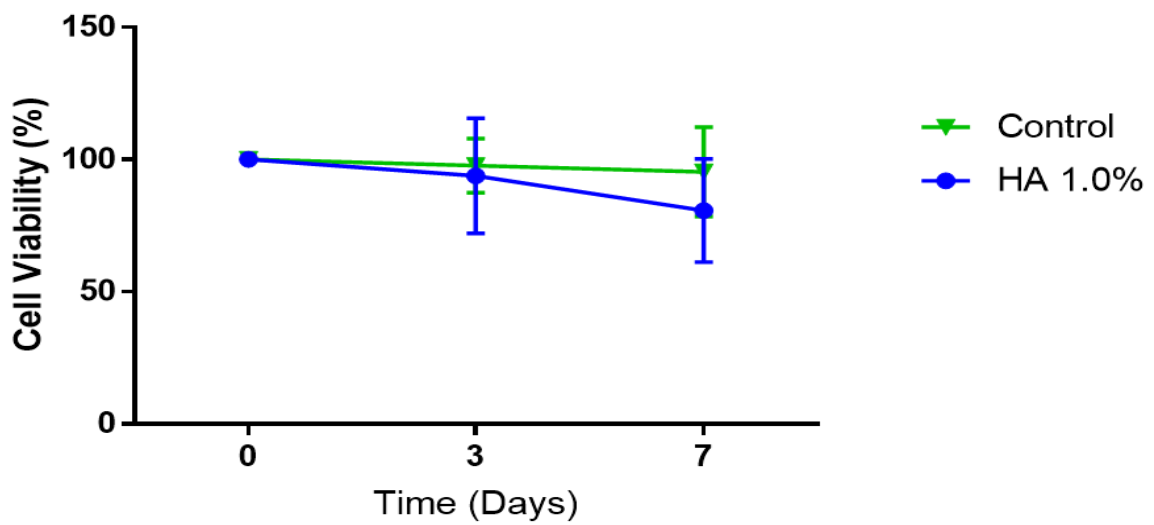
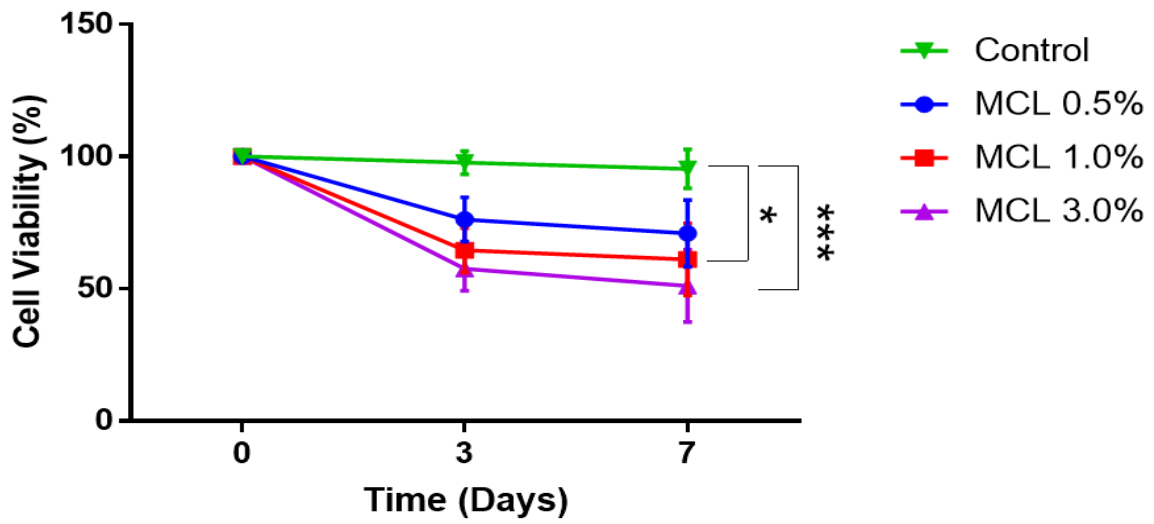
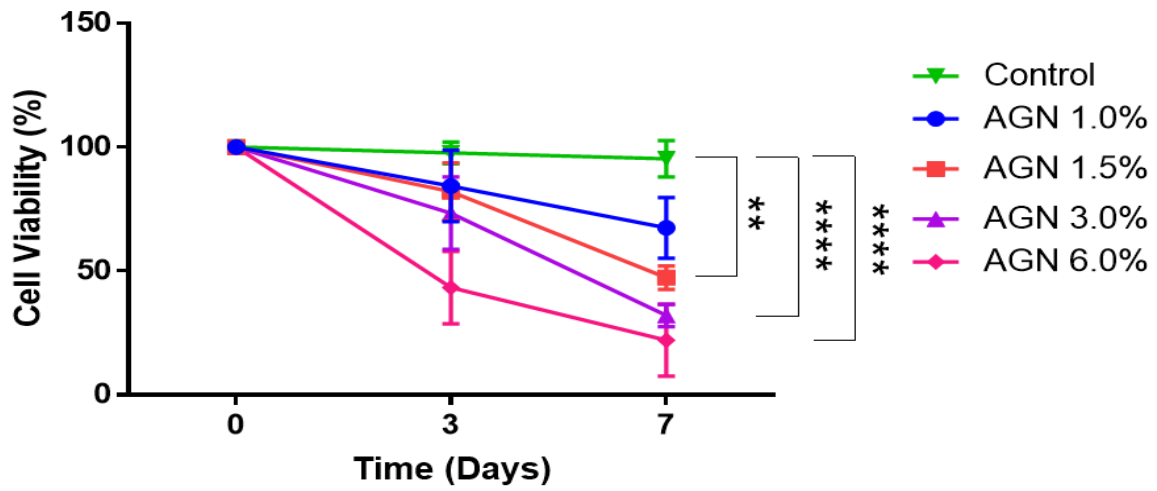
significantly higher than AGN 1% ( $24.2 \pm 3.0$  cells,  $p=0.04$ ), AGN 1.5% ( $22.8 \pm 3.4$  cells,  $p=0.019$ ) and HA 1.0% ( $20.3 \pm 3.5$  cells,  $p=0.001$ ). Furthermore, significant differences between mean numbers of cells on day 7 on the hydrogels were found between the CS 1.0% hydrogel ( $41.7 \pm 5.4$  cells) and AGN 1.0% ( $24.2 \pm 3.0$  cells,  $p=0.020$ ), AGN 1.5% ( $22.8 \pm 3.4$  cells,  $p=0.009$ ), MCL 1.0% ( $28.09 \pm 6.2$  cells,  $p=0.048$ ) and HA 1.0% ( $20.3 \pm 3.5$  cells,  $p=0.001$ ).



**Figure 4.3:** *Calcein AM and Ethidium Homodimer-1 staining of NG108-15 cells cultured on control and test hydrogels after 3 days. Representative fluorescent images were taken using widefield microscopy and are of hydrogels at 1.0% w/v concentration. Scale bar - 50μm.*



**Figure 4.4:** Quantification from Calcein AM and Ethidium Homodimer-1 staining used to calculate the percentage of live cells, or cell viability (%). Graphs for Comparisons of CS and COL are shown with controls (tissue culture plastic), calculated for 3 and 7 days.

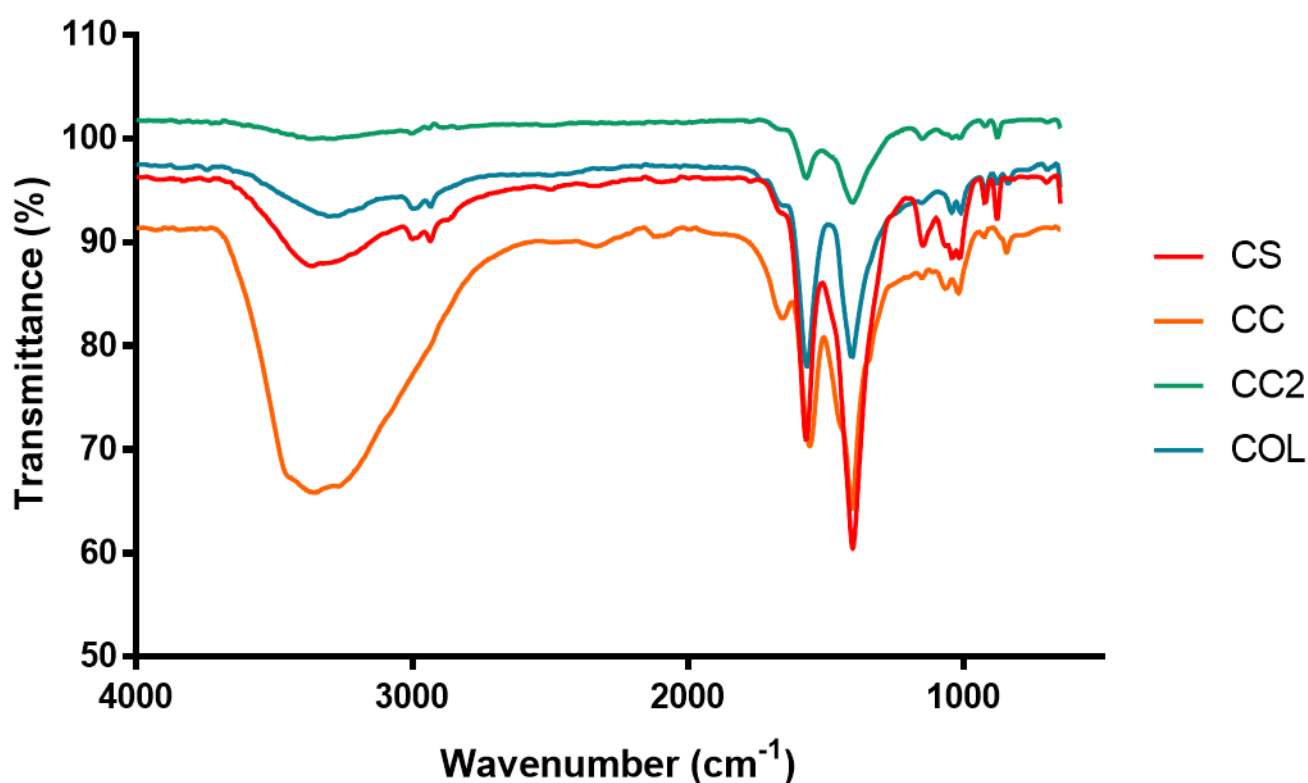


**Figure 4.5:** Cell viability quantification for AGN, MCL and HA compared to values derived from NG108-15 cells cultured on tissue culture plastic (control).



### 4.3.3 Fourier Transform Infrared Spectroscopy (FTIR)

Infrared spectra were used to confirm chitosan and collagen hydrogel blending, by analysis of functional groups present. Dry samples of CS, COL, CC (1:1 blend of chitosan and collagen) and CC2 (1:2 blend of chitosan to collagen), were tested in further experiments for use as a nerve guidance scaffold. FTIR spectra confirmed the presence of key functional groups as shown in Table 3.1 and spectra shown in Figure 4.6. N-H stretching was observed in collagen containing samples at  $3321\text{ cm}^{-1}$  and C-N stretching at  $1240\text{ cm}^{-1}$ . For chitosan, the large O-H stretch was observed at  $3315\text{ cm}^{-1}$ , C-H stretching at  $2917\text{ cm}^{-1}$  and C-O-C stretching at  $1152\text{ cm}^{-1}$ . The blends exhibited a mixture of the functional groups, some of which are present in both chitosan and collagen such as the N-H bending at  $1554\text{ cm}^{-1}$  and the C=O stretch or bend at  $1657\text{ cm}^{-1}$  and  $1641\text{ cm}^{-1}$  respectively.



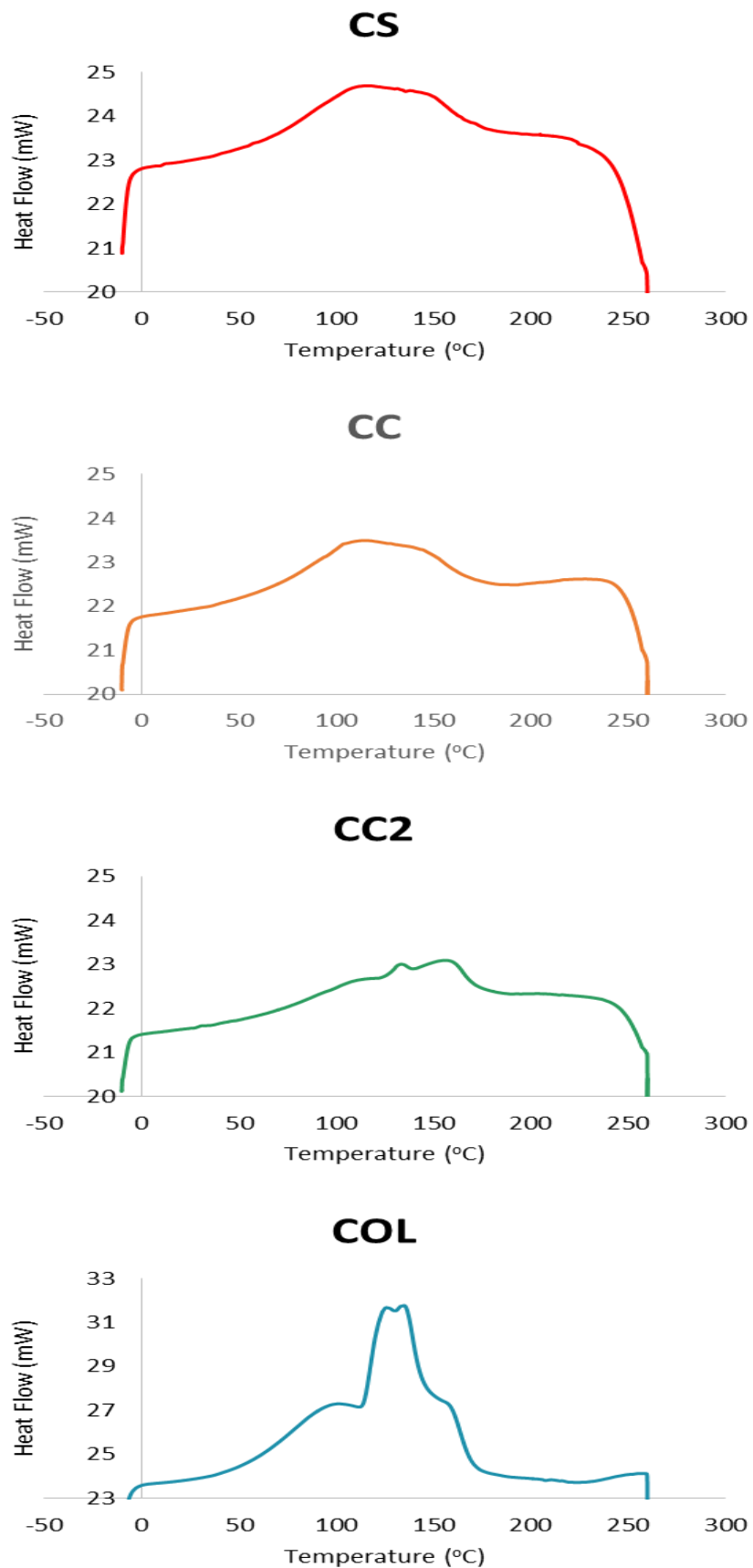
**Figure 4.6:** FTIR-ATR spectra in transmittance mode of CS, CC, CC2 and COL in their anhydrous states. The peaks from the spectra have been listed in Table 1.

Table 4.1: Functional groups present on FTIR spectra from CS, CC, CC2 and COL samples

<b>Wavenumber (cm<sup>-1</sup>)</b>	<b>Functional Group</b>
<b>3321</b>	N-H stretch
<b>3315</b>	O-H stretch
<b>3213</b>	O-H stretch
<b>3082</b>	N-H stretch
<b>2917</b>	C-H stretch
<b>1657</b>	C=O stretch, N=H bend, C-N stretch
<b>1641</b>	C=O bend
<b>1555</b>	N-H bend, C-N stretch
<b>1240</b>	N-H bend, C-N stretch
<b>1152</b>	C-O-C stretch

#### 4.3.4 Dynamic Scanning Calorimetry (DSC)

DSC analysis was carried out to confirm the thermal stability of the biopolymers tested, on dry samples. It was clear that chitosan, and collagen are thermally stable within the region of 0-37°C as the heat flow increased from 22.8mW to 23.1mW for CS and 23.6mW to 24.0mW for COL over this temperature range. Endothermic peaks were reached at 107.8°C (CS), 103.2°C (CC), 125.8°C (CC2) and 122.4°C (COL) corresponding to the melting temperature (Figure 4.7).

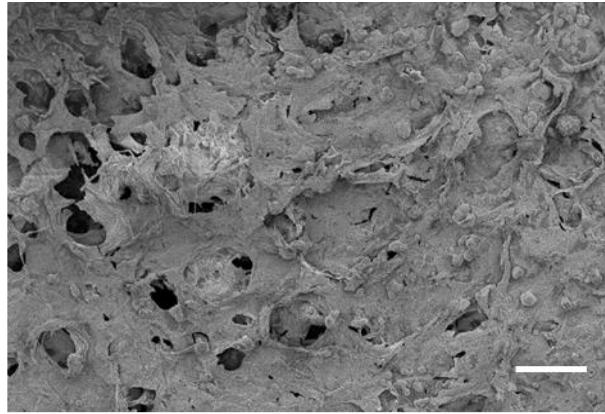


**Figure 4.7:** DSC thermograms for CS, CC, CC2 and COL for the heating cycle measured between  $-10^{\circ}\text{C}$  and  $260^{\circ}\text{C}$  showing the endothermic melting peaks. A positive heat flow indicates an endothermic peak.

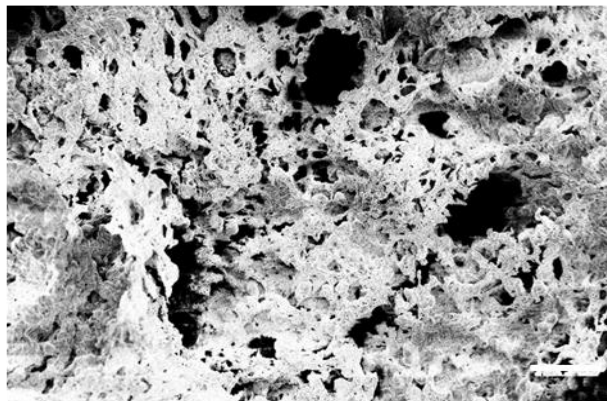
#### 4.3.5 Scanning Electron Microscopy (SEM)

Electron microscopy was used to reveal surface morphology of the hydrogels at fractures within the material after freeze-drying (Figure 4.8). At 100X magnification, CS was clearly porous with an aggregated appearance. Porosity was also observed in COL, and the blends (CC and CC2). Clear fibrils could not be seen in the CS, CC and COL hydrogels but were seen in CC2 samples. There were also fewer pores present in CC2 samples compared to CS, CC and COL however all samples had an interconnected structure even in samples containing 50% chitosan.

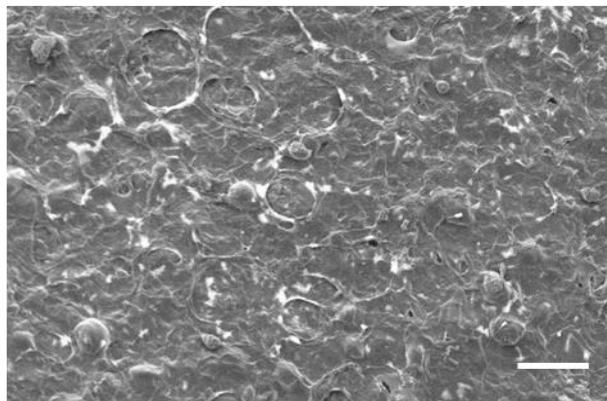
CS



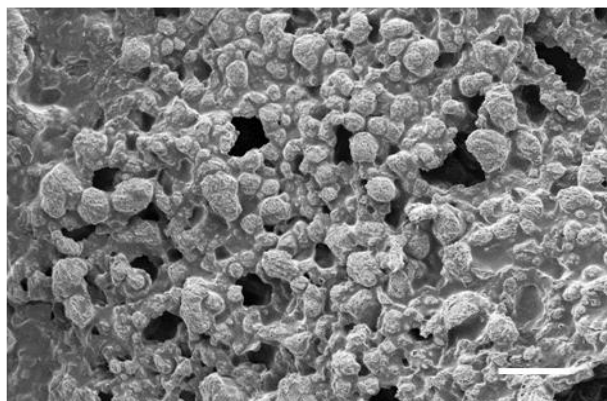
CC



CC2



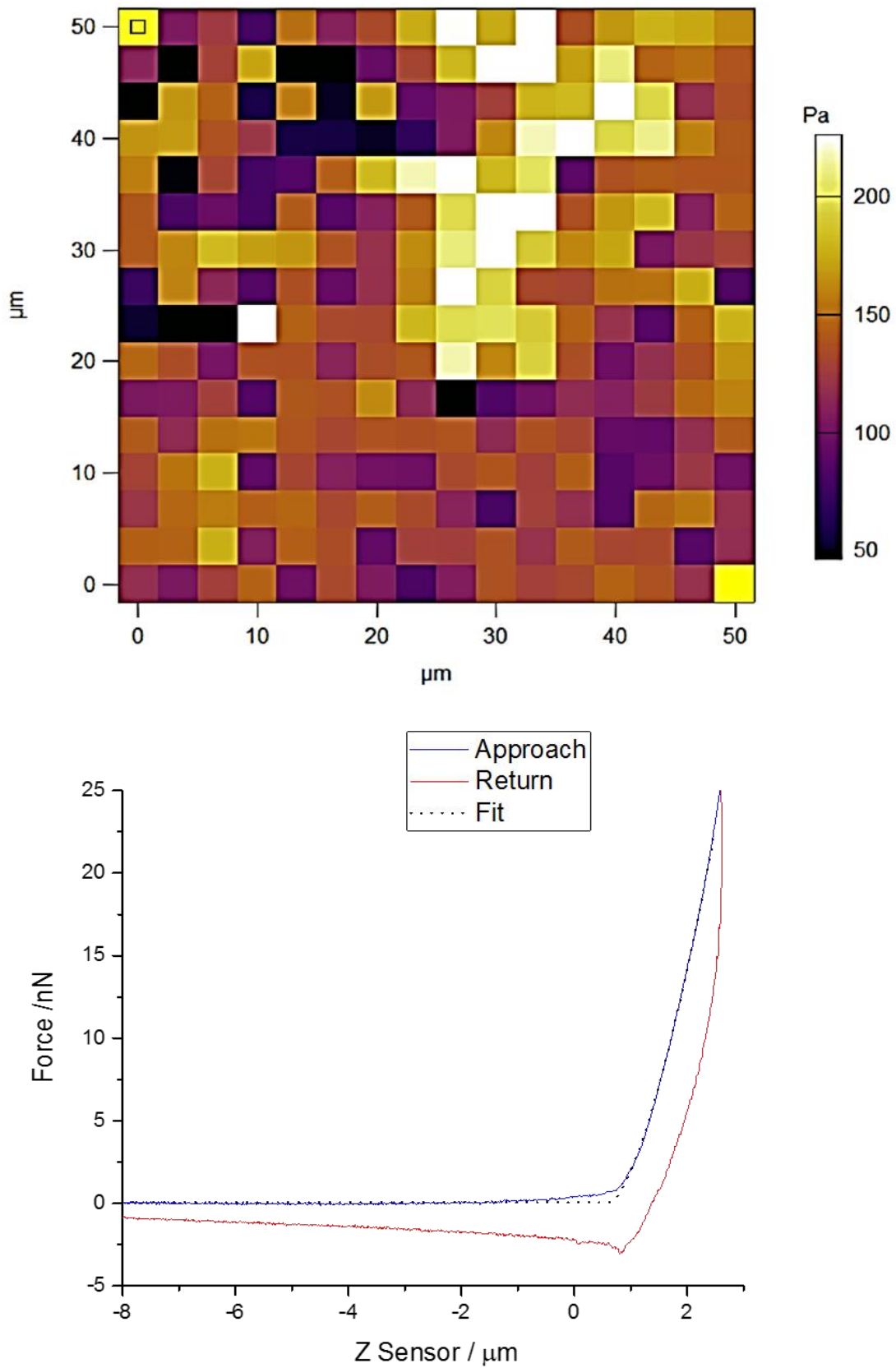
COL



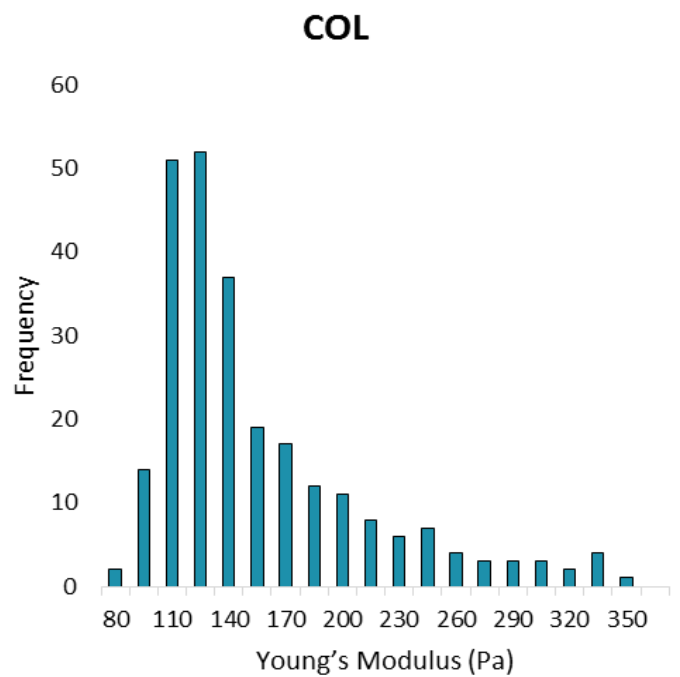
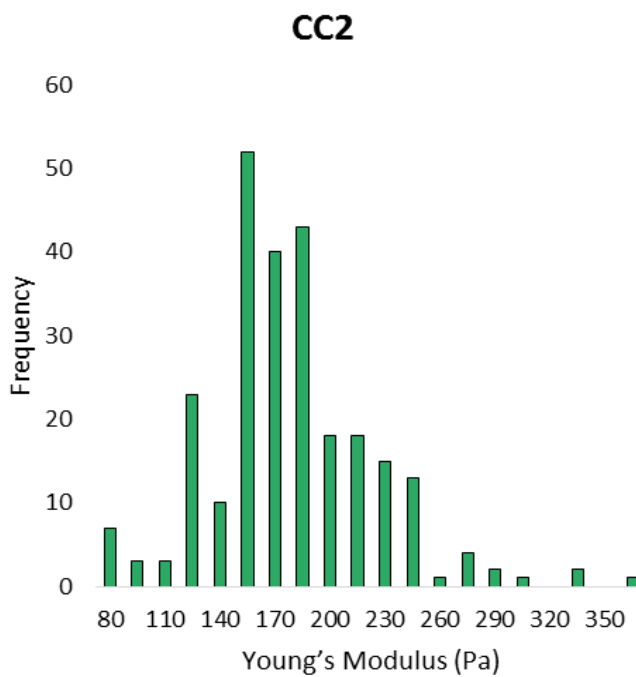
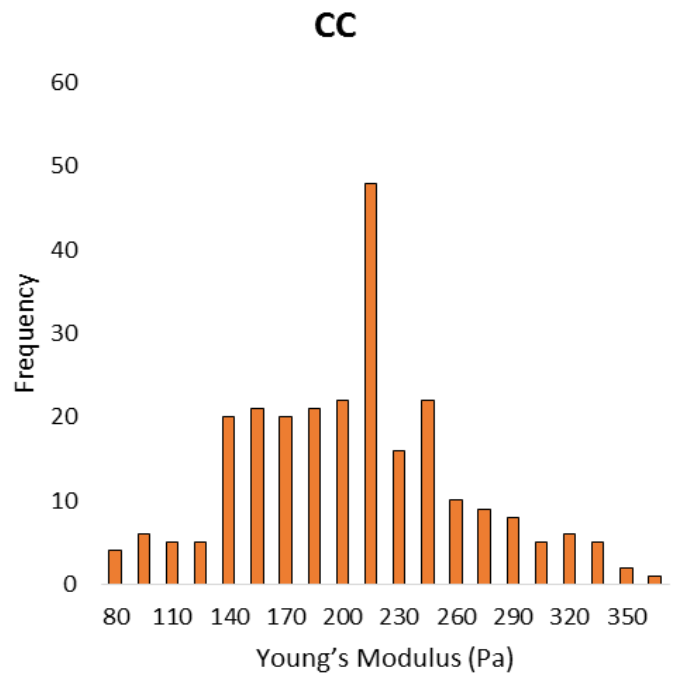
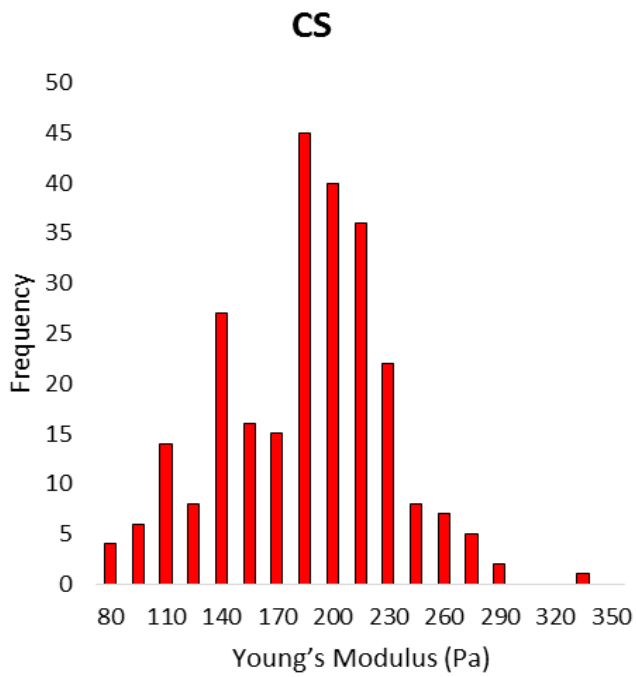
**Figure 4.8:** Representative SEM images of the hydrogels (CS, CC, CC2 and COL) following lyophilisation.

#### 4.3.6 Atomic Force Microscopy (AFM)

Atomic force microscopy was used to evaluate the bulk stiffness of the hydrogels in their wet state, to simulate their use in vivo, and compare the cellular responses characterised in later experiments as cell biomechanics may have been affected by the blending of COL with CS leading to either favourable or less favourable results. 256 regions on the hydrogel surface were measured to calculate the Young's modulus by relating the nano-indentation of the probe to the force from the hydrogel sampling area, the representative force curve shows a clear contact and return of the probe indicating no adhesion to the gel (Figure 4.9). The 256 measurements taken over the sampling area were then displayed in a histogram to show the distribution of stiffness measurements (Figure 4.10). The mean Young's Modulus was calculated as follows; 185.3 Pa (SD=63.1) for CS, 206.2 Pa (SD=69.0) for CC, 178.3 Pa (SD=66.8) for CC2 and 155.6 Pa (SD=66.7) for COL. Interestingly, inclusion of collagen into the blend had increased the range of the stiffness values which ranged between 80Pa and 305Pa for CS to between 80Pa and 365Pa for both CC and CC2.



**Figure 4.9:** Representation of a panel of measurements for AFM,  $n=256$ , showing the Young's Modulus value at each point (top). Representative force curve used to calculate the Young's modulus from the indentation, force exerted by the cantilever and the spring constant (bottom).

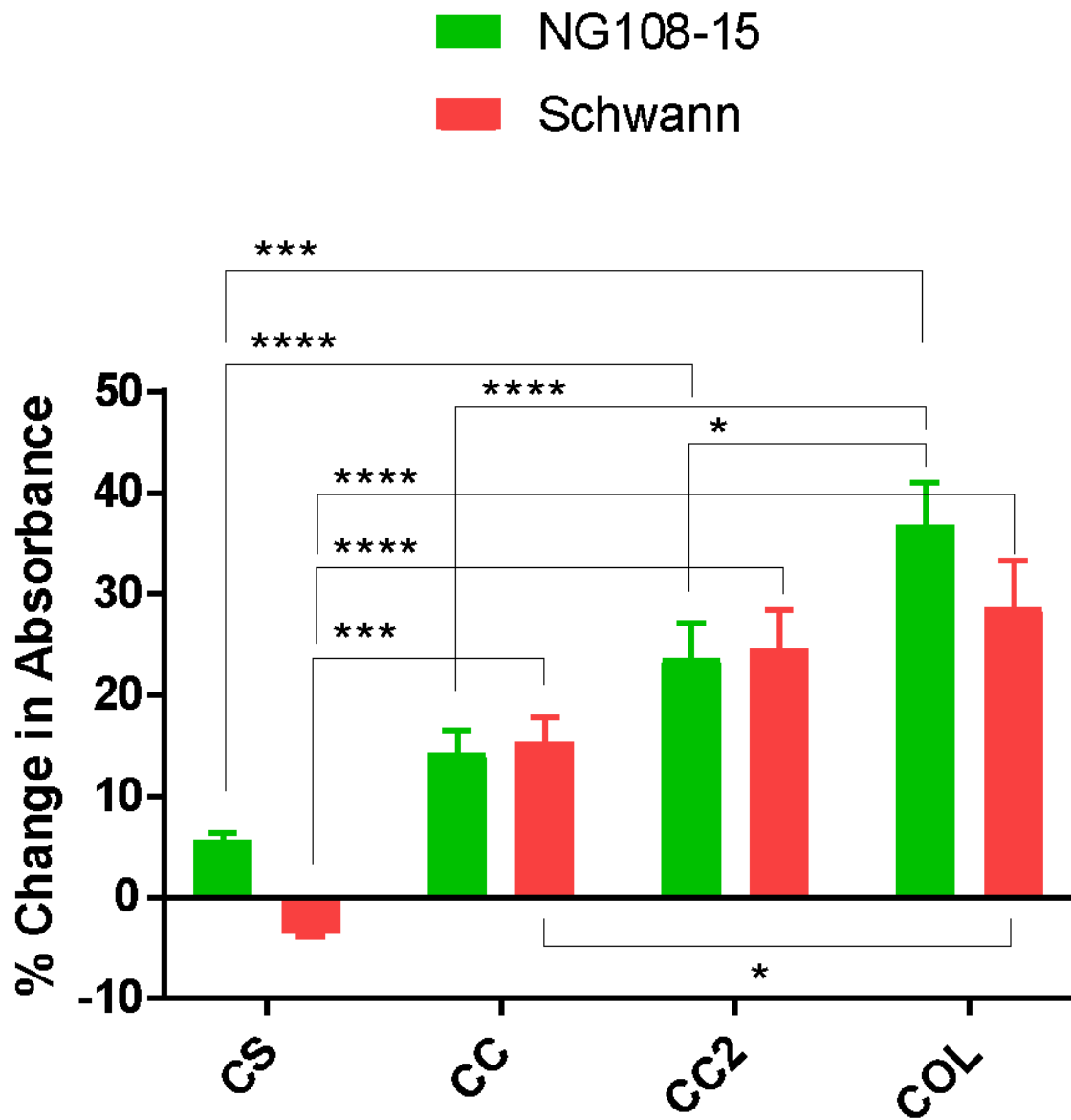


**Figure 4.10:** Histograms showing the distribution of Young's Modulus to show the stiffness of CS, CC, CC2 and COL hydrogels.



#### 4.3.7 Cell Proliferation Assessment with Alamar Blue Assay

Proliferation of both NG108-15 and Schwann cells was further calculated to confirm that the hydrogels (CS, CC, CC2 and COL) were able to support cell adhesion, growth and mitosis, as characterised previously on tissue culture plastic (section 3.3.1 and 3.3.4). The percentage change in absorbance of the Alamar Blue solution following incubation was calculated between day 3 and day 7 (Figure 4.11). NG108-15 cells demonstrated proliferation calculated by the percentage increase in absorbance value on all hydrogels ( $5.73 \pm 0.69\%$  on CS,  $14.32 \pm 2.21\%$  on CC,  $23.62 \pm 3.51\%$  on CC2, and  $36.79 \pm 4.21\%$  on COL). However, the increase on CS was the lowest calculated (75.8% less than CC2 and 84.5% lower than COL), which was statistically significant ( $p=0.0004$  and  $p<0.0001$  respectively). For NG108-15 cells, proliferation was greatest on COL and this difference was statistically significant compared to both blends ( $p<0.0001$  for CC and  $p=0.0167$  for CC2). Schwann cells were able to proliferate on all gels except CS where a  $3.61 \pm 0.26\%$  decrease was calculated, which was significantly lower compared to CC ( $p=0.0001$ ) and both CC2 and COL ( $p<0.001$  for both comparisons). Similar levels of proliferation were calculated on CC2 and COL ( $24.65 \pm 3.76\%$  and  $28.62 \pm 4.74\%$  respectively). However, the increase in CC ( $15.35 \pm 2.46\%$ ) was significantly lower than the value calculated on COL ( $p<0.0001$ ).



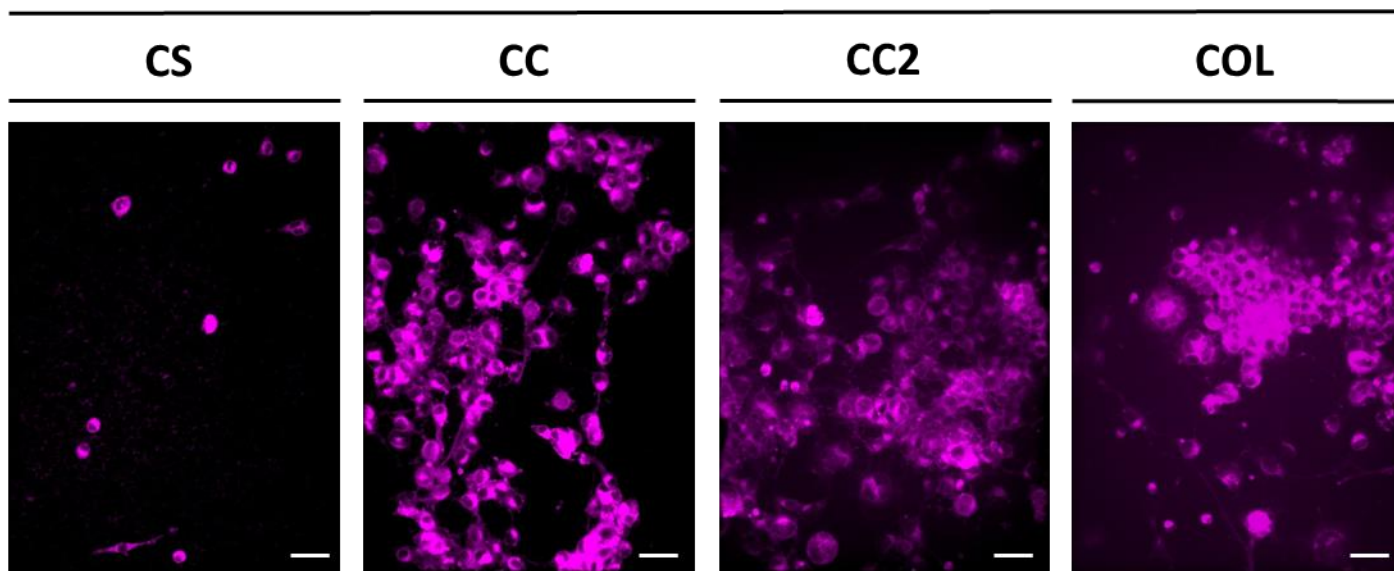
**Figure 4.11:** Percentage change in absorbance was calculated from Alamar Blue data on CS, CC, CC2 and COL for both NG108-15 and Schwann cells between day 3 and 7.

#### 4.3.8 Cell Mask Staining of NG108-15 Cells

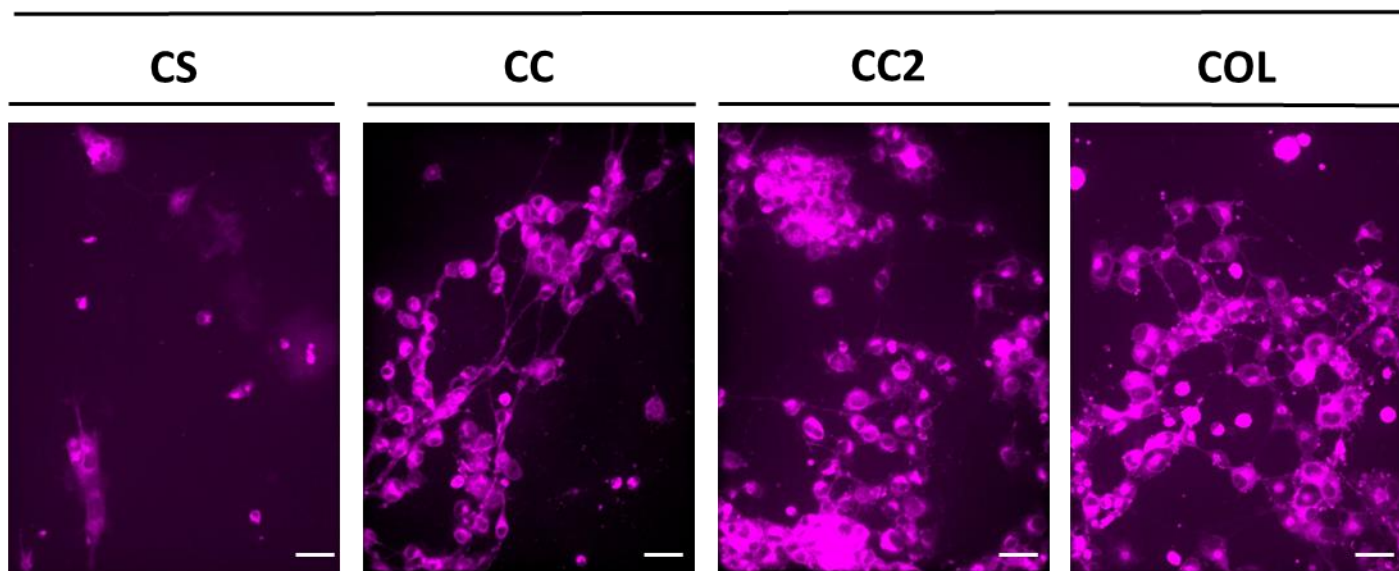
Plasma membrane staining was used to validate the observations made from the Alamar Blue assay (section 4.3.7) and qualitatively assess cell morphology of NG108-15 cells. At day 3, fewer neurites were observed however the cell bodies could be clearly seen and were rounded (Figure 4.12). Small filopodia protruding from the cell body could be imaged on cells cultured on collagen-containing hydrogels. On CC2 and COL, some neurites were present. By day 7, neurites were clearly visible on all hydrogels and there was a marked increase in cells with neurites on CC, CC2 and COL compared to CS.

Further, fewer cells had adhered to CS at both time points. 3D plots were also constructed to show the interactions of the cells cultured on the hydrogel at day 7 (Figure 4.13). The z-depth for the images was 120 $\mu$ m. Although some clumping of cells was observed, neurite extension on the hydrogels was also visible as in CC and CC2. Cells show the typical morphology of NG108-15 cells for all hydrogels as characterised previously (section 4.3.2) except CS where the cell bodies were markedly smaller and few neurites or filopodia were observed.

Day 3



Day 7



**Figure 112:** Cell Mask Plasma Membrane staining for NG108-15 cells cultured on CS, CC, CC2 and COL hydrogels at both 3 and 7 days. Scale bar - 50 $\mu$ m.

#### 4.3.9 Cell Mask Staining and Morphometric Analysis of Schwann Cells

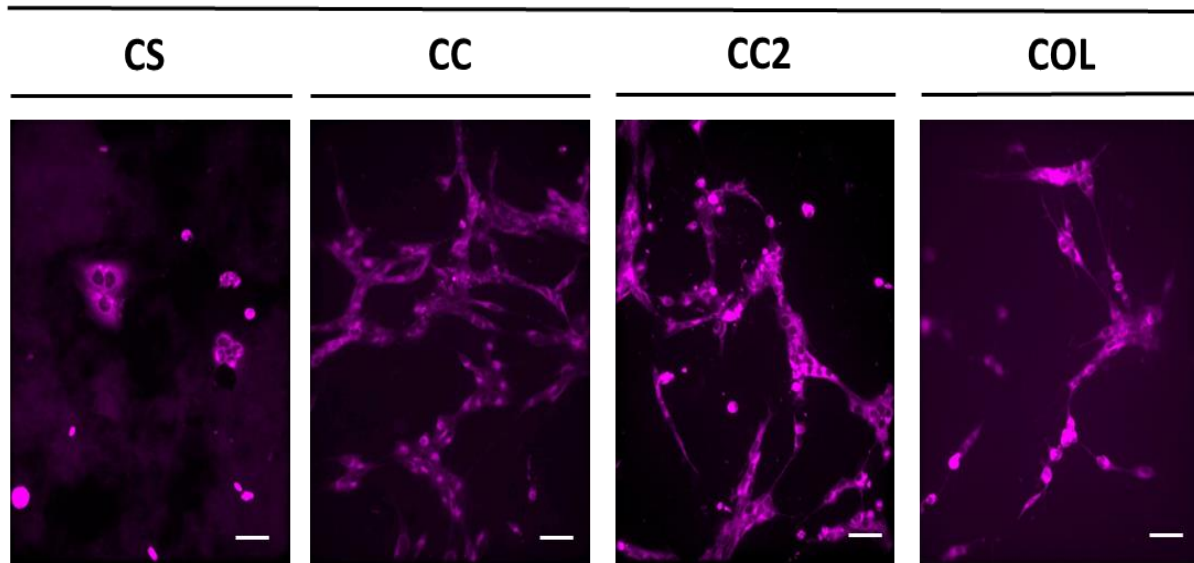
Quantitatively, Schwann cells showed a similar trend to NG108-15 cells as there were more adherent cells on CC, CC2 and COL hydrogels but not on CS. The cells were spindle shaped as previously characterised (section 3.3.4). Cell proliferation was clearly observed between 3 and 7 days, shown by the cluster populations of cells that had formed as a result (Figure 4.13). Schwann cells were rarely observed as individually isolated cells within the gel, but formed plasma membrane contacts with neighbour cells as seen by the Cell Mask staining. 3D plots show the arrangement of Schwann cells within the hydrogel, indicating that they clearly spread and polarised by day 7 using the hydrogel as a supportive scaffold (Figure 4.13).

Cell polarity was quantified, to compare the effect of the different hydrogel environments (Figure 4.14). At day 3, the greatest percentage of non-polar cells was measured on the CS hydrogel ( $89.1 \pm 6.3\%$ ). In contrast, the majority of cells were polarised by day 3 with only few non-polar cells on CC ( $13.3 \pm 2.4\%$ ), CC2 ( $16.4 \pm 2.6\%$ ) and COL ( $12.3 \pm 0.8\%$ ). Tukey's post hoc analysis confirmed that there were more non-polar cells on CS than polarised ( $p < 0.0001$ ). In contrast, there were predominately polarised cells on both CC and CC2 ( $p < 0.0001$ ). However, the population of cells analysed on COL was almost exclusively bipolar ( $p = 0.0001$  compared to non-polar cells and  $p < 0.0001$  compared to multipolar cells). By day 7, more cells had polarised in CS yielding  $33.7 \pm 4.6\%$  non-polar cells. The majority of cells maintained polarity when cultured on CC ( $34.3 \pm 2.4\%$  bipolar and  $62.1 \pm 3.5\%$  multipolar), CC2 ( $46.4 \pm 3.6\%$  bipolar and  $33.3 \pm 2.7\%$  multipolar) and COL ( $69.2 \pm 3.7\%$  bipolar and  $14.0 \pm 1.7\%$  multipolar). When comparing the sub-populations of cell morphology present on CS, there was no significant difference calculated. On CC, there were more polarised cells which remained significant ( $p < 0.0001$ ). On CC2, there was a significant bipolar population of cells compared to non-polar cells ( $p < 0.0001$ ) and there was a lower proportion of multipolar cells although less significant than the number of bipolar cells ( $p = 0.0242$ ). On the COL hydrogel, like the distribution at day 3, there were predominately bipolar cells which was statistically significant ( $p < 0.0001$ ).

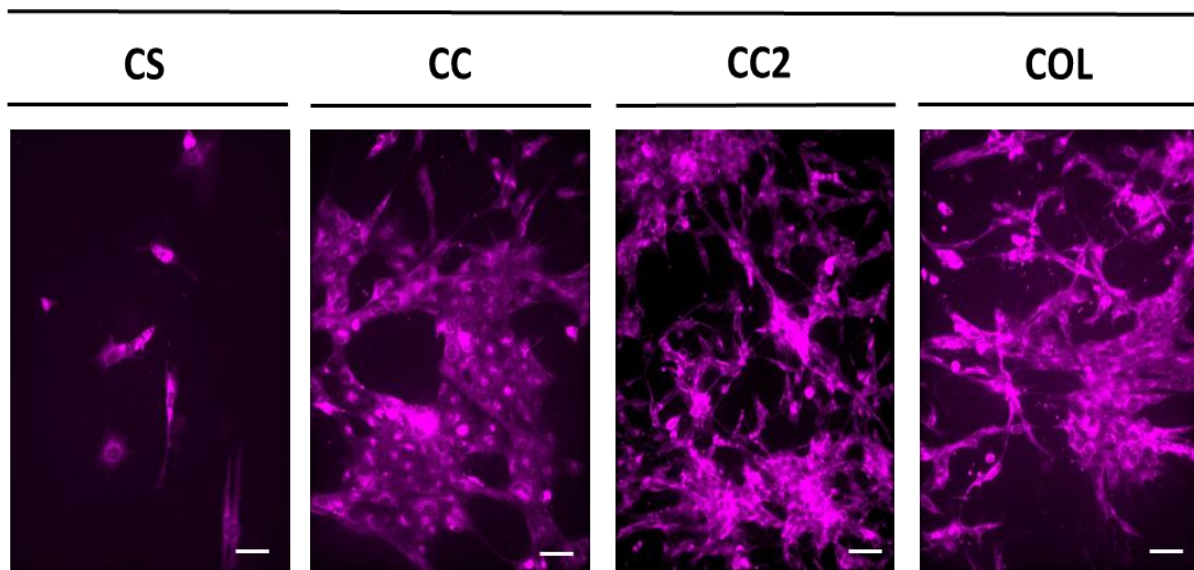
Cell area of Schwann cells was also quantified to evaluate the spreading of cells within the hydrogel environments (Figure 4.15). At day 3, the cells had a similar mean area regardless of the hydrogel; CS ( $275.92 \pm 44.62 \mu\text{m}^2$ ), CC ( $362.23 \pm 21.41 \mu\text{m}^2$ ), CC2 ( $372.54 \pm 43.63 \mu\text{m}^2$ ) and COL ( $331.14 \pm 36.46 \mu\text{m}^2$ ). By day 7, there were differences in cell spreading observed. The largest cell

area was calculated on COL ( $613.39 \pm 47.99 \mu\text{m}^2$ ), which was 158.6% higher than CS ( $237.81 \pm 17.64 \mu\text{m}^2$ ), 95.8% higher than CC ( $313.63 \pm 15.34 \mu\text{m}^2$ ), and 28.0% higher than CC2 ( $479.18 \pm 37.11 \mu\text{m}^2$ ). The difference between mean cell area for COL and CC2 was statistically significant ( $p=0.0174$ ), and the difference between cell area of cells on COL compared to CC and CS was highly significant ( $p<0.0001$ ). Additionally, the mean cell area on CC2 was significantly higher than CC ( $p=0.0007$ ) and CS ( $p<0.0001$ ).

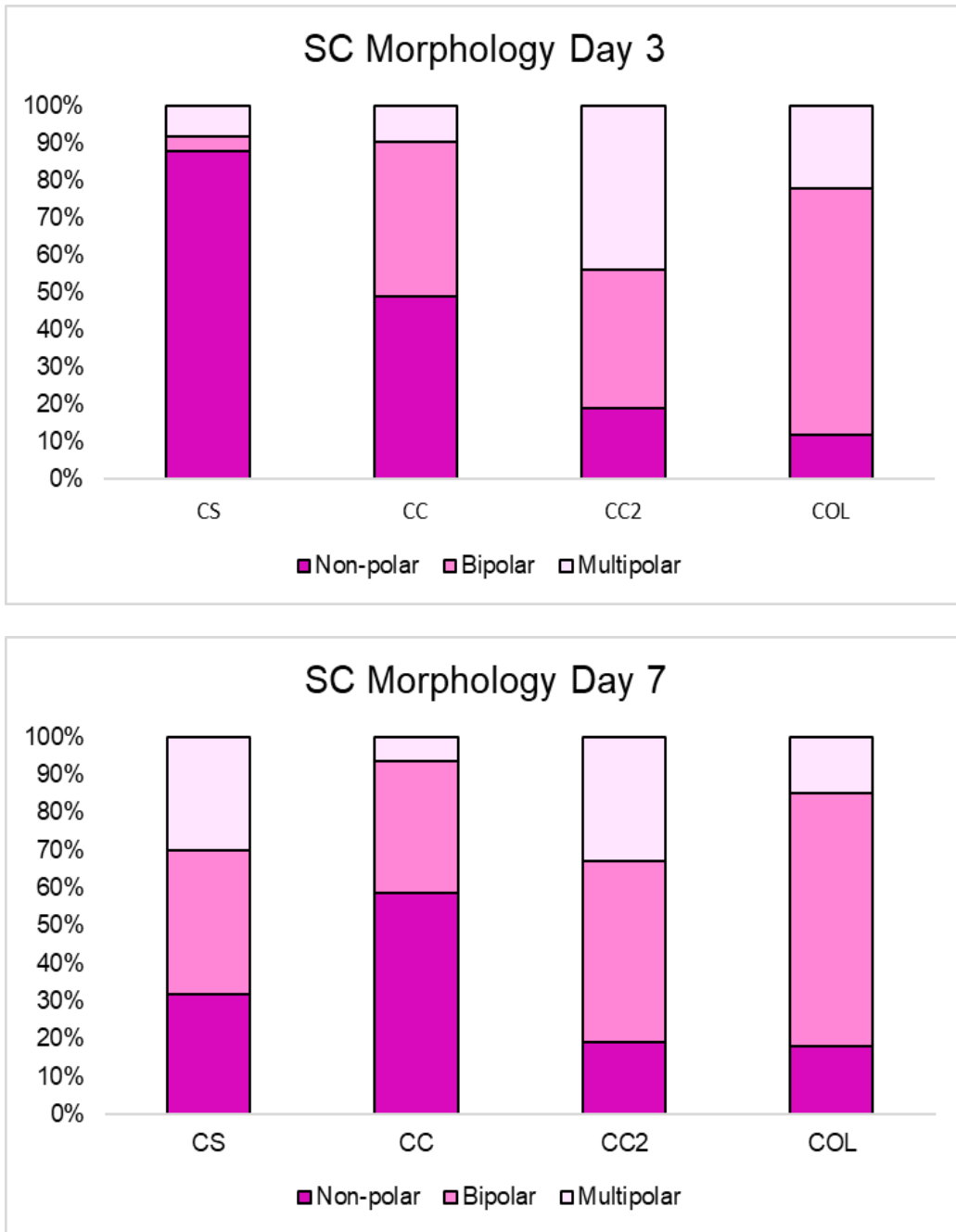
Day 3



Day 7

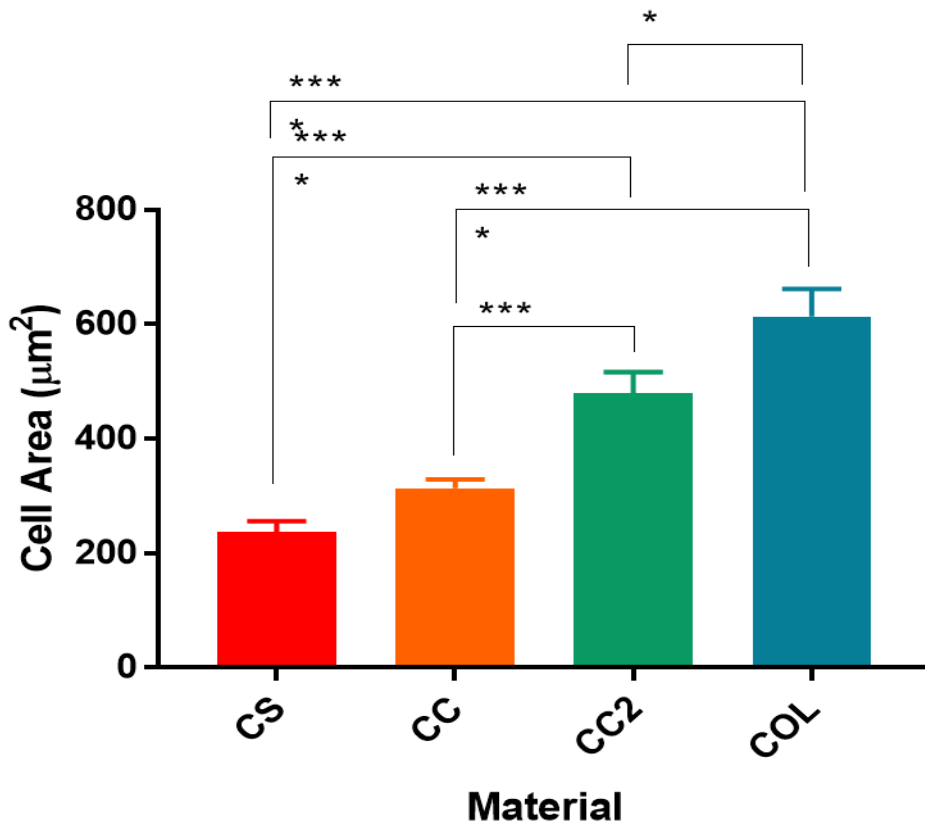
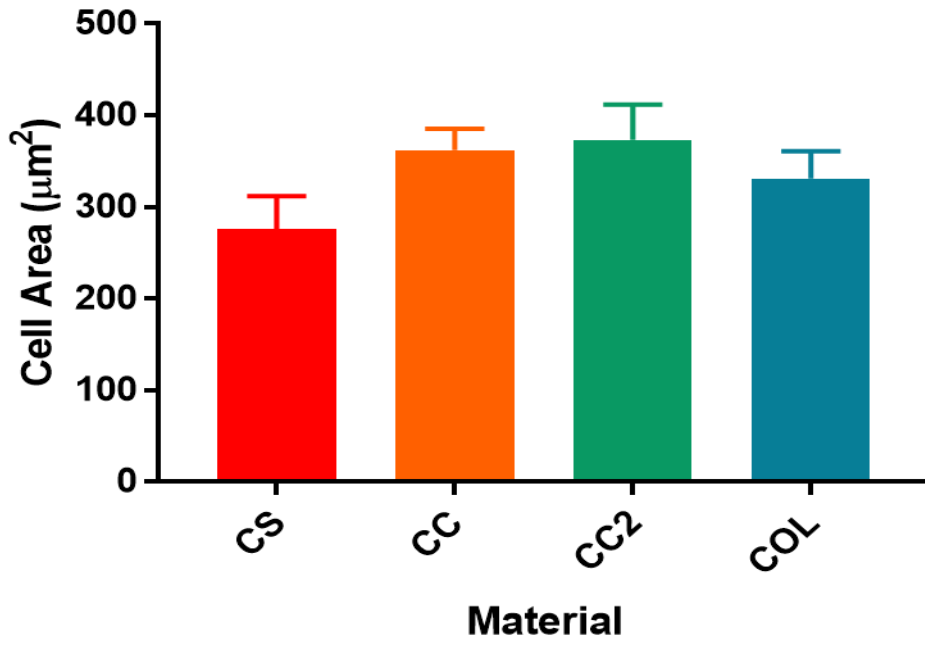


**Figure 4.13:** Cell Mask plasma membrane staining of Schwann cells cultured on CS, CC, CC2 and COL for 3 and 7 days. Scale bar - 50 $\mu$ m.



**Figure 4.14:** Quantification of Schwann cell morphology sub-types characterised as non-polar, bipolar and multipolar at both 3 and 7 days.





**Figure 4.15:** Bar charts showing the mean cell area calculations of Schwann cells cultured on CS, CC, CC2 and COL hydrogels for 3 days (top bar chart) and 7 days (bottom bar chart).

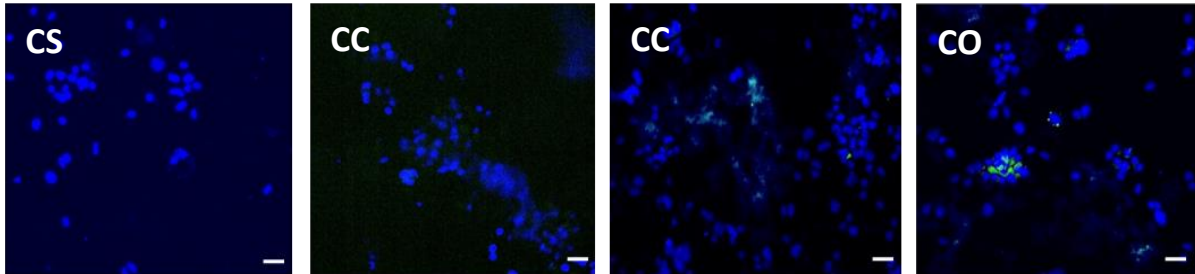
#### 4.3.10 Differentiation Analysis of NG108-15 Cells

Expression of markers for both neural differentiation and cell proliferation, MAP2 and Ki67 respectively, was assessed to confirm that NG108-15 cells could differentiate on the hydrogels (Figure 4.16 and 4.17 respectively). Cells were imaged on CS, CC, CC2 and COL from day 1 to day 7. Mean MAP2 expression was detected in NG108-15 cells from day 3 to day 7 on all hydrogels, ranging from  $86.8 \pm 5.3\%$  to  $97.4 \pm 0.9\%$ . However very minimal expression was observed in cells on day 1. This was confirmed when the expression levels were quantified and compared in statistical analyses, MAP2 expression was significantly lower on day 1 compared to day 3, 5 and 7 ( $p < 0.0001$  for all time points) (Figure 4.18). Ki67 expression peaked at day 1, converse to MAP2 expression. The high expression was observed on all hydrogels ( $83.4 \pm 4.7\%$  on CS,  $89.6 \pm 8.0\%$  on CC,  $87.4 \pm 3.5\%$  on CC2 and  $85.9 \pm 5.5\%$  on COL).

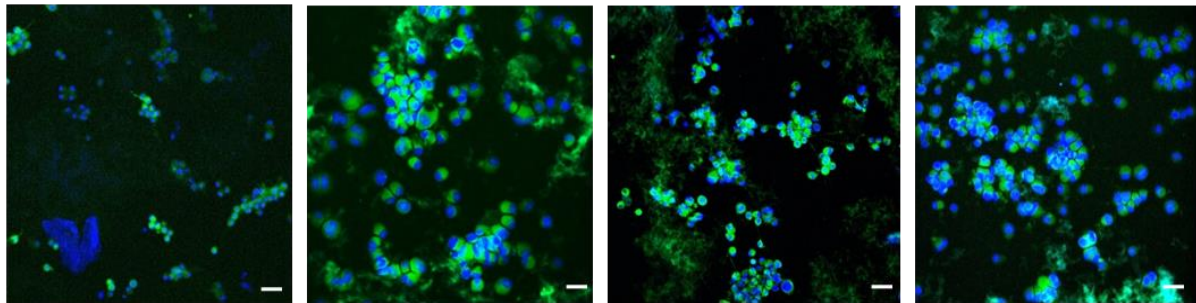
## MAP2 / Hoechst 33342

---

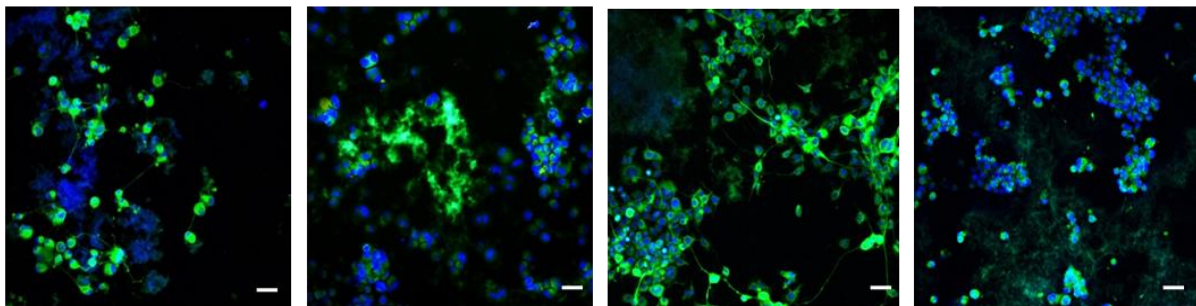
Day 1



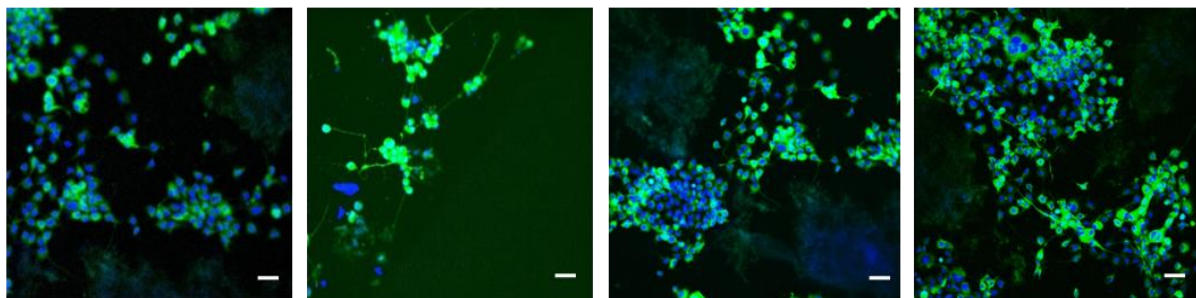
Day 3



Day 5



Day 7

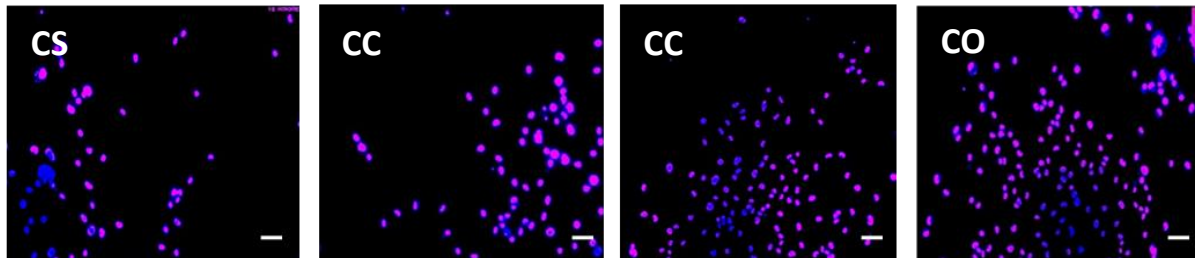


**Figure 4.16:** Immunocytochemical staining fluorescent micrographs of Microtubule Associated Protein 2 (MAP2) expression detected in NG018-15 cells cultured for 1, 3, 5 and 7 days on CS, CC, CC2 and COL. Scale bar - 50 $\mu$ m.

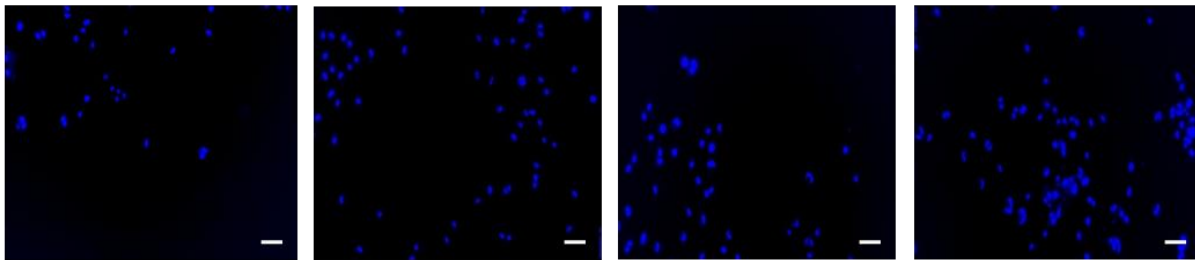
## Ki67 / Hoechst 33342

---

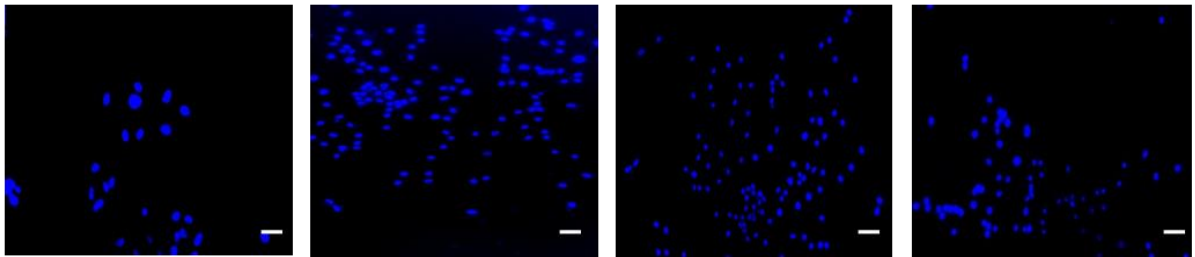
Day 1



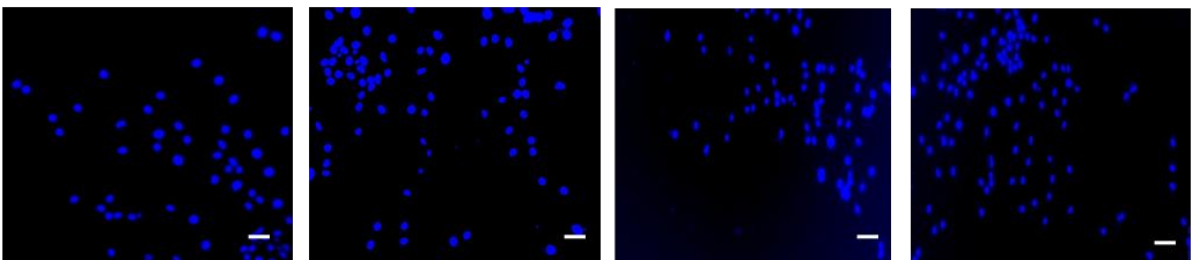
Day 3



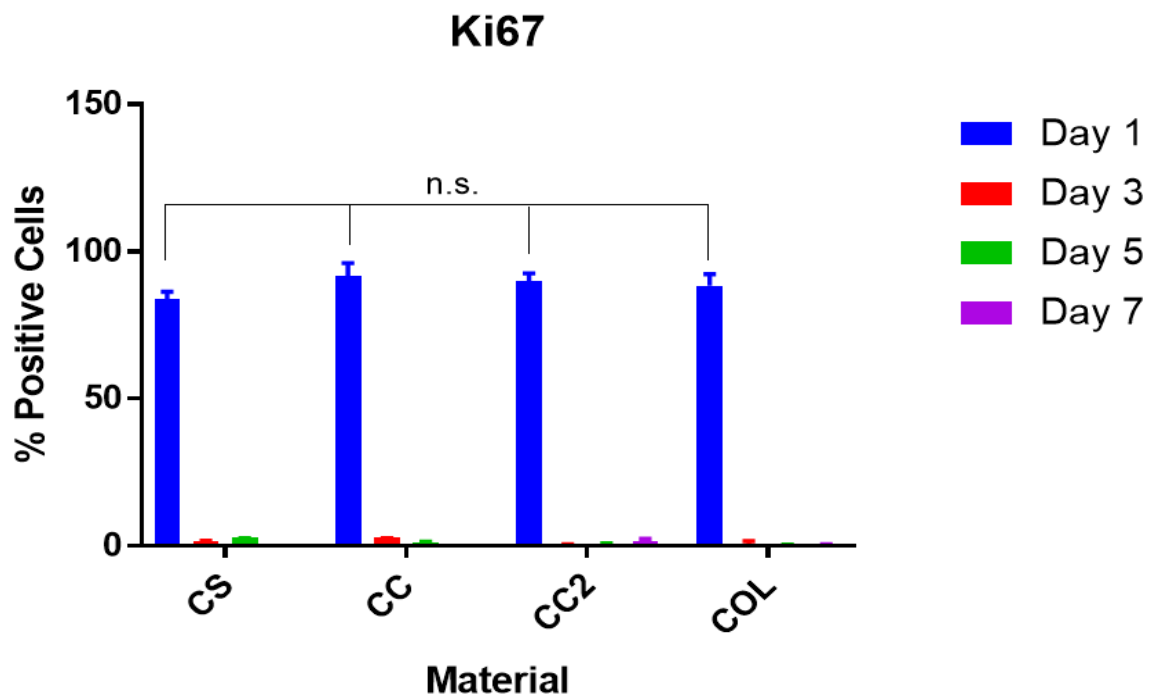
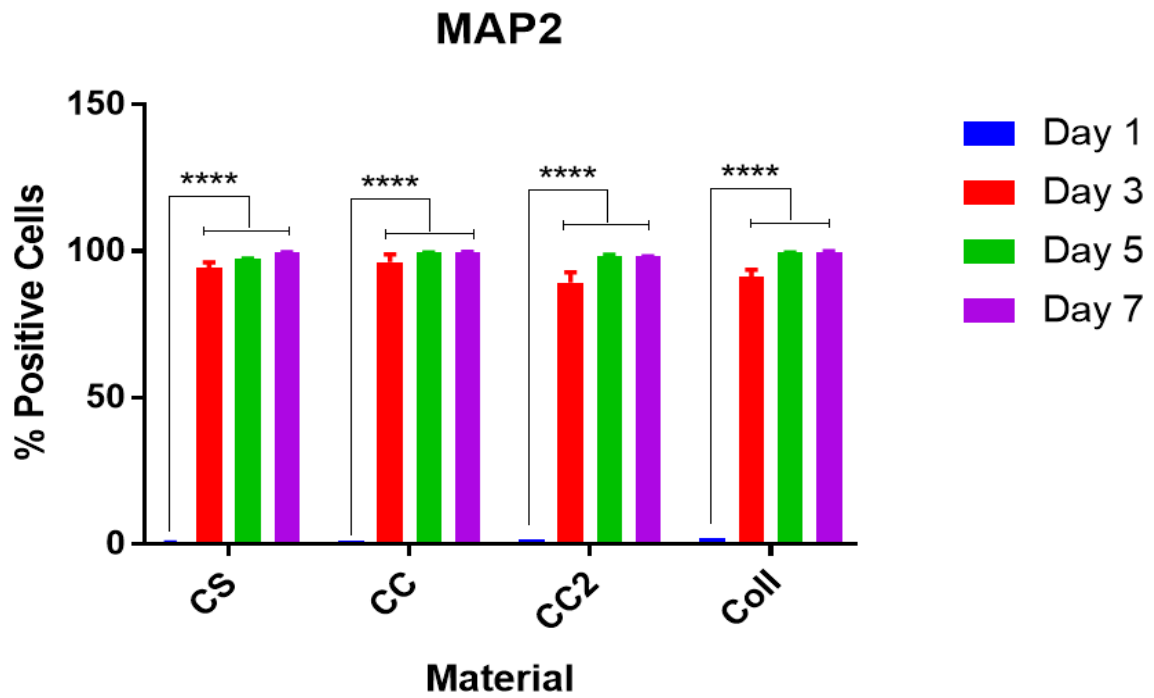
Day 5



Day 7



**Figure 4.17:** Immunocytochemical staining fluorescent micrographs of Ki-67 expression associated with cell proliferation within NG108-15 cells cultured on CS, CC, CC2 and COL at 1, 3, 5 and 7 days. Scale bar - 50 $\mu$ m.



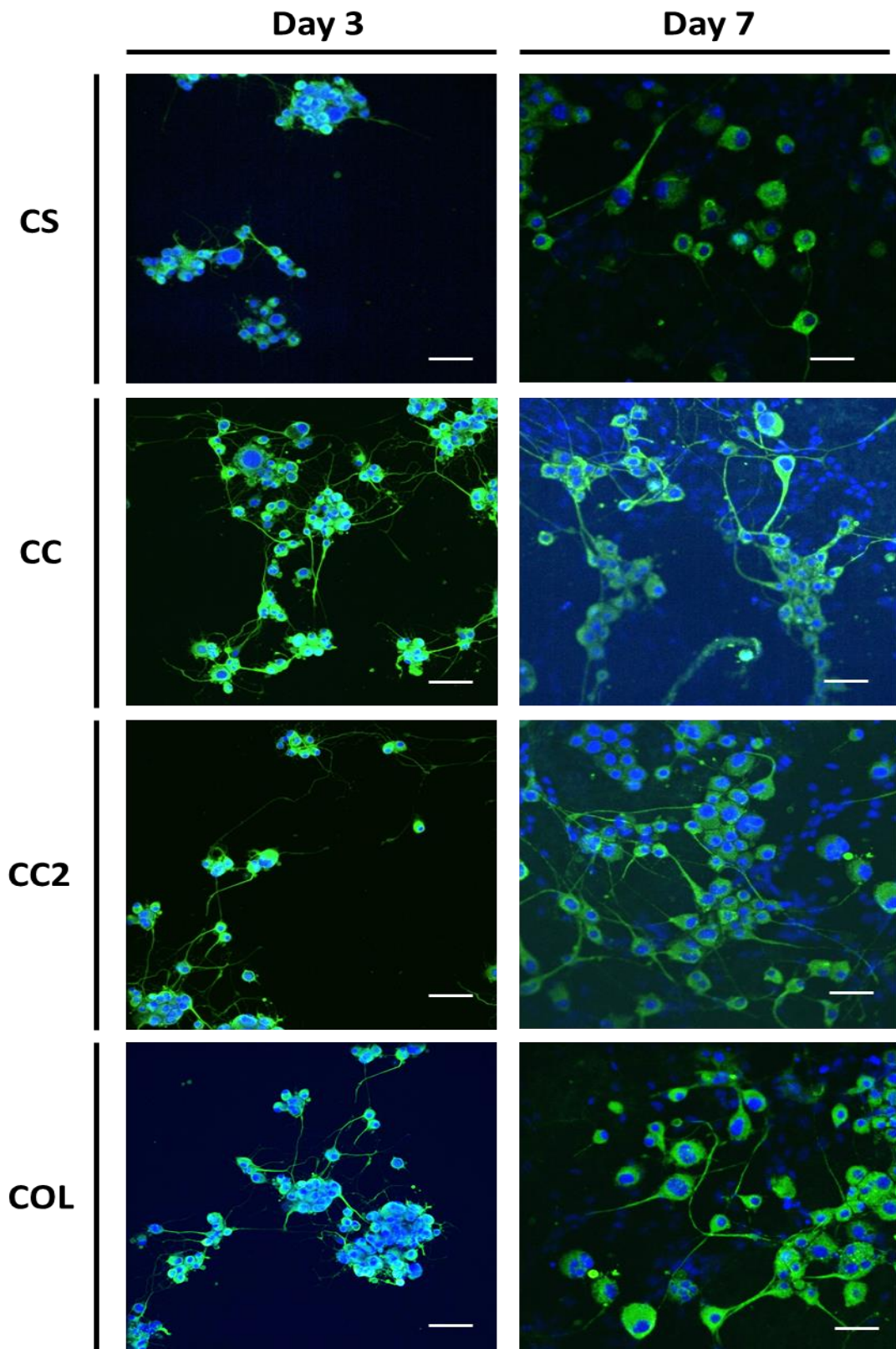
**Figure 4.182:** Quantification of MAP2 (top) and Ki-67 (bottom) expression from immunocytochemical staining for NG108-15 cells cultured on CS, CC, CC2 and COL at days 1, 3, 5 and 7.

#### 4.3.11 Neurite Quantification of NG108-15 cells Cultured on Hydrogels

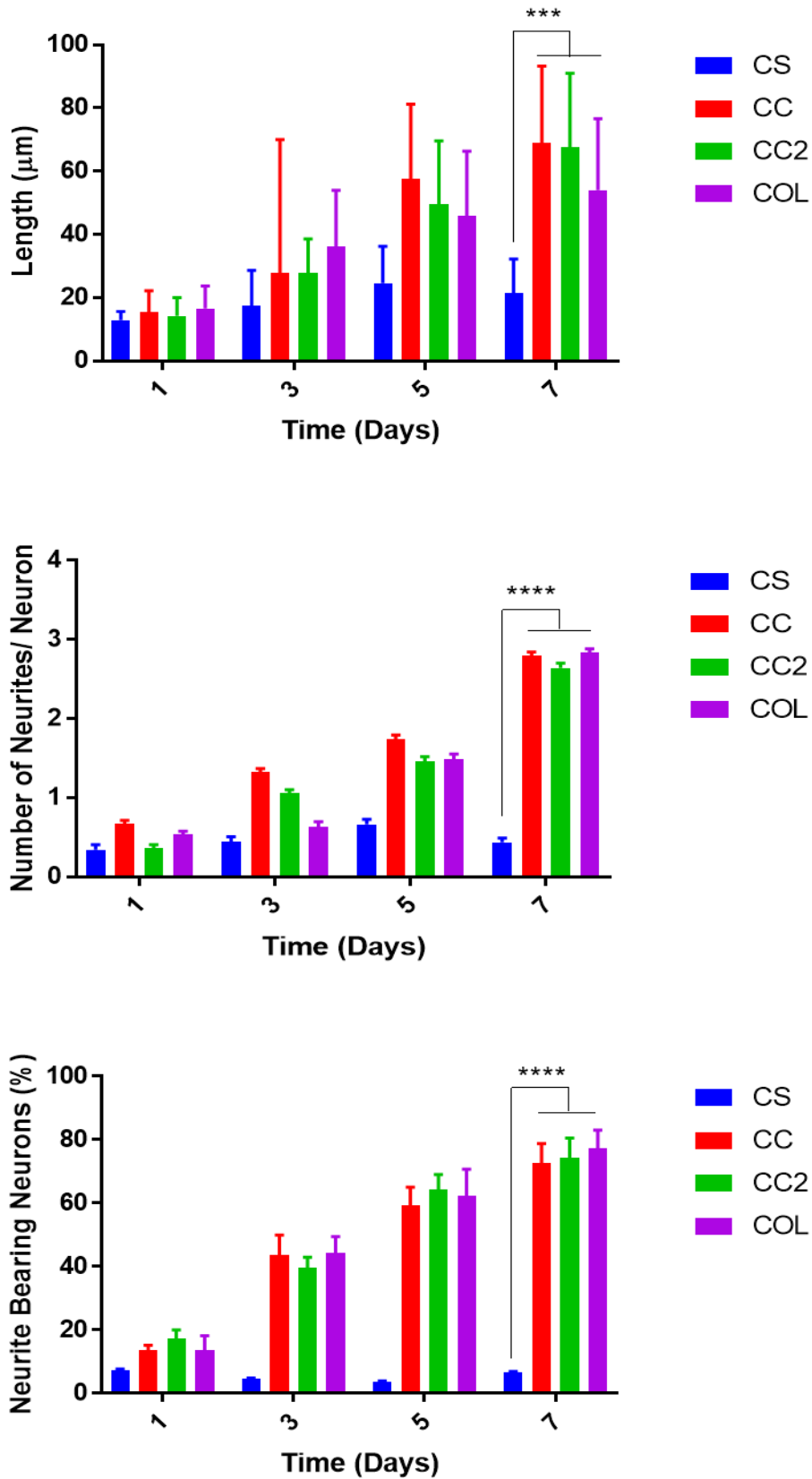
Neurite outgrowth was then quantified from NG108-15 cells cultured on the hydrogels. This was compared with the data from those previously characterised on tissue culture plastic, demonstrating the efficacy of the hydrogels in supporting neuritogenesis. NG108-15 cells were differentiated using the differentiation protocol established (section 4.2.1). At day 3, long neurites had extended from the cells cultured on CC, CC2 and COL but were rarely present from cells on CS (Figure 4.19). By day 7, the majority of cells had differentiated, and a network of neurites was observed on CC, CC2 and COL, demonstrating the hydrogels were suitable for encouraging neurite outgrowth. Some neurites were measured on CS at day 7, but to a much lesser extent when compared to the other materials.

Neurites were quantified as before (section 3.2.4). The mean neurite length increased by 347.2% on CC, 373.8% on CC2 and 224.9% on COL between day 1 to 7 (Figure 4.20). However, an increase in mean neurite length was not measured on CS, which only increased from  $12.85 \pm 0.92 \mu\text{m}$  to  $21.43 \pm 3.58 \mu\text{m}$ . This difference in mean length was calculated to be statistically significant between CS and CC/CC2 ( $p < 0.0001$ ) and COL ( $p = 0.0021$ ). A similar trend was seen when measuring the number of neurites present on each neuron in the field of view. By day 7,  $0.44 \pm 0.16$  mean neurites were measured on CS compared to  $2.79 \pm 0.15$  on CC,  $2.64 \pm 0.18$  on CC2 and  $2.83 \pm 0.15$  on COL respectively. The difference between these measurements was highly statistically significant ( $p < 0.0001$ ). The number of neurites bearing neurons was also measured and by day 7 was observed to increase by 10-fold to  $72.5 \pm 6.4\%$  on CC,  $74.2 \pm 7.0\%$  on CC2 and to  $77.3 \pm 5.76\%$  on COL but remained below  $6.6 \pm 0.47\%$  on CS. The difference between these means was also highly statistically significant ( $p < 0.0001$ ). These measurements demonstrated that neuritogenesis is highly dependent on the physicochemical forces present within the hydrogel.

**βIII Tubulin / Hoechst 33342**



**Figure 4.19:**  $\beta$ -III Tubulin expression stained by immunocytochemistry of NG108-15 cells cultured on CS, CC, CC2 and COL at day 3 and day 7. Representative images were taken by spinning disc confocal microscopy. Scale bar - 50 $\mu$ m.



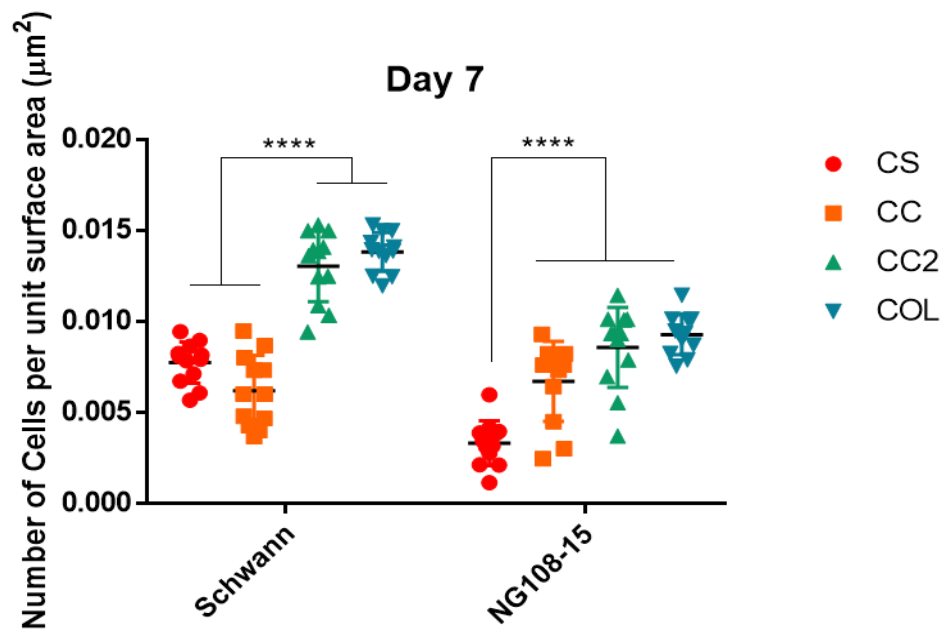
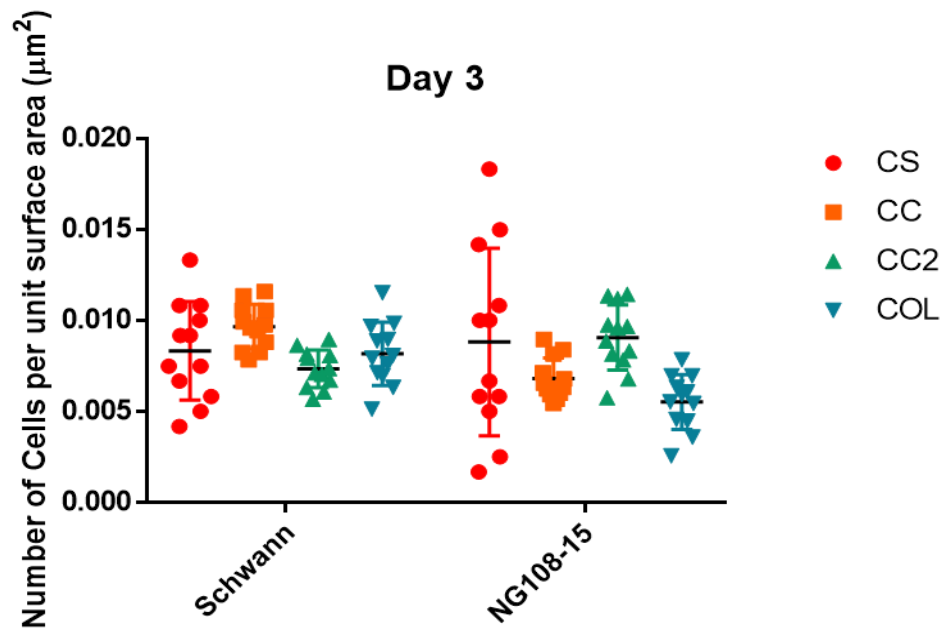
**Figure 4.20:** Quantification of measures for analysis of NG108-15 cell differentiation. Bar charts show mean neurite length (top), mean number of neurites per neuron (middle) and the percentage of neurite bearing neurons (bottom). Analysis was carried out on CS, CC, CC2 and COL hydrogels at 1, 3, 5 and 7 days.



#### 4.3.12 Cell Density Calculations on Hydrogels

Cell density was measured to compare the cell adherence properties of the hydrogels, which could influence the efficacy of the hydrogels when used in a NGC. Both Schwann cells and NG018-15 cells were quantified (Figure 4.21). For Schwann cells, at day 3, the number of cells did not differ ranging from  $0.0093 \pm 0.0025$  cells per  $\mu\text{m}^2$  on CC to  $0.0076 \pm 0.0019$  cells per  $\mu\text{m}^2$  on CC2. For NG108-15 cells, cell density peaked on CC2 ( $0.0087 \pm 0.0035$  cells per  $\mu\text{m}^2$ ) and was lowest on COL ( $0.0057 \pm 0.0033$  cells per  $\mu\text{m}^2$ ).

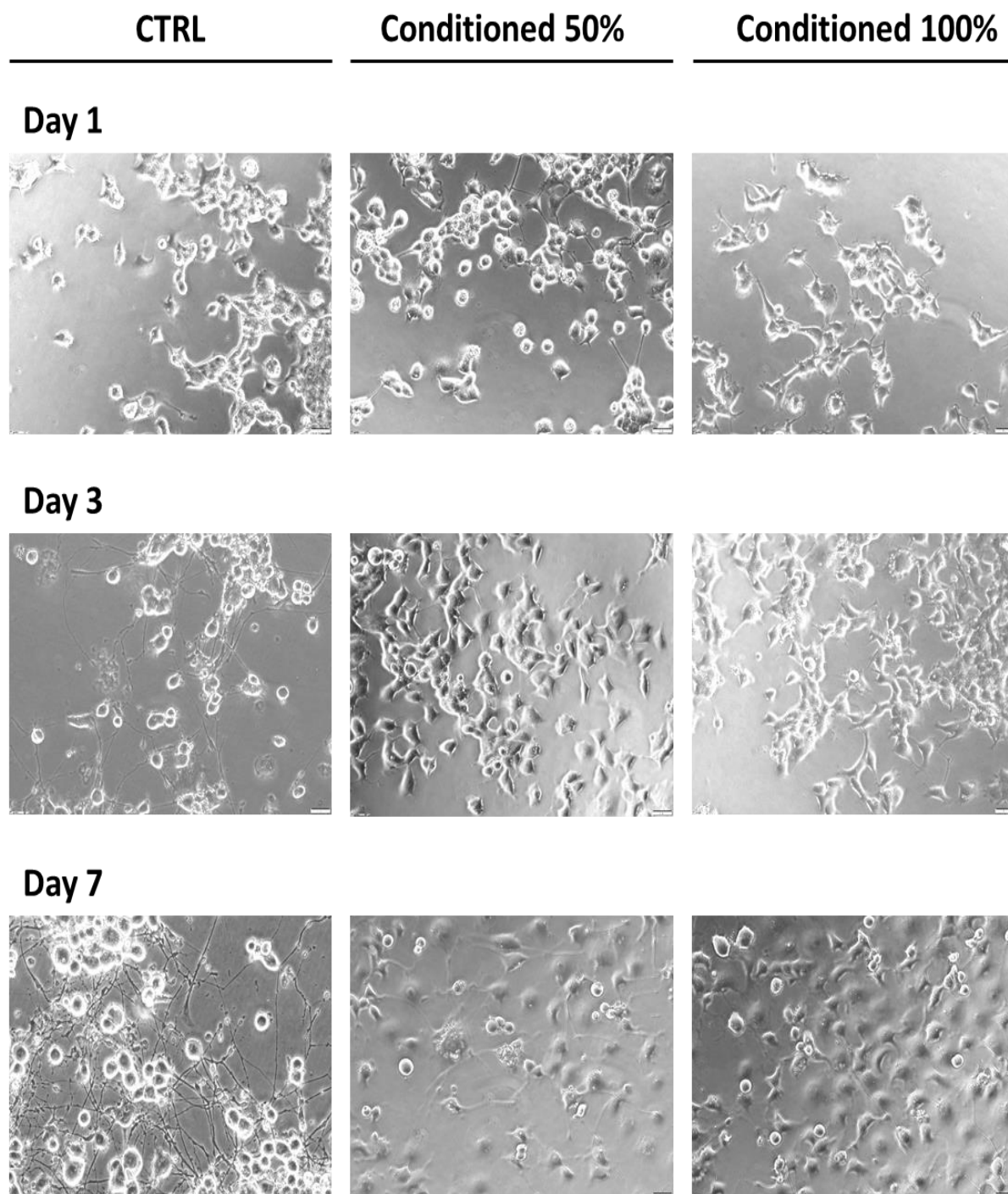
By day 7, some differences in cell density were calculated. For Schwann cells, cell density was high on CC2 ( $0.01304 \pm 0.00234$  cells per  $\mu\text{m}^2$ ) and COL ( $0.0138 \pm 0.0026$  cells per  $\mu\text{m}^2$ ) compared to CC ( $0.0062 \pm 0.0019$  cells per  $\mu\text{m}^2$ ) and CS ( $0.0077 \pm 0.0014$  cells per  $\mu\text{m}^2$ ). For NG108-15 cells, cell adherence increased as chitosan content decreased however the cell density increased for CC, CC2 and COL. Peak cell density was measured on COL ( $0.0093 \pm 0.0009$  cells per  $\mu\text{m}^2$ ). The density of cells was significantly higher on CC, CC2 and COL compared to CS for NG108-15 cells ( $p < 0.0001$ ).



**Figure 4.21:** Quantification of cell density for both Schwann and NG108-15 cells cultured on CS, CC, CC2 and COL for 3 and 7 days.

#### 4.3.13 NG108-15 Differentiation with Schwann Cell Conditioned Media

NG108-15 cell differentiation using the established protocol (CTRL) was compared with groups cultured in media conditioned with soluble factors from Schwann cell cultures growing on tissue culture plastic (Figure 4.22). Cells were cultured for up to 7 days and neurite outgrowth was assessed as this has been used as a marker for differentiation on both polyamide (section 3.3.10) and hydrogel (section 4.3.11) materials. NG108-15 cell differentiation was clearly optimal when using the established protocol, as the culture showed that a neuritic network had been established by day 7 on CTRL. Using conditioned media in a 50% v/v mixture with differentiation medium resulted in some cells undergoing neuritogenesis, a marker of differentiation, but also led to an increase in the overall number of cells, indicating that some cells were still proliferating. For cells that were incubated in the 100% conditioned medium for 7 days few neurites were observed; however, there was a marked increase in the number of cells.

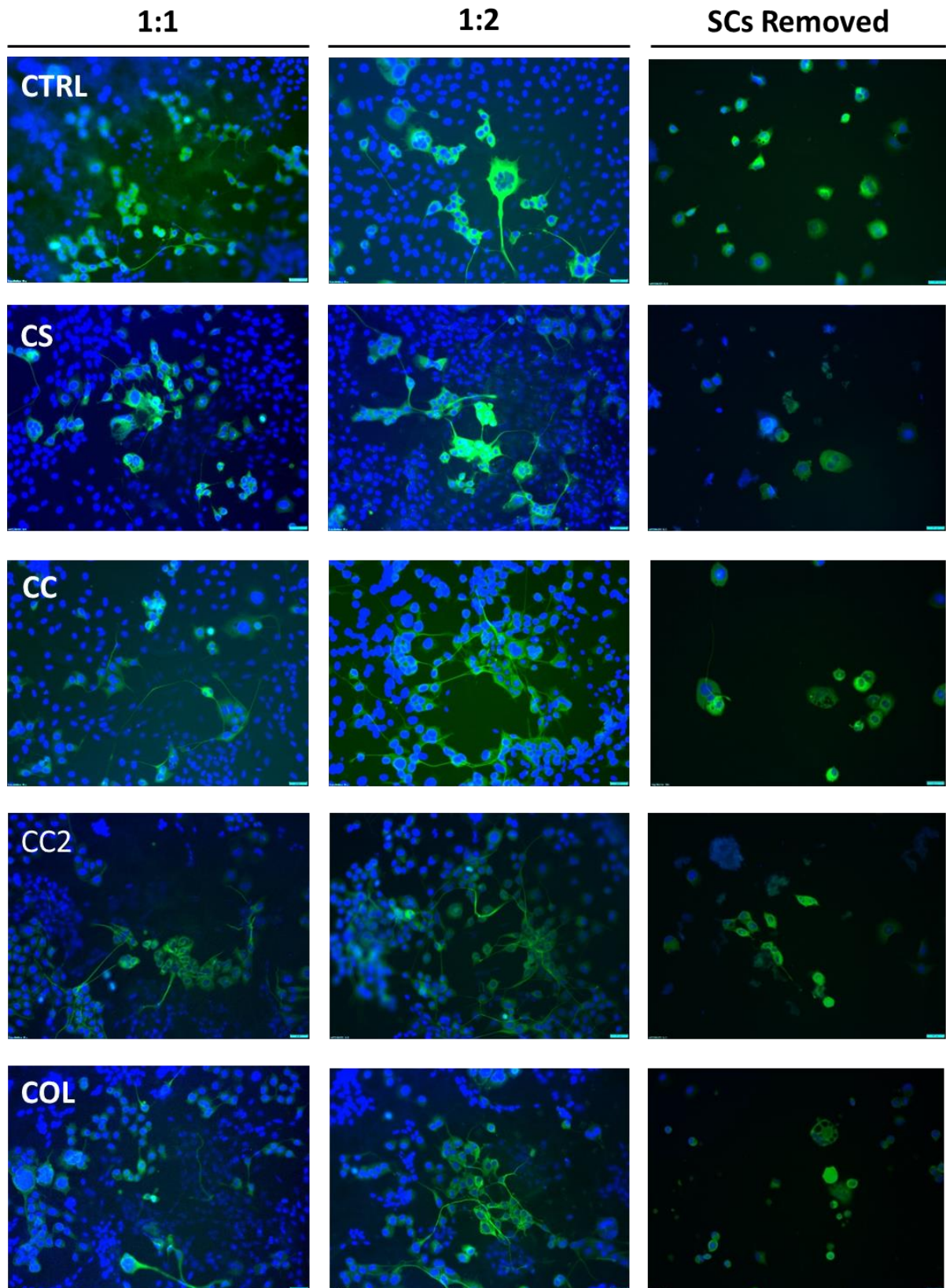


**Figure 4.22:** NG108-15 cell differentiation from conditioned Schwann cell media (50% or 100%) and controlled with Differentiation Media (CTRL) to assess neurite formation. Representative brightfield images showing the cells and neurites at day 1, 3, 5 and 7. Scale bar - 20 $\mu$ m.

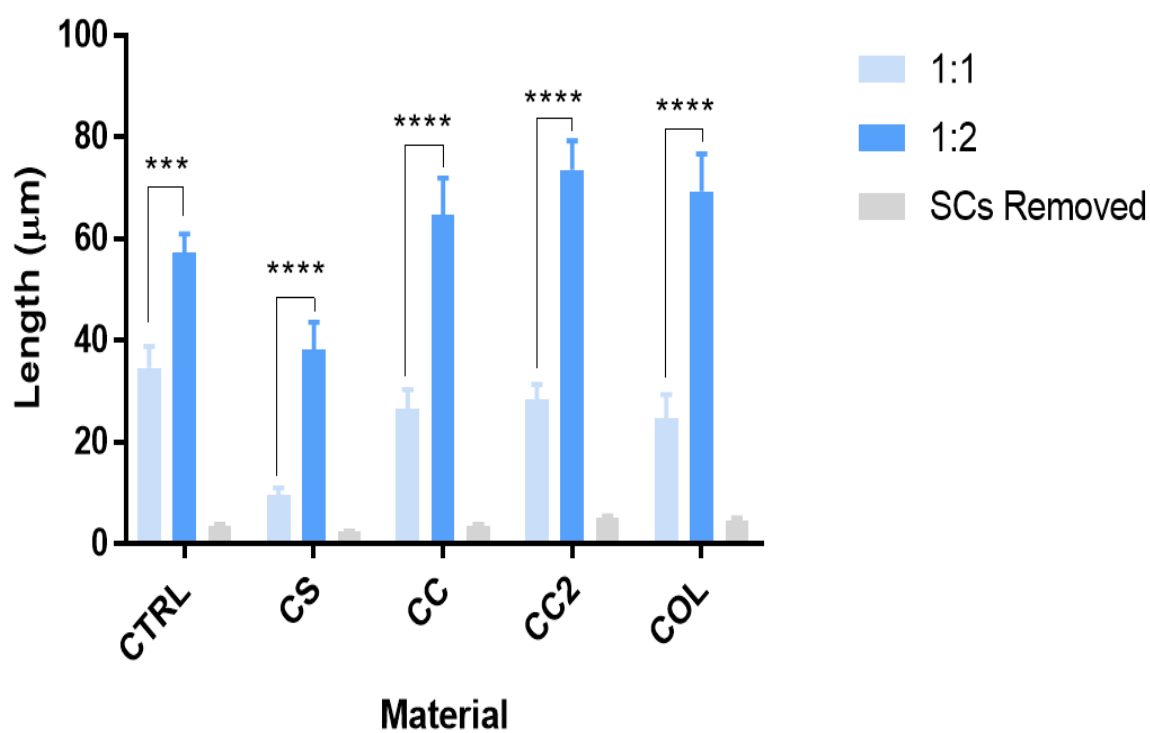
#### 4.3.14 Schwann Cell-Mediated NG108-15 Differentiation Analysis

To elucidate whether Schwann cell presence had an influence on NG108-15 cell neurite extension and whether this effect was confined to either CS-based or COL-based hydrogels, NG108-15 cells were co-cultured with Schwann cells (Figure 4.23). As the effect of co-culturing with Schwann cells was compared as well as the effect of changing the hydrogel, tissue culture plastic was used as a control (CTRL). When Schwann cells were cultured in a 1:1 ratio with NG108-15 cells, neurite extension was observed at day 7 on CTRL, CC, CC2 and COL but rarely on cells cultured on CS.

However, when the Schwann cell population was doubled, neurite extension was observed on all materials when using Schwann cell media containing 10% FCS. Interestingly, when Schwann cells were cultured on the materials, but were removed prior to NG108-15 seeding, the cells were incapable of extending neurites in the Schwann cell media. These effects were quantified by measuring the mean neurite length calculated in each condition (Figure 4.24). An increase of 123.1% was calculated on CTRL, 245.5% on CS, 138.4% on CC, 170.4% on CC2 and 173.1% on COL between the 1:1 and 1:2 Schwann to NG108-15 co-cultures. This increase was compared for statistical analysis, and the increase in mean neurite length difference was consistently significant ( $p=0.0003$  for CTRL,  $p<0.0001$  for CS, CC, CC2 and COL inclusively). The mean neurite length (peaking on CC2 at  $73.5 \pm 8.6 \mu\text{m}$ ) was comparable to levels measured between days 5 and 7 when NG108-15 cells were cultured using the established differentiation protocol (section 4.3.11).



**Figure 4.23:** Immunocytochemical staining of  $\beta$ -III Tubulin expression, counterstained with Hoechst 33342 for labelling nuclei, representative images of NG108-15 cells co-cultured in a 1:1 or 1:2 ratio with Schwann cells, or cultured on substrates from which Schwann cells were removed. Conditions for the co-culture included CTRL, CS, CC, CC2 and COL. Scale bar - 20 $\mu$ m.

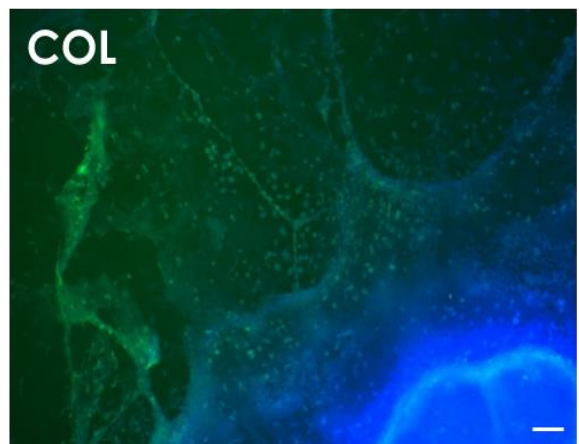
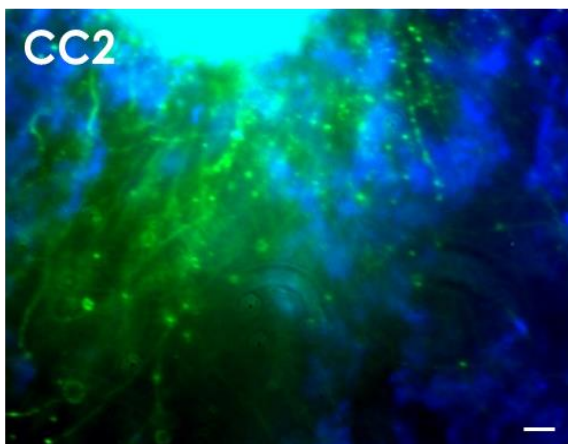
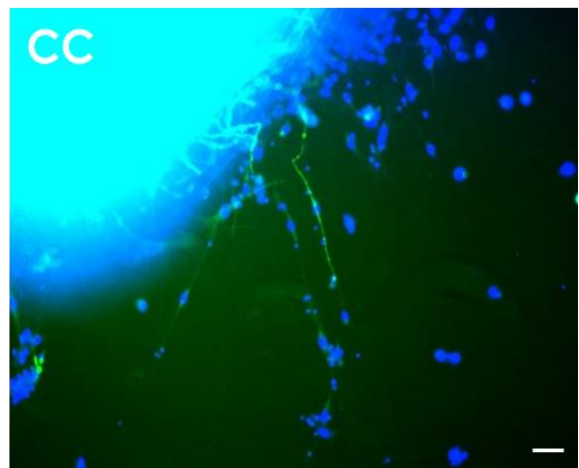
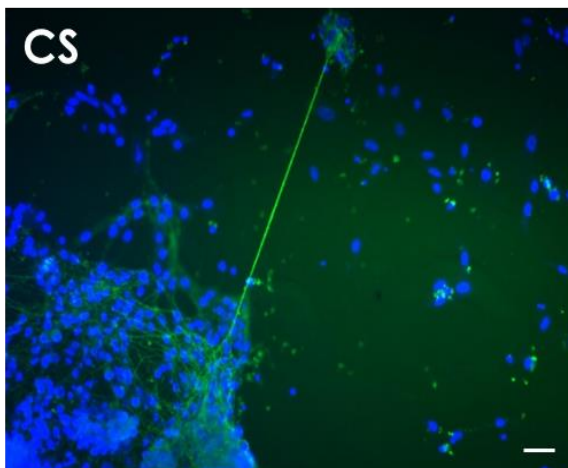
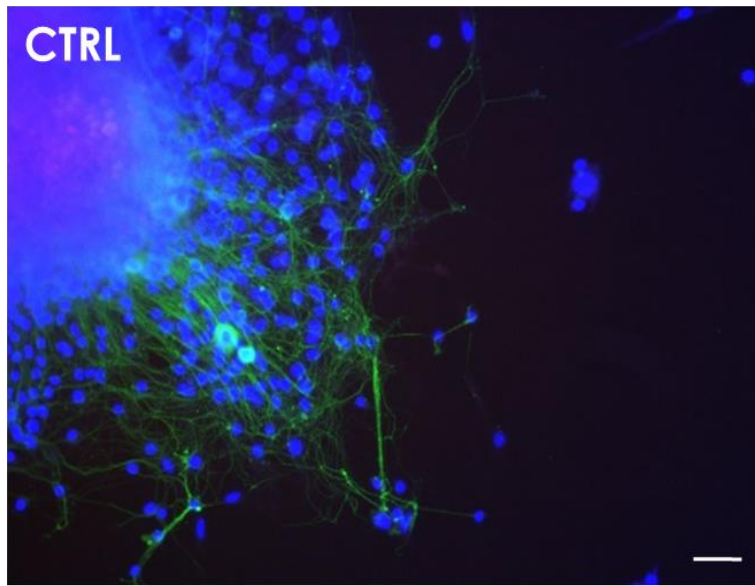


**Figure 4.24:** Quantification of mean neurite length measurements calculated from  $\beta$ -III positive cells for cells cultured in co-culture with Schwann cells (1:1 and 1:2) or when Schwann cells were removed. Calculations were carried out for CTRL, CS, CC, CC2

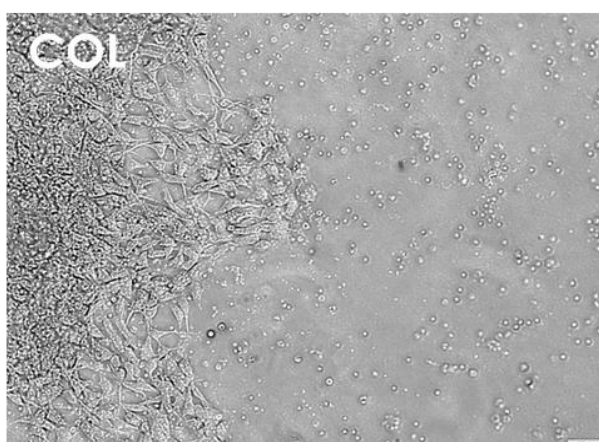
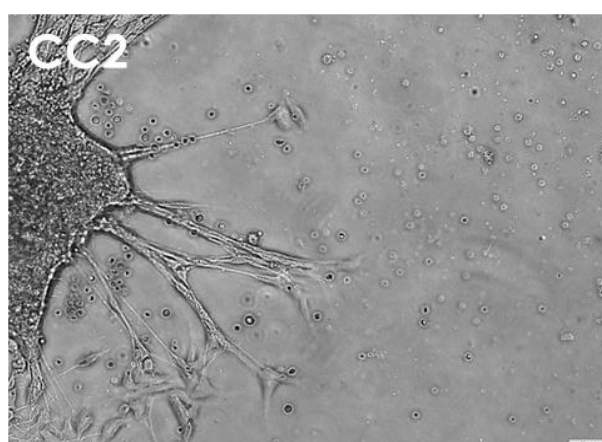
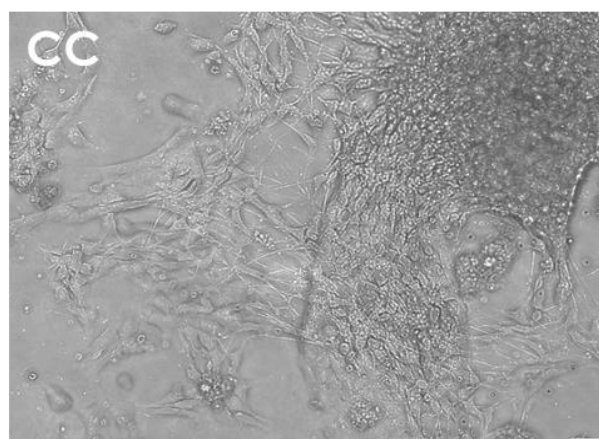
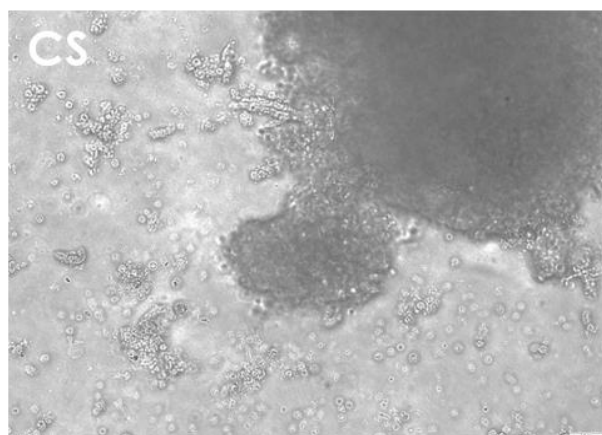
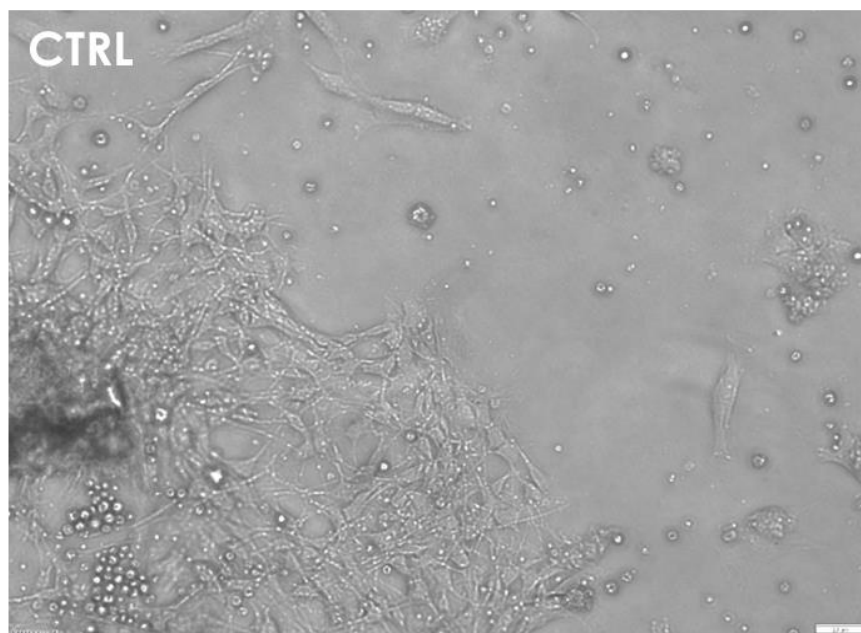
#### 4.3.15 Dorsal Root Ganglia Organotypic Culture

Dorsal root ganglia (DRGs) were cultured on the hydrogels to compare the data measured from NG108-15 and Schwann cells with an organotypic model of peripheral nerve. The tissue culture plastic surface was used as a negative control to compare neurite extension. The outgrowth was compared qualitatively, using fluorescence and brightfield microscopy (Figures 4.25 and 4.26 respectively). Neurite outgrowth was clearly observed on the CTRL surface demonstrating the use of organotypic culture in modelling neurite outgrowth. Outgrowth was similarly observed to occur on CC, CC2 and COL hydrogels but was limited on CS, which was also not supportive of DRG adhesion and resulted in limited outgrowth. Neurite outgrowth from DRGs was therefore quantified on the CTRL, CC, CC2 and COL materials for both mean outgrowth length and the orientation of the outgrowth (Figure 4.27). Mean length peaked on CC2 ( $259.9 \pm 16.9 \mu\text{m}$ ) and secondly on CC ( $250.2 \pm 32.7 \mu\text{m}$ ). The mean outgrowth length was similar on COL ( $213.0 \pm 18.6 \mu\text{m}$ ). Outgrowth length was lowest on the CTRL surface ( $156.8 \pm 11.2 \mu\text{m}$ ). A significant difference neurite outgrowth was measured when comparing the CTRL to COL ( $p=0.0091$ ) and to CC/CC2 ( $p<0.0001$ ). The angle of outgrowth was also measured and displayed onto histograms, outgrowths did not show any particular preference for sprouting and were uniform about the perimeter of the DRG explant (the area with the highest density of nuclei in Figure 4.25). This result demonstrated that the surfaces produced (CC, CC2 and COL) were isotropic in nature.

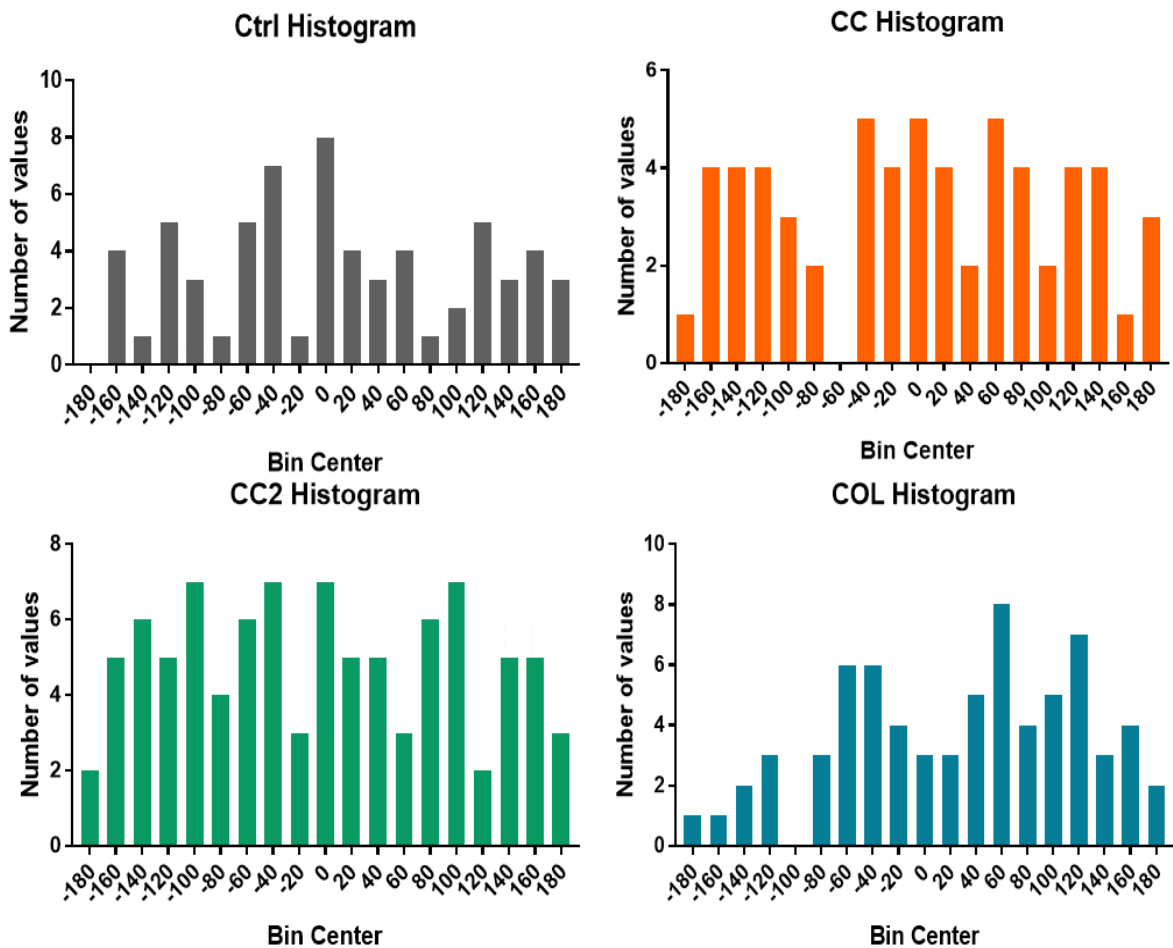
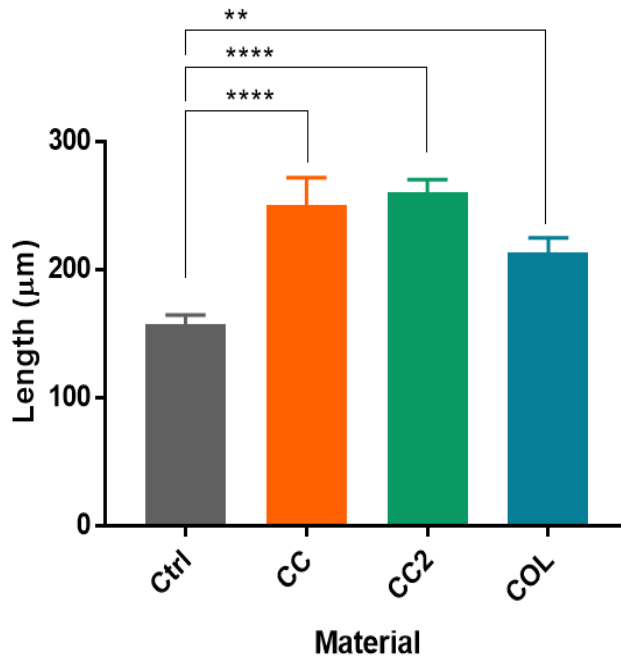




**Figure 4.25:** Immunocytochemical staining of DRGs with  $\beta$ -III tubulin, counterstained with Hoechst 33342, and imaged using widefield epifluorescence microscopy cultured on CTRL, CS, CC, CC2 and COL. Scale bar - 50  $\mu$ m.



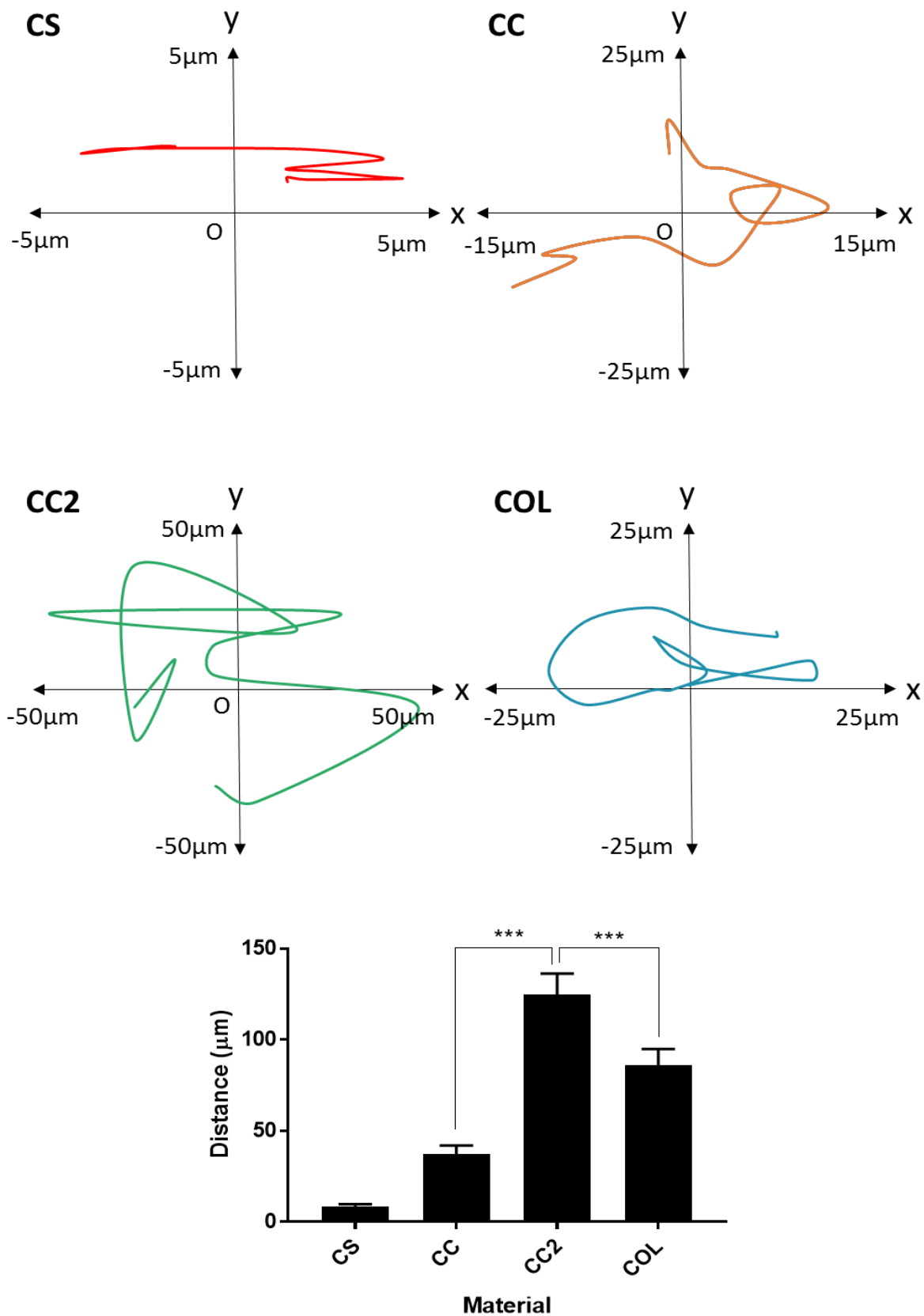
**Figure 4.26:** Representative images of DRGs imaged using Brightfield microscopy, cultured on CTRL, CS, CC, CC2 and COL. Scale bar - 50 $\mu$ m.



**Figure 4.27:** Quantification of neurite outgrowth from DRGS cultured on CTRL, CC, CC2 and COL materials. Histograms show the distribution of neurite outgrowth angles from the DRG explant.

#### 4.3.16 Schwann Cell Migration

Schwann cell migration was analysed to compare the speed of the Schwann cells as they interrogated the hydrogel environment on each material. Schwann cells could change their axis of orientation to a higher degree on CC2 compared to COL and CC. Schwann cells cultured on CS were often measured to remain moving along the axis of their polarity and had fewer degrees of freedom for changing orientation. Representative traces illustrate the findings (Figure 4.28). Measurement was restricted to 24 hours and cells cultured on CC2 were more capable of increased mean total track length. Distance was longest on CC2 ( $123.9 \pm 18.0 \mu\text{m}$ ), which was 40.9% higher than COL ( $87.4 \pm 15.8 \mu\text{m}$ ) and 184.2% higher on CC ( $43.6 \pm 7.9 \mu\text{m}$ ). These differences were statistically significant ( $p=0.00066$  for COL and  $p=0.00093$  for CC when compared to the mean track length of CC2). The mean speed was also compared amongst Schwann cells on the materials. Schwann cells speed was lowest on CS ( $0.00124 \pm 0.0002 \mu\text{m/s}$ ), which increased as the collagen content. The speed of cell migration within the 24 hour period was  $0.00232 \pm 0.0003 \mu\text{m/s}$  for CC,  $0.00283 \pm 0.0004 \mu\text{m/s}$  for CC2 and  $0.00359 \pm 0.0003 \mu\text{m/s}$  for COL. The difference between mean speed measured on CS and the other materials was statistically significant ( $p=0.00035$  for CC,  $p<0.0001$  for CC2 and for COL).

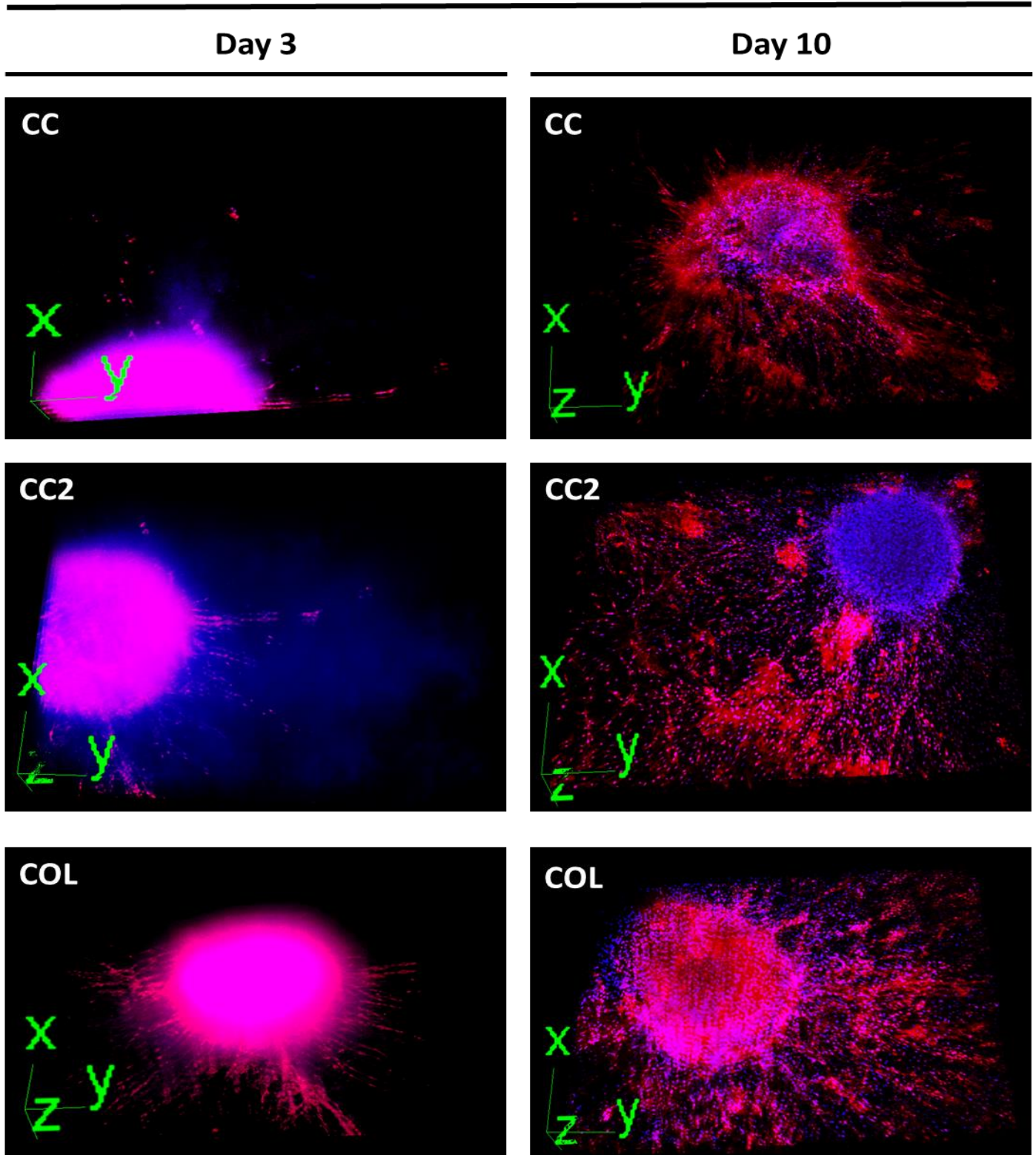


**Figure 4.28:** Representative traces of the track length of Schwann cells cultured on CS, CC, CC2 and COL over 24 hours (top panel of four Cartesian graphs). Traces were analysed and used to quantify the mean speed and distance travelled over the 24 hour period (bottom

#### 4.3.17 Gliospheroid Encapsulation and Migration Study

Schwann cells were encapsulated into collagen containing gels after confirmation that CC, CC2 and COL were supportive of DRG outgrowth (section 4.3.15). At day 3, S100 staining confirmed the presence of Schwann cells within the spheroid culture and some arrangement of Schwann cells into cords could be imaged (Figure 4.29). This was particularly pronounced in COL compared to CC and CC2 at day 3. By day 10, extension of the glial cells into the hydrogel from the spheroid was observed. On CC, cords of cells were observed up to  $134.5 \pm 34.6 \mu\text{m}$  from the periphery of the spheroid (Figure 4.29). However, the expansion of glia and migration of cells within the hydrogel was most evident for CC2 and COL. Clear bands of cells were observed radiating from the periphery of the spheroid. The migratory front of the cells measured  $254.4 \pm 43.7 \mu\text{m}$  in CC2 hydrogels and  $164.9 \pm 53.3 \mu\text{m}$  in COL hydrogels. The difference in migration between migration in CC and CC2 hydrogels was statistically significant ( $p=0.00094$ ). A significant difference in the migration distance of encapsulated cells was measured when CC2 and COL were compared ( $p=0.00085$ ).

S100 / Hoechst 33342



**Figure 4.29:** Spinning disc confocal fluorescent micrographs of S100 stained Schwann cells, counterstained with Hoechst 33342, by immunocytochemistry. Extension of glial cells within the CC, CC2 and COL hydrogels was imaged at day 3 and day 10 of gliospheroid encapsulation culture.

## 4.4 Discussion

### 4.4.1 Biocompatibility of Hydrogel materials with NG108-15 cells

The MTT assay was optimised to ensure that the cell adherence properties of the hydrogel systems would directly affect the results (absorbance at 570 nm), so that the model could simulate the adherence of neuroglial cells to the NGC material were it to be implanted in vivo. Through specific interactions between the plasma membrane and the biopolymer, the surface chemistry of the system is vital to ensuring that adhesion complexes can be set up to expedite cell expansion and colonisation of the injury site. This is particularly relevant for Schwann cells present within peripheral nerve. This will be assessed in detail following selection of the optimal hydrogel.

The reason the cytotoxicity studies were carried out using NG108-15 cells was to ensure that the system would host neural cells and support neurite sprouting, as this was earlier identified as a quantifiable phenomenon that could be used for material selection for use in the NGC (section 3.3.2). The results show that COL and CS were clearly able to support the expansion and maturation of NG108-15 cells. There was a general trend whereby increasing the hydrogel's concentration led to a decrease in MTT signal, which led to the generation of the hypothesis that lower concentration hydrogels, such as 1% COL and 1% CS (hypothesised to affect hydrated substrate stiffness: later confirmed by AFM in section 4.3.6). All the hydrogels have been examined for their use in the application of peripheral nerve repair in literature (reviewed in section 1.4.2 – 1.4.9). However, it is not common for hydrogel systems to be compared in a study with a uniform method whereas in these experiments this has been achieved. Where there was a highly significant difference between the MTT absorbance values for the negative control (cells on tissue culture plastic) and the lowest concentration hydrogel, as was the case for MCL and AGN, it is important that this confirmed that these hydrogels without further modification, would not support the expansion of cells in vivo. Calcein AM and Ethidium Homodimer-1 staining allowed for initial observations of neural cell morphology and could be compared to the cytotoxicity data. The staining confirmed that MCL and AGN did not support the adherence of the NG108-15 cells due to the rounded morphology imaged which produced significantly lower cell viability (section 4.3.2). The same trend was observed, particularly by day 7, where cell viability was significantly lower for the highest concentration hydrogels such as CS 1.5%, MCL 3.0% and AGN 6.0%.



These findings align with the literature, where it has been emphasised that ex-vivo polymerisation is required for peripheral nerve applications as the implant must be continuous and parallel to the direction of axonal outgrowth mimicking the column of Schwann cells that forms (Aurang et al., 2012). A key challenge in engineering neural tissue arises when emulating native histological structures hence the importance in quantifying neurite outgrowth as they extend across glial tissue in vivo and were hypothesised to extend across hydrogels which served to replace lost glial tissue (Woerly, 1997).

#### 4.4.2 Selection of Chitosan and Collagen and Mechanical Analysis

Following observations that both Chitosan and Collagen are biocompatible with NG108-15 cells, it was hypothesised that the unique properties of the biomaterials could complement one another by blending for use in the NGC because the collagen alone forms a low viscosity gel that is easy to rupture. As the increase in weight % of both CS and COL lead to decreased cell viability when assessed by MTT assay, the materials were blended in a 1:1 (CC) and 1:2 (CC2) ratio of CS to COL. These materials were evaluated by FTIR, DSC, SEM and AFM analyses to ascertain the material properties of the pure materials and the blends. Strong transmittance peaks for COL included nitrile, amine and amide peaks as expected, with both blends showing transmittance in these areas as detailed (Table 4.1). Further, for CS, strong transmittance peaks were observed for hydroxyl, carbonyl, amine and alkyl groups, indicative of the materials showing the glucosamine structure (Sionkowska et al., 2013). The DSC analysis revealed more evidence suggesting that the hydrogel blends were homogeneous as their melt curves showed endothermic peaks at approximately 150°C and increasing with the increase in COL content. The double peak measured on CC2 and COL also confirmed that collagen was dominant in these blends with the peak at 100°C attributed to the presence of water although a primary heating cycle up to 100°C was used to evaporate excess water from the dried samples before analysis (section 4.3.4).

When observed using SEM, it was clear that the materials were porous, three-dimensional and a network of polymer chains had formed which was sought after prior to cell culture to mimic the 3D structure of nerve (section 4.3.5). However, an interpenetrating network was not imaged on COL and could have influenced the mechanical properties assessed by AFM. Also, the freeze-drying method for obtaining SEM images of hydrogels has been used previously and could be

optimised by opting for cryo-SEM imaging to preserve the porous structure although this was not available in this project (Pourjavadi and Kurdtabar, 2007; Marmorat et al., 2016).

The Hertz model was chosen following the SEM observations which confirmed that the materials were isotropic and homogeneous for the hydrogel phase and it was assumed that the soft hydrogels would not deform the indenting probe. Young's moduli were fitted to the Hertzian model using the program (methodology detailed in section 4.2.6). Nanomechanical analysis is increasingly important for characterising the ECM or the exogenous hydrogel material and relating to cell morphology which is affected by substrate elasticity as biomechanics can affect the ability of cells to interact with the implant (Wenger et al., 2007; Dimitriadis et al., 2012). Elastic moduli confirmed the softness of the hydrogels studied ranging from 155Pa to 206Pa (section 4.3.6). At low concentrations, the gels were hypothesised to have higher swelling ratios, although not tested in this study, as there would be a less dense network of polymer chains and this can be conducive to cell infiltration in vivo (Kaczmarek and Sionkowska, 2017). Overall, CS and COL demonstrated a high degree of miscibility and offered low mechanical strength. However, crucially, the hydrogel was easily shaped which is beneficial for application to nerve where a specific, uniform diameter of the nerve is mimicked. The bulk elastic modulus was calculated through AFM analysis, although there was clearly a distribution of moduli as expected due to the distribution of hydrated pores within the hydrogel network as observed using SEM. Although the hydrogel was homogeneous and produced a clean gel which had not resorbed during cell culture, the system is capable of biodegradation and this is a parameter that can aid neuroglial cells to infiltrate the implant volume. Although not studied, this effect has been reported in literature where increasing the percentage of chitosan led to a slower degradation rate possibly due to the steric hindrance phenomenon between the chitosan and collagen chains after blending which delayed lysozyme enzymatic activity (Tangsadthukan et al., 2006). This effect could be beneficial in vivo where fast degradation of the hydrogel may be counterproductive if a critical number of regenerative Schwann cells have not colonised the implant.

#### 4.4.3 Cell Proliferation and Adherence

Blending natural polymers was used to achieve a higher degree of cell adherence. The CS/COL blends were examined in closer detail for their ability to host NG108-15 cells, Schwann cell, DRG explants and Gliospheroids. Specifically, the cell-adhesive properties of collagen has been utilised

to increase the efficacy of neural scaffolds when implanted in vivo (Georgiou et al., 2015). Due to the complexity of the nervous system, designing effective neural scaffolds is difficult as the mechanical properties must match the tissue, the scaffold must be reorganised or similar in histological architecture to the host site and the scaffold must facilitate the complex cell-to-cell signalling via neurotrophic/growth factors at play during post-injury events (Ayala-Camirero et al., 2017). NG108-15 cells were used as opposed to the PC-12 cell line for their robust cell culture and as a high throughput tool at the first level of assessing the hydrogel materials and later CS/COL blends. Then it was revealed that neurite extension was dependent on the presence of Schwann cells when cultured in growth media (section 4.3.14), not differentiation media as used when the culture method was optimised (section 3.3.1). Cell proliferation occurred at a faster rate on the COL-containing hydrogel systems which confirmed the cell-adherence properties of COL (as observed in section 4.3.8, 4.3.10, 4.3.11 and 4.3.14). However, this property was not demonstrated on CS hydrogels, where few NG108-15 cells were present, although the few cells present were shown to differentiate to a small extent (CellMask staining, section 4.3.9).

Further evidence for this was provided when MAP2 expression was quantified cells on all hydrogels, including CS, from day 3 of culture (section 4.3.10). Supplementary evidence that the NG108-15 cells had stopped proliferating following the media change to a differentiation media, was derived from the Ki-67 expression, which had significantly decreased between day 1 and 3 (Figure 4.17). Schwann cells were chosen to model the suitability of hydrogels as implants for peripheral nerve as there is widespread use of these cells in the literature and they are native to peripheral nerve, hence Rat Sciatic nerve derived cells were selected.

Schwann cell proliferation was markedly higher on the COL-containing hydrogels and the cells demonstrated strong interaction with these materials evidenced by the polarisation that occurred by 7 days (section 4.3.9). With increasing COL concentration, cell spreading increased which also supported the use of soft substrates as pure COL produced the largest cell areas and was the softest substrate when measured with AFM (sections 4.3.9 and 4.3.6 respectively). Hence softer substrates may lead to improved myelination in vivo.

#### 4.4.4 Neuroglial-Material Interaction Analysis

Neurite outgrowth was used as a parameter to demonstrate the efficacy of the blends in supporting axon outgrowth in vivo (section 4.3.11). It was clear that the hydrogels supported

neurite extension in cells cultured on CC, CC2 and COL, but this process was hindered on CS hydrogels. The number of neurites and percentage of cells that were bearing neurites followed the same pattern indicating that when COL and CS were blended together, the material was supportive of neural differentiation.

However, there was a general trend that CC and CC2 supported longer neurite length than COL when cells were differentiated using differentiation medium although not significant (Figures 4.19 and 4.20). However, when differentiation was Schwann cell-mediated, this trend was not observed, suggesting that the presence of Schwann cells accounts partially for mitigating the lack of a neurite outgrowth enhancing environment. This mechanism may have been due to the physical adherence of neurites to Schwann cells or the increase in mechanical properties that the presence of Schwann cells offers, which has been shown to affect hydrogel elasticity shown by fibroblasts (Smithmeyer et al., 2014). Although the PNS is not protected by bony cavities as the case for the CNS, the unique basal lamina and ECM within nerve has been proposed to influence Schwann cell proliferation and migration (Rosso et al., 2017). This hypothesis is further supported by work that demonstrates that YAP/TAZ co-activation led to increased expression of laminin receptors in Schwann cells, as laminin is a key structural component of the nerve ECM the mimicry of peripheral nerve ECM by use of hydrogels may be the limiting factor to encouraging effective mechanical signal transduction and encouraging myelination although this is not fully understood at present (Poitelon et al., 2016). In this study it was also demonstrated that Schwann cells were not able to produce a substantial level of secretory factors to encourage neurite outgrowth by 7 days and thus supports the hypothesis that the mechanical properties of the hydrogel should be a primary parameter investigated (section 4.3.6).

#### 4.4.5 Cell Migration Analyses

To further examine the suitability of the CS/COL blends for implantation as a PNS scaffold, the migration of Schwann cells was assayed as well as characterisation of neuro-glial cell outgrowth from DRG explant models. It was shown that when the DRGs were encapsulated by the hydrogels, there was a clear inhibitory effect of CS compared to the other hydrogels, which was indicated by the lower metabolic activity of cells cultured on CS measured by Alamar Blue assay (sections 4.3.15 and 4.3.7 respectively). The DRG culture is more complex than the single cell cultures that had been used so far in the study as the culture is organotypic and thus contains both glial cells and extending axons from sensory neurons present in the explant. The DRG was highly sensitive

and thus the culture was optimised to ensure that outgrowth was observed on the tissue culture plastic (CTRL) by using neurobasal media with a high FCS content (section 4.2.14).

The outgrowth of neurites was measured on CC, CC2 and COL and compared to CTRL, resulting in significant extension for all hydrogels. This was a key result for ensuring that cells were able to expand within the hydrogel and that the extensions showed a preference for the environment as demonstrated by the radial extensions measured (section 4.3.17). Single cell migration along the hydrogel surface was evaluated by cell tracking through live imaging over a 24 hour period (section 4.3.16). It was evident that cells were more restricted on CS surfaces compared to the blends, although even amongst a population of cells cultured on CC, CC2 and COL there were variations between migrational tracks. This qualitative observation that CS was not as supportive of cell migration was supported by the quantification which revealed that cells on CS were both slower and travelled the least in distance (Figure 4.29). However, the cells weren't highly mobile on any hydrogel and indicates that motility should be studied over a longer period or related to the enzymes on the Schwann cell membranes that degrade ECM to identify the processes by which Schwann cells navigate the injury site. Schwann cell migration was then studied further, using a gliospheroid model to simulate the outgrowth and expansion of Schwann cells infiltrating the hydrogel from injured nerve stumps (section 4.3.17). The results clearly demonstrated that Schwann cells, stained positive for neural crest marker S100, had infiltrated the hydrogel surrounding the spheroid by 10 days of culture and showed clear bands of cells forming similar to bands of Büngner as shown in other systems in literature (Jessen and Mirsky, 2016; Chen et al., 2018). This evidence of Schwann cell migration from the live imaging and gliospheroid culture correlated well with the evidence from the cell adhesion and proliferation studies to confirm that the hydrogels would be functional as an implant when introduced into a peripheral nerve repair model.

## Chapter 5: Animal Trial for Nerve Guidance Conduit

### 5.1 Introduction

Using the results generated in Chapter 3 and 4, and to satisfy the design criteria generated for the surgically implantable NGC product. CC2 hydrogel and PA6,6 were selected as the optimal materials. These materials were evaluated against a gold standard (autograft, reviewed in section 1.2.1) for their efficacy in vivo as a medical device. Autograft repair remains the reconstruction gold standard to ensure there is no tension between the proximal and distal stumps when repairing long nerve gap injuries where primary anastomosis is impossible (Millesi, 2007). In this work, NGCs were fabricated using PA6,6 as an outer wall material; some were additionally filled with CC2 hydrogels and all were implanted into transected rat Sciatic nerve repair models. The experimental groups were named 'Empty NGC', 'Filled NGC' and 'Autograft'.

A key aim for tissue engineering is to provide a graft material that mimics the ECM to provide continuity when pro-regenerative cells infiltrate the graft and reorganise the synthetic material into a tissue-like structure. Autografts provide a large supply of aligned collagen Type 1 and hence can speed up Schwann cell infiltration. CC2 hydrogel has been evaluated to be supportive of Schwann cell expansion in vitro (section 4.3.9 and section 4.3.17) (Bell and Haycock, 2012). Thus the hydrogel was used as a graft material as it was hypothesised that the increased rate of proliferation of Schwann cells in vitro (demonstrated in section 4.3.7) would encourage faster PNR. PA6,6 has been used as a NGC wall material for its strength (evaluated in section 3.3.15) and encouragement of cell attachment and alignment when embossed with grooves (sections 3.3.10 and 3.3.14 respectively).

For the in vivo investigation, nerve repair was compared for gap injury lengths of 10mm as this is the critical length identified to ensure that regeneration is correlated with the choice of NGC material and the design of the NGC as opposed to spontaneous recovery (evaluated in Table 1.4). The use of both chitosan and collagen has been investigated in PNR animal studies but the use of a chitosan/collagen blend as a novel NGC filling material has not been rigorously studied (Cui et al, 2018; Saeki et al., 2018; Li et al., 2018; Gonsalez-Perez et al., 2017). The use of PA6,6 as a NGC wall material has not been studied previously and therefore was evaluated as an empty NGC to control for the inclusion of CC2 hydrogel.

Another aspect of the design of this NGC that was investigated in the present study is the ability for the NGC to be implanted into the injured nerve using a sutureless technique. This is because when fixing the proximal or distal stumps of very fine nerve (<2mm in diameter) it is difficult to ensure that further tissue damage to the nerve's endoneurium does not occur, without using an operating microscope which is not always available. Hence, repair by suturing the epineuria to the NGC (although recognised as desirable) may in practice cause further damage to the nerve stumps and delay PNR; which is a critical factor in determining success (reviewed in section 1.5).

Sutureless repair also does not fully seal the regenerating stump from the surrounding non-nerve tissue and hence can lead to leakage of important cytokines from the stumps signalling to pro-regenerative Schwann cells (Barton et al., 2014). For instance, gelatin-elastin photo-crosslinked material has been evaluated for its adhesive properties and support of Schwann cell proliferation offering a stronger material than fibrin for sutureless repair of nerve (Soucy et al., 2018).

In the present study, the rat Sciatic nerve was regenerated in three experimental groups and was evaluated using functional and histological tests commonly used in the literature to ensure that data was comparable to current published work (reviewed in section 1.3.1). Gait analysis was evaluated by calculating the Sciatic Functional Index (SFI), derived from gait analysis, from paw prints as a measure of the plantar muscle group innervation following PNR (Margiana et al., 2017). Algesimetry was evaluated using the manual Von Frey monofilament assay, a test for mechanically induced allodynia (Haggerty et al., 2019). The Hargreaves test was also used to calculate relative levels of algesia between groups as a test for thermal hyperalgesia (Arthur-Farraj, 2012). Finally histological sections were analysed for proof of re-myelination and nerve outgrowth along the NGC by Haematoxylin and Eosin and Luxol fast blue staining (Carriel et al., 2014). These results were used to compare the efficacy of Empty NGCs, Filled NGCs and Autografts.

## 5.2 Materials and Methods

### 5.2.1 NGC Fabrication

PA6,6 sheets with a thickness of 200 $\mu$ m were cut into 12mm x 20mm sections for preparation of NGCs. Using a PDMS mould prepared by stereolithography (gift from Dr A Serio, Department of Tissue Engineering and Biophotonics, King's College London), 10 x 10  $\mu$ m grooves were embossed onto the PA6,6 sample by heating on a hot block at 220°C (determined to be just below the melting temperature for PA6,6 calculated by DSC in section 3.3.9). The PDMS stamp was placed onto the sample and wrapped in aluminium foil and placed on heat, with pressure from a 2kg weight, for 30s before being assessed for clean transfer of the microgrooves by brightfield microscopy. The cut sheets with grooves were then moulded into a rolled NGC by heating steel rods (2 mm in diameter) to 200°C, wrapping the sheet around and holding for 1 minute until the NGC had moulded to the same diameter. This resulted in a spiral shaped conduit that was sealed with adhesive only during surgery. NGCs were collected and sterilised by soaking in 90% ethanol for 1 hour, air-drying in a tissue culture hood under aseptic conditions and then exposing the NGCs to UV-irradiation for 20 minutes. Samples were placed in a sterile petri dish until used for surgical implantation (Chitnis et al., 2008).

### 5.2.2 Animals

All procedures were carried out under compliance with the Animals Scientific Procedures Act 1986, UK. Animal procedures were approved by the Animal Welfare Ethical Review Body at King's College London and licenced by the Home Office, UK, under Project Licence Number P4EC538B8 and Establishment Licence Number X24D82DFF. Male Wistar Rats were used for sciatic nerve transection and repair studies (Envigo, UK; n=12, <250g at purchase). Rats were housed in groups of three under a 12 hour light/dark cycle with access to food and water ad libitum and paper mesh for environmental enrichment.

### 5.2.3 Surgical Procedures

The first trial (pilot) was carried out to ensure that the PA6,6 NGC was safe for use when implanted as a biomaterial and was wrapped around the intact sciatic nerve (n=3). The second trial was used to examine the three experimental groups for sciatic nerve repair (n=9).



Rats were anaesthetised using vaporised Isoflurane gas in an induction chamber with an oxygen flow of 0.5L/minute. Isoflurane was vaporised to 5% for approximately 5 minutes. When anaesthesia had been induced, the rat was removed from the induction chamber and the skin of the hind leg on the left side was shaved quickly. The rat was returned to the induction chamber for a further 1-2 minutes to maintain anaesthesia. The rat was removed from the induction chamber and placed on the operating table which was covered with a sterile drape, and a nose cone fitted adjusting the isoflurane vaporiser concentration 2-3%. Tail flick and paw pinch tests were carried out to ensure no response occurred confirming anaesthesia to mechanical and painful force. The hind limb area was cleaned using ethanol wipes and the skin was excised open using a scalpel. The thigh muscles (biceps femoris and gluteal muscles) were exposed by blunt dissection to reveal the sciatic nerve. Once identified the sterile NGC was wrapped around the sciatic nerve and sealed around the circumference of the nerve for the trial (n=3 rats).

For the nerve transection and repair study, the sciatic nerve was fully transected by 6mm to produce a gap measuring 10mm (n=9 rats). The NGC was then placed carefully around the nerve stumps and wrapped tight and sealed to the stumps using histoacryl adhesive (B. Braun, UK) for Empty NGC subjects. For Filled NGC subjects, the nerve was repaired using the same method but prior to sealing the NGC 0.03 ml of CC2 hydrogel was injected into the conduit. For the Autograft subjects, instead of using an NGC, the sciatic nerve was transected and repaired with the excised tissue which was rotated and sutured back using 4-0 Vicryl sutures (Johnson and Johnson, UK). The sciatic nerve was repaired at the mid-thigh level, approximately halfway between the sciatic notch and bifurcation of the nerve. The nerve was placed into its original position and muscles were allowed to fold into place. The skin was sutured together using skin clips (from Harvard Apparatus, UK or Fine Science Tools, UK). 300µl Betamox antibiotic (150mg/ml concentration, Norbrook) was injected intramuscularly into the gastrocnemius muscle immediately after surgery and 3 days following. Opioid analgesia was also provided by subcutaneous injection immediately after surgery using Vetergesic Buprenorphine (0.05-0.1 mg/kg; Ceva, UK). Following surgery, the rats were placed in a cage with fresh bedding away from any draught to ensure that animals were not hypothermic for recovery and monitored for 2 hours after surgery to ensure recovery. Rats were monitored daily throughout and weighed at regular intervals to ensure that rats were mobile and feeding, a cut off of 4g weight loss was used to signify difficulty in mobility and rats would have been euthanised if this were the case. In the case of autophagia, signs of blood under

the toenails or lacerations to the paw, rats were euthanised by a schedule 1 method (Animals Scientific Procedures Act 1986). Animals were trained in all behavioural assays for 3 days prior to surgery to reduce exploration behaviours during testing which was deemed appropriate after pilot testing as such behaviours reduced (Bonin et al., 2014). Additionally, the Named Training and Care Office at the animal unit was consulted on the efficacy of the training schedule.

#### 5.2.4 Von Frey Testing

Animals were trained prior to surgery and tests were carried out 6 days following surgery until the experimental endpoint (30 days post operation for the pilot trial and 103 days post operation for the 3 full experimental groups). Specific Von Frey monofilaments were purchased (Ugo-Basile, Italy) which exert a force in Newtons when applied to the paw surface as follows: #2 (4.31 N), #4 (4.56 N), #6 (4.74 N), #8 (4.93 N) and #15 (5.18 N). Rats were placed in a plastic cage with a wire mesh fixed as the floor and were allowed to accommodate for 30 minutes until exploration behaviours had ceased. The up-down method was used to evaluate the paw withdrawal response in animals from the testing area of the mid-plantar hind paw sciatic nerve distribution. Testing was carried out on both ipsilateral (operated side) and contralateral (non-operated side) as control). Starting with #2 filament, the response or lack of response was recorded as an 'X' or 'O' respectively. If 'O' was recorded, then the successive filaments were used in ascending order until a response was recorded. Often no response was recorded giving a sequence of 'OOOOO' which indicated that no mechanical neuralgia was experienced. If a response, 'X', was recorded, then instead of using the higher filament for the next test, the lower filament was used i.e. #6 then #4. Filaments were applied until a maximum of three responses were recorded. These patterns were converted into quantifiable outcomes by using the Chaplan method (Chaplan et al., 1994). The 50% PWT (Paw Withdrawal Threshold) was calculated using the formula:

$$50\% \text{ PWT} = (10^{[X_f + \kappa\delta]})/10,000$$

Where  $X_f$  = value (log units) of the final Von Frey filament used,  $\kappa$  = tabular value for the pattern of filaments and responses used from Chaplan et al., 1994 (Supplementary Table 1) and  $\delta$  = mean difference (log units) between stimuli (which was 0.224).

#### 5.2.5 Hargreaves Testing

Hargreaves's method was used to assess thermal hyperalgesia (Hargreaves et al., 1988). Rats were placed into plastic boxes on a stage with a thin plastic floor, under which was placed a high-

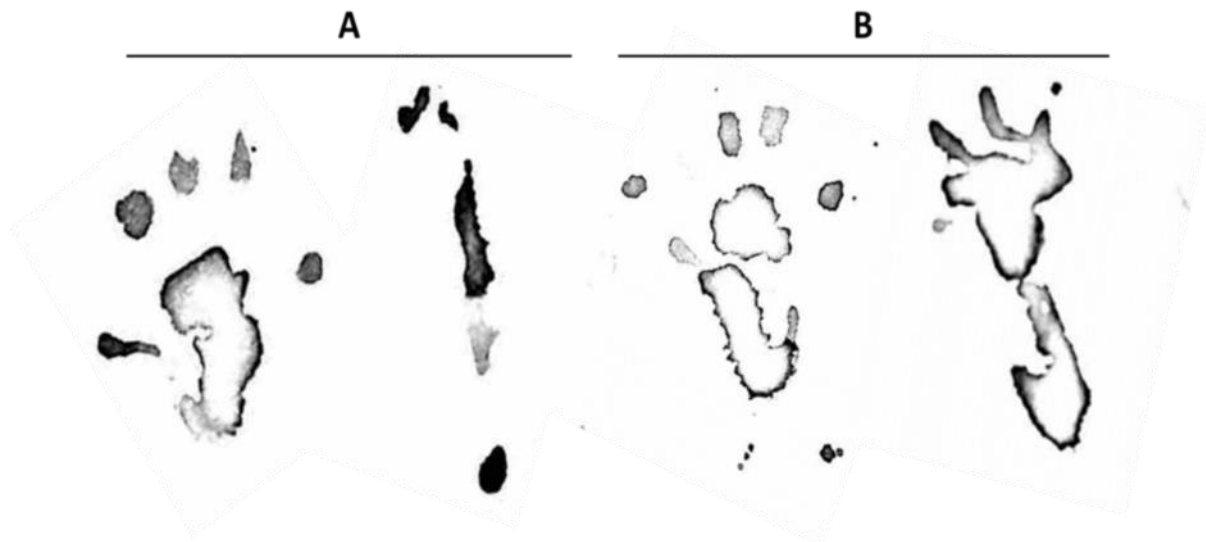
intensity light beam (Ugo-Basile, Italy). Animals were allowed to acclimatise to the surroundings by placing in the boxes for 30 minutes until the exploratory behaviour had stopped. The light beam was aimed at the plantar surface of the hind paw on both Ipsilateral (operated side) and Contralateral (non-operated side) paws. The intensity was set to 25% with a cut-off at 20 seconds (maximal response indicating no thermal hyperalgesia). The time to withdraw the paw (latency) was recorded 3 times with 5 minute intervals and averaged for quantification.

#### 5.2.6 Sciatic Functional Index (SFI)

The SFI was calculated to provide significant differences in toe spreading between the Ipsilateral and Contralateral sides. The values range from +10 (indicating full sciatic nerve function) to -100 (indicating complete transection of the nerve). The SFI is calculated as follows:

$$\text{SFI} = -38.5 \left( \frac{\text{EPL} - \text{NPL}}{\text{NPL}} \right) + 109.5 \left( \frac{\text{ETS} - \text{NTS}}{\text{NTS}} \right) + 13.3 \left( \frac{\text{EIT} - \text{NIT}}{\text{NIT}} \right)$$

Where E = experimental, N = normal, PL = plantar length, TS = toe spread (between digits 1 and 5) and IT = internal toes (between digits 2 and 4). All abbreviations are lengths measured in mm. Rats were trained to walk along paper with their hind legs dipped into food colouring to serve as ink prior to experimental data collection (lengths and representative prints supplied in Figure 5.1).



**Figure 5.1:** Representative paw prints of immediately post-surgery on the CONTRA side (A, left paw) and IPSI side (A, right paw). Representative paw prints of animals 103 days post operation on the CONTRA side (B, left paw) and IPSI side (B, right paw). Paw prints were used to measure the plantar and inter digit lengths to calculate the SFI.

### 5.2.7 Tensile Testing of Conduit Suture Method

NGCs were fabricated as described in 5.2.1 but were not filled with CC2 hydrogel. PA6,6 NGCs were all 12mm in length and 2mm in diameter. The gap injury was 10mm long but the conduits were 12mm to give some space to fix the proximal and distal stumps. Samples were either glued to tabs made of PA6,6 that measured 1 x 5 x 0.5 mm or samples were sutured with Vicryl 4.0 at both ends. Samples were loaded into a Universal Testing Machine (Instron 5569A, Norwood, Massachusetts) and loaded between two grips coupled to a 10KN load cell. Samples were pulled in tensile mode at a rate of 1mm/s until failure. The load (N) vs extension (mm) was plotted and Young's Modulus was calculated using the method described in section 3.2.13.

### 5.2.8 Histological Analysis

At the experimental end-point, rats were euthanised using schedule 1 methods. The sciatic nerve and NGC was exposed and fixed in 1% formalin solution. At least 15mm of nerve was excised to include the full NGC length. The samples were dehydrated in successive increasing ethanol solutions from 70% to 100% and then embedded in paraffin. Following embedding, histology slides were prepared by taking transverse sections (5µm thick) and incubated with haematoxylin (for 5 minutes) and eosin (for 2 minutes) with washes between stained with deionised water. Slides were rinsed using absolute alcohol and dehydrated. Slides were then cleared with xylene and mounted using pertex (Pilling et al., 2017).

Then the sections were stained with Luxol Fast Blue stain and counterstained with Cresyl Violet to show myelin and non-myelinating cells respectively (Abcam, UK) (Scholtz, 1977). Cresyl violet stain was also used to increase the contrast of Luxol fast blue stained cells. Sections were deparaffinised with fresh xylene for 5 minutes twice and hydrated in water and subsequently incubated in Luxol Fast Blue solution for 2 hours at 60°C. Samples were rinsed and differentiated by dipping into lithium carbonate solution 20 times. The samples were then further differentiated using the alcohol reagent supplied in the staining kit for a further 5 dips. Samples were immediately rinsed with deionised water to inhibit further differentiation. The samples were finally incubated with Cresyl Violet stain for 3 minutes and immediately rinsed with deionised water. Samples were dehydrated in absolute alcohol, cleared in xylene and mounted with coverslips using pertex.

Slides were imaged using a brightfield microscope. For image analysis, image J was used to take measurements of the axon diameter and myelin diameter. These measurements were used to calculate the G-ratio (myelin diameter/ axon diameter) and the myelin thickness (myelin diameter – axon diameter/ 2).

#### 5.2.9 Statistics

For data from the pilot trial, there were n=3 rats used. For experimental data there were n=3 rats per experimental group. Mean values were compared to reveal statistically significant differences by comparing using 2-way ANOVA with post-hoc Sidak's comparison and a confidence interval of 95%. These tests were chosen following normality testing with the three sigma test and adjustment to the significance level was used by the Sidak's test due to multiple comparisons in the ANOVA. Significance comparisons were carried out for the experimental data, for both Hargreaves test and SFI analysis. Statistical differences were not measured for the Von Frey data as by 56 days DPO (days post operation) signs of autophagy were present from 1 animal per group and were subsequently euthanised. Although this caused an n=2 for the remaining time points, statistical significance could still be calculated.

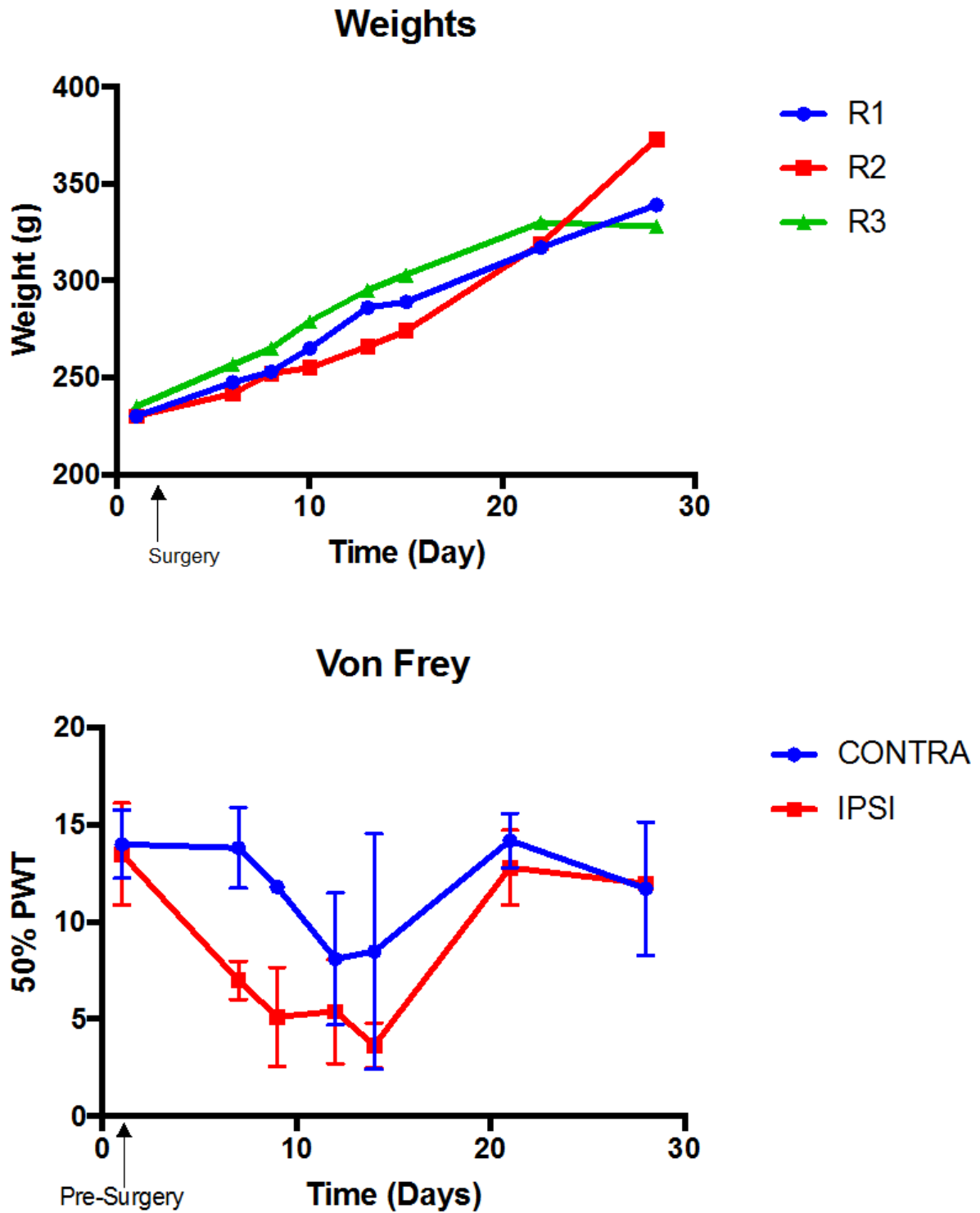
## 5.3 Results

### 5.3.1 Weight Data from Trial

Weights were measured from the rats involved in the trial of the NGC material (n=3 rats) (Figure 5.2). All 3 rats increased in weight from 234-237g at 1 day before surgery to 321-373g at day 29. There was no indication that the surgical procedure affected feeding habits.

### 5.3.2 Von Frey Data from Trial

The mean 50% PWT (paw withdrawal threshold) was calculated before surgery and after up to 29 days post operation for both the ipsilateral (IPSI) and contralateral (CONTRA) side (Figure 5.3). Pre-surgery levels were similar for both IPSI ( $14.1 \pm 3.78$ ) and CONTRA ( $14.3 \pm 1.65$ ). There was a clear difference in the 50% PWT which remained higher for the CONTRA side compared to the IPSI side. At 11 days post operation, the IPSI threshold was  $5.2 \pm 4.23$  whereas the CONTRA threshold was higher at  $7.6 \pm 4.84$ . 50% PWT had returned to baseline levels by 28 days post operation and was equal for both IPSI and CONTRA sides were ( $12.6 \pm 4.82$ ).



**Figure 5.2:** Weights from the 3 rats throughout the trial of the PA6,6 NGC over 29 days (top). Calculations plotted from Von Frey data used to calculate the 50% Paw Withdrawal Threshold (50% PWT) over 29 days (bottom) for both operated (IPSI) and non-operated (CONTRA) sides.

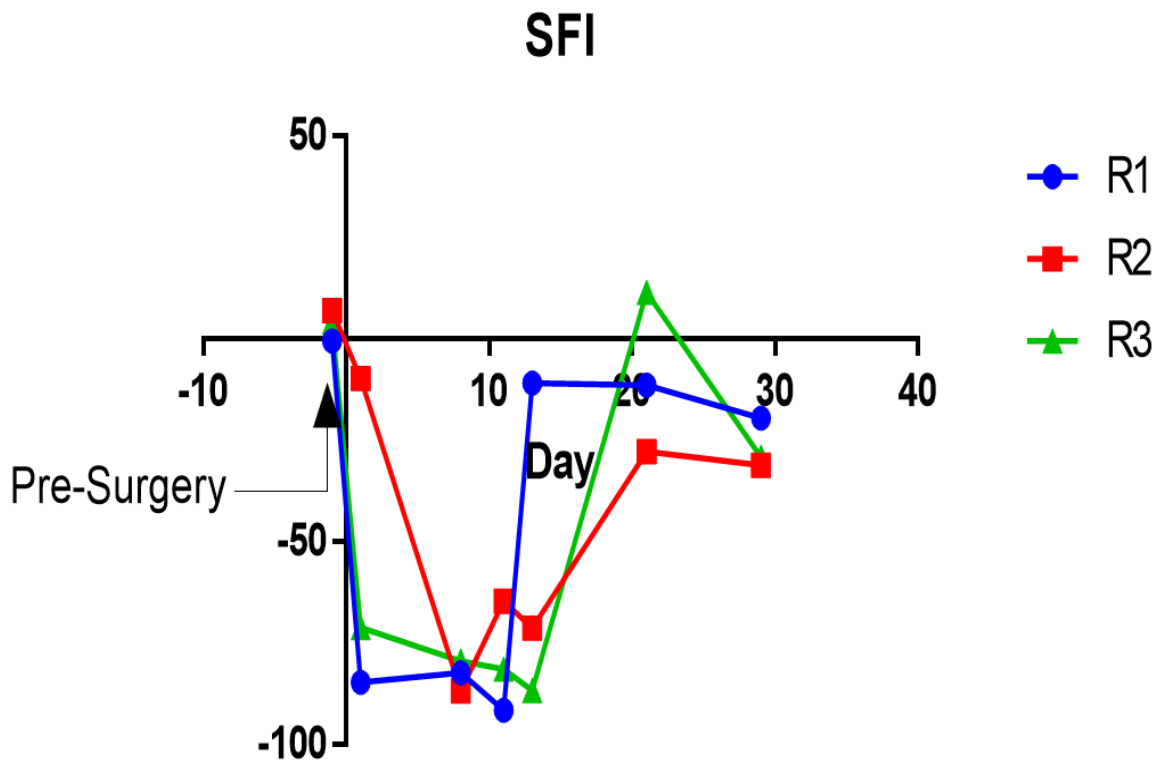
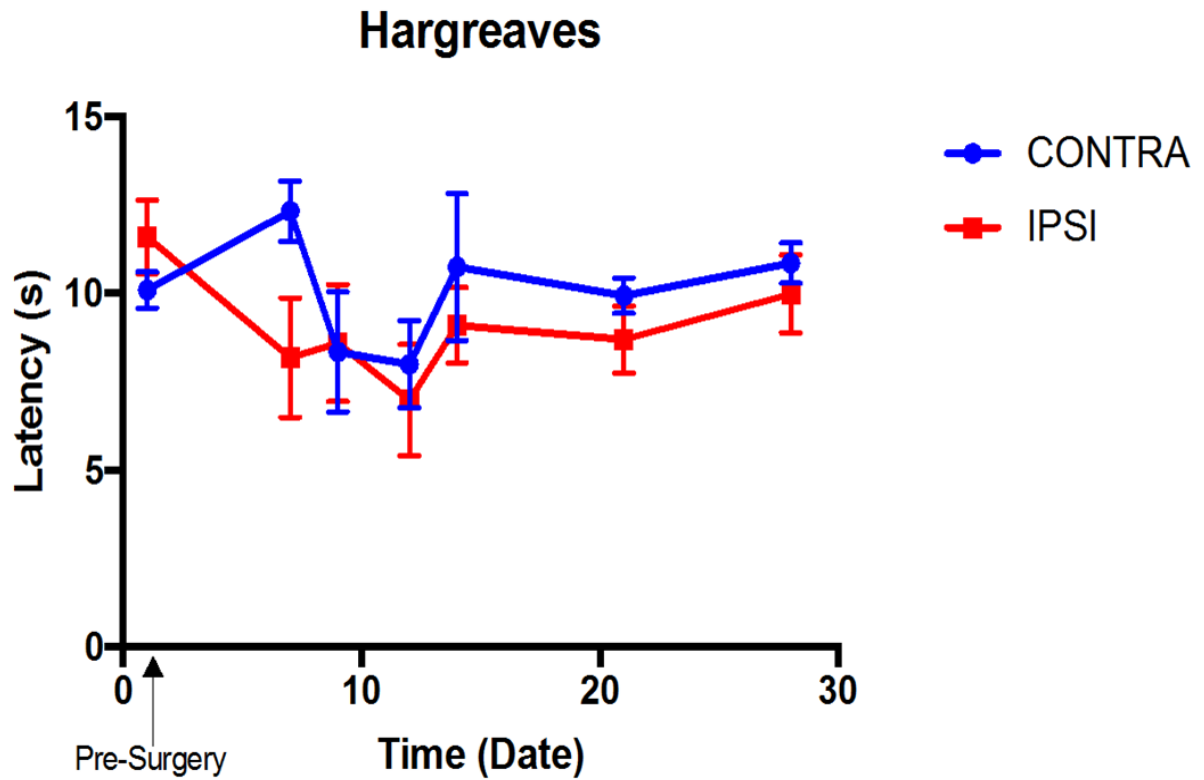
### 5.3.3 Hargreaves Data from Trial

The mean latency was measured for both the CONTRA and IPSI sides (Figure 5.3). The baseline data (pre-surgery) was calculated at  $10.1 \pm 1.41$  s (CONTRA) and  $12.3 \pm 1.11$  s (IPSI). A clear difference was measured between the operated and non-operated side at the time point following the surgical procedure. At 6 days post operation, the latency increased for the CONTRA side to  $13.2 \pm 1.46$  s and decreased on the IPSI side to  $8.4 \pm 2.63$  s. For all other time points, the mean latency was comparable for both sides culminating at  $10.6 \pm 0.42$  (CONTRA) and  $9.8 \pm 1.82$  s (IPSI).

### 5.3.4 Sciatic Functional Index (SFI) Data from Trial

The individual values were plotted for SFI calculations to show the general trend following the trial NGC surgery (Figure 5.3). Baseline levels calculated at the pre-surgery stage ranged between 0 and 8 for the index value. Following surgery, the index value decreased to the lowest limit recorded during the trail. Ranging from -88 to -62 at 8 days post-surgery. The SFI did not increase to reach baseline level but did increase to higher values close to the pre-surgery data. At 29 days post-surgery, index values ranged from -24 to -16.

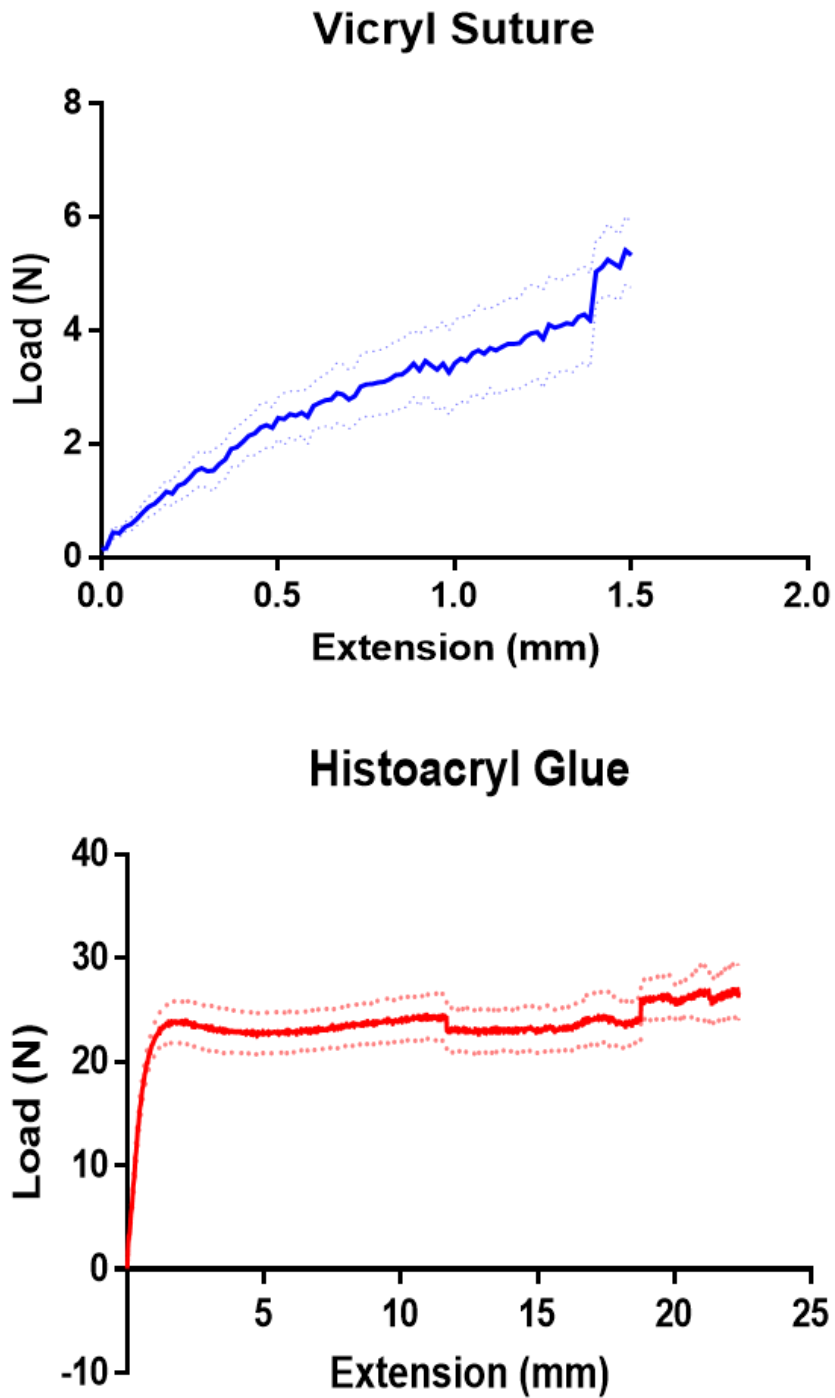




**Figure 5.3:** Mean latency values calculated from the Hargreaves testing for the pilot trial calculated for the pre-surgery baseline level to the endpoint at 29 days post-operation (top). SFI values were plotted for each rat from pre-surgery baseline levels to 29 days post-surgery (bottom).

### 5.3.5 Tensile Testing of NGC Adhesion Methods

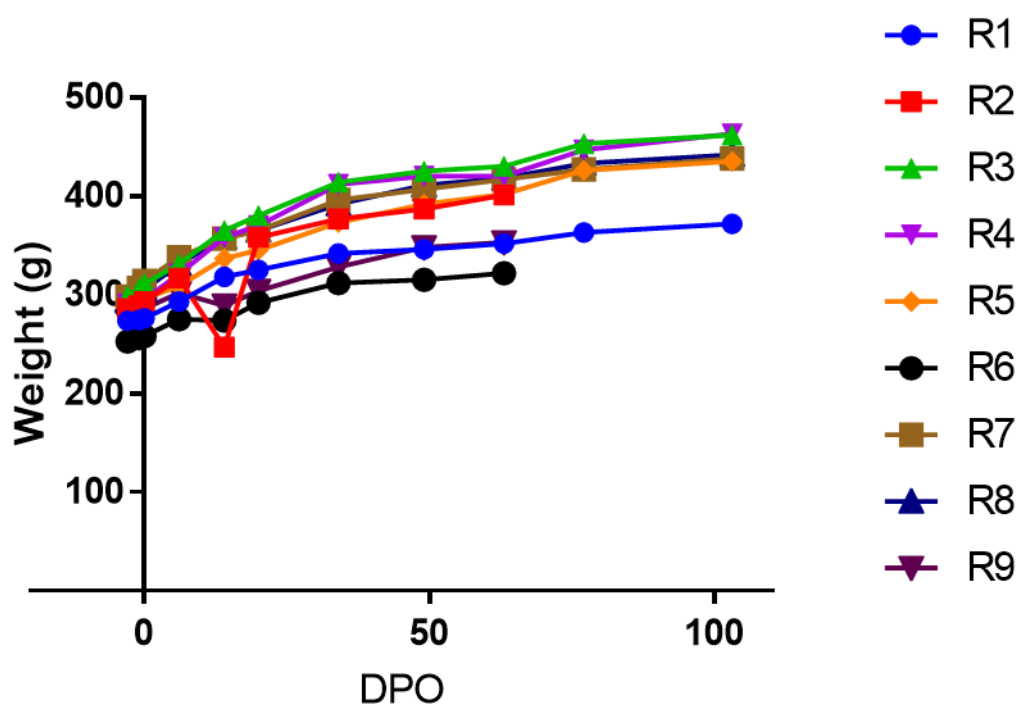
Tensile testing was conducted to compare the adhesion techniques available to fix the NGC into place during implantation (Figure 5.4). Comparing the extension of the NGC, with load applied, the use of Histoacryl glue meant that the NGC could bear larger loads prior to failure (rupture of the NGC or breakage of the bond). However, the use of Vicryl sutures led to smaller extension (mean extension was  $1.62 \pm 1.52$  (SD) mm) compared to the Histoacryl group (mean extension was  $20.94 \pm 9.85$  (SD) mm) before failure with decreased load bearing capability. When assessing the load bearing capability of the adhesion methods, the Histoacryl glue enables larger loads to be borne ( $25.93 \pm 6.42$  N) compared to the sutured NGCs ( $5.03 \pm 3.71$  N). Finally, the tensile stress at tensile strain was also compared. Tensile stress was higher on the Histoacryl NGCs ( $35.778 \pm 10.14$  MPa) compared to the Vicryl suture NGCs ( $8.817 \pm 6.13$  MPa).



**Figure 5.4:** Tensile testing to compare adhesion methods for the NGC, Vicryl suturing (blue graph) and Histoacryl bioadhesive glue (red graph) by extensometry under load. Standard Deviation (SD) are displayed for the margin of error shown by the dotted lines.

### 5.3.6 Weight Measurements for Full Experimental Subjects

Weights were recorded for each individual rat (n=9) without sorting into experimental groups. The weights increased for all rats over the experimental time points (Figure 5.5). At the pre-surgery time point, -3 DPO (days post operation) values ranged from 252.9 to 299.1 g. By 69 DPO, values ranged from 322 to 430 g meaning that the range increased between weights, however no animals had lost weight over this period. Between 69 and 103 DPO, only rats not euthanised due to autophagy were weighed (n=6). Nonetheless, animals increased in weight ranging from 435 to 463 g; the range had decreased at this time point and values were closer together.



**Figure 5.5:** Weights in grams of animals from pre-surgery stage (-3 DPO) to the experimental end point (106 DPO). DPO = days post operation.

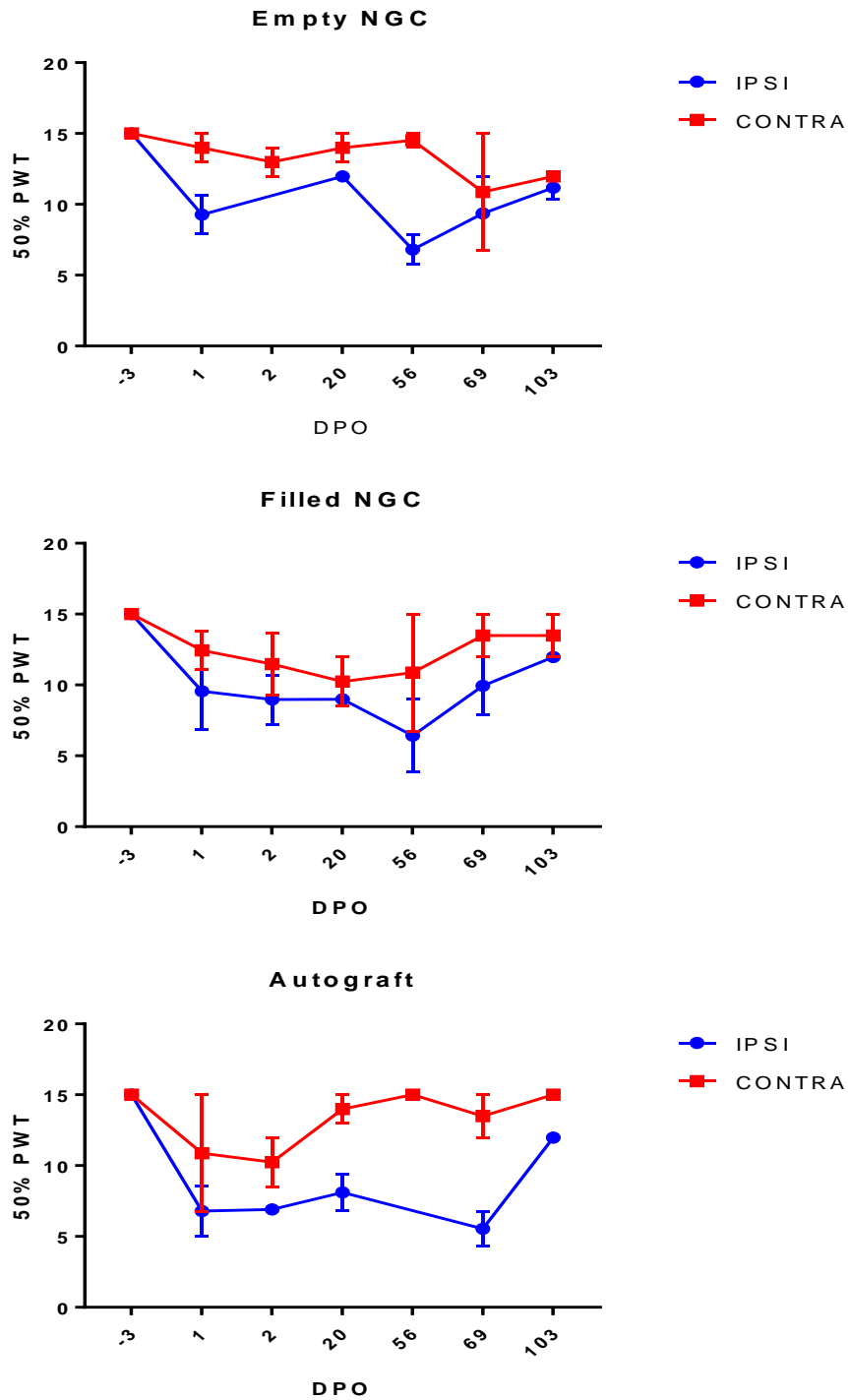
### 5.3.7 Von Frey Experimental Data

Von Frey data were converted to the 50% PWT value as conducted in the trial (Figure 5.6). Baseline recordings were taken 3 days before surgery (-3 DPO) and were calculated to be the maximal 50% PWT,  $15.0 \pm 0.00$ , for all groups (Empty NGC, Filled NGC and Autograft).

For the Empty NGC group, on the CONTRA side, 50% PWT did not deviate from the immediate post-surgery baseline level, decreasing from  $13.9 \pm 1.01$  on 1 DPO to  $12.0 \pm 0.00$  at 106 DPO. Although at 69 DPO, there was a reduction at 69 days with 50% PWT calculated to be  $10.9 \pm 4.13$ . On the IPSI side. However by 103 DPO, the mean CONTRA 50% PWT was  $11.98 \pm 0.00$ . On the IPSI side, mean 50% PWT values were similar to post-surgery levels at 1 DPO ( $9.3 \pm 1.34$ ) but had decreased to  $6.8 \pm 1.04$  by 56 DPO. Mean 50% PWT then returned to better than baseline level for the IPSI side to  $11.2 \pm 0.81$ .

For the Filled NGC group, on the CONTRA side, the immediate post-surgery mean 50% PWT was calculated at  $12.4 \pm 1.36$  (1 DPO) which remained reduced slightly to  $10.2 \pm 1.75$  on 20 DPO and returned to a higher baseline by 103 DPO to  $13.5 \pm 1.51$ . However, on the IPSI side, the mean 50% PWT post-surgery baseline was lower at  $9.6 \pm 2.73$  (-1 DPO) and returned to the same level by 69 DPO ( $9.9 \pm 2.04$ ), reducing slightly at 56 DPO to  $6.4 \pm 2.57$  and at 103 DPO to  $11.98 \pm 0.00$ . In summary the IPSI side had a lower threshold than the CONTRA side by the experimental end point.

For the Autograft group, on the CONTRA side, the 50% PWT was markedly high throughout the experiment increasing from  $10.9 \pm 4.13$  on -1 DPO to  $15 \pm 0.00$  on 103 DPO. However, there was a steep decrease in mean 50% PWT at 1 DPO ( $6.8 \pm 1.79$ ). This reduced further to  $5.5 \pm 1.20$  at 69 DPO but had returned to a higher level ( $12.0 \pm 0.00$ ) by 103 DPO. Overall, the CONTRA side produced higher values than the IPSI side at all time points.



**Figure 5.6:** Quantification of Von Frey data which was used to calculate the 50% PWT (Paw Withdrawal Threshold) at time points measured in Days Post Operation (DPO) for the three experimental groups: Empty NGCs, Filled NGCs and Autograft for both IPSI (operated side) and CONTRA (control, non-operated side).

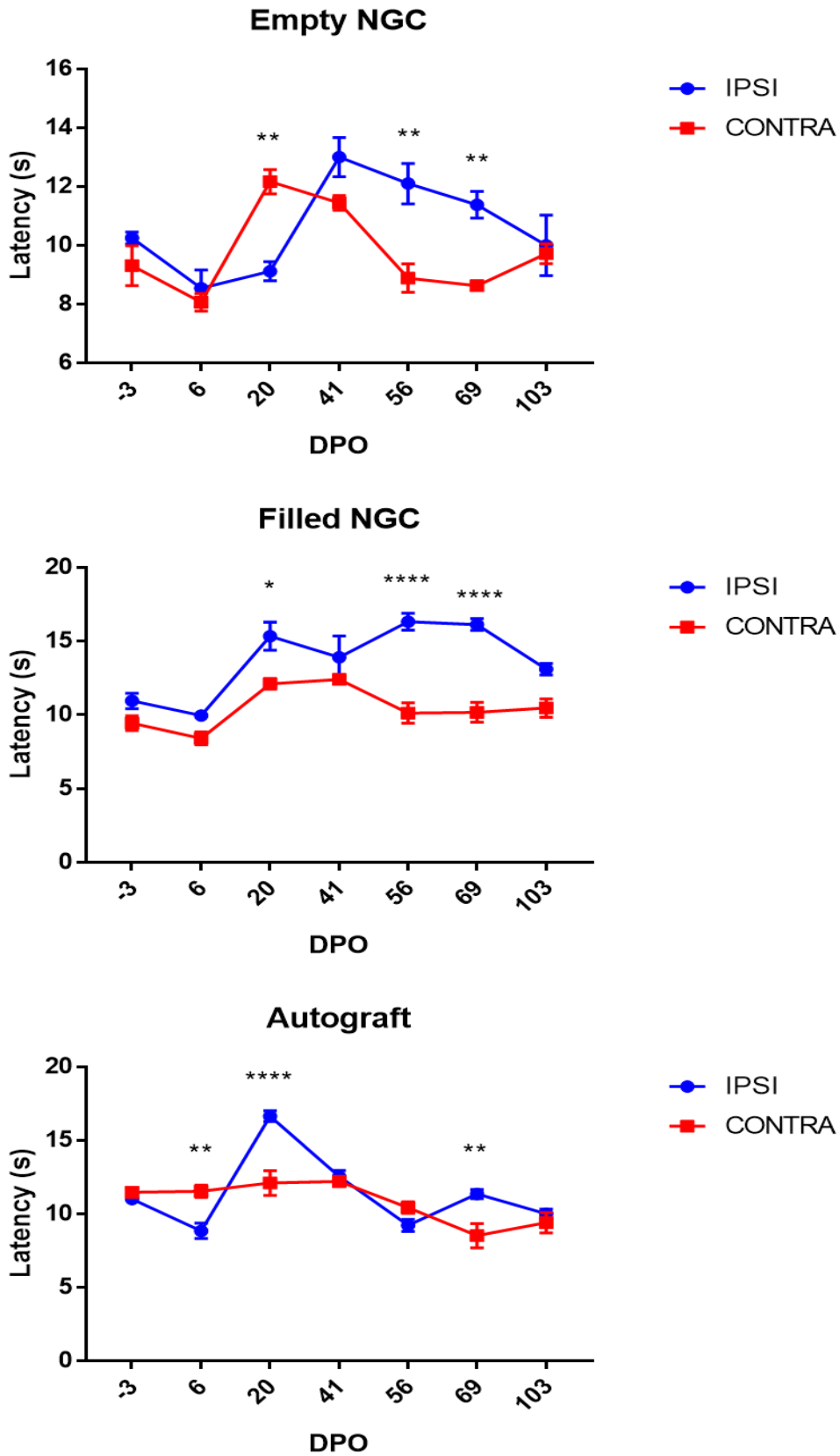
### 5.3.8 Hargreaves Test Analysis

The Hargreaves test was used to provide data on any experience of thermal hyperalgesia amongst the test groups by measuring the latency to withdraw the paw from a non-noxious thermal stimulus (Figure 5.7).

For the Empty NGC group, the mean pre-surgery latency was  $10.3 \pm 0.19$  s on the IPSI side and  $9.3 \pm 0.67$  s on the CONTRA side. Latency increased to a longer time by 41 DPO to  $13.0 \pm 0.65$  s on the IPSI side and  $11.4 \pm 0.24$  on the CONTRA side. These values returned to baseline levels at 103 DPO to  $10.0 \pm 1.03$  s on the IPSI side and  $9.72 \pm 0.34$  s on the CONTRA side. When comparing mean latency values for statistically significant differences between the IPSI and CONTRA sides, significant differences were calculated at 20 DPO ( $p=0.023$ ), 56 DPO ( $p=0.0013$ ) and 69 DPO ( $p=0.0067$ ).

A similar trend was observed for the Filled NGC group; however, values were markedly higher post-surgery and at the experimental endpoint. At the pre-surgery time point, mean latency was  $10.9 \pm 0.52$  s (IPSI) and  $9.4 \pm 0.49$  s (CONTRA). At 41 and 56 DPO, there was a clear difference between mean latency calculated. On 41 DPO, values were  $13.9 \pm 1.44$  s and  $12.4 \pm 0.20$  s for IPSI and CONTRA sides respectively. On 56 DPO, values were  $16.3 \pm 0.56$  s and  $10.1 \pm 0.69$  s for IPSI and CONTRA sides respectively. By 103 DPO, mean latency returned to baseline level for the CONTRA side ( $10.4 \pm 0.62$  s) but were increased from baseline on the IPSI side ( $13.1 \pm 0.39$  s). Significant differences were calculated when comparing mean latency between the IPSI and CONTRA sides at 20 DPO ( $0.0102$ ) and 56 and 69 DPO (both  $p<0.0001$ ).

For the Autograft group, mean latency increased following the surgery from  $11.0 \pm 0.34$  s (pre-surgery, -3 DPO) to a maximal level of  $16.6 \pm 0.37$  s on 20 DPO before returning to baseline levels,  $10.0 \pm 0.32$  s, on 103 DPO on the IPSI side. On the CONTRA side, levels were more constant, increasing from  $11.4 \pm 0.34$  s (pre-surgery, -3 DPO) to  $12.2 \pm 0.35$  s at 41 DPO and reducing to a lower level than pre-surgery on 103 DPO ( $9.4 \pm 0.68$  s). Significant differences were calculated to compare mean latency between the IPSI and CONTRA sides. Significant differences were calculated at 6 DPO ( $p=0.0047$ ), 20 DPO ( $p<0.0001$ ) and 69 DPO ( $p=0.0028$ ).

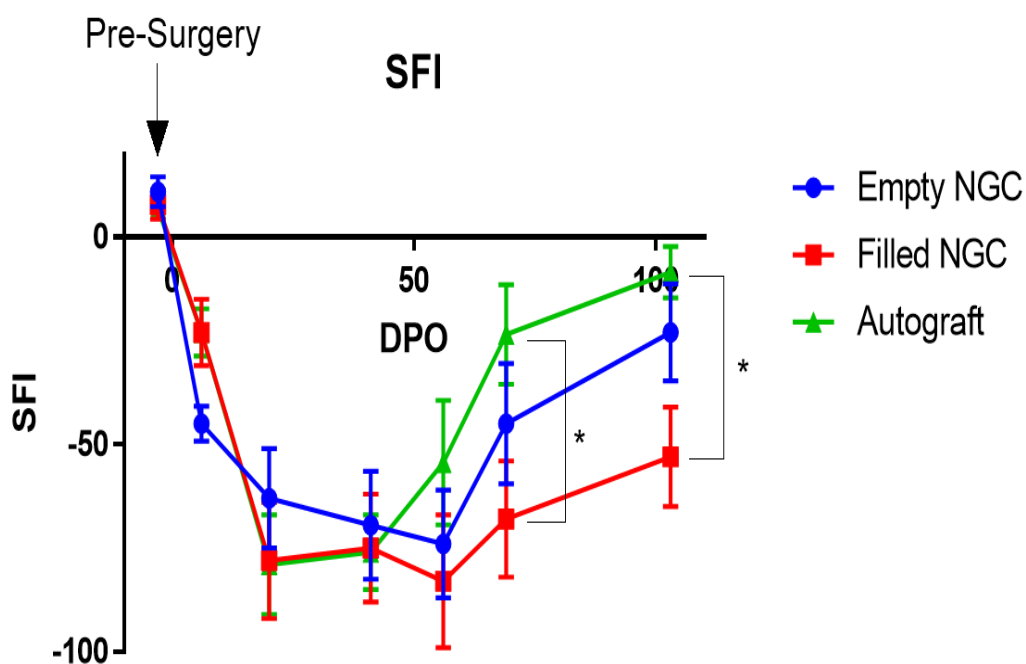


**Figure 5.7:** Quantification of thermal hyperalgesia data derived from the Hargreaves test for the experimental groups: Empty NGC, Filled NGC and Autograft. Mean latency (s) was plotted at each time point (DPO, Days Post Operation) for both IPSI (operated side) and CONTRA (non-operated side, control).



### 5.3.9 Sciatic Functional Index (SFI) Analysis

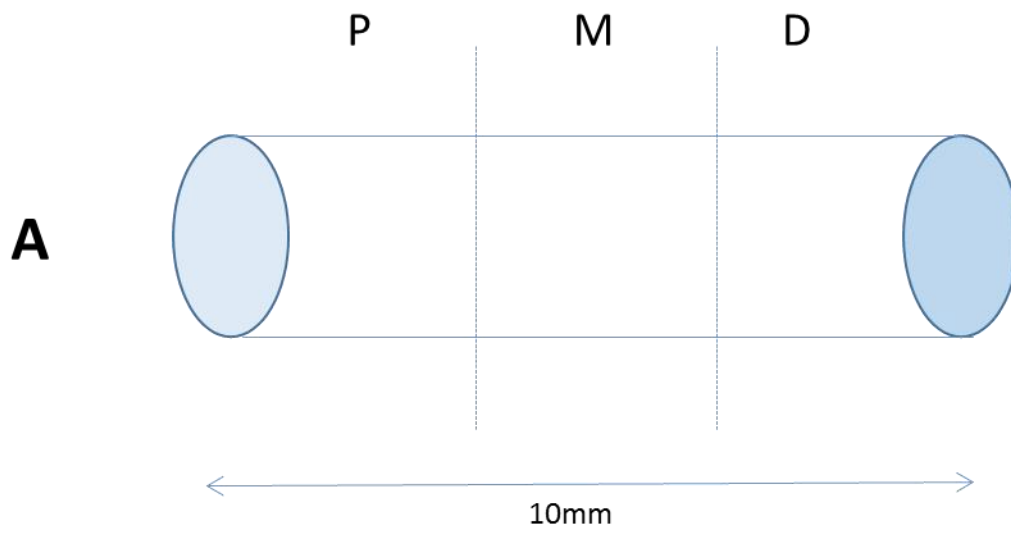
SFI was calculated to indicate the relative decrease in plantar spreading over the course of the experiment (Figure 5.8). For the Empty NGC, the pre-surgery mean SFI (-3 DPO) was  $10.9 \pm 3.62$ , which decreased to  $-74 \pm 13.0$  at 56 DPO and increased to  $-23 \pm 11.7$  at 103 DPO. For the Filled NGC group, the mean SFI was  $7.8 \pm 3.5$  at -3 DPO which decreased to  $-83 \pm 16.0$  at 56 DPO. The SFI recovered, although not to the pre-surgery level, by 103 DPO to  $-53 \pm 12.0$ . For the Autograft group, the mean SFI was  $6.7 \pm 1.4$  pre-surgery (-3 DPO) and decreased to a minimal value of  $-79 \pm 12.0$  at 20 DPO. From this time point, the mean SFI increased to  $-8.5 \pm 6.2$  at 103 DPO close to the pre-surgery value. Statistical analysis confirmed that there was a significant difference between the mean SFI for the Filled NGC and Autograft at 69 DPO and 103 DPO (for both comparisons,  $p=0.0183$ ).



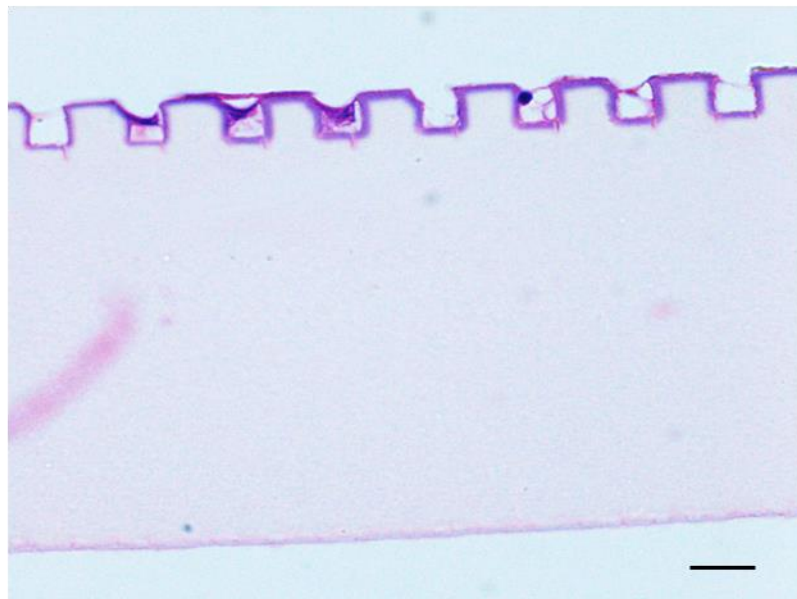
**Figure 5.8:** Quantification of the mean SFI calculated for the Ipsilateral (operated side) from pre-surgery to 103 days post operation (DPO) for Empty NGC, Filled NGC and Autograft experimental groups.

### 5.3.10 Haematoxylin and Eosin Staining

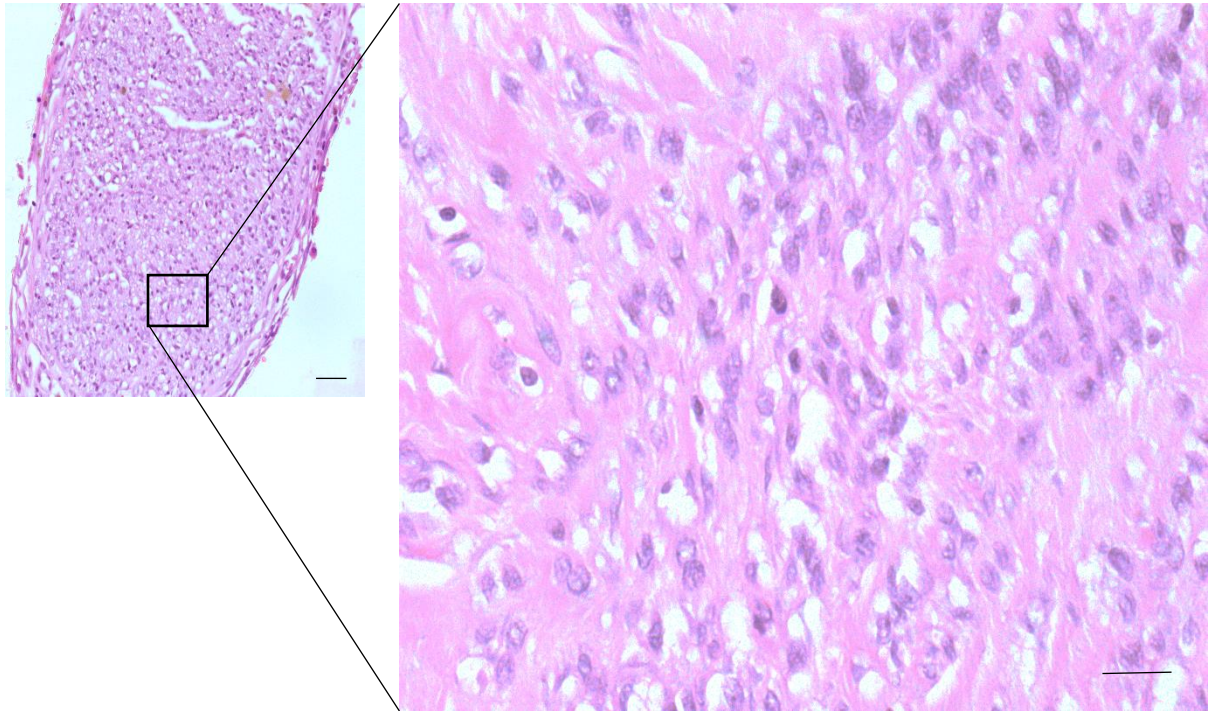
Haematoxylin and Eosin (H&E) staining provided images of tissue segments along the regenerated nerve at specific sections, proximal, middle and distal areas ('P', 'M' and 'D' in Figure 5.9). Figure 5.9A shows a schematic of the nerve conduit implanted, through which the regenerated nerve extended over the experimental time period. Figure 5.9B shows a section of the micro-grooved PA6,6 NGC that was implanted with few adherent cells. The H&E staining was used to demonstrate structural properties of the nerve which was then quantified for axon density by myelin staining (section 5.3.11). A transverse section showing the majority of the nerve diameter is shown at 10X magnification (Figure 5.10), the epineurium can be observed as the ensheathing cells that encircle the whole nerve section and the stained section has a polka dot appearance due to the non-stained axons and myelinating cells present which validates that the perineurium, endoneurium and axons are showing evidence of alignment due to the fibres arranged in a parallel formation.



**B**



**Figure 5.9:** Schematic showing sections removed for histological staining from the proximal (P), middle (M) and distal (D) portions of the regenerated nerve (A). Image to show the microgrooves present on the PA6,6 NGC internal luminal surface (C). Scale bar - 20 $\mu$ m.

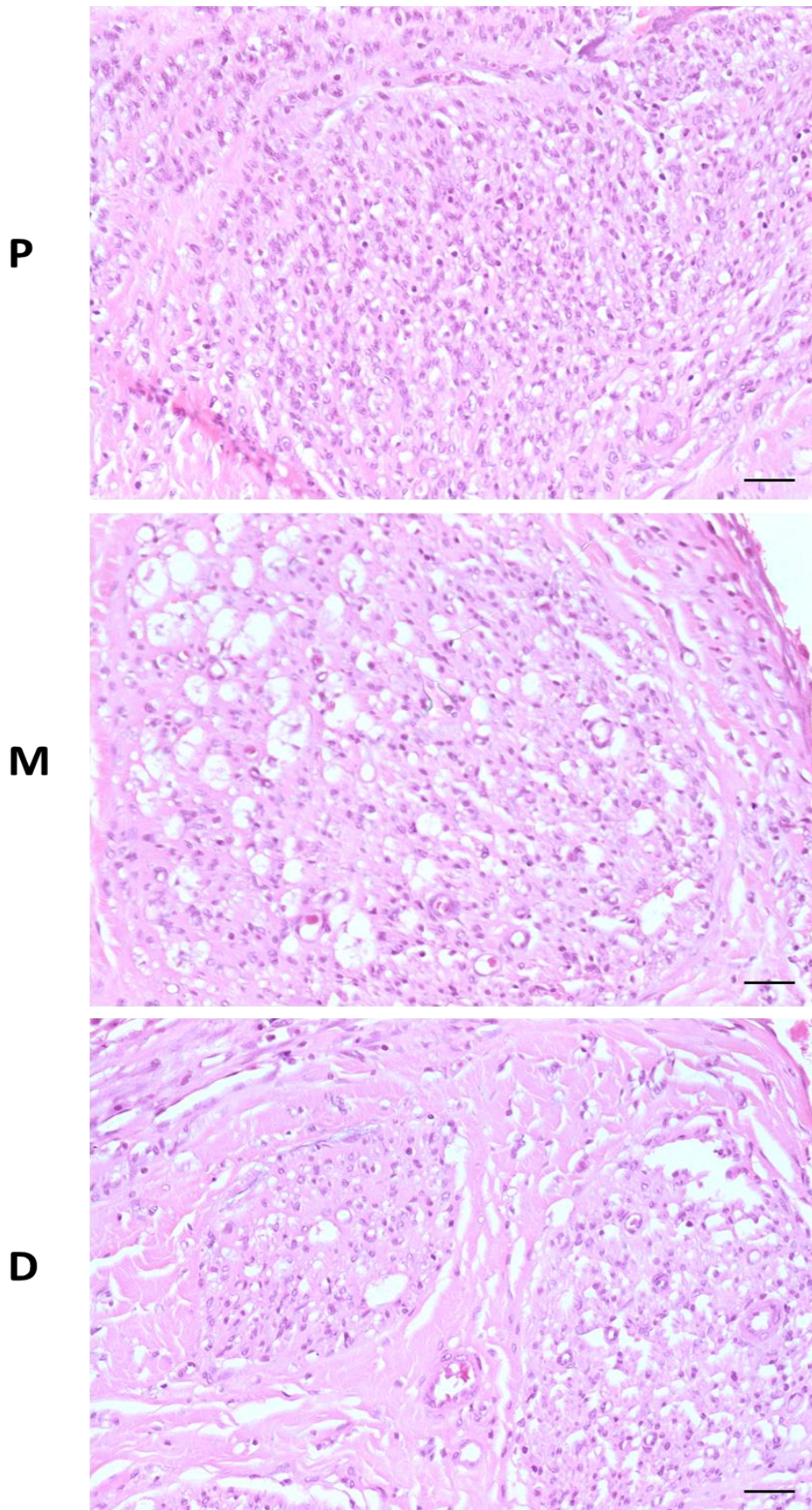


**Figure 5.10:** Transverse section of healthy nerve stained with Haematoxylin and Eosin (H&E) at low magnification (scale bar - 100µm) and high magnification (scale bar - 20µm).

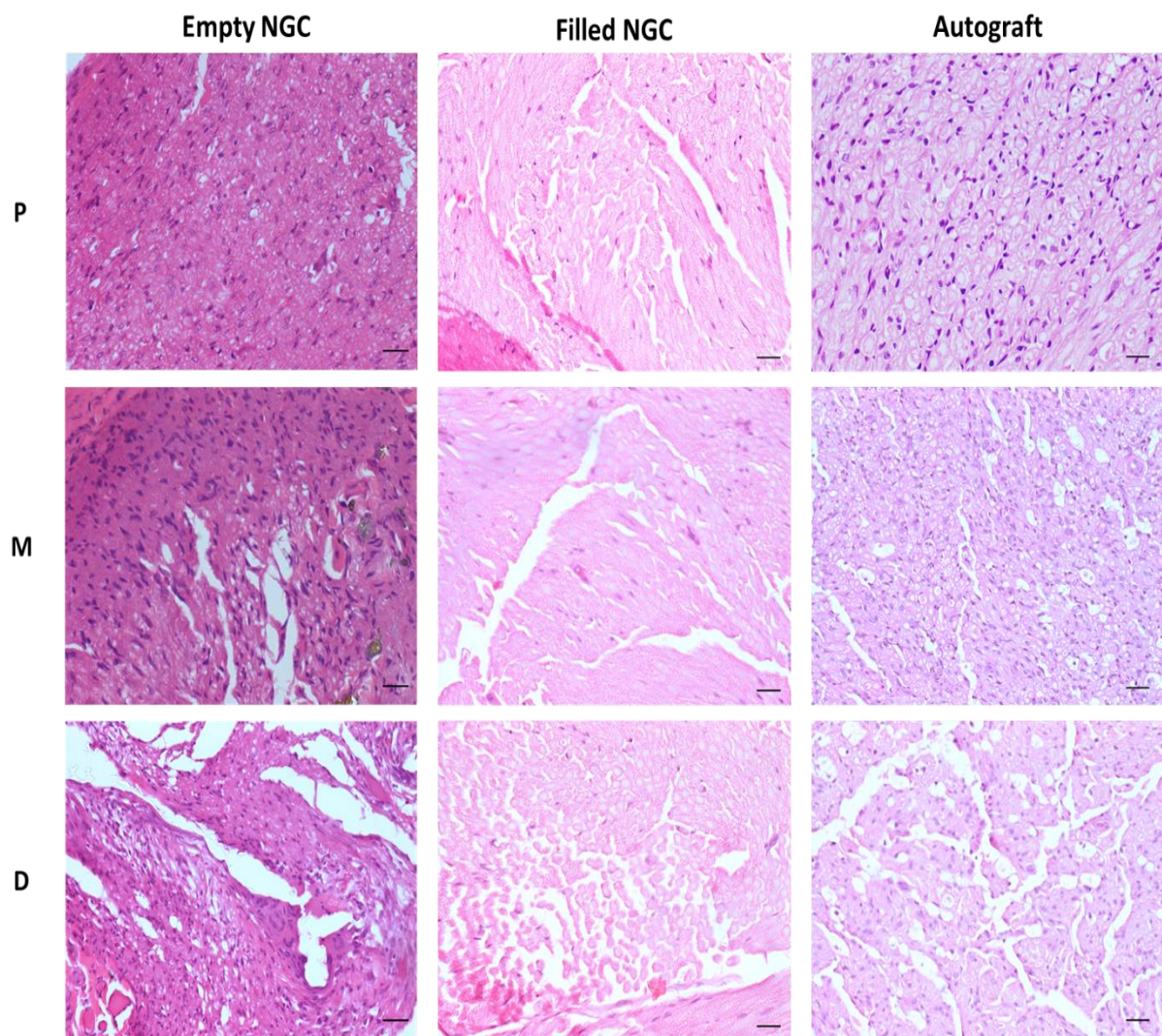
H&E staining was first completed on the control tissue from the 30 day trial of the PA6,6 NGC, the representative images show intact nerve anatomy with many Schwann cell nuclei present at the proximal, middle and distal levels (Figure 5.11).

The nerve tissue is organised into fascicles as evidenced by the close packing of axons seen as pale circles stained with haematoxylin (pale pink in Figure 5.11). The three experimental groups from the behavioural studies including Empty NGC, Filled NGC and Autograft groups were then stained to validate whether there was any histological evidence of nerve regeneration (Figure 5.12). For the Empty NGC group, the proximal section contained many Schwann cell nuclei, and axon-like structures. The high density of nuclei indicates that Schwann cells were able to infiltrate the NGC well during the experimental time period.

For the Filled NCG group, some nuclei of Schwann cells are present indicating that these cells have infiltrated the NGC although this was to a lesser extent than seen in the Empty NGC group specifically in the distal portion. Pale circles stained with eosin were visible at all sites (P, M and D) indicating the presence of extended axons, although these were stained with a specific myelin stain in section 5.3.11. When comparing the Autograft samples, a high density of axons was observed as well as Schwann cell nuclei. There was a higher degree of tearing of the tissue distally compared to proximal sections for all groups.



**Figure 5.11:** Healthy nerve tissue representative images of H&E staining from 30 day trial showing proximal (P), middle (M) and distal (D) sections. Scale bar – 20 $\mu$ m.



**Figure 5.12:** Representative H&E stained sections from the experimental groups (Empty NGC, Filled NGC and Autograft) at the proximal (P), middle (M) and distal (D) sites. Scale bar - 20 $\mu$ m.

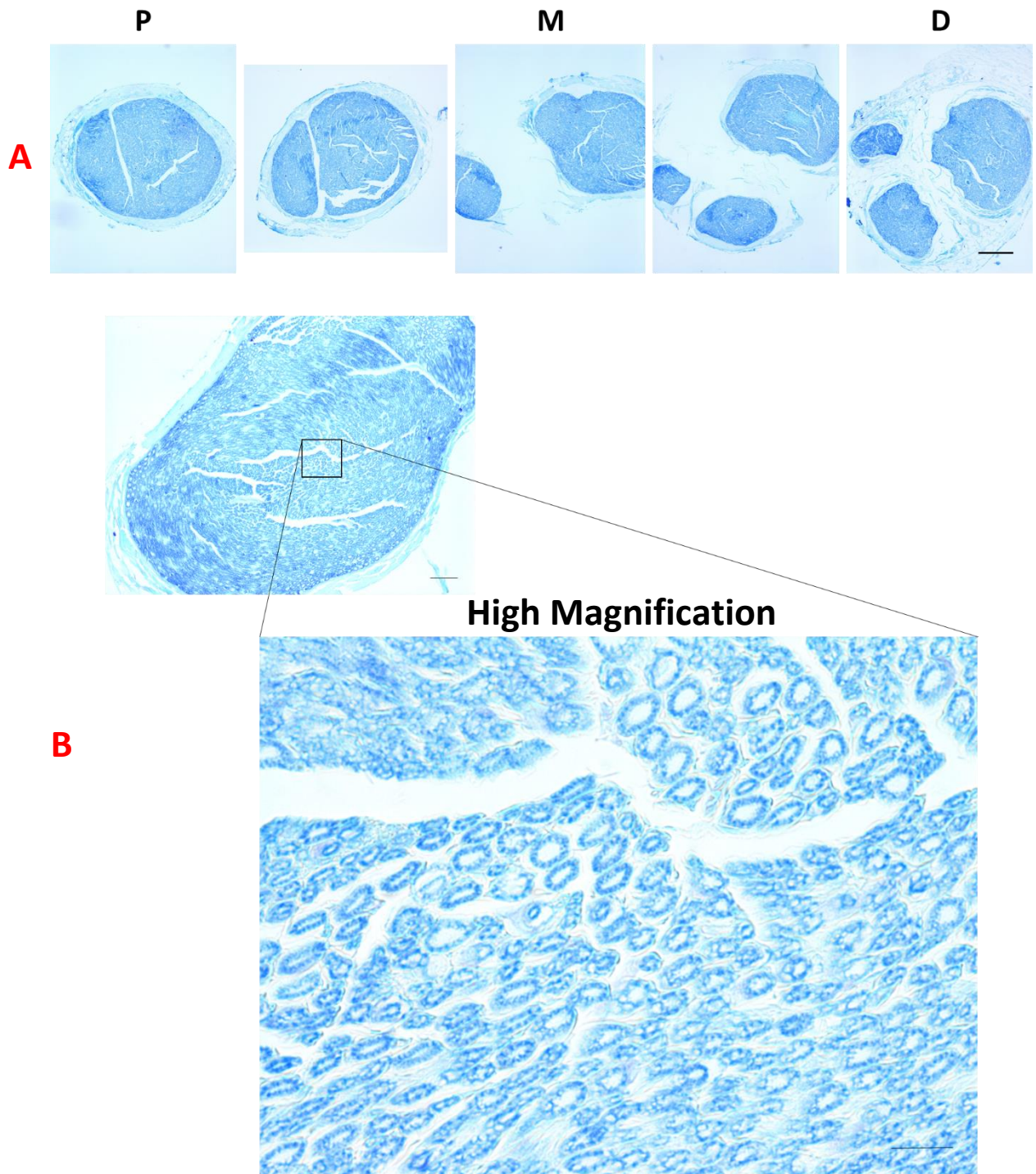
### 5.3.11 Luxol Fast Blue Staining

Luxol fast blue (LFB) stain was used to stain myelin expressing cells (Schwann cells). The nerve was imaged in the same manner at the proximal, middle and distal portions (P, M, and D respectively). An example nerve (healthy control) has been shown with sections taken at these sites (Figure 5.13A). At low magnification the gross anatomy of the nerve could be seen, showing the location of nerve fascicles (heavily stained with LFB) and connective tissue (less stained) (Figure 5.13B). The differentiation step was used to provide contrast between myelin structures and non-myelin structures, which can be clearly seen at high magnification where the blue rings present confirm the presence of myelinated axons.

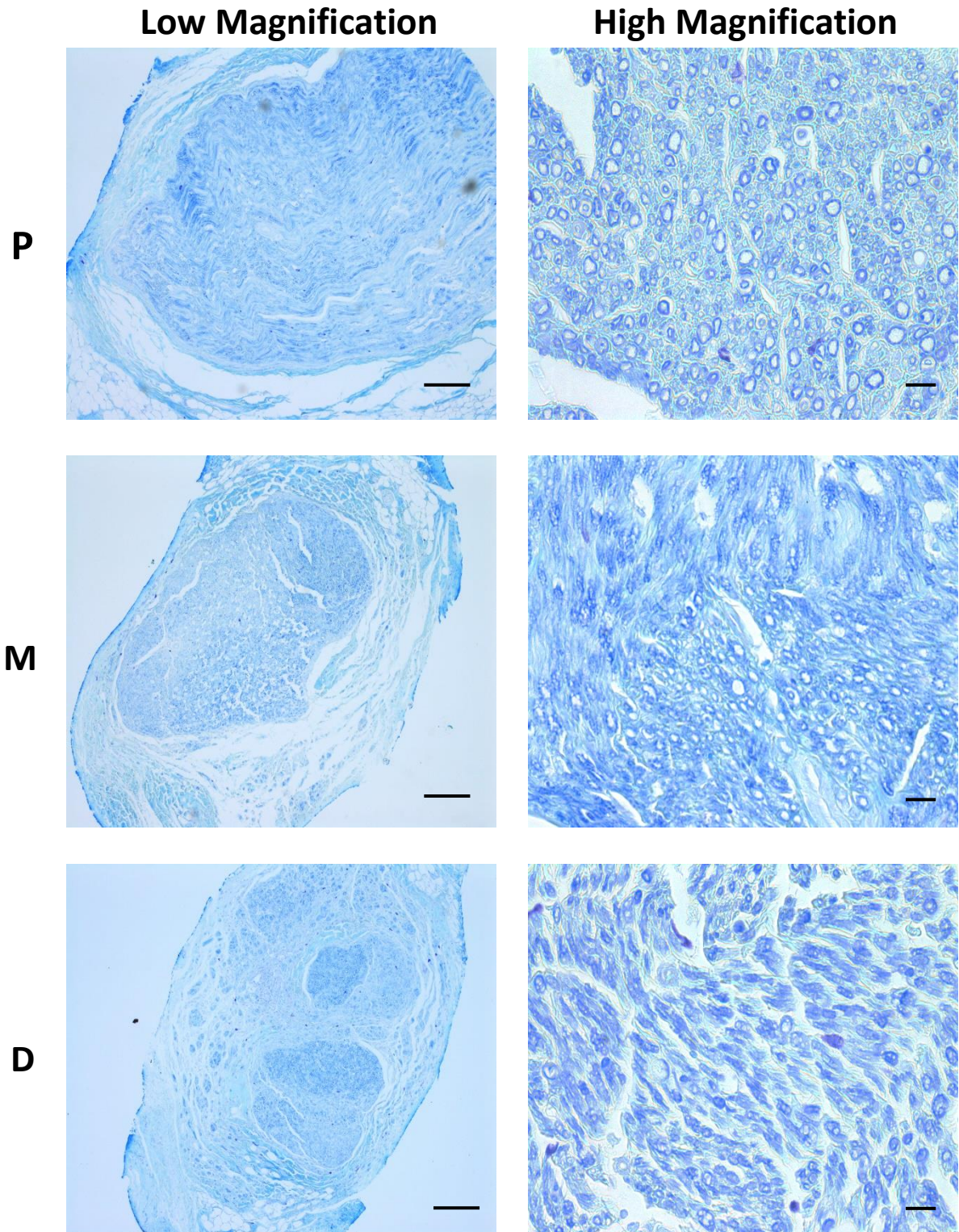
The experimental nerves were then observed closely for evidence of myelination and the degree of myelination qualitatively. For the Empty NGC group, there was clear evidence of myelination of the nerve at the three levels (P, M, and D) (Figure 5.14). The myelin thickness was thickest at the proximal and middle areas compared to the distal end which also had smaller diameter axons present.

For the Filled NGC, there was less evidence of myelination as the thickness of the myelin was less compared to the Empty NGC group and also the density of fibres was lower at the proximal and middle areas (Figure 5.15). However, at the distal portion, there were smaller axons with relatively thick myelination comparable to the distal portion of the empty NGC although the density of axons was lower. For the Autograft group, there was a clearly increased degree of myelination shown by the high density of myelin stained fibres, the close packing of the staining and thick myelin around the axons at all levels (P, M and D) (Figure 5.16).

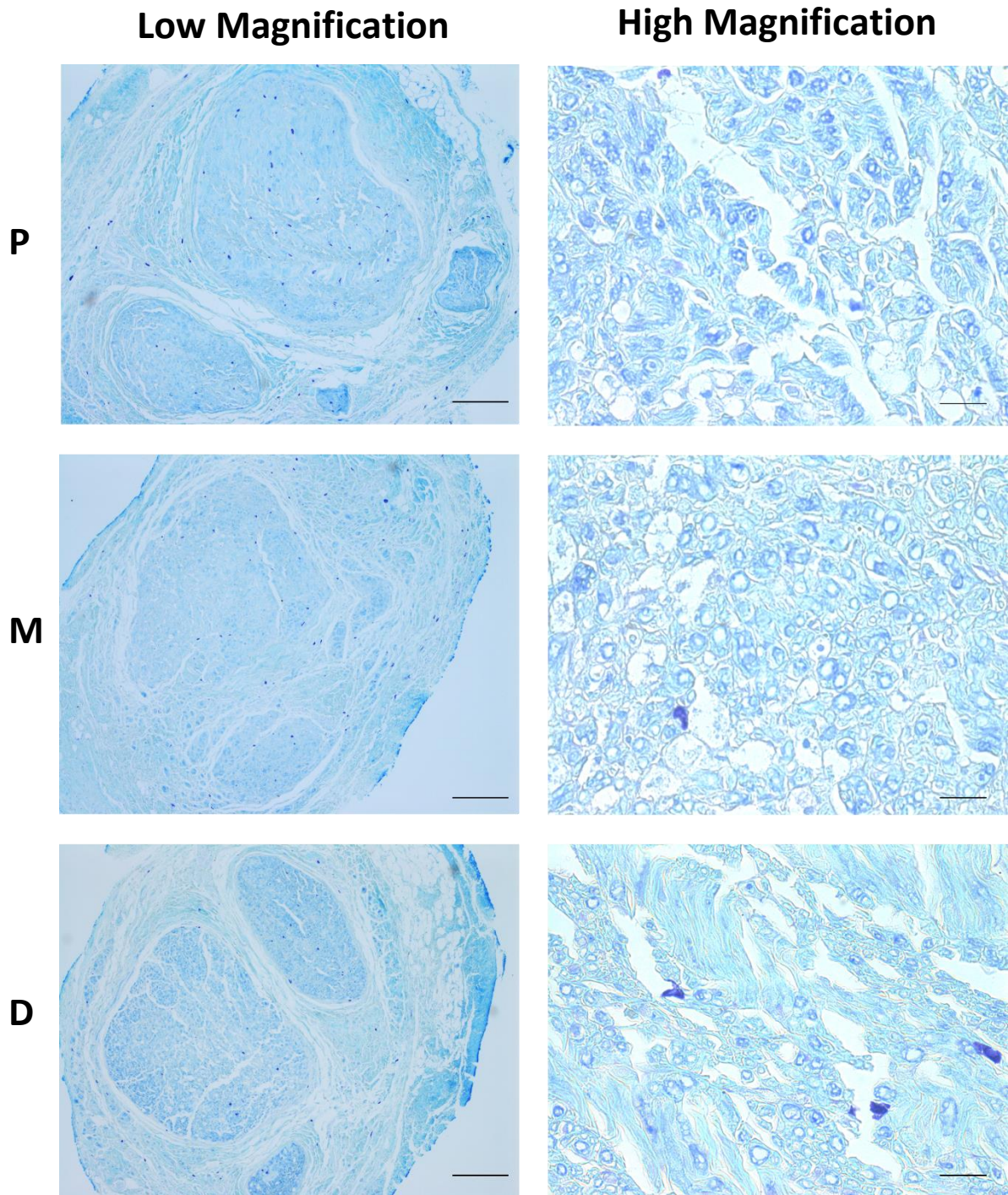




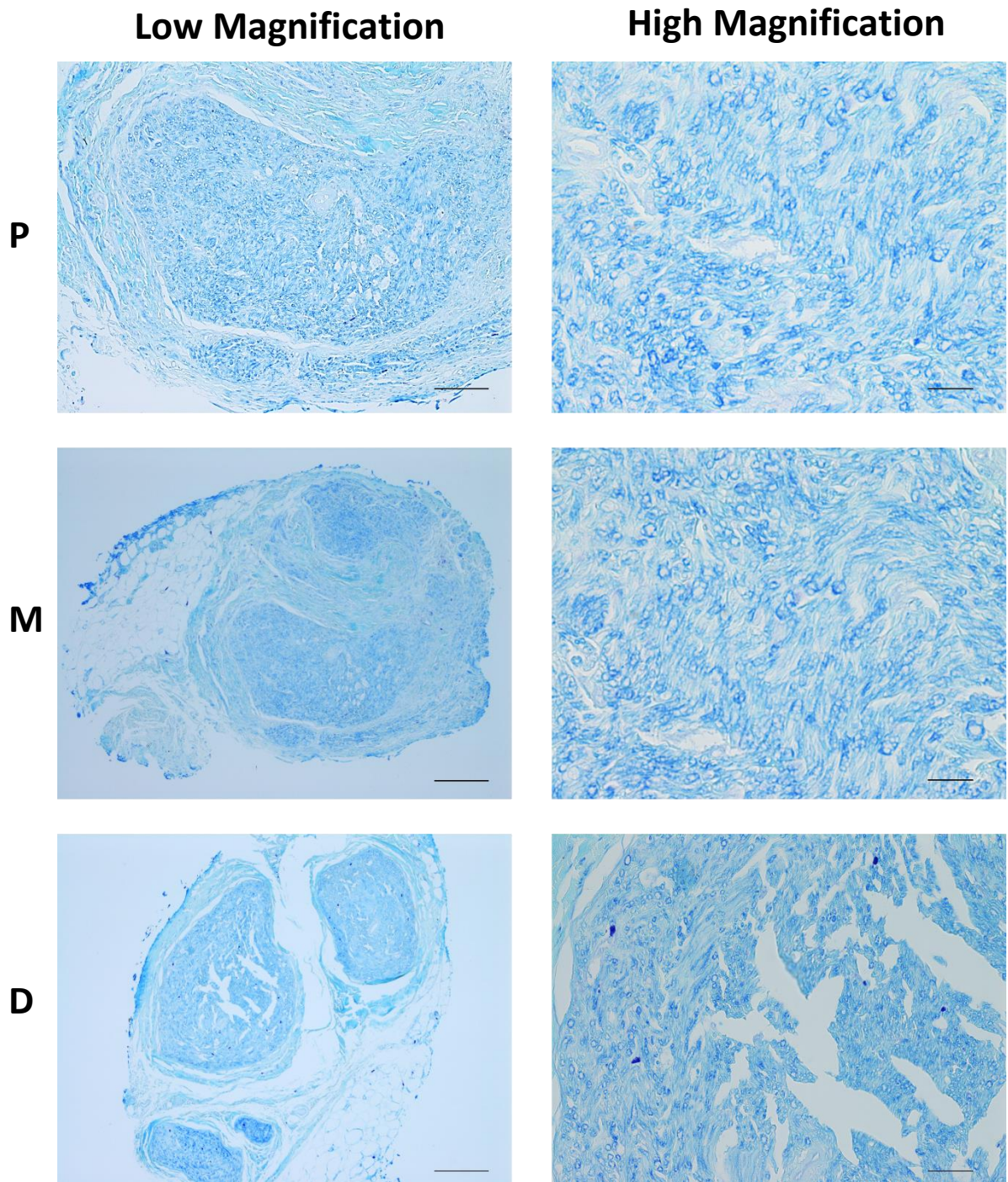
**Figure 5.13:** Series of sections through healthy nerve to show the gross anatomy at low magnification, scale bar - 200 $\mu$ m (A). High magnification image of LFB staining showing the myelinated axons (blue rings), scale bar at low magnification - 100 $\mu$ m, scale bar at low magnification - 20 $\mu$ m.



**Figure 5.14:** Representative brightfield images of LFB staining with Cresyl violet counterstain of Autograft at proximal, middle and distal portions of the nerve at low magnification (scale bar – 200 $\mu$ m) and at high magnification (scale bar - 20 $\mu$ m).



**Figure 5.15:** Representative brightfield images of LFB staining with Cresyl violet counterstain of Empty NGC at proximal, middle and distal portions of the nerve at low magnification (scale bar – 200 $\mu$ m) and at high magnification (scale bar - 20 $\mu$ m).



**Figure 5.16:** Representative brightfield images of LFB staining with Cresyl violet counterstain of Filled NGC at proximal, middle and distal portions of the nerve at low magnification (scale bar – 200 $\mu$ m) and at high magnification (scale bar - 20 $\mu$ m).

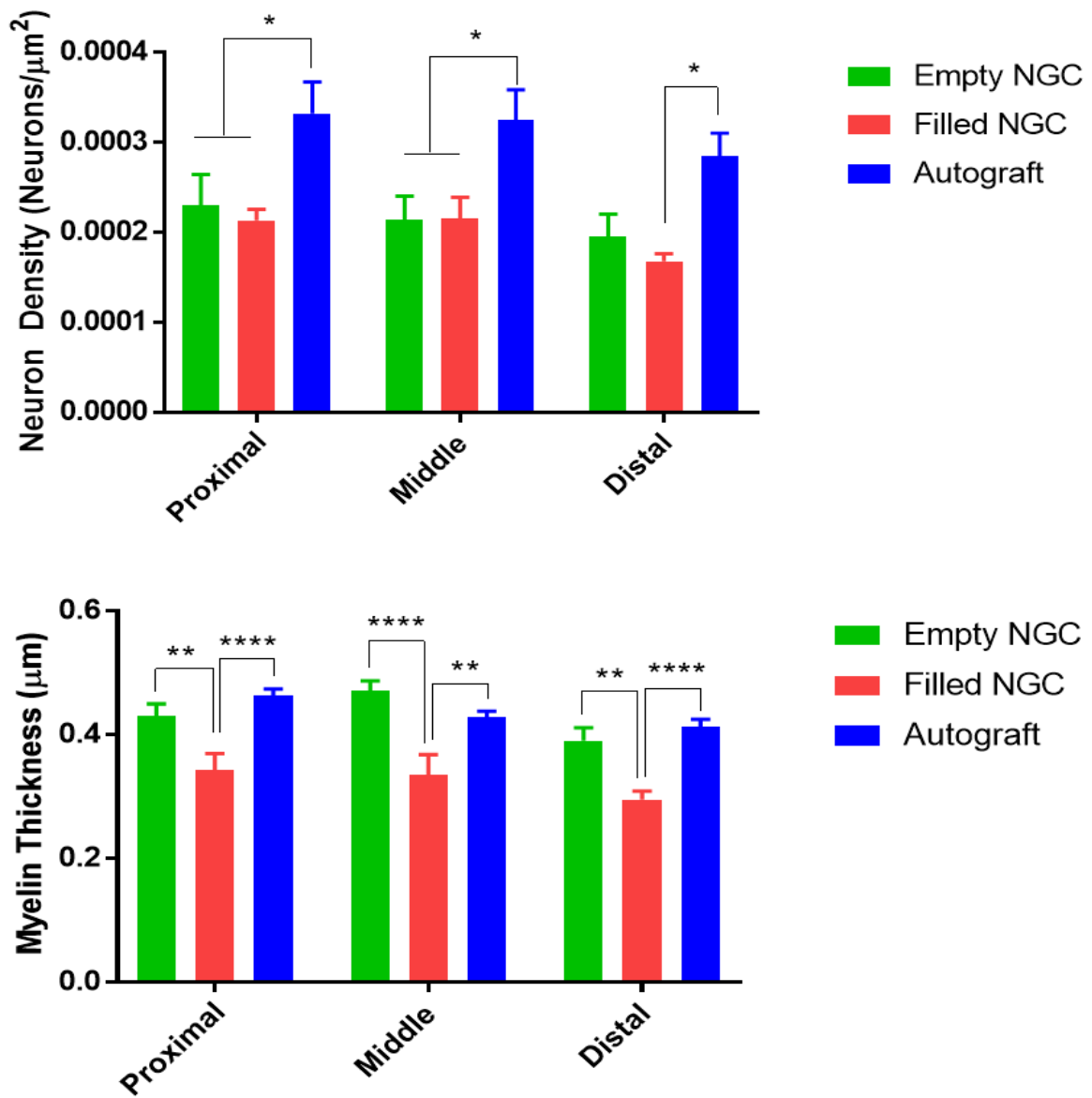
Following the LFB staining, the degree of myelination within the experimental tissues could be determined by calculating the density of myelinated neurons and the mean thickness of the myelin sheath at the three sites investigated (P, M and D). Neuron density was shown to increase when the Autograft was used as a nerve repair method when compared against the NGC test groups (Figure 5.17). At the proximal site, density was calculated at  $3.32 \times 10^{-4} \pm 3.49 \times 10^{-5}$  neurons per  $\mu\text{m}^2$  compared to  $2.30 \times 10^{-4} \pm 3.41 \times 10^{-5}$  neurons per  $\mu\text{m}^2$  (Empty NGC) and  $2.13 \times 10^{-4} \pm 1.24 \times 10^{-5}$  neurons per  $\mu\text{m}^2$  (Filled NGC). This difference was statistically significant ( $p=0.0334$  and  $p=0.0128$  respectively). The same trend was observed for the middle site. Neuron density was highest in the Autograft group ( $3.25 \times 10^{-4} \pm 3.32 \times 10^{-5}$  neurons per  $\mu\text{m}^2$ ) when compared to  $2.14 \times 10^{-4} \pm 2.62 \times 10^{-5}$  neurons per  $\mu\text{m}^2$  (Empty NGC) and  $2.17 \times 10^{-4} \pm 8.38 \times 10^{-5}$  neurons per  $\mu\text{m}^2$  (Filled NGC). These differences were also statistically significant when comparing the Autograft to Empty NGC ( $p=0.0204$ ) and Filled NGC ( $p=0.0220$ ). At the distal end, there was only a significant difference in neuron density when comparing the autograft ( $2.85 \times 10^{-4} \pm 2.52 \times 10^{-5}$  neurons per  $\mu\text{m}^2$ ) to the Filled NGC ( $1.68 \times 10^{-4} \pm 8.34 \times 10^{-5}$  neurons per  $\mu\text{m}^2$ ), which was also statistically significant ( $p=0.0146$ ).

The myelin thickness was also compared to investigate the Empty NGC and Filled NGC as nerve repair alternatives to the Autograft (Figure 5.17). Interestingly, the thickness of myelin was comparable between the Empty NGC and Autograft. At the proximal site, myelin thickness was highest for the Autograft ( $0.46 \pm 0.013 \mu\text{m}$ ) and Empty NGC ( $0.43 \pm 0.022 \mu\text{m}$ ) but lowest for the Filled NGC ( $0.34 \pm 0.027 \mu\text{m}$ ). These differences were statistically significant,  $p=0.0040$  and  $p<0.0001$  respectively). This trend was maintained throughout the nerve samples. At the distal end, the highest myelin thicknesses were for the Autograft ( $0.412 \pm 0.012 \mu\text{m}$ ) and Empty NGC ( $0.39 \pm 0.024 \mu\text{m}$ ) groups. The lowest myelin thickness was calculated for the Filled NGC ( $0.30 \pm 0.013 \mu\text{m}$ ). These differences were statistically significant for both Autograft ( $<0.0001$ ) and Empty NGC ( $p=0.0016$ ).

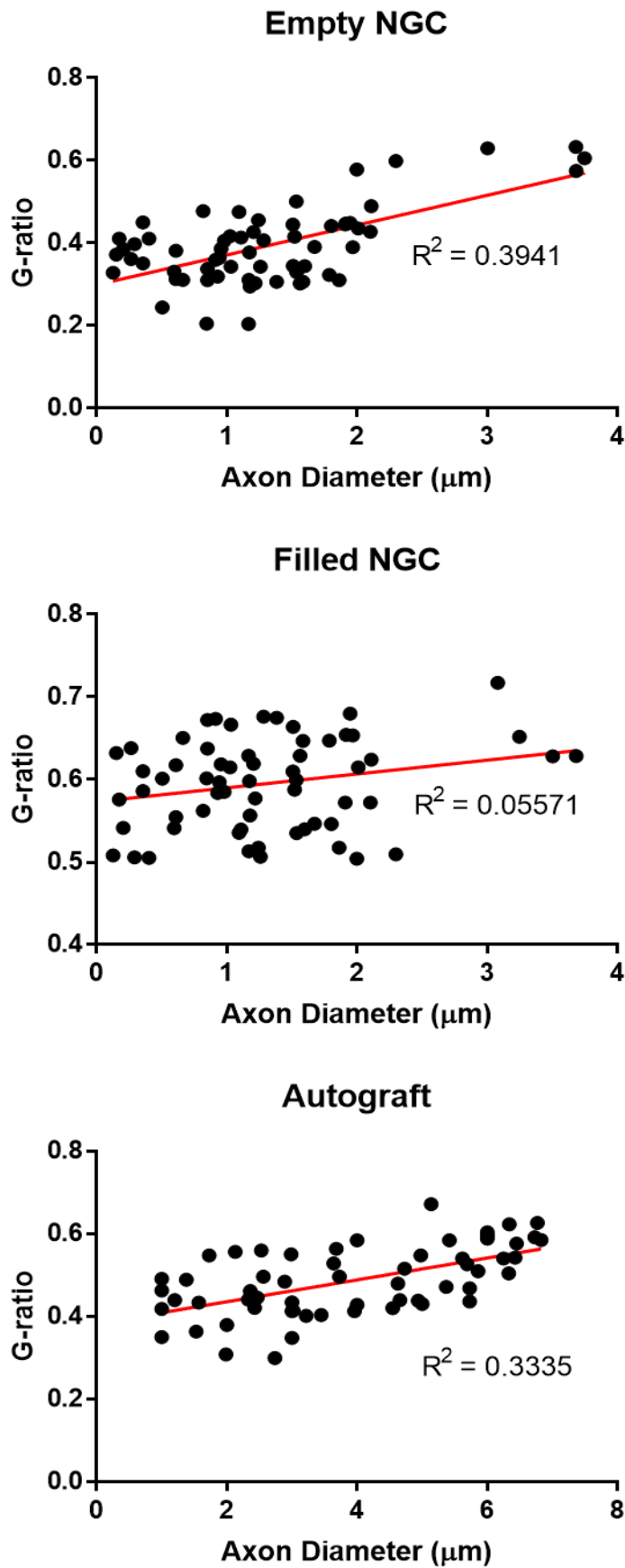
The G-ratio was calculated to show the myelin thickness with respect to the axon diameter (Figure 5.18). A range of G-ratios were calculated given the mixed population of small axons and large axons. This information was correlated to the axon diameter. Only myelinated neurons could be

Measured as these were stained. The coefficient of determination ( $R^2$ ) was calculated using linear regression analysis. The analysis demonstrated a relationship between the G-ratio and axon

thickness for the Autograft ( $R^2 = 0.3335$ ) and Empty NGC ( $R^2 = 0.3941$ ) groups showing that the smallest axons had the highest degree of myelination. Amongst the distribution of axons analysed, there was most axons that were less than  $2.2 \mu\text{m}$  for the Empty NGC and less than  $7.2 \mu\text{m}$  for the Autograft group. However, this relationship was not measured when assessing the Filled NGC ( $R^2 = 0.05771$ ), demonstrating a lower of positive correlation. Furthermore, most axons were less than  $2.4 \mu\text{m}$  although the G-ratio varied.



**Figure 5.17:** Bar charts showing the neuron density (top) and the myelin thickness mean calculations for the proximal, middle and distal portions of the nerve for each test group (Empty NGC, Filled NGC and Autograft).



**Figure 5.18:** Correlations of G-ratio (myelin thickness measure) to the distribution of axon diameters for the three test groups (Empty NGC, Filled NGC and Autograft).



## 5.4 Discussion

### 5.4.1 NGC Final Design

PA6,6 was chosen as a candidate material for use as an NGC material from analysis that supported the hypothesis that the PA6,6 tested was supportive of both glial adhesion, proliferation and alignment as well as NG108-15 neuritogenesis (section 3.3.10 and 3.3.14). The use of PA for cell culture has been previously described, although never tested in an in vivo model (Yoo et al., 2011; Batth and Thompson, 2018). For example, NG108-15 cell attachment and neurite outgrowth has been modelled on PA6,6 meshes.

The data supporting the biocompatibility of the material provided substantial evidence to investigate the use of PA6,6 films as an outer wall material of NGCs (section 3.3.6). Polyamides have been used in vivo for other uses including orbital floor reconstruction, suture material and for intrauterine device implants, thus offering a biocompatible and stable material for long term in vivo implantation (Kamal et al., 1981; Asher et al., 2018; Silas et al., 2018). The use of nylon sutures for ligating nerve and implanting NGCs has been reported extensively (Giddins et al., 1989; Farhadieh et al., 2015).

The long term effect of implantation for the use in nerve repair was investigated in the current study, for up to 103 days post operation. Data collected on animal weight and observations made on a daily basis confirmed no adverse effect of implanting sterile PA6,6 as all animal subjects were able to eat ad libitum and gained weight over the course of the trial (shown by the positive correlation between weight and time, Figure 5.5). A concern during the trial was autophagy which was non-specific to any of the groups trialled (Empty NGC, Filled NGC and Autograft). Nail biting behaviour and bleeding was observed, and the issue was discussed with the resident veterinary surgeon on the AWERB committee, King's College London.

Although signs of autophagy cannot be attributed to the presence of the PA6,6 material, as otherwise the subjects in the trial (non transected nerve data from section 5.3.1-5.3.4) would have shown these signs. From searching the literature, autophagy is a habit that rats display when encountering sensation and can be discouraged by using topical lidocaine to anaesthetise the digits, hydrocortisone to treat the inflammation and a bitter spray to deter the animal from autophagy (Haggerty et al., 2019). In future work, this would be a more suitable protocol as re-

evaluation of the severity of the procedure was not necessary as autophagy was not present in at least half of the subjects.

The use of the CC2 hydrogel was also assessed following the evidence that Schwann cells are able to navigate the 3D environment and proliferate (section 4.3.17). The initial trial (n=3 rats) was used to provide evidence to the AWERB that the implantation procedure did not cause lasting harm or suffering to the subjects and that the use of the PA6,6 NGC did not cause extensive compression on the nerve. The recovery period for the animals from the surgical procedure lasted 21 days when assessed by Hargreaves test (for thermal hyperalgesia) and Von Frey test (for mechanical allodynia) suggesting that sensation was conveyed by the sciatic nerve without extensive sensitisation or compression, although the nerve was not transected in this case. Sensitisation has been shown to be a particular concern in patients who were treated with allograft (Avance processed nerve graft) and therefore the reduction in thermal hyperalgesia provided evidence for the efficacy of the PA6,6 NGC in avoiding this when implanted (Nijran et al., 2019). The use of Histoacryl glue was selected as opposed to suturing the NGC into place during implantation as the glue bonding demonstrated more stability and increased load bearing capability (section 5.3.9). Although a high load is not expected to occur, it is important that the NGC could be sealed to the nerve ends to ensure that no leakage of the CC2 hydrogel occurred which was achieved by gluing (Barton et al., 2014).

#### 5.4.2 Behavioural Data

As reviewed in section 1.3.1, the selection of functional methods of testing the efficacy of NGCs is critical to providing comparable data to other research on NGCs. In the present study tests for mechanical allodynia by stimulation with non-noxious stimuli (Von Frey), tests for thermal hyperalgesia with non-noxious stimuli (Hargreaves) and tests for gait analysis (SFI) were used. From the Von Frey data, it was clear that recovery time was significantly extended following sciatic nerve transection which was expected to take up to 12 weeks (Kaplan et al., 2013). Animals were sensitive to the force exerted by the filaments at the pre-surgery stage although at some time points this sensitivity was lost, particularly during the recovery period (section 5.3.6). Sensitivity had returned to varying degrees dependent on the PNR method used.

Specifically, the CONTRA (non-operated side) remained at baseline levels but there was a clear difference for the ISPI side for Empty NGCs for which the withdrawal threshold decreased but

recovered by 103 days post operation (DPO). However, for filled NGCs, there was clearly an effect whereby the threshold decreased on both CONTRA and IPSI sides – indicating a level of allodynia. This could explain the inability to collect data for the Filled NGC group at 103 DPO for the IPSI side, as neurons may still have been undergoing myelination and non-myelinated pain fibres may still be regenerating. Data was not able to be retrieved on the IPSI side for the Empty NGC group at a much earlier time point possibly due to the animals being distracted or forgetting the training immediately after the operation (2 DPO). For the Autograft group, there was a clear difference between the IPSI side which decreased in threshold whereas the CONTRA side remained fairly constant close to baseline levels except immediately after surgery. This may provide evidence that when Schwann cells are available (as is the case in the autologous tissue provided by the autograft) there is faster recovery of sensitivity to mechanical stimuli. As there was a large decrease in 50% PWT for all groups following the surgery, this suggests that the allodynia experienced occurred as a result of C-fibre extension, the smallest nerve fibres) which may have been followed by larger fibre innervation giving rise to the recovery of sensitivity to mechanical stimulation and recovery of the pre-surgery baseline (reviewed in 1.1.2). The Hargreaves test data provided evidence that no hyperalgesia was present in the current format of the animal trial, which was important to confirm that the animals did not experience any increased pain from the NGC as this technology had never been assessed in vivo before. Further, the recovery of latency to withdraw the paw away from the thermal stimulus to baseline levels was demonstrated in the Empty NGC and Autograft groups, meaning that although sensation of thermal stimuli may have been reduced, it was not completely ablated as mean values did not approach the cut off time of 20s. Although this was demonstrated in the Filled NGC group, where values for latency increased above baseline between 20 and 69 DPO. Further, any decrease in latency may have been attributed to inflammation-induced hyperalgesia as was the case for the Empty NGC, occurring immediately after surgery and subsequent recovery.

These results were indicative of recovery of nerve sensation, although it is difficult to confirm that the responses were entirely due to transection and repair of the sciatic nerve, as it has been demonstrated that the plantar surface can be partly innervated by collateral reinnervation by the saphenous nerve (Gonzalez-Perez et al., 2017). It would be useful to remove this possibility as an optimisation to the current study design in future work, although care was undertaken to only stimulate the paw pad with heavy distribution of nerve fibres from the sciatic nerve.

Recovery of SFI scores indicated repair in the Empty NGC and Autograft groups, but there was a significant difference for the values measured from the Filled NGC group compared to the Autograft group (section 5.3.8). This indicates that filling the NGC with the current formulation of the CC2 hydrogel led to decreased motor innervation as plantar muscle tension was not present to the same degree as other groups, although it may be the case that regeneration of motor fibres was delayed not abolished. It is important to readdress the formulation and physical characteristics of the hydrogel, as it may have been a barrier despite the evidence of cell migration and expansion or the gel may not have been able to degrade as well when confined by the gluing method and the use of PA6,6 film which has a limited porosity. This could be a parameter to improve in future iterations of the current NGC.

#### 5.4.3 Histology

Histology was carried out to confirm that the micro-anatomy of the regenerated nerve resembled the structure of healthy nerve tissue to confirm the presence of both Schwann cells and axons which demonstrates functional recovery. For the initial trial, which occurred for 30 DPO, the presence of the NGC did not disrupt the nerve anatomy (as seen in Figure 5.11) indicating that the material was safe for use as a NGC. PA6,6 was then used as an NGC for implantation into the 10mm sciatic nerve gap injury to regenerate the nerve, which was observed for 103 days (as evaluated from behavioural data in section 5.4.2).

The NGC was compared to the same NGC filled with the CC2 hydrogel and also autograft, the control and gold-standard of repair, which was stained to detect nerve regeneration. As shown in Figure 5.12, Schwann cells had infiltrated through from the proximal site to the distal site when the PA6,6 NGC was used. Although the micro-grooved PA6,6 NGC did not remain closely associated to the nerve following staining due to hydrophilic property of PA6,6 meaning it detached during wax embedding, the material chosen for the NGC was stable and encouraged nerve regrowth through the NGC satisfying this design objective as established in section 2.1.2 (Figure 5.9B). In the case of the Autograft repair method, Schwann cells were supplied by using nerve tissue as a scaffold for regenerating axons and hence it was not surprising that there was a relatively high number of nuclei present (Hansen et al., 2016). However, it was promising that the nuclei density for the Empty NGC and Filled NGC groups were similar as shown by haematoxylin staining (section 5.3.10). However, the H&E staining doesn't specifically differentiate between myelin-expressing tissue (glial cells) and non-myelin tissue (neural cells)

hence Luxol Fast Blue staining with Cresyl Violet counterstain was used to visualise the myelin present in Schwann cells and myelinated axons (Carriel et al., 2014).

In depth analysis of the myelination was demonstrated through calculations taken from the LFB staining (Figures 5.14 to 5.16). The presence of myelinated axons at the proximal, middle and distal sites provided validation to the H&E results that the individual axons were able to extend through the test scaffold (Empty NGC, Filled NGC or Autograft) and that Schwann cells were able to extend through this same environment and closely associate with the neuronal axons. Although there were fewer myelinated axons present in the distal end of the samples, there was evidence of myelination and this can be correlated to the recovery of functional behaviours such as thermal sensitivity (shown by Hargreaves testing in section 5.3.8) and non-noxious mechanical sensitivity (shown by Von Frey tests in section 5.3.7). The results showed that there was comparable nerve regeneration amongst the Empty NGC and the Autograft, as there was a clear correlation between the myelin thickness, number of axons and density of axons measured in section 5.3.11.

These results also show that the lowest mean G-ratio was calculated from the autograft group which correlated to research on crushed Sciatic nerve tissue repaired with autograft, meaning that the presence of Schwann cells from the implanted tissue was conducive to a higher degree of myelination and hence expedited the functional recovery (Godinho et al., 2013). Nevertheless, the positive correlation between G-ratio and axon thickness for the Empty NGC demonstrated the capability for this implant device to support the formation of a tissue bridge between the proximal and distal stumps of the injured nerve, with a variety of small axons with healthy thick myelination. Thicker myelination has previously been shown to correlate with improved regeneration by activating Schwann cells and the lower level of myelination at the distal portion could be explained by the de-differentiation of Schwann cells distally whilst proximally Schwann cells remain differentiated (Ko et al., 2018).

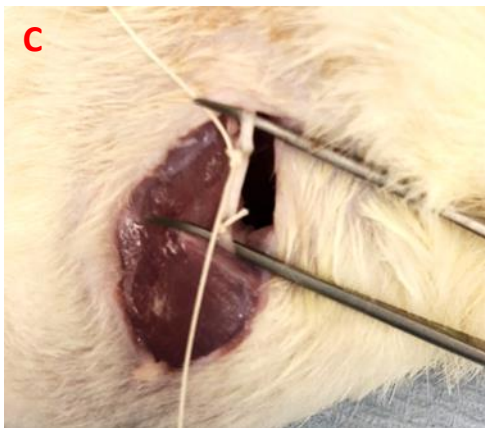
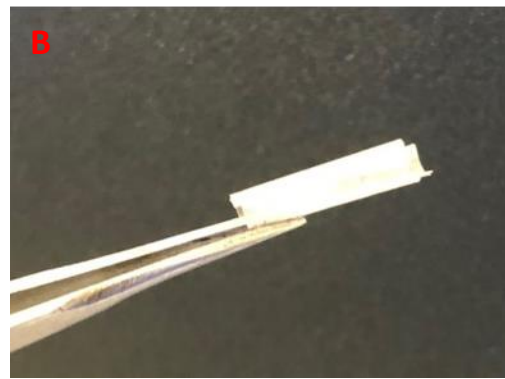
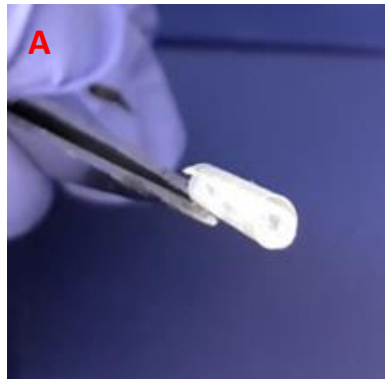
Nerve axons were capable of entering the distal stump for the Filled NGC group, however to a lesser degree than the other groups, and this information validates that the hydrogel material can support the infiltration of neurites although this effect could be enhanced to increase the level of functional recovery which was less than the other two repair methods investigated. The use of the PA6,6 as a tool to compress the gel and stabilise in place could provide an alternative to

cross-linking and matching the host tissue ECM mechanics although this aspect requires further optimisation (Georgiou et al., 2013).

Supplementary Figures

Supplementary Table 5.S1: Table showing patterns of Von Frey stimuli responses and conversion values to calculate 50% PWT

DPO	FILLED CONDUIT				50%PWT				AUTOGRAFT				EMPTY NGC				50%PWT								
	C	Luf	I	Ref	L	R	C	Luf	I	Ref	L	R	C	Luf	I	Ref	L	R	C	Luf	I	Ref	L	R	
0	00000	5.18 000000		5.18	15	15	00000		5.18 00000X	4.74	15	4.34	00000		5.18 000000		5.18	15	11.95				5.18	15	11.95
	0000000	4.93 0000000		4.93	10.36	6.91	000000X		4.93 000000X	4.93	6.74	5.77	0000000X		5.18 000000X		5.18	11.98	7.96				5.18	11.98	7.96
	0000000X	5.18 000000X		4.93	11.98	6.74	00000		5.18 000000X	5.18	#N/A	10.27	00000		5.18 000000X		4.93	15	7.91				4.93	15	7.91
	0000000X	5.18 000000X		5.18	11.98	11.98	000000X		5.18		11.98	#N/A	000000X		5.18			11.98	#N/A				5.18	11.98	#N/A
2	00000	5.18 000000		4.93	15	5.93	000000X		5.18 000000	4.93	11.98	6.91	000000X		5.18			11.98	#N/A				5.18	11.98	#N/A
	0000000	4.93 0000000		4.74	7.43	8.99	000000X		4.93		6.74	N/A	00000		5.18			6.74	15	#N/A			5.18	15	#N/A
	0000000X	5.18			11.98	#N/A	000000X		5.18 000000X	4.93	11.98	7.91	00000		5.18 000000X		5.18	15	11.98				5.18	15	11.98
20	0000000X	4.93 0000000		4.74	6.74	8.99	00000		5.18 000000	4.93	15	5.93	00000		5.18 000000X		5.18	15	11.98				5.18	15	11.98
	0000000X	5.18			11.98	#N/A	00000		5.18 0000000	4.74	15	10.46	000000X		5.18 000000X		5.18	11.98	11.98				5.18	11.98	11.98
56	0000000X	4.93 000000		4.31	6.74	3.66	00000		5.18		15	#N/A	00000		5.18 000000X		4.74	15	7.84				4.74	15	7.84
	00000	5.18 0000000		4.74	15	8.99	00000		5.18		15	#N/A	00000		5.18 000000X		4.93	14.05	5.77				4.93	14.05	5.77
69	00000	5.18 000000X		4.93	15	7.91	00000		5.18 000000X	5.18	15	6.74	00000		5.13 000000X		5.18	15	11.98				5.18	15	11.98
	0000000X	5.18 000000X		5.18	11.98	11.98	000000X		5.18 000000X	5.18	11.98	4.35	000000X		4.93 000000X		4.93	6.74	6.74				4.93	6.74	6.74
103	00000	5.18			15	#N/A	00000		5.18 000000X	4.93	15	11.98	000000X		5.18 000000X		5.18	11.98	10.36				5.18	11.98	10.36
	0000000X	5.18			11.98	#N/A	00000		5.18 000000X	4.74	15	11.98	000000X		5.18 0000000		4.93	11.98	11.98				4.93	11.98	11.98



**Figure 5.S1 Supplementary Figures:**

*A and B – Images to showcase the final NGC spiral shape and design.*

*C – Image to show the method of suturing used to seal the autograft as comparable to similar studies on PNR.*

*D – PA6,6 NGC during implantation into the Sciatic Nerve*



## Chapter 6: Thesis Discussion

### 6.1 Discussion

The aim of the work presented in this thesis was to establish a robust methodology to evaluate materials intended for use in peripheral nerve regeneration and to translate these materials into a usable medical device and evaluate key outcomes of nerve regeneration. Although there are many NGCs available, the theme of this research was to apply an engineering paradigm to correctly identify examinable design parameters (inputs) within the literature that are critical to the success of the device, as this has not been carried out before. As the design parameters have been selected, they were then evaluated through *in vitro* testing and in the animal model so that the data (outputs) could be used to inform future studies to optimise the design. Thus an iterative circle of work has been established to open up the field of research.

From literature search, it was identified that most NGCs available are cylindrical structures with an internal lumen. The luminal compartment may consist of additional materials which are intended to supply support to infiltrating neurites and encourage Schwann cell proliferation. Commonly, the NGC is biodegradable in order to limit extraneural pressure which has been shown to reduce regeneration (Nectow et al., 2012) and porous to encourage diffusion of neurotrophic factors which signal Schwann cells to carry out the repair programme after injury (Jessen and Mirsky, 2019). However, a high porosity can lead to leakage of important diffusible factors.

In addition, as medical devices NGCs must also be biocompatible and support the extension of axons which travel through the NGC to re-establish connection from the proximal to the distal stumps produced following injury and restore nerve function. It is obvious that a suitable NGC that can be used to replace the current use of autografts would comprise multiple design features as discussed e.g. porous, biocompatible, supportive of neural cell function and degradable. However, there are many complicated NGCs that have been prototyped and tested *in vivo* that only reach a comparable level of regeneration to autografting. For example, engineered neural tissue uses aligned Schwann cells as an implantable medical device for nerve regeneration, however when assessed for myelination, they resulted in comparable G-ratios and myelin thickness in the most dense regions of the nerve containing axons (Georgiou et al., 2015). Another system comprising a synthetic poly( $\epsilon$ -caprolactone) resulted in hindered nerve

regeneration as a result of including aligned electrospun fibres which may inhibit axon extension by providing a barrier not a pathway for growth despite promising results in vitro (Daud et al., 2012). These studies demonstrate the difficulty in engineering nerve tissue due to the many cell types present within the injury environment responding to distinct cell signalling cues. Even the use of cell adhesive motifs to promote Schwann cell adherence by inclusion of poly(dopamine) and arginylglycylaspartic acid (RGD) in conjunction with an electrically conductive graphene scaffold led to potential results indicating myelination although the myelin thickness was still greatest in the autograft group and not the designed conduit despite pre-loading with Schwann cells (Qian et al., 2018).

Despite these advances, the nature of this project was to identify critical factors that need improving in NGC design and to evaluate these parameters using models. Hence, the causes of nerve repair were analysed and summarised to be mainly trauma-related (section 1.2.4). Ideally repair of nerve damaged during trauma would occur as soon as possible, as the longer the nerve is not repaired the higher the likelihood of loss of nerve function as shown by the clinical data (Gerth et al., 2015). If nerve repair surgery occurs as soon as possible following trauma, then the medical device used for repair must be readily available at the required size. Therefore, the NGC design presented focusses on an efficient implantation procedure to increase the likelihood of nerve regeneration. The advantage of designing the NGC presented in this thesis was that the 200 $\mu$ m wall thickness allows the sheet of thermoplastic PA6,6 to be rolled to the correct size and this shape can be set using a steel rod heated to below the melting temperature (210°C). This means that the NGC loose structure can be predetermined before packaging so that in the clinic, the NGC can be approximated to the injury and rolled around the nerve stumps to the correct size before being sealed using a bioadhesive glue (in this thesis histoacrylate glue was used, section 5.2.3). The design for sutureless repair presented another advantage as the use of sutures in nerve repair can lead to increased trauma of the perineurium and increased fibrosis and loss Schwann cells as only Schwann cells at the proximal stump remain differentiated whereas many cells are lost due to Wallerian degeneration (Dahlin, 2008 and reviewed in section 1.2).

The process of implanting the NGC including injection of the hydrogel for the Filled NGC lasted 15 minutes from exposing the nerve and fitting the device with histoacryl glue, hence the speed of implantation as a design output was effectively evaluated. This feature should be further studied and compared to operating time associated with fitting NGCs available clinically.

The use of PA6,6 has not been reported for use as a wall material in PNR however the results outlined in this thesis support the use of polyamides for this application, especially as they can be used to provide versatile structures which may increase the rate of regeneration. The inclusion of regular microgrooves provided an interesting insight into the use of hot embossing as a method for controlling neural alignment, as the microgrooves could be embossed with high efficacy (Figure 5.9). However, the size of the grooves presents another area for further study. Although outside the scope of this thesis, neural cell patterning by use of microgrooves could encourage axons in vivo to guide towards the distal target (Mobasseri et al., 2015). However, it is important to provide a physical cue at the scale of the tissue and not individual axons as it was evident that microgrooves on the NGC surface did not affect the most central axons shown by LFB staining even though they were aligned shown by the parallel arrangement of fibres (section 5.3.11). This parameter for instance would be re-evaluated as a non-critical feature of the NGC unless the microgroove scale was increased and hence wouldn't feature in the next iteration of the in vivo experiments until a suitable hypothesis could be postulated for the inclusion of microgrooves at this size (10µm in height) from further in vitro work or new literature.

The inclusion of a hydrogel system was selected as a key design feature due to the need for continued contact between the NGC and the proximal nerve stump in order to mimic the action of autografted tissue which provides a pathway for the infiltrating axons (Carballo-Molina and Velasco, 2015). The use of collagen and chitosan hydrogels was selected through successive assays to measure the biocompatibility and cell viability of both neural and glia cells (section 4.3.7). Both materials were chosen in conjunction as there was clear evidence that chitosan provided viscoelastic stiffness properties whereas the use of collagen provided cell adhesive substrates and this led to the hypothesis that the CC2 hydrogel would provide optimal cell infiltration in vivo after characterising neural differentiation mediated by Schwann cells (section 4.3.14) and cell encapsulation (section 4.3.17) in vitro. However, the use of the hydrogel (Filled NGC) did not lead to increased functional outcomes as there the results from the in vivo trial indicated that rats receiving the hydrogel were not able to sense the non-noxious mechanical force from the Von Frey apparatus (section 5.2.4) and the Hargreaves test results showed that these rats were not as responsive to the thermal stimulus (section 5.2.5) although rats in the Empty NGC and Autograft groups returned to baseline levels for both tests by 103 DPO.

Interestingly, these results correlated with the histology which revealed that the Filled NGC did contain myelinated axons but there was a reduction in axon density and myelin thickness and further the lack of correlation between the G-ratio and axon thickness revealed that the myelination process may have been incomplete (section 5.3.11). The inclusion of the hydrogel system is a key parameter which requires further optimisation as the in vitro results which demonstrated that the gel supports a higher degree of neurite extension was not backed up by the in vivo results which showed that re-innervation of the nerve was slowest. This may be attributed to the lower number of animals used in the study (3 rats per group) or further characterisation of the hydrogel system may demonstrate why the cells were not as capable of infiltrating the gel. The gel biodegradability was not studied in this project, and it may be the case that the hydrogel had degraded too quickly to encourage the cells to proliferate within it, further work on Schwann cell proliferation within the hydrogel and closer inspection of the cell encapsulation assay could provide an understanding of how these cells migrate through the hydrogel and whether the compression from the NGC PA6,6 wall meant that efficient nutrient exchange should be further examined.

Although the functional tests used in this study provided insight into the re-innervation of the Sciatic nerve following the repair surgery, the measures were not directly relatable to the extent of nerve regeneration. For instance, the Sciatic nerve functional index is reliant on clear footprints, however raising of the paw following surgery was a common feature amongst animals regardless of the experimental group and this was not mitigated by use of the opioid analgesic to reduce pain sensitivity (Figure 5.8). It was clear that the SFI did provide an overall trend for assessment however as all animals returned close to the baseline levels (a positive value for SFI). This could be improved by measuring gait with video recording as this could lead to more reliable results which could have been affected by ink smudging in the current study. Also, the use of mechanical allodynia and thermal sensitivity assays (the Von Frey and Hargreaves tests respectively) as measures of nerve regeneration could be improved as although these tests ensure that non-noxious stimuli are applied, they don't directly measure the sensory or motor feedback response over time.

Nerve conduction velocity, two-point discrimination and electromyography tests may provide an increased insight into the speed of action potential propagation as a function of remyelination.

Electromyography for example provide a direct means of investigating the re-innervation of the nerve by motor axons however this would require additional expertise in electrophysiology.

The design outputs from this thesis that were obtained include an NGC of the correct proportions that could be handled and implanted within 15 minutes, that was biocompatible and non-toxic and encouraged axon infiltration accompanied by re-myelination. These aspects of the NGC can now be fine-tuned in future work or used in conjunction with the new design outputs generated as areas for future work.

## 6.2 Conclusions

In conclusion, this thesis demonstrates a new pathway for generating hypotheses related to generating a medical device with optimal properties to enhance nerve regeneration within the rat sciatic nerve model for peripheral nerve transection and repair to a functional level. The NG108-15 and Schwann cell culture method has been optimised and shown to be robust for modelling an array of both solid and hydrogel materials in 2D cultures as well as modelling cell encapsulation in organotypic and gliospheroid cultures in 3D. The work has established a methodology for examining materials intended for use in vivo as nerve repair materials, including assays for biocompatibility, cytotoxicity, cell adhesion, cell spreading, cell differentiation and cell excitability.

These measurable outputs were obtainable because the design stage which is not often reported or formally arranged in scientific papers was defined by using inputs derived from the literature to identify key parameters of a NGC that must be controlled for validation testing including a flexible conduit that is safe for long term implantation, sutureless and supportive of neuroglial interactions. The in vitro culture and material characterisation were used to develop two test NGCs; the Empty NGC and Filled NGC. These designs have been shown to encourage axon re-innervation within rat Sciatic nerve following nerve transection and crucially the Empty conduit provided comparable levels of remyelination to the Autograft (control) group. This translational work has proven that PA6,6 is a suitable neural scaffold and that the chitosan/collagen hydrogel warrants further research before being justified as more promotive of nerve regeneration than the control. Therefore, further work on the hydrogel system and optimisation of the current NGC format is justified to bring about impactful clinical benefit in managing nerve injuries that result from trauma or iatrogenic causes.

## Chapter 7: Future Work

A level of nerve regeneration was achieved by using the PA6,6 based NGC in the current study and this design was compared to the autograft as a control repair strategy. However, more validation is required to provide enough evidence to suggest that the PA6,6 NGC can replace the Autograft as a standard PNR method.

The in vitro experiments using model cells for PNR relied on Schwann cells and NG108-15 as representative glial and neural cells respectively. Experiments using Schwann cells relied on identification of these cells by morphology or staining for the S100 protein, however this gave no insight into the relative activity of these cells when cultured on different surfaces (i.e. changes in the physico-chemical environment). Therefore, markers for Schwann cell function on the prospective scaffolds could give key indications into the adhesion forces between the cell membrane and the polymer, for example staining for vimentin can allow for quantification of cell adhesion complexes or measuring gene expression in these cells by real-time polymerase chain reaction (RT-PCR) can provide differences between relative expression of genes involved in cell adhesion. For the NG108-15 cells, the model provided a means to categorise the expected neural response to the scaffolds examined. However, as it was specifically the axonal response being measured, it would be more useful to separate the cell bodies from the neurites by using specially designed chambers. This could be further optimised by staining specifically for the axon and then quantifying these processes and the hydrogel could be optimised to support axon extension. Another method for increasing the relevance of the cell models chosen would be to increase the use of the DRG model, as this provides a direct comparison of simultaneous neuro-glial interactions on the scaffold being tested and consists of primary tissue which is a closer representative of neural tissue. Experiments on DRGs would be optimised to further examine the interactions of the extensions in 3D space which could be followed at more imaging time points (between 3 and 10 days) and for longer to examine the upper limit to the length to which the neurites can extend. The hydrogel system could be further investigated as the materials characterisation only confirmed the properties of the hydrated hydrogel, however if the materials were freeze-dried a porous structure could be modified to include cell adhesive chemistry, release neurotrophic factors and optimised to encourage efficient nutrient diffusion. Furthermore, it would be beneficial to combine more electrophysiological tools to examine how neuronal physiology is affected by the scaffold properties. However, this would ideally be carried

out on primary neurons derived from the DRG or primary motor neurons which could then be characterised for their relative excitability. However, when comparing the in vitro model of nerve repair to the in vivo model, it is rare to trace the excitability of nerve tissue other than following nerve conduction velocity which increases as the level of myelination increases. Electromyography offers an alternative electrophysiological measure, but this is an indirect measurement of the nerve excitability by measuring the compound muscle action potential. A more invasive technique would involve field recordings from the regenerated nerve directly and has not been described in the literature.

Further work to improve the NGC as a medical device would ideally involve the use of stem cells that could differentiate into Schwann cells as a readily available source of pluripotent cells that can increase functional recovery by encouraging remyelination of fibres and faster axon extension. This may be why the Autograft promotes superior nerve regeneration. Stem cells could be either induced Pluripotent Stem Cells (iPSCs) or Mesenchymal Stem Cells (MSCs) as both populations have been shown to increase myelination measures in PNR when differentiated into neural crest-like cells (Kimura et al., 2018).

Crucially, rather than looking into expanding the Schwann cell population by use of stem cells, macrophages could be used to drive angiogenesis as this lineage of cells have been shown to promote nerve regeneration during hypoxia by forming contact-mediated pathways for Schwann cells to infiltrate the implant and could encourage efficient nutrient exchange more quickly which may expedite recovery (Cattin et al., 2015).

Future work for the in vivo portion of the thesis would involve optimising the behavioural testing and the histology. Besides requiring more animals and more time points for data collection to validate the trends seen amongst the three repair methods investigated (Empty NGC, Filled NGC and Autograft), the behavioural tests chosen could more closely match the clinical objectives sought after. Measuring electromyography and nerve conduction velocity provide quantified measures of motor and sensory functions. The animal trials could also be carried out more objectively by using an independent reviewer or second assessor of the animal responses as errors may be made when discerning the behaviours. Further, the histology could be imaged at a higher resolution to calculate the myelin thickness more precisely, given that the G-ratio (a measure of myelination) was derived from images using a 40X objective, by using transmission electron microscopy (TEM).

## V: Acknowledgements

My Father has often told me that certain people appear in life and totally change it for the better; this is certainly true. I am deeply grateful to Dr Ian Thompson for his kind heart, belief in my ability and above all loving friendship. Ian, you have passed to me a gift that you were fortunate to receive from the late Professor Larry Hench, and I in return treasure your generosity of time and thought into my development and our life-long friendship to come.

This PhD and important journey of discovery would not be possible without the scientific encouragement of my supervisory panel. Here, I thank Dr Eileen Gentleman and Professor Agi Grigoriadis for your commitment to making the project more rigorous, your generosity and kindness in including me in your respective research groups.

My family have fought hard to provide stability and the best opportunities in education one could experience. I will forever be grateful to my parents, Sukhbinder and Sukhpal, for their love and encouragement. My grandmother, Biji, for her love. My older brothers and sister-in-law, Tajinder, Parminder and Aman, for their belief in the wonderful benefits of Higher Education and parenting. I also thank my identical twin brother, Karan, for being there with me every step of the way – I have had the privilege of sharing every milestone with you and you inspire me. I also thank my nieces and nephews (Kim, Serenna, Aaryann and Yuvraj), for their interest in my endeavours. I want to thank my close friends without whom I would have lacked the encouragement to enjoy the time; Marcin Kotarba, Rachel Foulger, Rachel Ademokun, Vicky Ansell, Louise Tearle, Matthew Slauson, Claudia Newbury, Anna Korzeniowska, Dr Carly Schott and Suzette Lust.

During this PhD, Floor 17 of Guy's Tower has been a place of fantastic challenge and opportunity. I would like to thank the academics who have provided critical input; Professor Richard Cook, Professor Lucy di Silvio, Professor Sanjukta Deb, Dr Lorenzo Veschini, Dr Andrea Serio, Hassan Farah, Pete Pilecki, Dr Lilis Iskandar and Dr Petros Mylonas. In addition, I thank Marzieh Sandi for her kind support and the laughs we have had together in the office.

And finally, without reserve, I thank the wonderfully talented and bright medical students that I have supervised during this project. You have provided intellectual stimulation, support and friendship amongst the 18 months we spent together in the lab. I am grateful to be friends (Aditi



Nijhawan, Devyani Shete and Siddarth Raj) and I hope that our work has been a source for personal development as well as helping in your training.

#### VI: Publications/ Abstracts

Batth, A. and Thompson, I. (2018). Nylon as an in vitro scaffold for three-dimensional study of neural cells. *Journal of Biomedical Materials Research Part A*, 106(6), pp.1575-1584.

Batth, A. and Thompson, I. (2018) 'In Vitro Assessment for Peripheral Nerve Regeneration: Study of a Biphasic Nylon and Chitosan/Collagen Conduit.' *J Dent Res* Vol 97B

Shete, D., Batth, A., Nijhawan, A., Choudhary, J. and Thompson, I. (2019). Producing Neurospheroids and Hydrogels to Create a Three-dimensional in Vitro Model for the Use of Conduits in Peripheral Nerve Regeneration. *Neurosurgery*, 84(5), pp.E272-E272.